## NOTICE

## AVIS

The quality of this microform is heavily dependent upon the quality of the original thesis submitted for microfilming. Every effort has been made to ensure the highest quality of reproduction possible.

La qualité de cette microforme dépend grandement de la qualité de la thèse soumise au microfilmage. Nous avons tout fait pour assurer une qualité supérieure de reproduction.

If pages are missing, contact the university which granted the degree.

S'il manque des pages, veuillez communiquer avec l'université qui a conféré le grade.

Some pages may have indistinct print especially if the original pages were typed with a poor typewriter ribbon or if the university sent us an inferior photocopy.

La qualité d'impression de certaines pages peut laisser à désirer, surtout si les pages originales ont été dactylographiées à l'aide d'un ruban usé ou si l'université nous a fait parvenir une photocopie de qualité inférieure.

Canada

UNIVERSITY OF ALBERTA

NUMERICAL INVESTIGATION OF ECCENTRICALLY LOADED
TIED HIGH STRENGTH CONCRETE COLUMNS

BY

© JUEREN XIE

A THESIS
SUBMITTED TO THE FACULTY OF GRADUATE STUDIES AND RESEARCH
IN PARTIAL FULFILLMENT OF THE REQUIREMENTS FOR THE DEGREE OF

DOCTOR OF PHILOSOPHY

DEPARTMENT OF CIVIL ENGINEERING

EDMONTON, ALBERTA

FALL 1994

The author has granted an irrevocable non-exclusive licence allowing the National Library of Canada to reproduce, loan, distribute or sell copies of his/her thesis by any means and in any form or format, making this thesis available to interested persons.

L'auteur a accordé une licence irrévocable et non exclusive permettant à la Bibliothèque nationale du Canada de reproduire, prêter, distribuer ou vendre des copies de sa thèse de quelque manière et sous quelque forme que ce soit pour mettre des exemplaires de cette thèse à la disposition des personnes intéressées.

The author retains ownership of the copyright in his/her thesis. Neither the thesis nor substantial extracts from it may be printed or otherwise reproduced without his/her permission.

L'auteur conserve la propriété du droit d'auteur qui protège sa thèse. Ni la thèse ni des extraits substantiels de celle-ci ne doivent être imprimés ou autrement reproduits sans son autorisation.

Canada

Name **Xie, Jueren**

Dissertation Abstracts International is arranged by broad, general subject categories. Please select the one subject which most nearly describes the content of your dissertation. Enter the corresponding four-digit code in the spaces provided.

**Civil Engineering**
SUBJECT TERM

0 5 4 3  **U·M·I**
SUBJECT CODE

## Subject Categories

# THE HUMANITIES AND SOCIAL SCIENCES

**COMMUNICATIONS AND THE ARTS**
| | |
|---|---|
| Architecture | 0729 |
| Art History | 0377 |
| Cinema | 0900 |
| Dance | 0378 |
| Fine Arts | 0357 |
| Information Science | 0723 |
| Journalism | 0391 |
| Library Science | 0399 |
| Mass Communications | 0708 |
| Music | 0413 |
| Speech Communication | 0459 |
| Theater | 0465 |

**EDUCATION**
| | |
|---|---|
| General | 0515 |
| Administration | 0514 |
| Adult and Continuing | 0516 |
| Agricultural | 0517 |
| Art | 0273 |
| Bilingual and Multicultural | 0282 |
| Business | 0688 |
| Community College | 0275 |
| Curriculum and Instruction | 0727 |
| Early Childhood | 0518 |
| Elementary | 0524 |
| Finance | 0277 |
| Guidance and Counseling | 0519 |
| Health | 0680 |
| Higher | 0745 |
| History of | 0520 |
| Home Economics | 0278 |
| Industrial | 0521 |
| Language and Literature | 0279 |
| Mathematics | 0280 |
| Music | 0522 |
| Philosophy of | 0998 |
| Physical | 0523 |

| | |
|---|---|
| Psychology | 0525 |
| Reading | 0535 |
| Religious | 0527 |
| Sciences | 0714 |
| Secondary | 0533 |
| Social Sciences | 0534 |
| Sociology of | 0340 |
| Special | 0529 |
| Teacher Training | 0530 |
| Technology | 0710 |
| Tests and Measurements | 0288 |
| Vocational | 0747 |

**LANGUAGE, LITERATURE AND LINGUISTICS**
| | |
|---|---|
| Language | |
| General | 0679 |
| Ancient | 0289 |
| Linguistics | 0290 |
| Modern | 0291 |
| Literature | |
| General | 0401 |
| Classical | 0294 |
| Comparative | 0295 |
| Medieval | 0297 |
| Modern | 0298 |
| African | 0316 |
| American | 0591 |
| Asian | 0305 |
| Canadian (English) | 0352 |
| Canadian (French) | 0355 |
| English | 0593 |
| Germanic | 0311 |
| Latin American | 0312 |
| Middle Eastern | 0315 |
| Romance | 0313 |
| Slavic and East European | 0314 |

**PHILOSOPHY, RELIGION AND THEOLOGY**
| | |
|---|---|
| Philosophy | 0422 |
| Religion | |
| General | 0318 |
| Biblical Studies | 0321 |
| Clergy | 0319 |
| History of | 0320 |
| Philosophy of | 0322 |
| Theology | 0469 |

**SOCIAL SCIENCES**
| | |
|---|---|
| American Studies | 0323 |
| Anthropology | |
| Archaeology | 0324 |
| Cultural | 0326 |
| Physical | 0327 |
| Business Administration | |
| General | 0310 |
| Accounting | 0272 |
| Banking | 0770 |
| Management | 0454 |
| Marketing | 0338 |
| Canadian Studies | 0385 |
| Economics | |
| General | 0501 |
| Agricultural | 0503 |
| Commerce-Business | 0505 |
| Finance | 0508 |
| History | 0509 |
| Labor | 0510 |
| Theory | 0511 |
| Folklore | 0358 |
| Geography | 0366 |
| Gerontology | 0351 |
| History | |
| General | 0578 |

| | |
|---|---|
| Ancient | 0579 |
| Medieval | 0581 |
| Modern | 0582 |
| Black | 0328 |
| African | 0331 |
| Asia, Australia and Oceania | 0332 |
| Canadian | 0334 |
| European | 0335 |
| Latin American | 0336 |
| Middle Eastern | 0333 |
| United States | 0337 |
| History of Science | 0385 |
| Law | 0398 |
| Political Science | |
| General | 0615 |
| International Law and Relations | 0616 |
| Public Administration | 0617 |
| Recreation | 0814 |
| Social Work | 0452 |
| Sociology | |
| General | 0626 |
| Criminology and Penology | 0627 |
| Demography | 0938 |
| Ethnic and Racial Studies | 0631 |
| Individual and Family Studies | 0628 |
| Industrial and Labor Relations | 0629 |
| Public and Social Welfare | 0630 |
| Social Structure and Development | 0700 |
| Theory and Methods | 0344 |
| Transportation | 0709 |
| Urban and Regional Planning | 0999 |
| Women's Studies | 0453 |

# THE SCIENCES AND ENGINEERING

**BIOLOGICAL SCIENCES**
| | |
|---|---|
| Agriculture | |
| General | 0473 |
| Agronomy | 0285 |
| Animal Culture and Nutrition | 0475 |
| Animal Pathology | 0476 |
| Food Science and Technology | 0359 |
| Forestry and Wildlife | 0478 |
| Plant Culture | 0479 |
| Plant Pathology | 0480 |
| Plant Physiology | 0817 |
| Range Management | 0777 |
| Wood Technology | 0746 |
| Biology | |
| General | 0306 |
| Anatomy | 0287 |
| Biostatistics | 0308 |
| Botany | 0309 |
| Cell | 0379 |
| Ecology | 0329 |
| Entomology | 0353 |
| Genetics | 0369 |
| Limnology | 0793 |
| Microbiology | 0410 |
| Molecular | 0307 |
| Neuroscience | 0317 |
| Oceanography | 0416 |
| Physiology | 0433 |
| Radiation | 0821 |
| Veterinary Science | 0778 |
| Zoology | 0472 |
| Biophysics | |
| General | 0786 |
| Medical | 0760 |

**EARTH SCIENCES**
| | |
|---|---|
| Biogeochemistry | 0425 |
| Geochemistry | 0996 |

| | |
|---|---|
| Geodesy | 0370 |
| Geology | 0372 |
| Geophysics | 0373 |
| Hydrology | 0388 |
| Mineralogy | 0411 |
| Paleobotany | 0345 |
| Paleoecology | 0426 |
| Paleontology | 0418 |
| Paleozoology | 0985 |
| Palynology | 0427 |
| Physical Geography | 0368 |
| Physical Oceanography | 0415 |

**HEALTH AND ENVIRONMENTAL SCIENCES**
| | |
|---|---|
| Environmental Sciences | 0768 |
| Health Sciences | |
| General | 0566 |
| Audiology | 0300 |
| Chemotherapy | 0992 |
| Dentistry | 0567 |
| Education | 0350 |
| Hospital Management | 0769 |
| Human Development | 0758 |
| Immunology | 0982 |
| Medicine and Surgery | 0564 |
| Mental Health | 0347 |
| Nursing | 0569 |
| Nutrition | 0570 |
| Obstetrics and Gynecology | 0380 |
| Occupational Health and Therapy | 0354 |
| Ophthalmology | 0381 |
| Pathology | 0571 |
| Pharmacology | 0419 |
| Pharmacy | 0572 |
| Physical Therapy | 0382 |
| Public Health | 0573 |
| Radiology | 0574 |
| Recreation | 0575 |

| | |
|---|---|
| Speech Pathology | 0460 |
| Toxicology | 0383 |
| Home Economics | 0386 |

**PHYSICAL SCIENCES**

**Pure Sciences**
| | |
|---|---|
| Chemistry | |
| General | 0485 |
| Agricultural | 0749 |
| Analytical | 0486 |
| Biochemistry | 0487 |
| Inorganic | 0488 |
| Nuclear | 0738 |
| Organic | 0490 |
| Pharmaceutical | 0491 |
| Physical | 0494 |
| Polymer | 0495 |
| Radiation | 0754 |
| Mathematics | 0405 |
| Physics | |
| General | 0605 |
| Acoustics | 0986 |
| Astronomy and Astrophysics | 0606 |
| Atmospheric Science | 0608 |
| Atomic | 0748 |
| Electronics and Electricity | 0607 |
| Elementary Particles and High Energy | 0798 |
| Fluid and Plasma | 0759 |
| Molecular | 0609 |
| Nuclear | 0610 |
| Optics | 0752 |
| Radiation | 0756 |
| Solid State | 0611 |
| Statistics | 0463 |

**Applied Sciences**
| | |
|---|---|
| Applied Mechanics | 0346 |
| Computer Science | 0984 |

| | |
|---|---|
| Engineering | |
| General | 0537 |
| Aerospace | 0538 |
| Agricultural | 0539 |
| Automotive | 0540 |
| Biomedical | 0541 |
| Chemical | 0542 |
| Civil | 0543 |
| Electronics and Electrical | 0544 |
| Heat and Thermodynamics | 0348 |
| Hydraulic | 0545 |
| Industrial | 0546 |
| Marine | 0547 |
| Materials Science | 0794 |
| Mechanical | 0548 |
| Metallurgy | 0743 |
| Mining | 0551 |
| Nuclear | 0552 |
| Packaging | 0549 |
| Petroleum | 0765 |
| Sanitary and Municipal | 0554 |
| System Science | 0790 |
| Geotechnology | 0428 |
| Operations Research | 0796 |
| Plastics Technology | 0795 |
| Textile Technology | 0994 |

**PSYCHOLOGY**
| | |
|---|---|
| General | 0621 |
| Behavioral | 0384 |
| Clinical | 0622 |
| Developmental | 0620 |
| Experimental | 0623 |
| Industrial | 0624 |
| Personality | 0625 |
| Physiological | 0989 |
| Psychobiology | 0349 |
| Psychometrics | 0632 |
| Social | 0451 |

UNIVERSITY OF ALBERTA

RELEASE FORM

NAME OF AUTHOR:     JUEREN XIE

TITLE OF THESIS:  NUMERICAL INVESTIGATION OF ECCENTRICALLY
                  LOADED TIED HIGH STRENGTH CONCRETE COLUMNS

DEGREE:     DOCTOR OF PHILOSOPHY
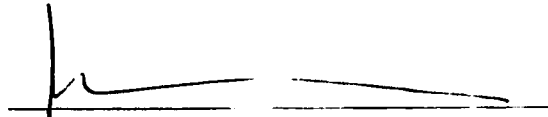
YEAR THIS DEGREE GRANTED: 1994

Xie Jueren

DEPARTMENT OF CIVIL ENGINEERING,
UNIVERSITY OF ALBERTA,
EDMONTON, ALBERTA, CANADA T6G 2G7

Oct 6th, 1994

UNIVERSITY OF ALBERTA

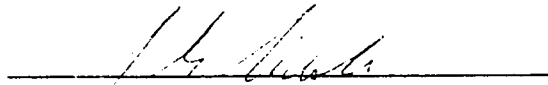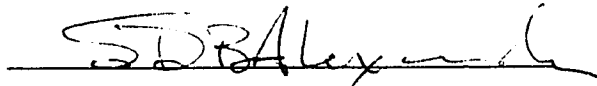FACULTY OF GRADUATE STUDIES AND RESEARCH

THE UNDERSIGNED CERTIFY THAT THEY HAVE READ, AND RECOMMEND TO THE FACULTY OF GRADUATE STUDIES AND RESEARCH FOR ACCEPTANCE, A THESIS ENTITLED NUMERICAL INVESTIGATION OF ECCENTRICALLY LOADED TIED HIGH STRENGTH CONCRETE COLUMNS SUBMITTED BY JUEREN XIE IN PARTIAL FULFILLMENT FOR THE DEGREE OF **DOCTOR OF PHILOSOPHY**.

DR. A. E. ELWI (CO-SUPERVISOR)
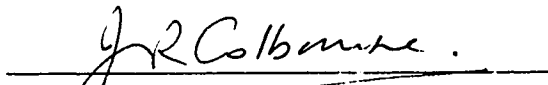
DR. J. G. MACGREGOR (CO-SUPERVISOR)

DR. S. D. B. ALEXANDER

DR. F. E. HICKS

DR. J. R. COLBOURNE

DR. D. MITCHELL (EXTERNAL EXAMINER)

DATE: Oct. 6, 1994

# ABSTRACT

High strength concrete is a new construction material with enormous potential. Structures using high strength concrete are becoming more and more popular. However, the application of high strength concrete to structures, especially in seismic regions, is questioned as the ductility of the material is poor under unconfined conditions. The ductile performance of reinforced concrete columns can be improved if provided with sufficient transverse reinforcement.

The mechanical properties of three high strength concretes containing silica fume are investigated. The test results are used to modify and calibrate a fracture energy-based non-associated plasticity model for high strength concrete. The model is verified by analyzing four tied high-strength concrete columns tested by Ibrahim and MacGregor at University of Alberta. The finite element analysis has successfully captured the load-deformation response, along with important information such as the strain softening and spalling of the cover, the development of a triaxial stress state of concrete in the column core, and the yielding of ties.

A parametric study of tied high strength concrete columns subjected to eccentric loading is conducted. Twenty-one specimens forming nine series are analyzed. The parameters involved in the analysis are the configuration, size and yield strength of ties, concrete strength, depth of cover, and amount of longitudinal reinforcement. The behavior of these specimens in both pre-peak and post-peak regimes is discussed.

Results of the parametric study are used to examine the performance of ACI Code sections related to tied concrete members. It is found that the ACI Code seismic design requirement of minimum transverse reinforcement is sufficient and necessary for tied high strength concrete columns. On the other hand, the ACI Code rectangular stress block over-estimates the moment capacity of high strength concrete columns. Modifications of related parameters in the ACI Code are suggested.

# ACKNOWLEDGMENT

# TABLE OF CONTENTS

# LIST OF TABLES

# LIST OF FIGURES

# LIST OF SYMBOLS

## CHAPTER TWO

$a_1,...a_4$ = constants in a suggested constitutive model;

$b$ = width of notched beam;

$d$ = height of notched beam;

$D$ = diameter of cylinder specimen;

$f_c'$ = compressive cylinder strength;

$f_{ct}$ = split cylinder strength;

$G_{cr}^I$ = tensile fracture energy;

$h$ = height of the notch;

$H$ = height of cylinder specimen;

$k$ = confinement factor;

$L$ = length of splitting cylinder and notched beam;

$mg$ = weight of notched beam;

$P$ = load acting on the specimen;

$\delta$ = load point displacement of notched beam;

$\delta_{max}$ = the rupture displacement of notched beam when load drops zero;

$\sigma_1$ = confining stress on a triaxially loaded cylinder (positive for compression);

$\sigma_3$ = longitudinal stress on a triaxially loaded cylinder (positive for compression).

## CHAPTER THREE

$A_h, B_h, C_h$     = hardening ductility parameters;

$A_s, B_s$     = softening parameters for fracture energy expression;

$c_0$     = cohesion parameter at peak;

$c_r$     = cohesion parameter at residual;

$c_s$     = cohesion parameter during softening;

$D, E, F$     = parameters for dilation function $m_Q$;

$E$     = linear elastic operator;

$F()$     = failure criterion or loading surface in terms of arguments inside parentheses;

$F_r()$     = residual strength envelop in terms of arguments inside parentheses;

$f_c'$     = uniaxial compressive strength;

$f_t'$     = uniaxial tensile strength;

$G_f^I$     = fracture energy release in direct tension;

$h_c$     = equivalent crack spacing;

$h_t$     = tensile crack spacing;

$h_e$     = finite element height;

$I_1, J_2, J_3$     = three stress invariants;

$\bar{J} = <I_1, \sqrt{J_2}, J_3>$     = stress invariant vector;

| | |
|---|---|
| $k$ | = hardening parameter; |
| $k_0$ | = initial hardening parameter; |
| $\bar{m} = \dfrac{\partial Q}{\partial \bar{\sigma}^*}$ | = normal vector to plastic potential surface $Q$ in principal stress space; |
| $m_0$ | = frictional parameter at peak; |
| $m_Q$ | = frictional function for non-associated flow; |
| $m_r$ | = frictional parameter at residual; |
| $m_s$ | = frictional parameter during strain-softening; |
| $Q(\,)$ | = plastic potential in terms of arguments inside parentheses; |
| $R_d = \sqrt{2J_2}$ | = the deviatoric length; |
| $R_h = I_1 \cdot \sqrt{3}$ | = the hydrostatic length; |
| $u_f$ | = crack-opening displacement; |
| $\Delta u_f$ | = increment of crack-opening displacement; |
| $u_r$ | = rupture displacement; |
| $X_p$ | = ductility measure which defines accumulated plastic strain at peak; |
| $\Delta \underset{\sim}{\varepsilon}$ | = tensor of total strain increment; |
| $\Delta \underset{\sim}{\varepsilon_e}$ | = tensor of elastic strain increment; |
| $\varepsilon_f$ | = equivalent tensile fracture strain; |
| $\Delta \bar{\varepsilon}_f$ | = vector of principal tensile fracture strain increment; |

$\varepsilon_p$          = length of plastic strain trajectory;

$\Delta \varepsilon_p$          = tensor of plastic strain increment;

$\Delta \bar{\varepsilon}_p$          = vector of principal plastic strain increment;

$\Delta \lambda$          = plastic multiplier for finite increment;

$\underset{\sim}{\sigma}$          = stress tensor;

$\sigma_i$          = i=1, major principal stress; i=2, intermediate principal stress; i=3, minor principal stress;

$\bar{\sigma}^*$          = vector of principal stress;

$\sigma_x', \sigma_y', \sigma_z'$     = stress deviators;

$\sigma_t$          = degradation of tensile strength;

$\theta$          = angle of similarity;

$\langle \; \rangle$          = McCauley brackets which extract the positive components inside the brackets.

## CHAPTER FOUR

$A_h$, $B_h$, $C_h$ $\quad$ = hardening ductility parameters;

$A_s$, $B_s$ $\quad$ = softening parameters for fracture energy expression;

E $\quad$ = modulus of elasticity;

$f_c'$ $\quad$ = uniaxial compressive strength;

$f_t'$ $\quad$ = uniaxial tensile strength;

$f_y$ $\quad$ = yield strength of longitudinal reinforcement;

$f_{yh}$ $\quad$ = yield strength of transverse reinforcement;

$G_f'$ $\quad$ = fracture energy release in direct tension;

$P_1$ $\quad$ = primary axial load;

$P_2$ $\quad$ = secondary load applied eccentrically;

$r$ $\quad$ = the ratio of distance from the compression face to the height of cross-section;

$\{\delta(\Delta U)\}$ $\quad$ = solution correction during iterations;

$\{\Delta U\}$ $\quad$ = incremental solution;

$\varepsilon_c$ $\quad$ = strain on compression face;

$\varepsilon_t$ $\quad$ = strain on tension face;

$\gamma_u$ $\quad$ = tolerance for the displacement control.

# CHAPTER FIVE

$A_h$, $B_h$, $C_h$  = hardening ductility parameters;

$A_s$, $B_s$  = softening parameters for fracture energy expression;

$A_{ch}$  = cross-sectional area of a structural member measured out-to-out of transverse reinforcement;

$A_g$  = gross cross-sectional area;

$A_{sh}$  = total cross-sectional area of rectangular hoop reinforcement;

E  = modulus of elasticity;

$f_c'$  = uniaxial compressive strength;

$f_t'$  = uniaxial tensile strength;

$f_{yh}$  = specified yield strength of transverse reinforcement;

$G_f'$  = fracture energy release in direct tension;

$h_c$  = cross-sectional dimension of column core measured center-to-center of confining reinforcement;

$M$  =  moment about center line;

$\sum M_e$  = the sum of moments, at the center of the joint, corresponding to the design flexural strength of the columns framing into that joint;

$\sum M_g$  = the sum of moments, at the center of the joint, corresponding to the design flexural strength of the girders framing into that joint;

$P$  = total axial load;

$s$  = spacing of ties;

$\rho_g$        = longitudinal reinforcement ratio;

$\rho_t$        = equivalent transverse reinforcement ratio.

# CHAPTER SIX

$C$        = resultant force, equivalent to the axial load $P$;

$b$        = width of cross-section;

$d$        = depth of cross-section;

$h$        = height of compression zone;

$K_1$        = ratio of the average compressive stress to the maximum compressive stress;

$K_2$        = ratio of distance between the extreme fiber and the resultant of compressive stress to distance between the extreme fiber and the neutral axis;

$K_3$        = ratio of the maximum compressive stress to the cylinder strength;

$M$        = moment about center line;

$M_1$        = peak moment;

$M_2$        = the moment equal to $M_1/2$;

$M_3$        = the moment associated with $P_3$;

$M_c$       = predicted moment capacity based on ACI Code 318-89;

$M_c^*$       = predicted moment capacity based on proposed $K_2$ value;

$P$       = total axial load;

$P_1$       = the axial force associated with $M_1$;

$P_2$       = the axial force associated with $M_2$;

$P_3$       = peak axial force;

$P_c$       = the axial force associated with $M_c$;

$P_c^*$       = the axial force associated with $M_c^*$;

$W_m$       = energy absorbed (moment part);

$W_p$       = energy absorbed (axial load part);

$W_{total}$       = total energy absorbed;

$\varepsilon_c$       = strain on compression face;

$\varepsilon_u$       = limiting strain for design.

# CHAPTER ONE

# INTRODUCTION

## 1.1 Background to the Problem

High strength concrete is generally defined as concrete with compressive strength in the range of 60 to 100 MPa. Concrete with compressive strength greater than 100 MPa is called ultra-high strength concrete. Besides its high compressive strength, many previous experiments have shown that the material has a higher modulus of elasticity, a non-ductile mode of failure, and a larger strain at maximum stress than normal strength concrete.

High strength concrete has been attractive to structural engineers. Use of the material to construct the columns in tall structures is extremely advantageous as substantial savings in material quantities can be made. In addition, more free floor space is achieved due to reduction of column cross-sections. However, the application of high strength concrete to structures, especially in seismic zones, is questioned since the material has very poor ductility when unconfined. The post-peak behavior under confined conditions is also largely unknown.

Recently, several investigations have been conducted on the performance of tied high strength concrete columns. Experiments of concentrically loaded high strength concrete columns by Cusson et al. (1994), Bjerkeli et al. (1990) and Yong et al. (1988) found that the ductility performance of columns can be improved with increasing lateral confinement by transverse reinforcement. The work was extended to experiments of eccentrically loaded high strength and ultra-high strength concrete columns by Ibrahim and MacGregor (1994). It was concluded by Ibrahim and MacGregor that while it seems to have no effect on the maximum capacity of the section prior to spalling of the concrete cover, the lateral confinement of cross-section has a significant effect on the ductility behavior and the failure mechanism of concrete columns. It was suggested by Ibrahim and MacGregor that the parameters defining the rectangular stress block in current ACI Code, which is mainly based on experiments and engineering practice for low and medium

1

strength concretes, are not conservative for the design of rectangular or triangular high strength and ultra-high strength concrete sections.

A stress analysis of tied high strength concrete columns is very helpful in order to reach a complete understanding of the failure mechanism, the stress distribution pattern in the columns, and the role of transverse reinforcement. This understanding can be achieved through a finite element analysis of the problem with a verified and reliable model. Finite element analysis also provides a practical and alternative approach for the parametric study of tied concrete columns.

## 1.2  Literature Review

### 1.2.1  Experimental Research

Experimental investigation of tied reinforced concrete columns has been a hot research topic in the last two decades after a hiatus of nearly 40 years. Researches on the performance of spiral columns with low, medium and high strength concrete were conducted by Ahmad and Shah (1982), and Martinez et al. (1984). There have been several experimental investigations of low and medium strength concrete columns with rectilinear transverse reinforcement (Sargin et al. (1971), Mander et al. (1988) and Sheikh et al. (1990)).

Experiments on tied high strength concrete columns have been conducted by a number of researchers in recent years. Muguruma et al. (1983) tested four unconfined concrete columns and 14 tied columns under concentric loading. The concrete strength ranged from 34.9 to 89.2 MPa. The cross-sectional dimension was 147.4 x 147.4 mm. Yong et al. (1988) tested 24 tied concrete columns ($f_c'$=83.6 to 93.5 MPa) under concentric loading. The columns had a 152mm x 152mm cross-section and a height of 450mm. Cusson et al. (1994) tested 27 columns ($f_c'$=52.6 to 113.6 MPa) under concentric loading. The columns had the cross-sectional dimension of 235mm x 235mm and height of 900mm. Ibrahim and MacGregor (1994) tested 15 rectangular cross-section columns and six triangular cross-section columns ($f_c'$=59.3 to 130.6 MPa) under combined axial load

2

and moment. Details of the experimental program by Ibrahim and MacGregor (1994) will be reviewed in Chapter 4.

Due to the nature of this study, only a few of the findings and conclusions by Yong et al. (1988), Cusson et al. (1994) and Ibrahim and MacGregor (1994) are reviewed here.

**Yong et al. (1988)** found that instead of collapsing in a very brittle fashion, the confined concrete columns failed in a more ductile and gradual way. The peak stress and strain and especially the ductility for concentrically loaded columns increased with the volumetric ratio of the lateral steel, but not proportionally. Depth of cover had no effect on the peak stress and strain. Increasing the number of longitudinal bars and distributing them around the core perimeter increased the effectiveness of the confinement of the concrete core.

**Cusson et al. (1994)** observed that, despite the lower confinement efficiency of high strength concrete compared to lower strength concrete, a large strength gain and ductile behavior of confined high strength concrete columns were obtained when adequate detailing of longitudinal and transverse reinforcement was used. It was concluded that an increase of the tie yield strength would result in an enhancement of the strength and toughness gains only for well-confined specimens with a large ratio of lateral reinforcement. It was found that the behavior of high strength concrete columns was characterized by the sudden separation of the concrete cover at the weakness planes created by a dense steel cage. This early spalling of concrete cover resulted in a loss of axial capacity before any lateral confinement came into effect.

**Ibrahim and MacGregor (1994)** made a number of conclusions based on their test program:

(1)  The reinforced concrete specimens had different behavior depending on the amount of lateral reinforcement. The spacing of the ties and the volumetric ratio of the confining steel were the main factors affecting the behavior of the columns. Rectangular specimens with very light confinement reinforcement failed when the concrete cover spalled off with buckling of the longitudinal bars near the compression face. The columns showed brittle behavior. Other specimens with more confinement steel had short and steep descending branches, however their failure

3

was not as explosive as the tests of plain concrete specimens. Only the highly confined specimens showed a ductile post-peak behavior.

(2) The flexural stress-strain curves of the reinforced rectangular specimens prior to spalling of the concrete cover were similar to the stress-strain curves of the plain concrete specimen with similar concrete strength.

(3) The assumption of linear strain distribution in the compression zone was found to be true even for strain values that are very close to failure.

(4) Design code recommendations for maximum tie spacing in non-seismic regions were found to be too liberal for high strength and ultra-high strength concrete sections. An eccentrically loaded column designed with the maximum tie spacing may have a sudden and brittle failure at the spalling of the concrete cover.

(5) The parameters defining the ACI rectangular stress block are not conservative for the design of rectangular or triangular high strength and ultra-high strength concrete sections.

## 1.2.2 Finite Element Analysis

A successful finite element analysis of concrete structures requires a workable and reliable material model. Previous research on constitutive relations necessary to construct such a model will be reviewed in Chapter 3. The application of the finite element method to tied concrete columns is still in a very initial stage. There have been only a few published studies in this field, all limited to concentrically loaded columns.

**Chen and Mau (1989)** simulated the behavior of spirally reinforced circular concrete columns under axial compression tested by Ahmad and Shah (1982). Six specimens (75mm in diameter and 150mm in height) with different amounts of hoops were analyzed. The concrete strength was between 26.2 MPa and 37.92 MPa. The model used was a plastic-fracturing formulation originally developed by Bazant and Kim (1979). Chen and Mau recalibrated the model based on the then published axial and multi-axial test results. Comparisons of the simulated results with those from reported tests indicated

4

good agreement, with the exception that the model seemed to be too stiff for unconfined specimens. The stress distribution patterns over the cross-section were presented at the tie level and mid-section. It was found that the variation of axial stresses was particularly severe near the outside surface at the tie level. Only in a region away from the surface of the column, a nearly uniform stress state is achieved.

**Abdel-Halim et al. (1989)** conducted an analytical study for concrete confinement in tied columns loaded concentrically. Some of the specimens were tested by Scott et al. (1982). The specimens were 1200mm tall and 450mm x 450mm in cross-sectional dimension. The compressive strength of concrete was 25 MPa. Four different tie configurations were studied. The model used was originally established by Cedolin et al. (1977) who idealized the behavior of the concrete material by an isotropic nonlinear-elastic model and established approximate expressions for the secant bulk modulus and secant modulus. Due to lack of the test results of tensile strain-softening then, it was assumed improperly that the descending stress-strain curve in tension is a straight line with the rupture strain equal to twice the strain at the peak stress. The concrete in the core and cover was modeled with three-dimensional solid (eight-node brick) element. Both the transverse reinforcement and the longitudinal reinforcement were represented with truss elements. It was claimed that the finite element approach favorably predicted the results obtained experimentally. It was concluded that both the strength and ductility of tied columns increased as the volumetric ratio of the lateral ties increased. The relationship between gain in strength of the confined concrete and the volumetric ratio of the lateral steel was found to be approximately linear.

## 1.3 Objectives

The objective of this study is to investigate the performance of tied high strength concrete columns under eccentric loading. The work is divided into the following six stages:

(1)  To carry out a constitutive test program for high strength concrete in order to define the behavior under confined triaxial stress conditions.

(2)  To develop a reliable finite element model for high strength concrete structures.

(3)  To verify the finite element model against the observed behavior of the tied high strength concrete columns tested by Ibrahim and MacGregor (1994).

(4)  To study the failure mechanism of tied high strength concrete columns.

(5)  To conduct a parametric study of tied high strength concrete columns under eccentric loading in order to define the effects of tie spacing, volumetric ratio of transverse reinforcement and other factors on both the pre-peak and post-peak behavior.

(6)  To examine the performance of the current design code sections related to tied high strength concrete columns.

## 1.4  Organization of the Thesis

The literature review on tied high strength concrete columns is presented in Chapter 1. The literature reviews of constitutive properties and finite element models are included in Chapter 2 and Chapter 3 respectively.

Chapter 2 gives a description of the constitutive test program of high strength concrete, along with a discussion of the test results. Chapter 3 starts with a review of the finite element model proposed by Pramono and Willam (1989). It also includes the modification and calibration of the model based on the constitutive test. Chapter 4 presents the finite element analysis of tied high strength concrete columns tested by Ibrahim and MacGregor (1994). Chapter 5 presents the parametric study of tied high strength concrete columns. Examination of the current design code is made in Chapter 6 based on the results of the parametric study. Finally, in Chapter 7, the work accomplished is summarized. Some conclusions and recommendations for future work are made.

# CHAPTER TWO

# MECHANICAL PROPERTIES OF HIGH STRENGTH CONCRETE CONTAINING SILICA FUME

## 2.1 Introduction

High strength concrete is a new structural material on which a full-fledged investigation of mechanical properties is necessary. A knowledge of high strength concrete behavior in triaxial compression is needed to allow examination of the design rules of tied and spiral columns and other confined structures incorporating this material. In addition, experimental results of high strength concrete under tension and uniaxial and triaxial compression form an essential part in establishing a finite element constitutive model.

High strength concrete, according to the recent CEB/FIP report (1991), is defined as: "All concrete with a compressive cylinder strength above the present existing limits in national codes, i.e. about 60 MPa, and up to 130 MPa, the practical upper limit for concretes with ordinary aggregates."

## 2.2 Previous Research

The mechanical properties of concrete include its behavior in tension, uniaxial and triaxial compression. An extensive research was conducted by Slate et al. (1987) who examined the splitting cylinder strength and compressive stress-strain behavior for concrete with compressive strength of 59 MPa. The test series for uniaxial compression involved the cylinder specimens with two different sizes: 6in. x 12in. (152mm x 305mm, Diameter x Height) and 4in. x 8in. (102mm x 203mm). Among other researchers was Swamy (1986) who studied the elasticity properties and compressive stress-strain behavior for concrete with silica fume with compressive strength of 80 to 89 MPa. Swamy's tests were n 100mm cubes and 100mm x 100-500mm prisms.

In the past decade, extensive attention was focused on the strain-softening behavior of concrete in both tension and compression. There are two alternative

approaches to determine the tensile fracture energy of concrete: the direct tension test (Reinhart, 1984, Gopalaratnam, et al., 1984, and Willam, et al., 1985) and the notched beam test (Hillerborg, 1985C, and Peterson, 1980). These contributions, however, were mainly on low and medium strength concrete. To the best of the author's knowledge, there is no published experimental investigation on the tensile strain-softening behavior of high strength concrete.

Previous work on triaxial compression includes the classical test series by Richart, Brandtzaeg, and Brown (1928) with 64 tests on 4in. x 8in. (100mm x 200mm) cylinders, the test series of low strength concrete ($f_c' = 32$ MPa) by Palaniswamy and Shah (1974) with 25 tests on 3in. x 9in. (76mm x 230mm) cylinders, the test series of low strength concrete ($f_c' = 22.1$ MPa) by Willam, Hurlbut and Sture (1985) with five tests on 2.125in. x 4.25in. (54mm x 108mm) cylinders, the test series of low, medium and high strength concrete ($f_c' = 25$, 60 and 80 MPa) by Jensen et al. (1990) and Bjerkeli et al. (1990), and the test series of concentrically loaded spirally-reinforced high strength concrete columns by Morales et al. (1982).

Many researchers dealt with their triaxial test results using a linear regression equation: $\sigma_3 = f_c' + k\sigma_1$, in which $\sigma_3$ is the triaxial strength, $\sigma_1$ is the confining pressure, $f_c'$ is the unconfined compressive strength, and $k$ is the confinement factor. It has been well recognized that the confinement factor is close to 4.0 for low and medium strength concrete. Results reported by Bjerkeli et al. (1990), however, show that this factor reduces to about 3.0 for normal density concrete with a compressive cylinder strength above 80 MPa, and to about 1.5 for lightweight aggregate concrete. Recent research work by Martinez et al. (1984), Ahmad and Shah (1982), Dal Busco (1988) and Bjerkeli et al. (1990) has shown that lateral confining pressure caused by spiral or hoop ties has less effect in increasing the ultimate concrete stress and strain in cores of high strength concrete compared to lower strength concrete.

## 2.3 Scope

This chapter presents an experimental investigation of the mechanical properties of high strength concrete. In this investigation, three high strength concretes containing silica fume were cast and tested. The concretes were designed to have compressive cylinder

strengths of 60, 90 and 120 MPa. The tests carried out included the compressive cylinder, split cylinder, notched-beam and triaxial compression tests. The objective was to determine the compressive cylinder strength, split cylinder tensile strength, tensile fracture energy and maximum and residual triaxial compressive strengths.

Based on the test results, some observations were made on the concrete behavior in uniaxial compression, tension and triaxial compression. The relationship between the confinement and the maximum and residual strengths of concrete in triaxial compression was studied. The test results have been used to modify a finite element constitutive model for high strength concrete.

## 2.4 Design of Concrete Mixes

Three batches of high strength concrete were cast with the target compressive cylinder strengths of 60, 90, and 120 MPa (8700, 13050 and 17400 psi) after 28 days of curing. The mix designs for these three batches (labeled type A, B, and C) are listed in Table 2.1. The materials used made a 0.085 m$^3$ (3 cu. ft.) batch of fresh concrete for each type.

The concrete contained gravel aggregate with a maximum size of 14 mm (0.55in.). The petrographic analysis of the coarse aggregate indicated that the fraction retained on a 2.5 mm sieve is primarily composed of orthoquartzite (62.3%), quartzite (14.0%) and hard sandstone (10.5%). The results of the petrographic analysis of the fine aggregate indicated that it was composed primarily of hard quartz rock types such as orthoquartzite (18.9%), quartzite (54.9%), hard sandstone (4.3%) and chert (4.9%). The fineness modulus for the fine aggregate was 2.55.

The cement was type I. The water/cement ratios were in the range of 0.22 to 0.32. To achieve this low w/c ratio and maintain adequate workability, it was necessary to use a lignin sulphonate superplasticizer (produced by ConChem) as a water reducing admixture. In addition, silica fume was used in all three types of concrete. The amount of silica fume used increased as the target compressive strength increased.

## 2.5  Behavior in Uniaxial Compression

The specimens for the uniaxial compressive cylinder tests were nominally 100 mm in diameter and 200 mm in height cast in reusable plastic molds. Three specimens were tested for each type of concrete. The tests were conducted in a 2700 kN (600 Kip) MTS rock testing machine. The machine had an axial stiffness of 2440 kN/mm. The tests were carried out under modified stroke control in which the controlling function was

$$stroke = \frac{P}{4000} + 0.3174(1 - e^{-P/205}) \quad (mm) \tag{2.1}$$

where $P$(kN) is the load acting on the specimen and $e$ is the base of natural logarithms. This was done to make it possible to follow the descending branch of the stress-strain curve. The ends of the cylinders were ground to a flat surface using a lathe and a carborundum tool. No additional sulphur cap was added.

The geometry of specimens and test results are listed in Table 2.2. The stress-strain curves for concrete are presented in Fig. 2.1 to Fig. 2.3 for concrete types A, B, and C respectively. The strains were determined for the overall change of length of the specimen.

It can be seen that the strengths and the stress-strain curves for the three samples of each type of concrete were very consistent. The descending part of the stress-strain curve becomes steeper as the concrete strength increases. This suggests that high strength concrete could be penalized by its poor ductility. It can also be noted that when the compressive strength increases, the stress-strain response in the descending part becomes more dynamic. This could be due to the difference of the failure mode of each type of concrete. For type A concrete, since the rigidity of concrete is considerably less than the radial rigidity of the loading platens, the platens provide a considerable lateral restraint to the ends of a specimen. A cone was formed at the ends of the specimen at collapse as shown in Fig. 2.4. For types B and C concrete, the cone was only partially formed due to less confinement on its ends. Vertical cracks extended to the ends of the specimens of type B and C concrete and eventually became major cracks which resulted in major splitting of these specimens into longitudinal pieces up to the ends at and after peak loading (as shown in Fig. 2.5 for type C concrete). The jagged descending branches of the stress-strain curves in Figs.2.2 and 2.3 resulted from this major splitting. The load dropped upon the formation of splitting, then built up again until more splitting occurred or parts of the cylinder crushed.

10

## 2.6 Behavior in Tension

There are two important parameters for concrete in tension: the tensile strength and the fracture energy which reflects how concrete behaves in strain softening. In this study, the tensile strength was measured using split cylinder tests and the fracture energy was determined using notched beam tests.

### 2.6.1 Tensile Strength

In this part of the investigation, three samples of each type of concrete were tested using the split cylinder method in accordance with ASTM C330. The specimens had a diameter $D = 153$ mm and a length $L = 300$ mm and were made in reusable plastic molds. The split cylinder tests were conducted on a Tate-Emery testing machine. The actual geometry and the test results for the three types of concrete are listed in Table 2.3.

The split cylinder tensile strength, $f_{ct}$, was calculated by:

$$f_{ct} = \frac{2P}{\pi \, LD} \tag{2.2}$$

in which $P$ is the maximum splitting load recorded by the machine.

Table 2.3 shows that the split cylinder tensile strength increases as the uniaxial compressive strength of the concrete increases. As expected, the increase is not directly proportional to the cylinder compressive strength.

For normal weight concrete, Carrasquillo et al. (1981) recommended the following relationship between the split cylinder strength and the cylinder uniaxial compressive strength:

$$f_{ct} = 0.54\sqrt{f_c'} \tag{2.3}$$

In this investigation, the constant had higher values, in the range of 0.63 to 0.68. However, the number of samples for both types of tests is not sufficient to draw a general conclusion.

11

## 2.6.2 Strain Softening in Tension

There are two alternative test approaches to quantify the strain softening of concrete in tension, the direct tension test and flexural tests on notched beams. Both types of tests must be conducted under stroke control in order to capture the descending part of the load-deflection curve. Both types of tests can be used to determine the fracture energy, an important mechanical property for concrete in tensile strain softening (Hillerborg, 1985B).

In this study, three notched beams for each type of concrete were tested to determine the tensile fracture energy. The load was applied through a steel platen which moved at a constant rate until the beam broke into two parts. The movement of the steel platen was recorded as the load-point-displacement. A load cell attached to the steel platen was used to measure the magnitude of the force applied. The test specimen and procedure were in accordance with RILEM Draft Recommendation 50-FMC (1985).

The test results of load vs load-point-displacement are presented in Fig. 2.6 to Fig. 2.8 for concrete types A, B, and C respectively. The dimensions and test results are given in Table 2.4.

The tensile fracture energy, according to Peterson (1980), was calculated by:

$$G_{cr}^I = \frac{\int_0^{\delta max} P(\delta)d\delta + mg\frac{\delta max}{2}}{(d-h)b} \qquad (2.4)$$

in which $\delta$ is the load point displacement, $\delta_{max}$ is the rupture load point displacement, $P(\delta)$ is the load applied, $mg$ is the self-weight of the notched beam, $d$ and $b$ are the height and the width of the cross-section, and $h$ is the height of the notch.

It should be mentioned that an error was made in sawing the notch in specimen A2. Also specimen C1 was tested under some mis-alignment of the load point. Excluding these two samples, average values of the fracture energy were obtained as shown in the last column of Table 2.4.

The data in Table 2.4 suggest that the tensile fracture energy increases with increasing compressive strength. The increase is again not directly proportional to the compressive cylinder strength. As shown in Figs. 2.6, 2.7 and 2.8, the post-peak part of the load-displacement response becomes steeper as the concrete compressive strength increases. This indicates that the notched beam is more brittle for higher strength concrete.

## 2.7 Behavior under Triaxial Compression

In this study, triaxial compression tests were conducted on eleven specimens under different confinement levels for each of three types of high strength concrete described in the previous section.

### 2.7.1 Testing Apparatus and Test Procedure

The triaxial compression experiments were performed in a modified Hoek rock mechanics triaxial cell which accepts a NX-core size specimen of dimension 110 mm in height by 55.5 mm in diameter. The Hoek cell, shown in Fig. 2.9 can apply an axisymmetric confining pressure varying from zero to 70 MPa, which was generated by a manually operated pressure supply. A flexible polyurethane membrane is used to isolate the specimen from the pressurized fluid. The membrane is not attached to the specimen or the loading ram, but rather, is held in place by fluid pressure acting on the membrane flanges, and reacting on the Hoek cell end caps.

Axial displacements were transmitted to the specimen by a steel loading ram and an MTS servo-controlled loading frame. No friction reduction was applied at the interface between the steel loading ram and the concrete specimen. This introduced a radial restraint boundary condition at the specimen ends as is typical in cylinder tests.

The concrete specimens were cast by placing the concrete into the membrane with its base sealed. The ends of specimens were ground to a flat surface in a lathe, so that full contact between the steel loading platens and the ends of the specimen was ensured. In order to reduce the pressure sensitivity to radial displacements, only load histories with constant pressure were performed. The axial load was applied after the response due to the confinement became stable.

Eleven different confinement levels were applied in each test series with the highest held to about 50% of the uniaxial compressive cylinder strength for each type of concrete. Confinement ratios are shown in Table 2.6 for all specimens. Some of the cylinders tested with zero confinement were in air. Others had the membrane in place. The presence of the membrane provided a small degree of confinement which increased the uniaxial compressive strength by about 10% relative to that of those tested in air.

## 2.7.2 Test Results and Discussion

The longitudinal stress versus average longitudinal strain results from all triaxial compressive tests are shown in Figs. 2.10, 2.11 and 2.12 corresponding to concrete types A, B, and C respectively. Some qualitative observations can be made based on the test results:

*Maximum Strength* — The longitudinal stress increases with increasing strain from the beginning up to a peak, and then drops. The peak stress level is related to the confinement level. The higher the confinement, the higher the maximum strength the concrete can reach.

*Residual Strength* — In the descending part of the stress-strain curve, the rate of stress decrease becomes slower with increasing longitudinal strain. Eventually, the stress tends to a constant stable level called the residual strength. This residual strength is a function of the confinement. Usually, higher confinement gives a higher residual strength.

*Ductility* — The strain corresponding to the maximum strength increases for higher confinement. On the other hand, the slope of the descending curve immediately after the peak point becomes smaller with increasing confinement. It can then be concluded that confinement greatly improves the ductility. On the other hand, increasing the uniaxial compressive strength results in poorer ductility.

*Failure Modes* — For concrete with no confinement or confinement less than 15% of $f_c'$, the failure mode consists primarily of longitudinal tensile splitting. In type A concrete, axisymmetric cones were formed at the exterior contact with the loading platens. For concrete with high confinement, the failure mode was highly distributed with little

14

localized damage. This allowed the stress-strain curve to vary smoothly for concrete under higher confinement.

The test results of the maximum strength and residual strength are listed in Table 2.5. The maximum strength was calculated from the maximum load capacity recorded by the MTS machine in the test. The residual strength was determined as the point on the descending branch of the stress-strain curve where the slope of remaining part of the descending curve is less than 2% of the slope of the initial rising part of the stress-strain curve. This approach is different from that used by Willam, Hurlbut and Sture (1985). Although not explicitly indicated in Hurlbut's report (1985), the residual strength reported there appears to be the strength when the displacement reaches the equivalent of 700% of the displacement at the peak loading. Since the maximum strain reached in his test was $20 \times 10^{-3}$, Hurlbut concluded that there is no strain softening for triaxial compression specimens (with $f_c' = 22.1$ MPa) with confinement greater than 3.45 MPa (15.6% of $f_c'$). Figures 10, 11 and 12 indicate that even when the confinement ratio is 50% of $f_c'$, the stress level still drops slightly after the peak stress for the concrete tested.

### 2.7.3 Empirical Equations for Triaxial Compressive Strength

In the design of triaxially compressed structures, it is important to have equations relating the maximum strength and the confinement stress. Such equations can be established using linear or non-linear regression analysis. In this report, R-square values were computed after the regression analysis to indicate how well a calculated regression line fits a data set. An R-square value of unity indicates a precise fit. Deviation from an R-square value of unity indicates decreasing precision.

The results of linear regression of the maximum strength are shown in Fig. 2.13. It was found that the slopes of linear regression for the three types of concrete vary from 4.67 to 4.24 as concrete strength increases from 60 MPa to 120 MPa. The R-square values of linear regression vary from 0.986 to 0.940. This finding was also reported by Jensen et al. (1990), who concluded that the slope becomes smaller as the compressive cylinder strength becomes higher. However, the values of the slope reported here are greater than those reported by Jensen. In Jensen's report, the slopes varied from 4.1 to 2.0 as the concrete strength increased from 25 MPa to 80 MPa. It should be noted that linear regression is an inaccurate estimate since the relationship between the maximum strength

15

and the confinement is non-linear for high strength concrete. When subsets of data with increasing confinement are examined, the apparent slope becomes smaller.

To express the non-linear relationship between the maximum strength and confinement, a parabolic equation was chosen. The equation can take the form:

$$\frac{\sigma_3}{f_c'} = \sqrt{1 + k(\frac{\sigma_1}{f_c'})} \qquad (2.5)$$

which automatically passes through the point of uniaxial compression. Here $\sigma_3$ represents the longitudinal compressive peak stress, while $\sigma_1$ represents the confining pressure and $k$ is a constant. The results of regression are shown in Fig. 2.14 for type A, B and C concrete. Obviously regression using the parabolic equation is a much better representation than the linear regression. The values of parameter $k$ are also shown in Fig. 2.14. It was found that the R-square values here (0.992 to 0.990) are much closer to unity than those in linear regression.

The parameter $k$ can be related to $f_c'$ through the relation:

$$k = 21.2 - 0.05 f_c' \qquad (2.6)$$

which gives a very good estimate of k for types A and C concrete, but slightly under-estimates $k$ for type B concrete. This relation was obtained using regression of the values of $k$ given in Fig. 2.14. It should be noted that Eqs. 2.5 and 2.6 are valid only for confinement ratios up to 50%.

## 2.8 Specimen Size Effect

According to ASTM standard C31 and C39, the specified compressive strength $f_c'$ is measured by compression tests on cylinders with 6in. (152mm) in diameter and 12in. (304mm) in height. Cylinder diameters may have an effect on the concrete strength. An extensive discussion on this issue was made by Bartlett and MacGregor (1994).

According to the 'weakest link' theory (Madsen, et al., 1986), specimens with large volumes are more likely to contain a defect and so fail at lower applied stress.

Carrasquillo, et al. (1981) found that the average ratio of compressive strengths of 6in. x 12in. (152mm x 305mm) to 4in. x 8in. (102mm x 203mm) cylinders was close to 0.90 regardless of strength and test age. Material test of high strength concrete by Ibrahim and MacGregor (1994) showed that under moist cured conditions, the compressive strengths of 100mm x 200mm cylinders are higher than those of 150mm x 300mm cylinders. The differences are about 0.5% to 17% from batch to batch. There is no conclusive relationship between the strengths of the two different specimen sizes.

In this study, the uniaxial compression test was done on 100mm x 200mm cylinders, while the triaxial test was done on 55mm x 110mm cylinders. Six of 55mm x 110mm cylinders were tested without confinement. No test was done on 150mm x 300mm cylinders. From Figs. 2.1, 2.2 and 2.3, the results of 100mm x 200mm cylinders are very consistent for all three concrete types. This suggests that the test results of 100mm x 200mm cylinders are quite reliable. However, the results of unconfined 55mm x 110mm cylinders are less consistent. One explanation is that for high strength concrete cylinders with very small sizes, the uniaxial compression test results are very sensitive to the test conditions, end restraints and test alignment. On the other hand, tests of confined 55mm x 110mm cylinders are more stable, and hence the results are more reliable.

Despite the controversies surrounding the size effect on strengths, the strengths of 100mm x 200mm cylinders will be used as concrete strengths in this study as they are the most reliable sources available among the test groups.

Table 2.1 Mixture design of high strength concrete

| Type | A | B | C |
|---|---|---|---|
| Target Compressive Strength at 28 Days | 60 MPa | 90 MPa | 120 MPa |
| H2O (Water) | 107.2 N | 110.8 N | 97.0 N |
| Cement | 333.7 N | 391.6 N | 449.4 N |
| w/c | 0.321 | 0.283 | 0.216 |
| Gravel | 918.0 N | 872.2 N | 916.7 N |
| Sand | 633.2 N | 449.4 N | 462.8 N |
| Silica Fume | 40.0 N | 43.6 N | 49.8 N |
| Superplasticizer | 820.0 ml | 1340.0 ml | 1540.0 ml |
| Compressive Strength Achieved (Days) | 60.2 MPa (29) | 92.2 MPa (35) | 119.0 MPa (39) |

Table 2.2 Specimen geometry and test results in uniaxial compression

| Type | Specimen | Diameter $D$ (mm) | Height $H$ (mm) | Maximum Stress (MPa) | Average $f_c'$ (MPa) |
|---|---|---|---|---|---|
| A* | A1 | 99.5 | 199.5 | 59.61 | 60.20 |
| | A2 | 100.0 | 201.0 | 60.58 | |
| | A3 | 100.5 | 203.0 | 60.42 | |
| B* | B1 | 104.0 | 200.0 | 90.42 | 92.21 |
| | B2 | 99.0 | 200.0 | 93.17 | |
| | B3 | 100.0 | 196.0 | 93.03 | |
| C* | C1 | 100.0 | 200.0 | 120.6 | 119.0 |
| | C2 | 99.0 | 201.0 | 116.6 | |
| | C3 | 99.0 | 204.0 | 119.8 | |

* The A series was 29 days old at the time of testing, B series was 35 days old and C series was 39 days old

Table 2.3  Specimen geometry and test results in splitting test

| Type | Speci-men | Diameter $D$ (mm) | Length $L$ (mm) | Maximum $P$ (kN) | $f_{ct}$ (MPa) | Average $f_{ct}$ (MPa) |
|---|---|---|---|---|---|---|
| A* | A1 | 153.0 | 299.0 | 330.0 | 4.59 | |
| | A2 | 153.0 | 300.0 | 367.0 | 4.99 | 4.95 |
| | A3 | 153.0 | 301.0 | 380.0 | 5.25 | |
| B* | B1 | 153.0 | 302.0 | 480.0 | 6.61 | |
| | B2 | 153.0 | 302.0 | 460.0 | 6.34 | 6.36 |
| | B3 | 153.0 | 302.0 | 445.0 | 6.13 | |
| C* | C1 | 153.0 | 302.0 | 530.0 | 7.30 | |
| | C2 | 153.0 | 302.0 | 510.0 | 7.03 | 7.44 |
| | C3 | 153.0 | 302.0 | 580.0 | 7.99 | |

\* The A series was 29 days old at the time of testing,
B series was 35 days old and C series was 39 days old


Table 2.4  Specimen geometry and test results for the notched beam test

| Type | Speci-men | $d \times b \times L$ (mm) | $h$ (mm) | $mg$ (KN) | $\delta_{max}$ (mm) | $\int P(\delta)d\delta$ | $G^I_{cr}$ (N/mm) | Average $G^I_{cr}$ (N/mm) |
|---|---|---|---|---|---|---|---|---|
| A* | A1 | 102 x 102 x 800 | 50 | 0.209 | 2.24 | 0.563 | 0.150 | |
| | A2[+] | 102 x 102 x 750 | 51 | 0.206 | 1.85 | 0.860 | 0.202 | 0.152[#] |
| | A3 | 102 x 102 x 800 | 50 | 0.206 | 1.50 | 0.663 | 0.154 | |
| B* | B1 | 102 x 103 x 800 | 52 | 0.214 | 1.68 | 0.701 | 0.171 | |
| | B2 | 100 x 103 x 780 | 50 | 0.207 | 1.32 | 0.556 | 0.135 | 0.172 |
| | B3 | 102 x 104 x 800 | 52 | 0.211 | 1.60 | 0.921 | 0.209 | |
| C* | C1[++] | 102 x 103 x 800 | 51 | 0.211 | 1.36 | 0.485 | 0.120 | |
| | C2 | 100 x 103 x 800 | 51 | 0.207 | 1.68 | 0.754 | 0.184 | 0.191[##] |
| | C3 | 101 x 103 x 800 | 50 | 0.214 | 1.54 | 0.885 | 0.199 | |

\* The A series was 29 days old at the time of testing,
B series was 35 days old and C series was 39 days old.

+ Error in sawing notch.

++ Load point mis-aligned.

# Average $G^I_{cr}$ does not include the result of specimen A2.

## Average $G^I_{cr}$ does not include the result of specimen C1.

Table 2.5   Results of the triaxial compression tests

| Type (Curing Days) | Specimen | Confinement Ratio $\sigma_1 / f_c'$ | Maximum Strength Ratio $(\sigma_3 / f_c')_{max}$ | Residual Strength Ratio $(\sigma_3 / f_c')_{res}$ |
|---|---|---|---|---|
| A (29 Days) $f_c' = 60.2$ MPa $f_{ct}' = 4.95$ MPa | A1 | 0.038 | 1.339 | 0.703 |
| | A2 | 0.088 | 1.621 | 0.977 |
| | A3 | 0.138 | 1.788 | 1.299 |
| | A4 | 0.000 | 1.135 | 0.000 |
| | A5 | 0.337 | 2.606 | 2.344 |
| | A6 | 0.487 | 3.210 | 2.950 |
| | A7 | 0.387 | 2.858 | 2.550 |
| | A8 | 0.188 | 2.020 | 1.585 |
| | A9 | 0.238 | 2.273 | 1.859 |
| | A10 | 0.014 | 0.970 | 0.483 |
| | A11* | 0.000 | 1.070 | 0.000 |
| B (35 Days) $f_c' = 92.2$ MPa $f_{ct}' = 6.36$ MPa | B1 | 0.041 | 1.403 | 0.657 |
| | B2 | 0.090 | 1.688 | 0.932 |
| | B3 | 0.139 | 1.965 | 1.205 |
| | B4 | 0.188 | 2.107 | 1.627 |
| | B5 | 0.237 | 2.264 | 1.822 |
| | B6 | 0.285 | 2.545 | 2.037 |
| | B7 | 0.179 | 2.167 | 1.486 |
| | B8 | 0.385 | 2.832 | 2.450 |
| | B9 | 0.482 | 3.183 | 2.850 |
| | B10 | 0.000 | 1.047 | 0.000 |
| | B11* | 0.000 | 0.942 | 0.000 |
| C (39 Days) $f_c' = 119$ MPa $f_{ct}' = 7.44$ MPa | C1 | 0.051 | 1.448 | 0.630 |
| | C2 | 0.101 | 1.783 | 0.956 |
| | C3 | 0.151 | 1.898 | 1.203 |
| | C4 | 0.202 | 2.109 | 1.456 |
| | C5 | 0.252 | 2.200 | 1.645 |
| | C6 | 0.303 | 2.361 | 1.923 |
| | C7 | 0.403 | 2.658 | 2.402 |
| | C8 | 0.504 | 3.087 | 2.780 |
| | C9* | 0.000 | 0.821 | 0.000 |
| | C10 | 0.000 | 0.826 | 0.000 |
| | C11 | 0.000 | 0.965 | 0.000 |

*   Specimens were tested in air.
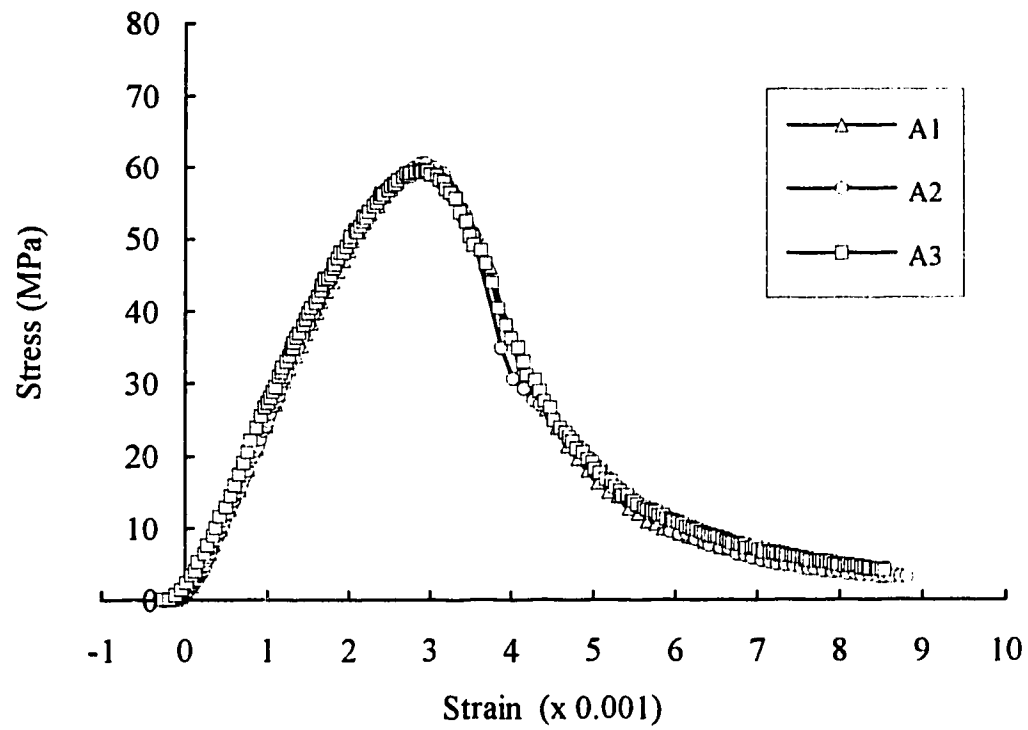
Fig.2.1   Stress-strain response of uniaxial compression tests
(Type A concrete)
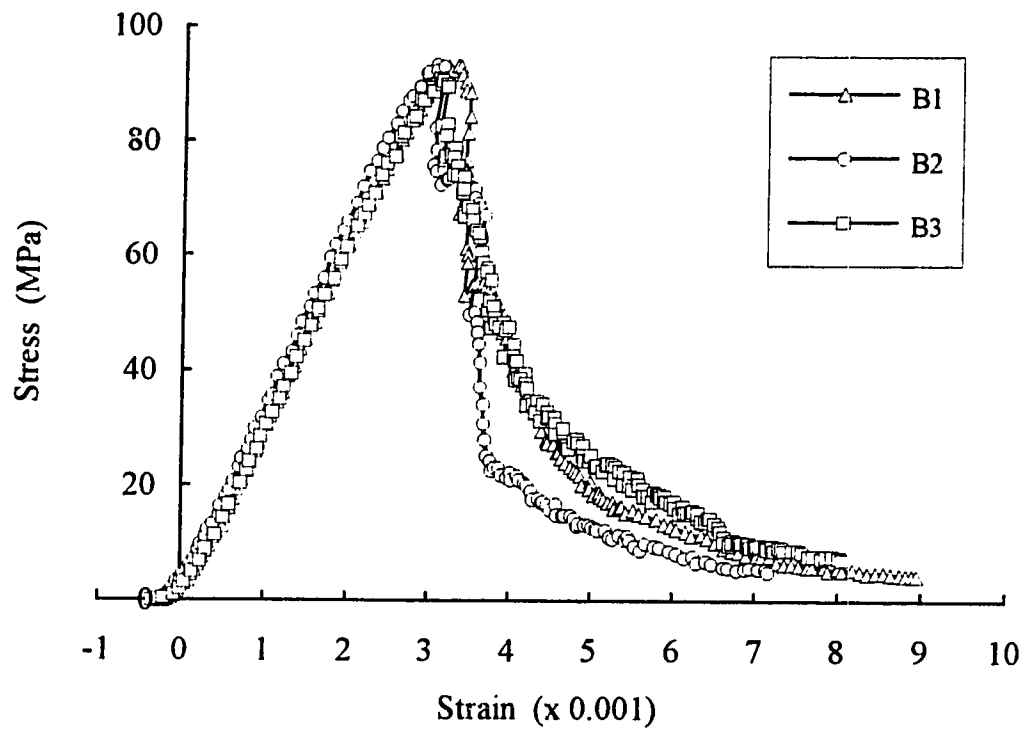
Fig.2.2  Stress-strain response of uniaxial compression tests
(Type B concrete)
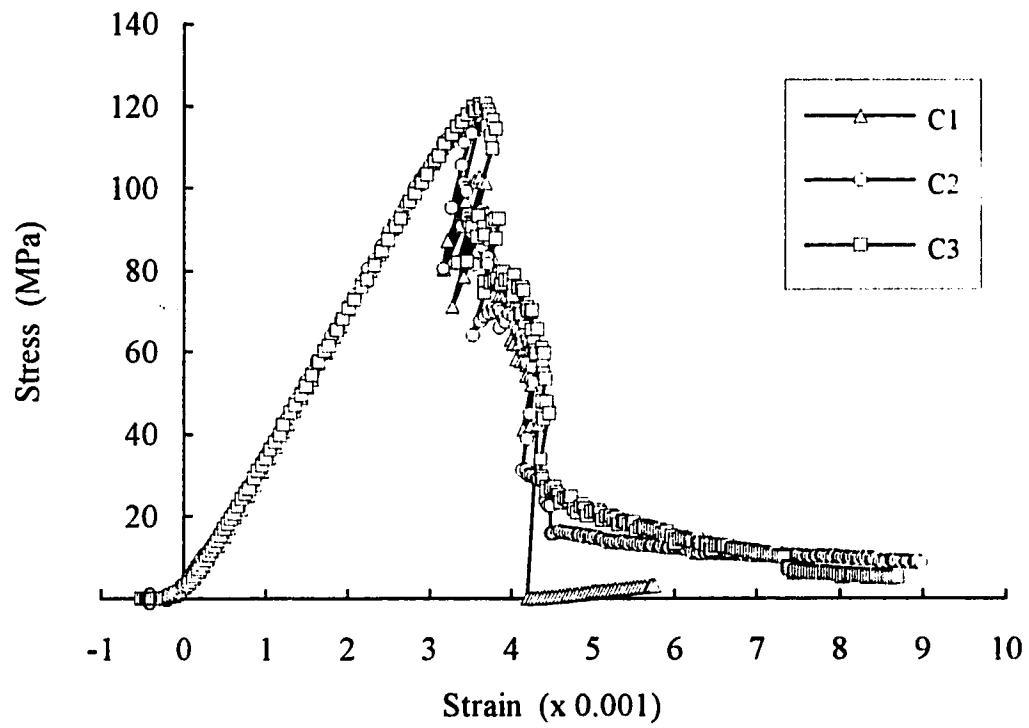
Fig.2.3  Stress-strain response of uniaxial compression tests
(Type C concrete)

Fig.2.4   Failure mode of uniaxial compression tests
(Type A concrete)
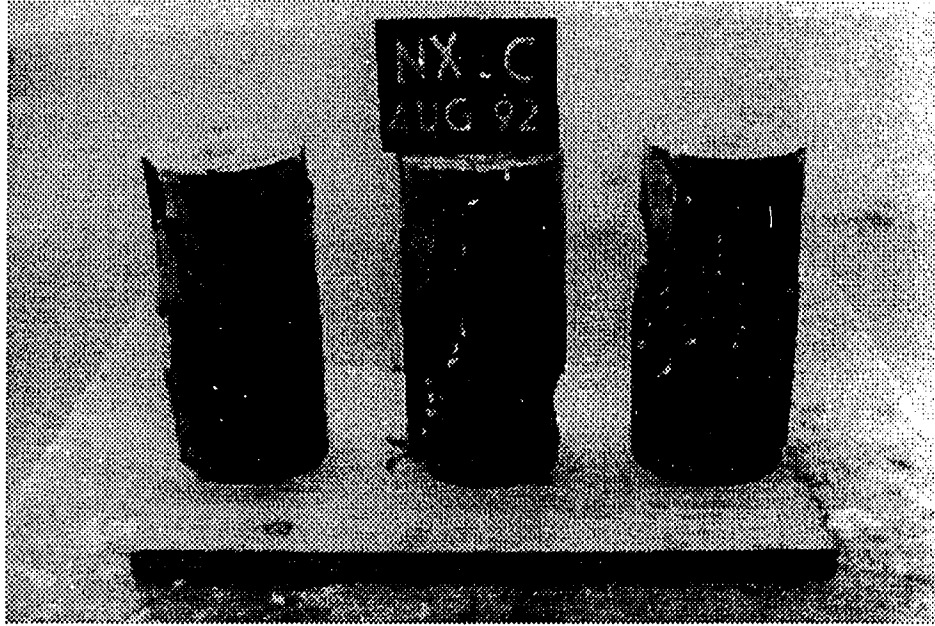
Fig.2.5  Failure mode of uniaxial compression tests
(Type C concrete)
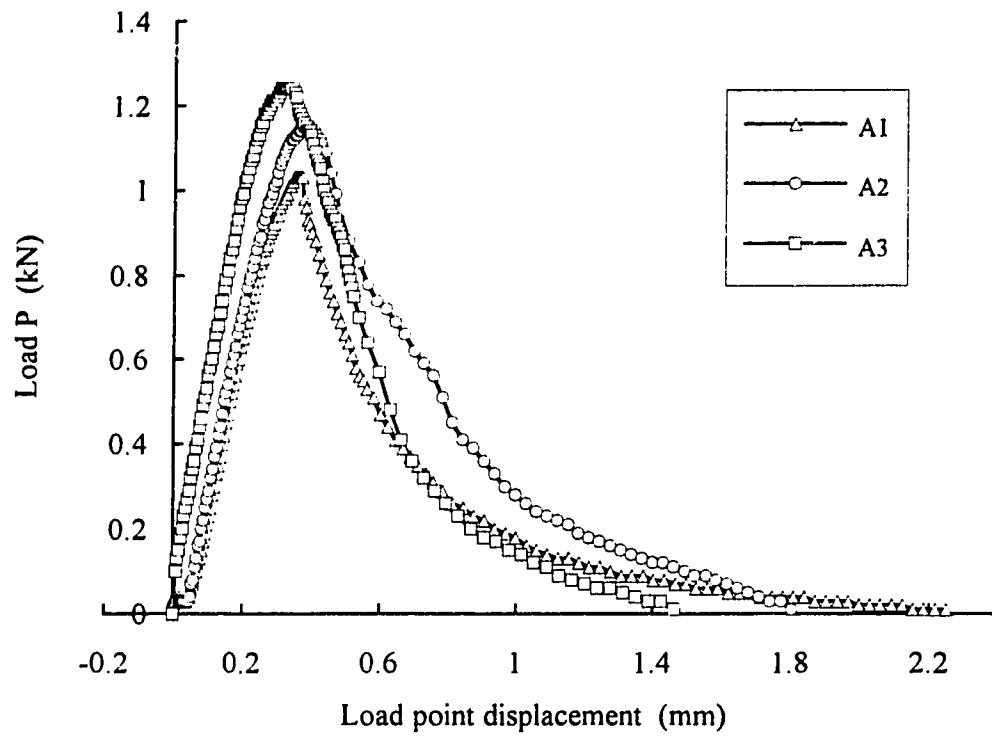
Fig.2.6  Load vs load-point-displacement for the notched beam tests
(Type A concrete)
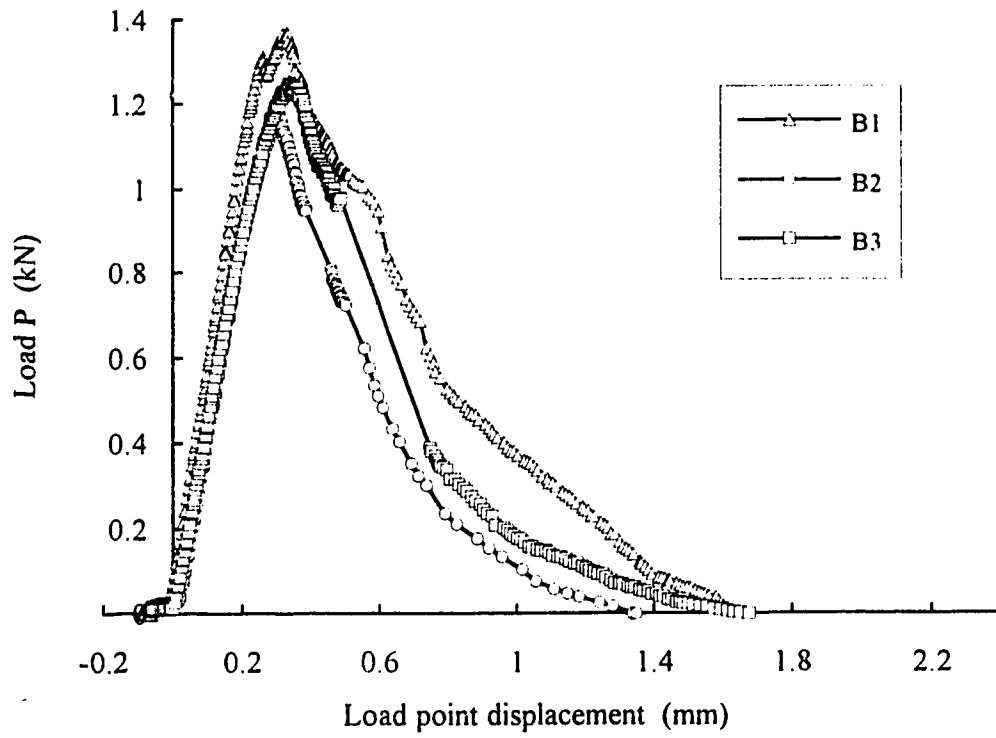
Fig.2.7  Load vs load-point-displacement for the notched beam tests
(Type B concrete)
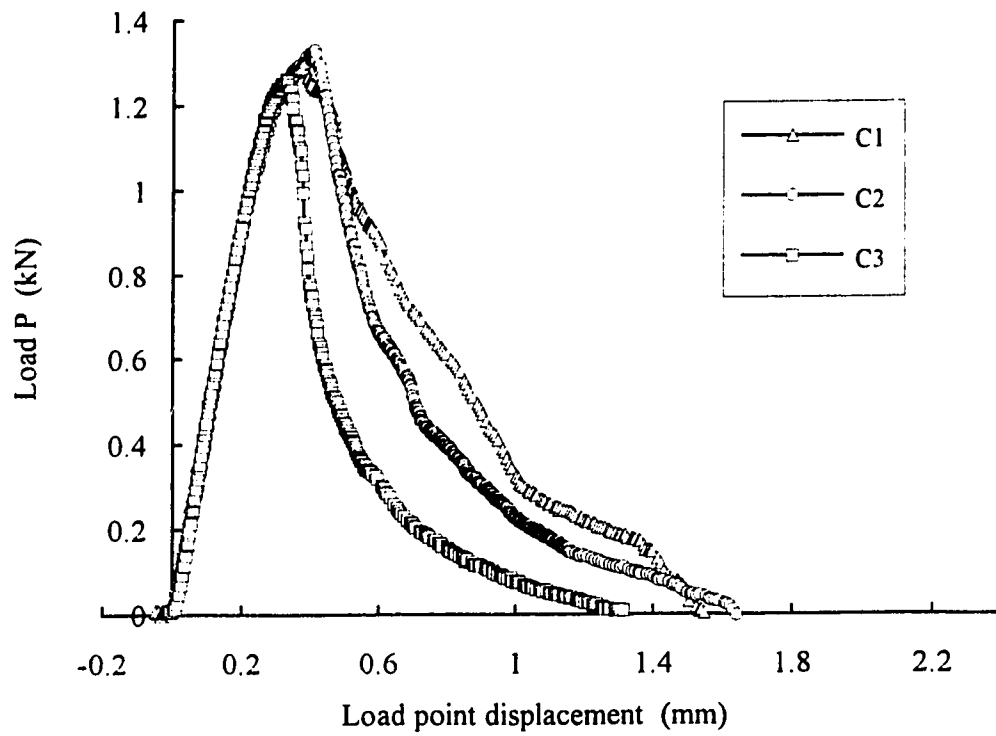
Fig.2.8   Load vs load-point-displacement for the notched beam tests
(Type C concrete)
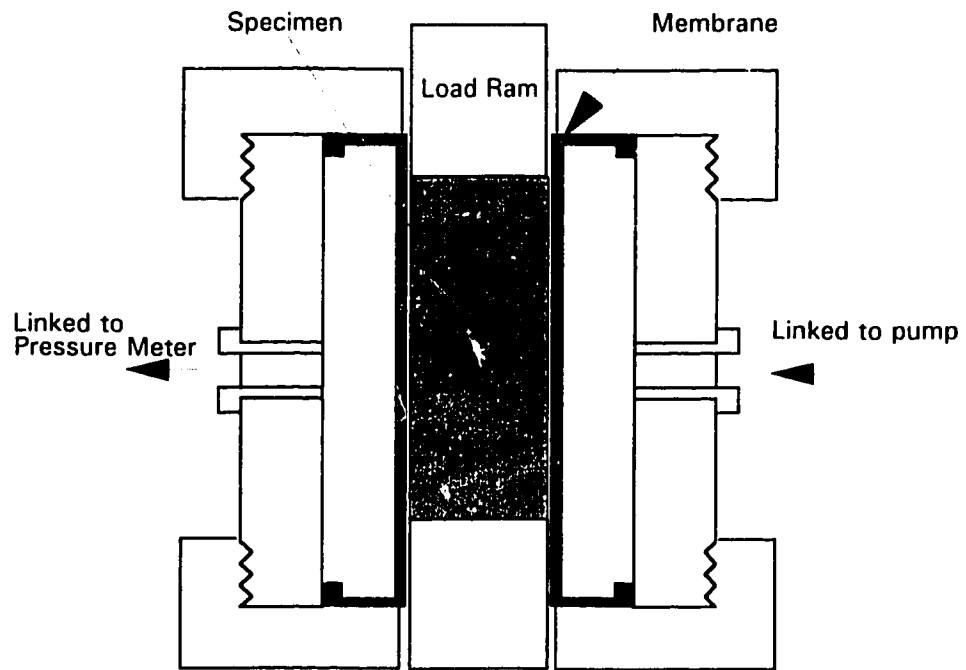
Fig.2.9 Cross-sectional view of triaxial Hoek cell
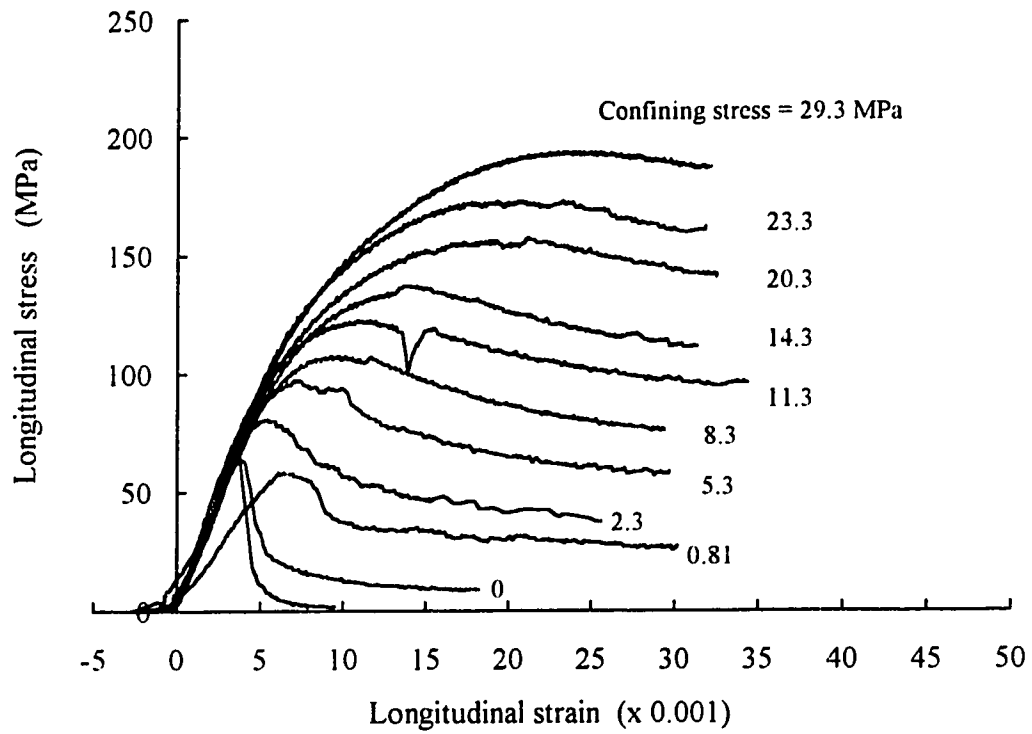
Fig.2.10  Longitudinal stress vs longitudinal strain
for triaxial compression tests (Type A concrete)

30
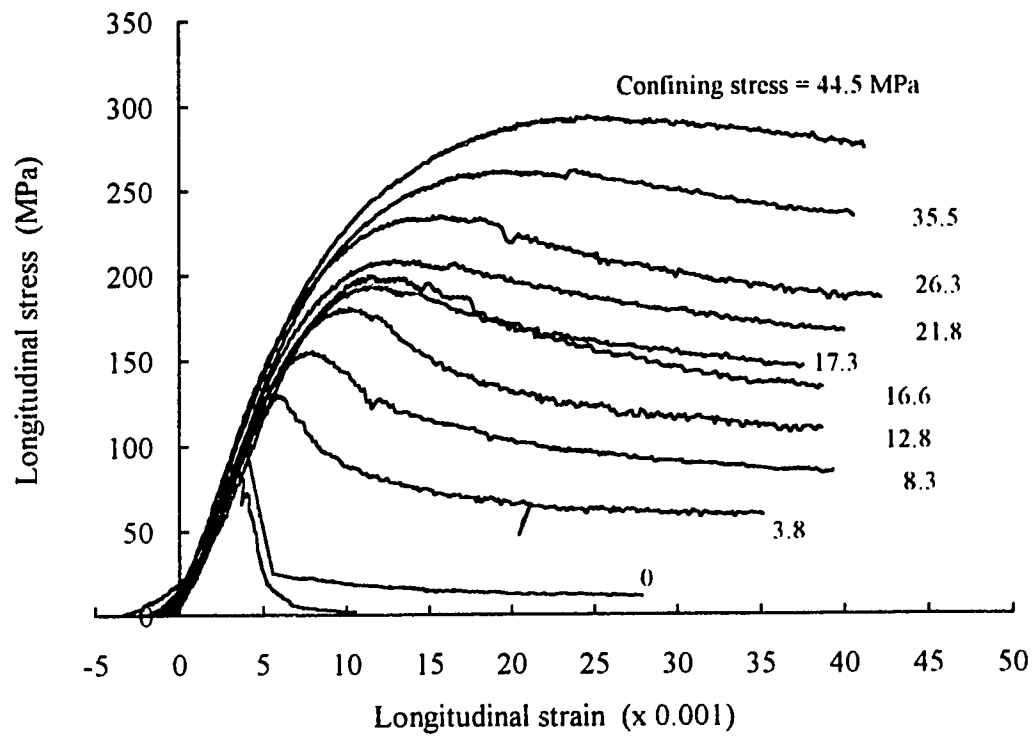
Fig.2.11　Longitudinal stress vs longitudinal strain
for triaxial compression tests (Type B concrete)
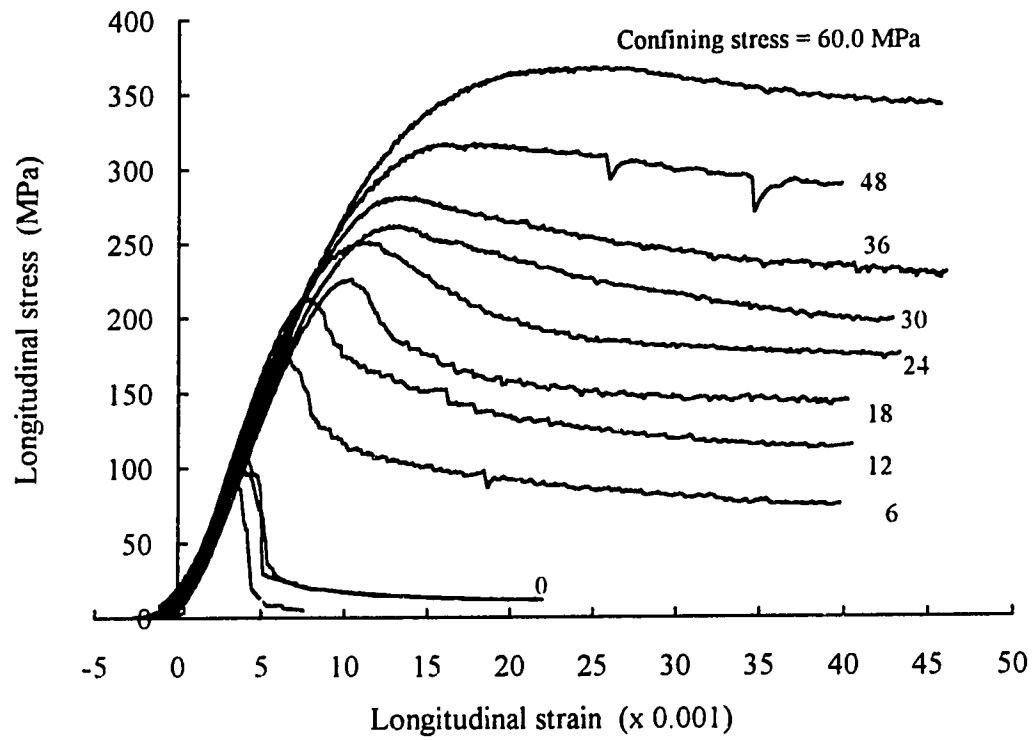
Fig.2.12   Longitudinal stress vs longitudinal strain
for triaxial compression tests (Type C concrete)

| Regression Equation | $\sigma_3/f_c' = a + b\,\sigma_1/f_c'$ | | |
| --- | --- | --- | --- |
| Type | A | B | C |
| $f_c'$ (MPa) | 60.2 | 92.2 | 119.0 |
| $f_{ct}$ (MPa) | 4.95 | 6.36 | 7.44 |
| Constant | 1.12 | 1.19 | 1.07 |
| Slope | 4.67 | 4.45 | 4.24 |
| $R^2$ Value | 0.986 | 0.962 | 0.940 |
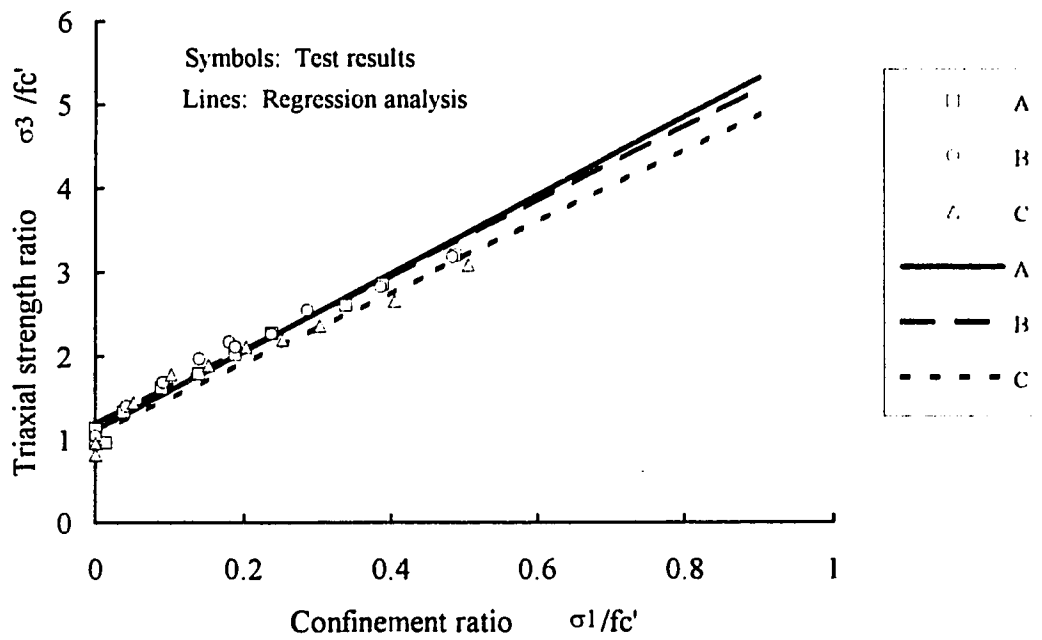


Fig.2.13　Linear regression of maximum strength
in triaxial compression

| Regression Equation | $\sigma_3/f_c = \sqrt{(1+k\,\sigma_1/f_c)}$ | | |
|---|---|---|---|
| Type | A | B | C |
| $f_c'$ (MPa) | 60.2 | 92.2 | 119.0 |
| $f_{ct}$ (MPa) | 4.95 | 6.36 | 7.44 |
| $k$ | 18.2 | 17.9 | 15.2 |
| $R^2$ Value | 0.992 | 0.991 | 0.990 |
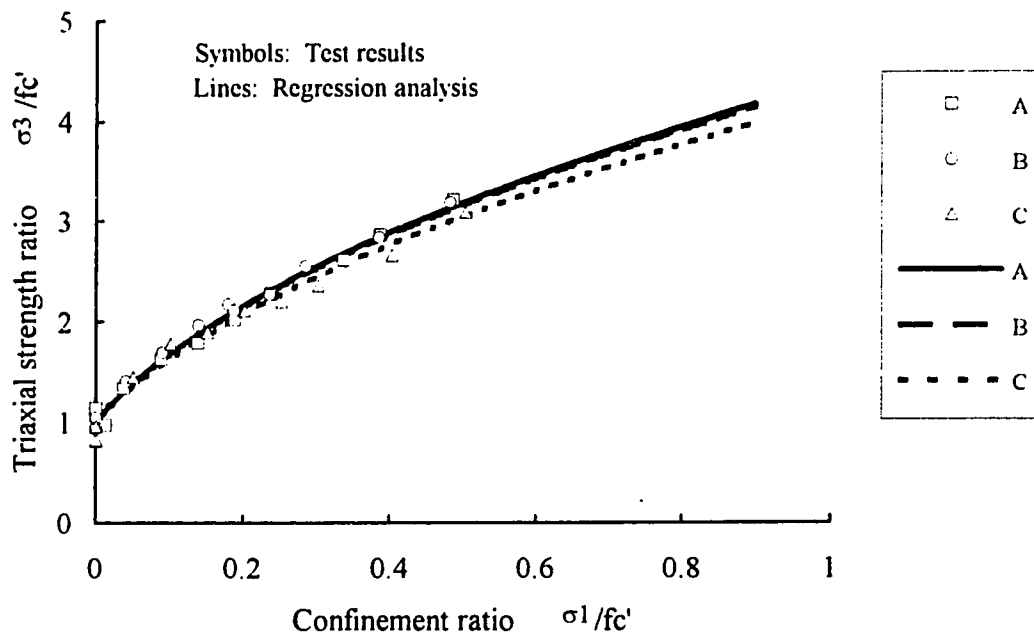


Fig.2.14   A parabolic equation for the maximum strength
in triaxial compression

# CHAPTER THREE

# CONSTITUTIVE MODEL FOR HIGH STRENGTH CONCRETE

## 3.1 Introduction

With the rapid development of modern numerical analysis techniques and high-speed digital computers, the finite element method has become an increasingly important tool for analyzing structures. There are two major reasons for the increasing application of finite element models to concrete structures. First, although experiments have played a significant role in the research on concrete structures, they are expensive when extensive data are needed for structures with various dimensions, under various loading types and with various boundary conditions. A parametric study using finite element model becomes an affordable and, therefore, an alternative means. In addition, tests cannot provide as much insight into the complicated pattern of stress distribution as revealed by a numerical simulation. In some situations, for safety considerations, a test has to be terminated when a specimen experiences instability or major damage. Instead, a finite element analysis can be carried out beyond the maximum strength of a structure provided that the analysis tool is robust, the formulation is rigorous, and the analysis has been shown to agree with tests. From this point of view, a numerical analysis provides supplementary information over experiments.

This chapter starts with a concise state-of-the-art review of finite element methods for concrete structures. The outlines of a fracture-energy based plasticity model proposed by Pramono and Willam (1989) are introduced. The Pramono and Willam model is extended to full three dimensional stress states. This model is calibrated for high strength concrete based on the tests conducted at University of Alberta (Chapter 2).

## 3.2. Review of Previous Work

Application of the finite element method to concrete structures was first attempted by Ngo and Scordelis (1967). Since then, tremendous progress in all aspects of finite element modeling of reinforced concrete has been made. Most efforts made in the past have been directed towards improving the mathematical description of the constitutive relations of concrete materials. During the last decade, research interest has been shifted to implementing the knowledge of fracture mechanics of concrete into constitutive models. There are many types of concrete models. Some of the well known categories include equivalent strain models (Darwin and Pecknold, 1977), nonlocal models (Bazant and Ozbolt, 1992), nonlinear elasticity model (Stankowski and Gerstle, 1987) and plasticity based fracture models (Bazant and Kim, 1979, Maekawa and Okamura, 1983, Han and Chen, 1985, and Pramono and Willam, 1989). Normally, the more concrete behavior phenomena one tries to capture, the more material constants one may have to deal with. In plasticity-based models, however, the number of unknowns is significantly reduced, which is credited to the postulated rules of the mathematical theory of plasticity. In addition, a plasticity model allows a much more realistic and comprehensive representation of various aspects of inelastic behavior. In particular, it gives good fits of the group of uniaxial, biaxial, and triaxial tests, provides failure conditions and strain-softening branches as part of the constitutive relation, gives correct lateral strains and most importantly, corrects volume changes as well as represents unloading and cyclic loading.

The model proposed by Maekawa and Okamura (1983) assumes concrete is composed of constituent elements located in parallel. Each element behaves as a strain-hardening material. Each constituent element loses its ability to support stress when the element stress reaches its fracture strength. The application of the model is very limited since the model is based on two dimensional loading conditions.

Han and Chen (1985) proposed a non-uniform hardening model with a closed initial yield surface. The failure surface encloses all the loading surfaces and serves as a bounding surface, which is assumed to remain unchanged during loading. The shapes of the deviatoric sections of the loading surfaces are assumed to be similar to those of the failure surface, but their meridians are different. During hardening, the loading surface expands and changes its shape from the initial yielding surface to the final shape that matches with the failure surface. The model, however, does not include strain-softening. Recently, Yamaguchi and Chen (1991) developed a finite element method to trace the micro-crack propagation in concrete under compressive loading. Concrete is modeled as a

two-dimensional, two-phase composite consisting of a mortar matrix and circular aggregate inclusions. Micro-cracks are allowed to develop both in the mortar and at the interfaces between the aggregates and the mortar, while the aggregates remain intact.

Bazant and Kim (1979) combined the incremental plasticity and fracturing (micro-cracking) material theories to obtain a nonlinear triaxial constitutive relation that is incrementally linear. The model uses a jump-kinematic hardening rule for unloading, reloading and cyclic loading. In the case of continuous tensile cracks, the theory applies only to the solid (albeit micro-cracked) concrete between the cracks. The model was used by Chen and Mau (1989) to perform a successful analysis of spiral columns despite the fact that the residual level of strength is too high for unconfined columns.

Pramono and Willam (1989) developed a fracture energy-based plasticity formulation of plain concrete. The formulation covers the full load-response spectrum in tension as well as in compression. The concrete model is based on the non-associated flow theory of plasticity with hardening in the pre-peak regime and fracture energy-based softening in the post-peak regime. The model was based on and calibrated with Hurlbut's tests (1985) on low strength concrete under triaxial compression and uniaxial compression and tension.

## 3.3 The Fracture-Energy Based Plasticity Model (Pramono and Willam, 1989)

Pramono and Willam's model (1989) forms the basis of the model used in this study. This choice was made for many reasons. The model uses a unified formulation for both tension and compression. A non-associated plastic flow is used to account for the volume changes. This gives the model an added flexibility and allows a better fit of concrete behavior. The strain-softening concept is included for concrete in tension, compression and triaxial compression. The model has the ability to fit triaxial compression tests, which is a very important aspect in analyzing confined columns.

The model implies that the material behaves elastically as long as the stress state lies within an initial yield surface. When loading progresses beyond the initial yield surface, plastic flow occurs and the yield surface hardens isotropically up to a failure surface. In this range, the plastic strain rate is governed by a plastic potential different from the yield

37

function. The hardening rule is thus non-associated. Moreover, the resulting constitutive matrix is not symmetric.

As plastic flow continues beyond that necessary to reach the failure surface, the material behavior becomes isotropic softening. Here the strength surface degrades to a residual surface. Flow is now governed by the refinement to satisfy the energy of fracture.

In the following the various concepts described above are presented. The presentation is largely based on Pramono and Willam (1989). The modifications necessary to apply the model to high strength concrete are introduced and extension of the model to full three dimensional behavior is presented in Section 3.4.

### 3.3.1 Leon's Triaxial Strength Failure Criterion

The failure criterion described by Leon was proposed originally in 1936 (Ramano, 1969) for the shear strength of concrete under combined tension-compression. This strength formulation combines the two-parameter Mohr-Coulomb friction law and the one-parameter tension cut-off condition of Rankine. The isotropic failure criterion is conveniently expressed in terms of the major and minor principal stresses as:

$$F(\vec{\sigma}^*) = F(\sigma_1, \sigma_3) = (\frac{\sigma_1 - \sigma_3}{f_c})^2 + m_0 \frac{\sigma_1}{f_c} - c_0 = 0 \qquad (3.1)$$

in which $\vec{\sigma}^*$ is the principal stress vector, $\sigma_1$ is usually thought of as the confining stress while $\sigma_3$ is the compressive stress. Here tension is positive. The influence of the intermediate principal stress, $\sigma_2$, is omitted similar to the Tresca and Coulomb conditions of maximum shear.

The triaxial failure condition is characterized by the uniaxial compressive strength $f_c'$, the frictional parameter $m_0$ and the cohesion $c_0$. The latter has a value of 1.0 at failure. The friction parameter $m_0$ is determined by substituting a uniaxial tension state in Eq.3.1 $(\sigma_3 = 0, \sigma_1 = f_t')$. This results in:

$$m_0 = \frac{f_c'^2 - f_t'^2}{f_t' f_c'} \qquad (3.2)$$

38

in which $f_t'$ is the tensile strength. The triaxial failure envelope of Leon is represented in Fig.3.1 in a principal stress sectional view (Fig.3.1a) and a hydrostatic view (Fig.3.1b).

The performance of the Leon criterion is illustrated in Fig.3.2, in which $R_d = \sqrt{2J_2}$ is the deviatoric length and $R_h = I_1/\sqrt{3}$ is the hydrostatic length. The stress invariants $I_1$ and $J_2$ are defined by Eq. 3.20. The different triaxial strength data of the concrete literature (Richart, 1928; Mills, 1970; and Launay, 1970) compare well with the compressive and tensile meridians of Leon model when a relatively large ratio of uniaxial strength values is used, such as $f_t'/f_c' = 1/12$. The triaxial strength data from the material tests at University of Alberta (Chapter 2) is included in Fig.3.3 for the compressive meridians only. The Type A concrete is for $f_c'$=60MPa, Type B for $f_c'$=90MPa, and Type C for $f_c'$=120MPa. It can be seen from Fig.3.3 that the test data fits the Leon's compressive meridians well for Type A and Type B concrete. For Type C concrete, the theoretical prediction slightly over-estimates the triaxial compressive strength.

## 3.3.2 Isotropic Hardening Model for Pre-Peak Behavior

The isotropic hardening mechanism involves, in this case, an initial loading surface that grows in a self-similar fashion when a hardening parameter, $k$, increases monotonically from an initial value $k = k_0 > 0$ to a final value at peak $k = k_p = 1$:

$$F(\sigma_1,\sigma_3,k) = [(1-k)\frac{\sigma_1^2}{f_c'^2} + \frac{\sigma_1-\sigma_3}{f_c'}]^2 + k^2 m_0 \frac{\sigma_1}{f_c'} - k^2 c_0 = 0 \qquad (3.3)$$

Different loading stages in a meridian plane are depicted in Fig.3.4 for concrete with $f_c'$=75 MPa.

The constitutive model assumes that the material is initially isotropic and remains pointwise isotropic during the entire deformation history irrespective of the orientation and magnitude of the principal stress components and inelastic deformations. The total strain increment can be decomposed into independent elastic and plastic components:

$$\Delta\varepsilon = \Delta\varepsilon_e + \Delta\varepsilon_p \qquad (3.4)$$

The elastic response is governed by the linear isotropic operator $\underset{\sim}{E}$:

$$\Delta \sigma = \underset{\sim}{E} \cdot \Delta \varepsilon_e \tag{3.5}$$

*Nonlinear Hardening Response*

The strain-hardening hypothesis describes the current state of the inelastic deformation process in terms of a scalar-valued kinematic variable $\varepsilon_p$ which defines the length of the plastic strain trajectory. During progressive plastic deformations, the value of the hardening parameter increases according to an ellipsoidal function of $\varepsilon_p$. The influence of confinement on the rate of hardening is introduced in term of a ductility measure $x_p$, which defines the accumulated plastic strain at peak in terms of the lateral confinement. As a result the hardening parameter $k = k(\varepsilon_p, x_p)$ is expressed as a monotonically increasing elliptic function of the plastic strain:

$$k = k_0 + \frac{1 - k_0}{\varepsilon_p} \sqrt{2 \varepsilon_p x_p - \varepsilon_p^2} \tag{3.6}$$

The equivalent plastic strain increment is defined as the Euclidean norm of the plastic strain increment:

$$\Delta \varepsilon_p = \sqrt{\Delta \bar{\varepsilon}_p^T \cdot \Delta \bar{\varepsilon}_p} \tag{3.7}$$

in which $\Delta \bar{\varepsilon}_p$ is the vector of principal plastic strain increments. The ductility measure $x_p$ introduces the effect of confining pressure on the rate of hardening here in terms of a quadratic polynomial of the major principal stress, $\sigma_1$:

$$x_p = A_h (\frac{\sigma_1}{f_c})^2 + B_h \frac{\sigma_1}{f_c} + C_h \tag{3.8}$$

The ductility parameters $A_h$, $B_h$ and $C_h$, are dimensionless deformation parameters that are calibrated from laboratory experiments.

Plastic volumetric change in concrete does not necessarily agree with an associated flow rule. The performance of the constitutive model is extremely sensitive to the hydrostatic component of the underlying flow rule. For the sake of flexibility a non-associated flow rule is adopted which defines the plastic strain rate as:

$$\Delta \bar{\varepsilon}_p = \Delta \lambda \, \bar{m} \quad \text{with} \quad \bar{m} = \frac{\partial Q}{\partial \bar{\sigma}^*} \tag{3.9}$$

The plastic multiplier $\Delta \lambda$ controls the magnitude while the gradient $\bar{m}$ controls the direction of the plastic strain increment. The plastic potential for non-associated flow is based on a modification of the loading surface:

$$Q(\sigma_1, \sigma_3, k, m_Q) = [(1-k)\frac{\sigma_1^2}{f_c'^2} + \frac{\sigma_1 - \sigma_3}{f_c'}]^2 + k^2 m_Q \frac{1}{f_c'} - k^2 c_0 = 0 \tag{3.10}$$

with the friction function defined in terms of the major principal stress, $\sigma_1$, as:

$$\frac{\partial m_Q}{\partial \sigma_1} = D \exp[E(\frac{-\sigma_1 + f_t'}{f_c'})] + F \tag{3.11}$$

The material parameters $D$, $E$, and $F$ are calibrated from triaxial test results.


### 3.3.3 Isotropic Softening Model for Post-Peak Behavior

The fracture energy-based strain-softening flow is formulated in terms of the fracture mode and is extended to compressive splitting and shear faulting. The fracture process in direct tension was discussed earlier by Hillerborg, et al. (1976). Similar conclusions were reached by von Mier (1984) for the failure behavior of concrete in uniaxial compression.

There has been a controversy whether and how proper fracture properties can be extracted from experiments on laboratory specimens and components for objective description of strength degradation. In the Willam model a smeared description was used in which microscopic as well as macroscopic discontinuities in the form of discrete cracks are distributed and represented by equivalent continuum concepts.

There are different types of descriptions for the strength degradation in the post-peak zone, including linear and bi-linear expressions. In all expressions, the area underneath the stress versus crack opening displacement curve is kept as a constant, $G_f^I$, the fracture energy in direct tension. In the Pramono and Willam model (1989), an exponential expression is adopted with a best fit of the Hurlbut (1985) direct tension test. The expression relates the crack width defined as total change of length in the crack process zone to the crack width at complete rupture:

$$\sigma_t = f_t' \exp(-5\frac{u_f}{u_r}) \tag{3.12}$$

in which $u_r$ is the rupture displacement and $u_f$ is the crack-opening displacement.

In the triaxial loading cases, the strain-softening becomes more complicated. However, there are still some common features in the strength degradation. Based on the triaxial test of high strength concrete, the concrete under triaxial compression experiences strain-softening after the minor stress reaches the peak. The slope of the descending curve becomes smaller and smaller as strain increases. There is a stress level, called residual strength by Pramono and Willam (1989), at which the slope of the descending stress-strain curve is insignificant. Pramono and Willam suggested an expression for the residual strength envelope:

$$F_r(\sigma_1,\sigma_3) = (\frac{\sigma_1-\sigma_3}{f_c'})^2 + m_r\frac{\sigma_1}{f_c'} = 0 \tag{3.13}$$

in which, $m_r$ is the residual frictional parameter.

The intermediate softening stage is defined by the modification of the peak strength condition (Eq.3.3) as follows:

$$F_r(\sigma_1,\sigma_3) = (\frac{\sigma_1-\sigma_3}{f_c'})^2 + m_s\frac{\sigma_1}{f_c'} - c_s = 0 \tag{3.14}$$

in which $c_s$ is the cohesion ratio during strain-softening:

$$c_s = \frac{\sigma_t}{f_c'}$$

(3.15)

and $m_s$ is a frictional parameter during softening. It is prorated linearly between $m_r$ and $m_0$:

$$m_s = m_r - (m_r - m_0)c_s$$

(3.16)

*Equivalent Strain-Softening*

Since strain-softening occurs not only in tension but also in compression and confined compression, Pramono and Willam (1989) adopt the 'equivalent tensile fracture strain', $\varepsilon_f$, to monitor the degradation of the triaxial strength envelopes. The measure of the incremental equivalent tensile fracture strain is suggested as:

$$\Delta \varepsilon_f = \sqrt{<\Delta \bar{\varepsilon}_f>^T <\Delta \bar{\varepsilon}_f>}$$

(3.17)

The McCauley brackets, $<\ >$, extract the tensile components of the principal fracture strain increment $\Delta \bar{\varepsilon}_f$.

For the case of direct tension, since only the strain increment in the major stress direction will be accounted for, the incremental crack-opening displacement can be determined by:

$$\Delta u_f = h_t \Delta \varepsilon_f$$

(3.18)

in which $h_t$ is tensile crack spacing or height of the tension specimen which is used as a reference length. When the smeared crack model is used, $h_t$ will be substituted for by $h_e$, the element height.

For the cases other than direct tension, measuring of crack-opening displacement is not so straightforward. But an 'equivalent crack-opening displacement' can be introduced as:

$$\Delta u_f = h_c \Delta \varepsilon_f$$

(3.19)

43

Here $h_c$ is called 'gage length' or the 'equivalent crack spacing' for cases other than direct tension. The determination of $h_c$ depends on types of failure modes which can be effected by the confinement.

## 3.4 Modification And Calibration of the Model

Pramono and Willam's model was originally developed based on low strength concrete data. The model needs to be calibrated for high strength concrete. The fracture energy related parameters have to be obtained. In addition, since the loading state of concrete in confined columns is strongly three-dimensional, the original model has to be modified to include the capacity for three-dimensional stress analysis.

### 3.4.1. Ductility Measure $X_p$

The ductility measure $X_p$ is determined using Eq.3.8. Pramono and Willam (1989) evaluated a set of parameters $A_h$, $B$ and $C_h$, for low strength concrete. This set of parameters is not suitable for high strength concrete as its hardening behavior is different from that of low strength concrete. In this study, new sets of $A_h$, $B_h$ and $C_h$, are obtained for high strength concrete based on the tests presented in Chapter 2.

It can be seen from Eqs.3.6 and 3.3 that $C_h$, is equal to the plastic strain $\varepsilon_p$, at stress peak for the uniaxial compression state. Therefore, $C_h$, is obtained based on the test result of uniaxial compression. On the other hand, $A_h$, and $B_h$ mainly account for the ductility performance in uniaxial tension and triaxial compression. $A_h$, and $B_h$ can evaluated based on the best fit of the uniaxial tension test and the triaxial compression test. Unfortunately, the tests presented in Chapter 2 do not include uniaxial tension tests. Instead, the value used by Pramono and Willam (1989), $X_p=3\times10^{-5}$ for uniaxial tension, is also used here. Three sets of $A_h$, $B_h$ and $C_h$, are included in Table 3.1 for concretes with compressive strength of 60, 90 and 120MPa.

44

## 3.4.2 Equivalent Crack Spacing $h_c$

The 'crack spacing' has been an important concept in the strain softening analysis of concrete. It links the fracture strains and crack openings. In Pramono and Willam's model, an 'equivalent crack spacing' $h_c$ was introduced to represent fracture of concrete under different loading conditions.

Promano and Willam (1989) defined $h_c$ using an energy approach. It was based on the assumption that the strain energy in splitting compression could be equivalent to that in direct tension. An empirical expression for $h_c$ was suggested by Promano and Willam:

$$\frac{h_t}{h_c} = A_s(\frac{\sigma_l}{f_c'} - \frac{f_t'}{f_c'})^4 + B_s(\frac{\sigma_l}{f_c'} - \frac{f_t'}{f_c'})^2 + 1 \tag{3.20}$$

in which $h_t$ is the cracking spacing in direct tension.

Eq.3.20, however, was not successful in modeling unconfined concrete and concrete with low-confinement. The fracture energy of concrete in compression was over-estimated in the expression which made the model unrealistically stiff.

Based on the test results of high strength concrete at University of Alberta (Chapter 2), a new definition for $h_c$ is suggested. The equivalent cracking spacing $h_c$ here is also defined as a function of the confining stress, $\sigma_l$. The new definition is different depending on whether the confining stress is compressive or tensile:

$$\frac{h_t}{h_c} = A_s\sqrt{(1 + B_s\frac{\sigma_l}{f_c'})} \qquad \text{when } \sigma_l < 0 \tag{3.21A}$$

$$\frac{h_t}{h_c} = 1 - (1 - A_s)(1 - \frac{\sigma_l}{f_t})^2 \qquad \text{when } 0 \le \sigma_l \le f_t' \tag{3.21B}$$

in which $A_s$ and $B_s$ are internal material parameters to be determined based on the test results. Note these two parameters are defined differently from those in Pramono and Willam's expression. Parameter $A_s$ can be determined using Eq.3.21B based on the best fit of test results of uniaxial compression. With $A_s$ obtained, $B_s$ can be determined using Eq.3.21A with the best fit of the triaxial compression tests. Three sets of $A_s$, and $B_s$ are included in Table 3.1 for concretes with compressive strength of 60, 90 and 120MPa.

Adopting a strength degrading response in the post peak regime of behavior can result in mesh dependency as shown by Bazant (1976). To avoid this type of mesh dependency the energy of fracture is normalized through the element size to maintain a constant release rate. In this study, it is suggested that when concrete is under direct tension, the element height is used as equivalent crack spacing. There will be no correction of $h_c$ for concrete in triaxial compression as the corresponding failure mode is distributed. A correction on $h_c$ will be applied in cases between direct tension and triaxial compression as a function of the third stress invariant.

### 3.4.3 Extension of the Model to Three Dimensional Loading Cases

Although various finite element models have been proposed and developed for concrete, application of the plasticity theory has been limited to in-plane and axisymmetric loading cases. The difficulty of extending a two-dimensional plasticity model to a three-dimensional one basically comes from lack of the transformation matrix from the general stress tensor $\sigma$ which has components of $<\sigma_x, \sigma_y, \sigma_z, \tau_{xy}, \tau_{yz}, \tau_{zx}>^T$ to principal stress vector $\bar{\sigma}^* = <\sigma_1, \sigma_2, \sigma_3>^T$. As shown in the previous section, the loading surface and the potential surface are expressed in terms of principal stress components $\sigma_1$ and $\sigma_3$. However, differentiation of these two surfaces should always be against the general stress tensor $\sigma$ in a finite element formulation.

*Transformation Matrix for Stresses*

From solid mechanics, the three stress invariants are defined as:

$$I_1 = \sigma_x + \sigma_y + \sigma_z \tag{3.20A}$$

$$J_2 = \tfrac{1}{2}[\sigma_x'^2 + \sigma_y'^2 + \sigma_z'^2] + \tau_{xy}^2 + \tau_{yz}^2 + \tau_{zx}^2 \tag{3.20B}$$

$$J_3 = \sigma_x'\sigma_y'\sigma_z' - \sigma_x'\tau_{yz}^2 - \sigma_y'\tau_{zx}^2 - \sigma_z'\tau_{xy}^2 + 2\tau_{xy}\tau_{yz}\tau_{zx} \tag{3.20C}$$

Here, $\sigma_x'$, $\sigma_y'$ and $\sigma_z'$ are stress deviators:

$$\sigma_x' = \sigma_x - (\sigma_x + \sigma_y + \sigma_z)/3$$

$$\sigma_y' = \sigma_y - (\sigma_x + \sigma_y + \sigma_z)/3$$

$$\sigma_z' = \sigma_z - (\sigma_x + \sigma_y + \sigma_z)/3$$

A stress invariant vector $\bar{J} = < I_1, \sqrt{J_2}, .I_3 >$ can be introduced for simplicity. Also an array of general stress $\{\sigma\}$ is introduced which includes all the stress components of the general stress tensor $\underset{\sim}{\sigma}$. It is defined as: $\{\sigma\} = < \sigma_x, \sigma_y, \sigma_z, \tau_{xy}, \tau_{yz}, \tau_{zx} >^T$

The principal stress vector can be expressed as:

$$\bar{\sigma}^* = \begin{Bmatrix} \sigma_1 \\ \sigma_2 \\ \sigma_3 \end{Bmatrix} = \frac{2\sqrt{J_2}}{\sqrt{3}} \begin{Bmatrix} sin(\theta + 2\pi/3) \\ sin\,\theta \\ sin(\theta - 2\pi/3) \end{Bmatrix} + \frac{I_1}{3} \begin{Bmatrix} 1 \\ 1 \\ 1 \end{Bmatrix} \tag{3.21}$$

in which $\theta$ is generally called the angle of similarity and is defined as

$$\theta = \frac{1}{3} sin^{-1} \left[ -\frac{3\sqrt{3}}{2} \frac{J_3}{(J_2)^{3/2}} \right] \text{ with } (-\pi/6 < \theta < \pi/6). \tag{3.22}$$

The gradient of a yield surface is defined as

$$\frac{\partial F}{\partial \{\sigma\}} = \frac{\partial F}{\partial \bar{\sigma}^*} \frac{\partial \bar{\sigma}^*}{\partial \{\sigma\}} \tag{3.23}$$

Here $F$ is a scalar function and $\dfrac{\partial \bar{\sigma}^*}{\partial \{\sigma\}}$ is called transformation matrix of stresses.

Since $\bar{\sigma}^*$ and $\bar{J}$ are uniquely invariable, it can be shown that:

$$\frac{\partial \bar{\sigma}^*}{\partial \{\sigma\}} = \frac{\partial \bar{\sigma}^*}{\partial I_1} \frac{\partial I_1}{\partial \{\sigma\}} + \frac{\partial \bar{\sigma}^*}{\partial \sqrt{J_2}} \frac{\partial \sqrt{J_2}}{\partial \{\sigma\}} + \frac{\partial \bar{\sigma}^*}{\partial J_3} \frac{\partial J_3}{\partial \{\sigma\}} \tag{3.24}$$

in which

47

$$\frac{\partial \bar{\sigma}^*}{\partial I_1} = <\frac{1}{3}, \frac{1}{3}, \frac{1}{3}>^T \qquad (3.25A)$$

$$\frac{\partial \bar{\sigma}^*}{\partial \sqrt{J_2}} = <-\frac{2}{\sqrt{3}}\frac{\sin(2\theta-2\pi/3)}{\cos(3\theta)}, -\frac{2}{\sqrt{3}}\frac{\sin(2\theta)}{\cos(3\theta)}, -\frac{2}{\sqrt{3}}\frac{\sin(2\theta+2\pi/3)}{\cos(3\theta)}>^T \qquad (3.25B)$$

$$\frac{\partial \bar{\sigma}^*}{\partial J_3} = <-\frac{\cos(\theta+2\pi/3)}{J_2\cos(3\theta)}, -\frac{\cos(\theta)}{J_2\cos(3\theta)}, -\frac{\cos(\theta-2\pi/3)}{J_2\cos(3\theta)}>^T \qquad (3.25C)$$

and

$$\frac{\partial I_1}{\partial \{\sigma\}} = <1,1,1,0,0,0> \qquad (3.26A)$$

$$\frac{\partial \sqrt{J_2}}{\partial \{\sigma\}} = \frac{1}{2\sqrt{J_2}} <\sigma_x', \sigma_y', \sigma_z', 2\tau_{xy}, 2\tau_{yz}, 2\tau_{zx}> \qquad (3.26B)$$

$$\frac{\partial J_3}{\partial \{\sigma\}} = <(\sigma_y'\sigma_z' - \tau_{yz}^2 + J_2/3), (\sigma_x'\sigma_z' - \tau_{xz}^2 + J_2/3), (\sigma_x'\sigma_y' - \tau_{xy}^2 + J_2/3),$$

$$2(\tau_{yz}\tau_{xz} - \sigma_z'\tau_{xy}), 2(\tau_{xz}\tau_{xy} - \sigma_x'\tau_{yz}), 2(\tau_{xy}\tau_{yz} - \sigma_y'\tau_{xz})> \qquad (3.26C)$$

If $\dfrac{\partial F}{\partial \bar{\sigma}^*}$ is given, provided $\dfrac{\partial \bar{\sigma}^*}{\partial J}$ and $\dfrac{\partial J}{\partial \{\sigma\}}$ can be worked out from (3.25) and (3.26), the differentiation of a scalar function $F$ against the general stress $\dfrac{\partial F}{\partial \{\sigma\}}$ can be determined.

## 3.5 Implementation of the Model

Pramono and Willam's model requires a solver for a non-symmetric system to account for non-associated plastic flows. The program 'ABAQUS' is selected as a base program as it has such a capacity.

'ABAQUS' is a non-linear finite element program developed by Hibbitt, Karlsson and Sorensen Inc. (1993). The 'ABAQUS' Version 5.3 was mounted in the SUN workstation facility at the Department of Civil Engineering, University of Alberta. The mounted 'ABAQUS' version was written in the FORTRAN 77 language. Pramono and Willam's model was coded and implemented as a user subroutine 'UMAT' into 'ABAQUS'.

'ABAQUS' provides various different choices for the solution strategy. In this study, the displacement control approach, along with the modified Newton-Raphson iteration method will be used.

## 3.6 Performance of the Calibrated Model

Performance of the calibrated model was examined by simulating uniaxially and triaxially compressed cylinder tests. Material parameters, including ductility parameters and stain softening parameters (both included in Table 3.1), were determined based on the test of high strength concretes at University of Alberta (Chapter 2).

Due to the symmetry of the geometry, loading condition and boundary conditions, only a quarter of the cylinder is modeled with three element columns in the radial direction and six element layers along the height. The element type used is axisymmetric eight-node quadratic rectangular. To simulate the effect of the loading platen on the top of the specimen, the deformation along the top of the concrete cylinder is suppressed. The analysis is carried out using displacement control with the movement of the top of the cylinder as a monitor. A schematic representation of the mesh division is presented in Fig.3.5.

49

Results of the analysis are presented in Fig.3.6A, B and C for concretes with compressive strength of 60, 90 and 120MPa respectively. It can be seen that the finite element model, generally speaking, captures the stress-strain behavior well for uniaxially and triaxially loaded cylinders. The maximum stress point and the residual stress level from the numerical analysis are acceptable as compared with the test results.

Table 3.1   Material parameters for high strength concretes

| Concrete Type | A | B | C |
|---|---|---|---|
| E (MPa) | 26110 | 31930 | 35870 |
| $f_c'$ (MPa) | 60.2 | 92.2 | 119.0 |
| $f_t'$ (MPa) | 4.95 | 6.36 | 7.44 |
| $G_{cr}^I$ (N/mm) | 0.152 | 0.171 | 0.191 |
| $A_h$ | 0.02142 | 0.00745 | 0.01792 |
| $B_h$ | -0.032 | -0.036 | -0.036 |
| $C_h$ | 0.0025 | 0.0025 | 0.0022 |
| $A_s$ | 24.0 | 24.0 | 24.0 |
| $B_s$ | -4 | -4 | -4 |
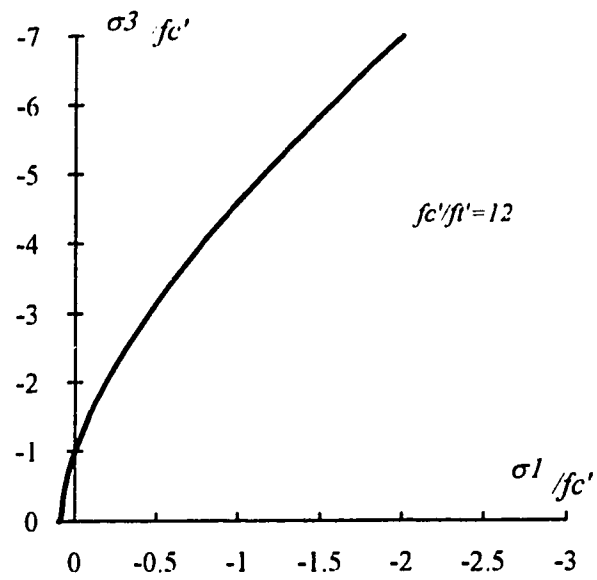
(a) Principle stress section
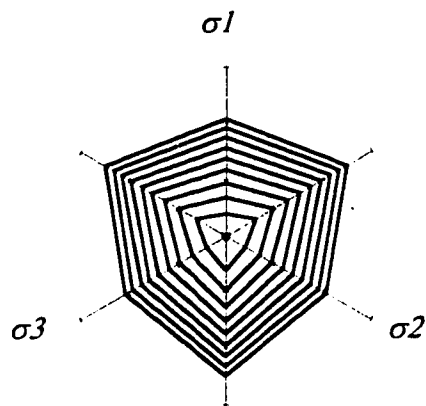


(b) Hydrostatic view of failure envelope

Fig.3.1   Triaxial failure envelope of Leon's model
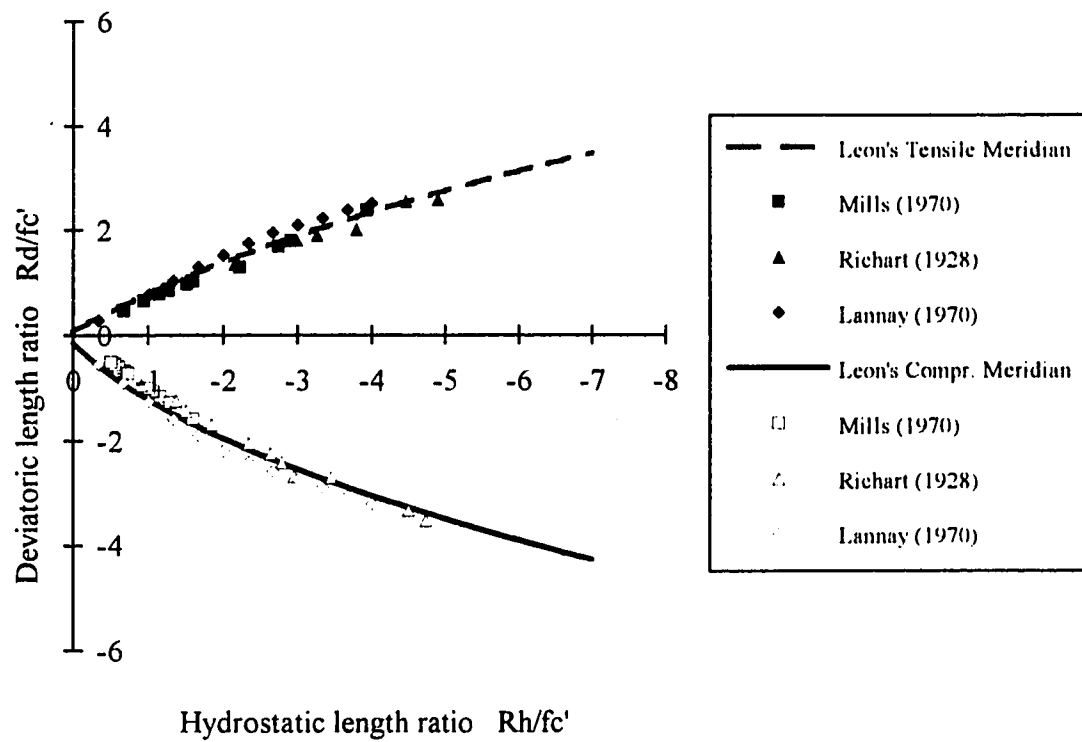
Fig.3.2   Leon's tensile and compressive ɛ ɛridians with test results

Fig.3.3   Leon's compressive meridians with test results from University of Alberta
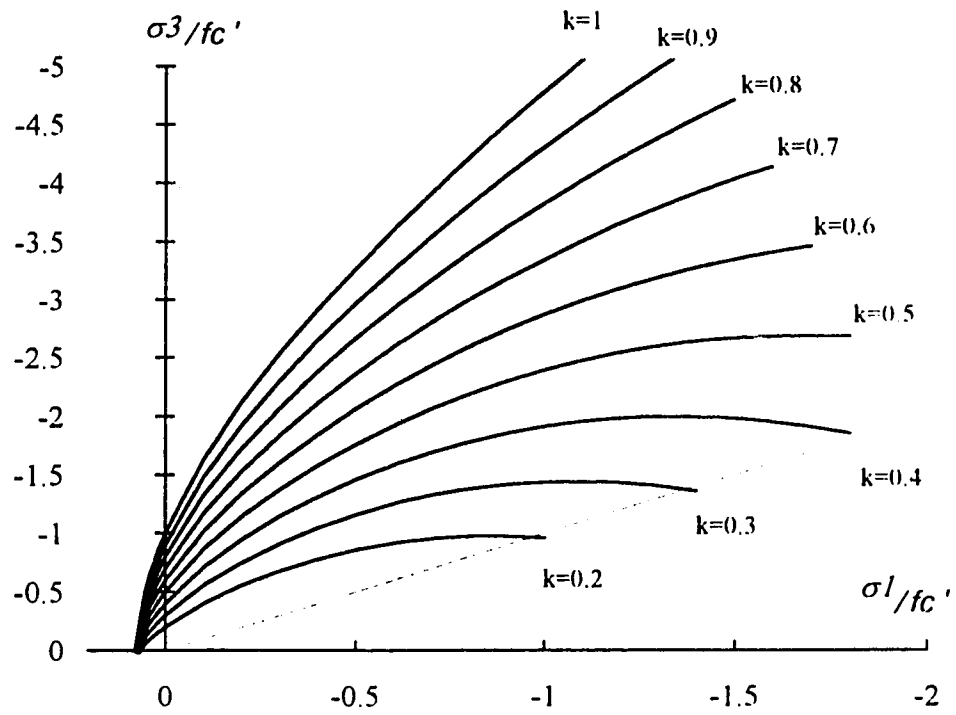
Fig.3.4 Loading surface of isotropic hardening model

Axial load



Rigid body elements

Confining
Stress

55.5
mm

27.5mm
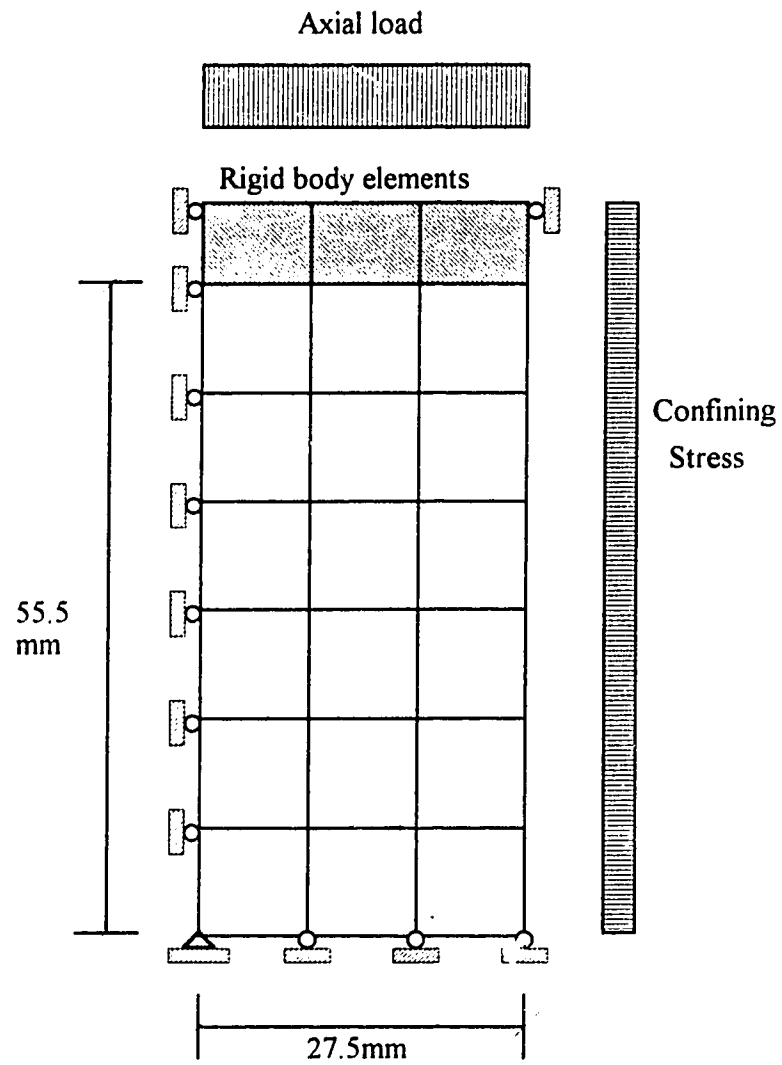
Fig.3.5 Schematic representation of mesh division of a cylinder
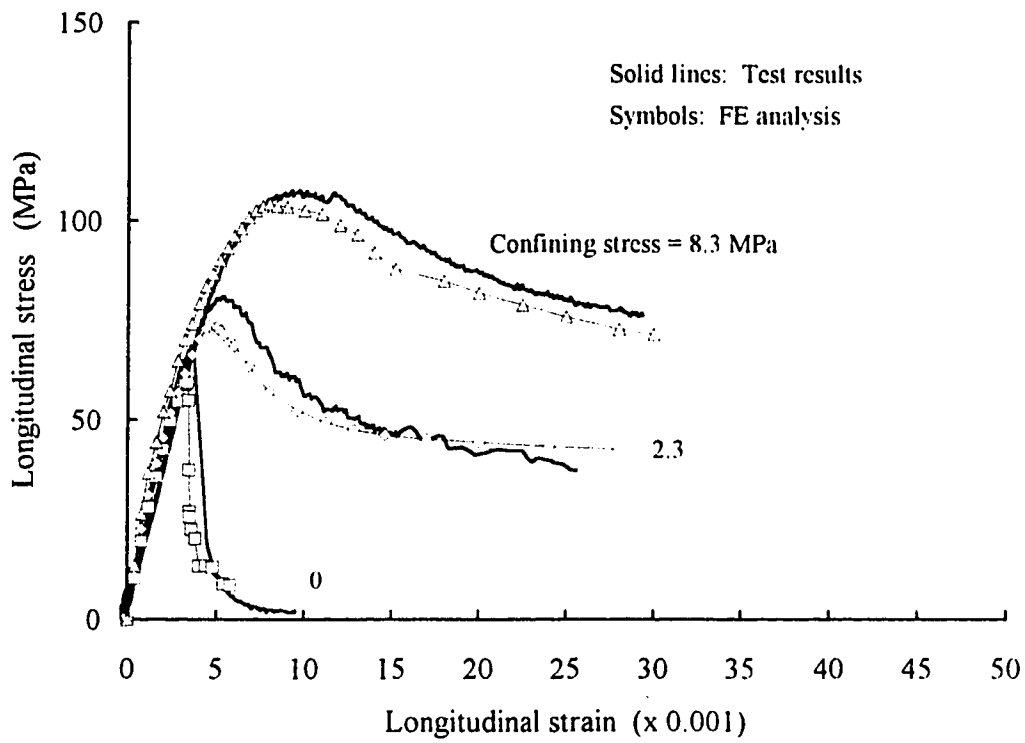
Fig.3.6A  Analysis of cylinder test of Type A concrete

57
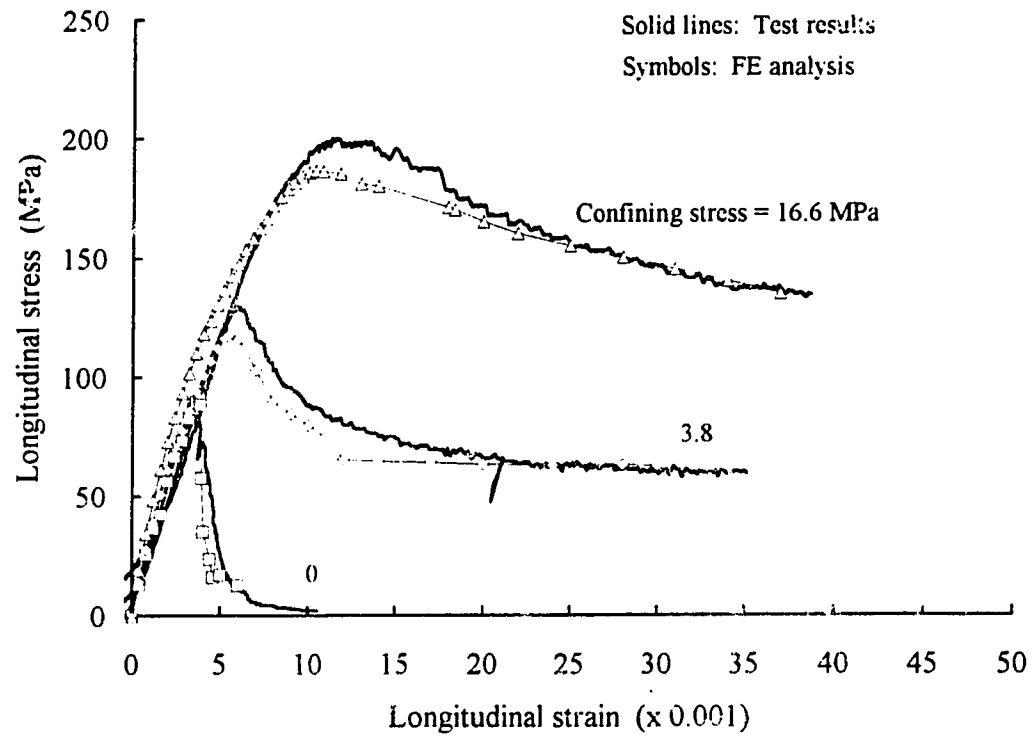
Fig.3.6B   Analysis of cylinder test of Type B concrete

58
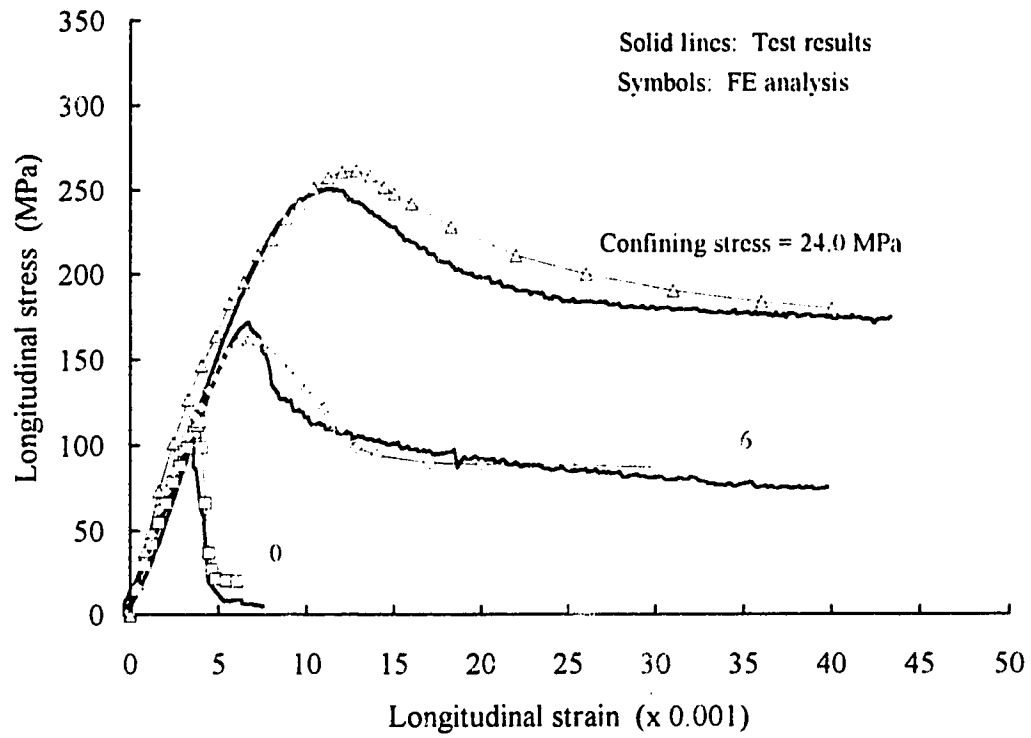
Fig.3.6C   Analysis of cylinder test of Type C concrete

# CHAPTER FOUR

# ANALYSIS OF TESTED HIGH STRENGTH CONCRETE COLUMNS

## 4.1 Introduction

A series of experiments of tied high strength concrete columns were conducted at University of Alberta by Ibrahim and MacGregor (1994). The objective of the tests was to study the parameters defining the ACI rectangular stress block and the stress-strain relationship of eccentrically loaded high strength concrete columns. There were two types of the test specimens, one with rectangular cross sections and another with triangular cross sections.

In order to verify the adequacy of the constitutive model described in Chapter 3, a simulation of some of the Ibrahim and MacGregor (1994) test results was carried out. Four of the test specimens with rectangular cross sections, V2, V7, V13 and V16, are analyzed using the modified Pramono and Willam finite element model. In addition, the simulation provides a theoretical insight into the failure mechanism of tied concrete columns.

This chapter starts with a brief description of the Universit   ⁄ Alberta experimental program. Numerical results of the four test specimens are presented. The load-deformation relations, stress distribution patterns in the columns, and stresses in the ties are discussed. Based on the numerical analysis and experimental observations, conclusions are made on the failure mechanism of tied concrete columns. The effect of transverse reinforcement on the failure is studied.

## 4.2 Review of The University of Alberta Experimental Program

### 4.2.1 Test Specimens

The test specimens were C-shaped as shown in Fig.4.1 with two types of cross sections, rectangular and triangular. The work presented here only addressed the rectangular specimens. The dimensions of the cross-sections of the rectangular specimens were 200x300mm in the test region. The main parameters involved were concrete strength and spacing of the transverse reinforcement. Details of concrete strength, reinforcement and test methods for Specimens V2, V7, V13 and V16 are listed in Table 4.1. The end blocks of specimens were designed to have flexural and shear strengths well in excess of the loads applied in the test. This was to assure that failure would occur in the test region as intended. The cross section shown is for Specimens V2, V7 and V13. Specimen V16 had eight longitudinal bars and rectangular plus diamond shaped ties.

These specimens were chosen to represent a variety of conditions. Specimens V7, V13 and V16 were identical except that the spacing and amount of transverse ties were changed and the concrete strength was also changed. All three were tested under a triangular strain distribution with zero strain on the left hand face in Fig. 4.1. Specimen V2 was tested under a constant eccentrically applied load which results in maximum compression on the left hand face in Fig.4.1 and near zero strain on the right hand face.

### 4.2.2 Test Set-up

There were two vertical loads $P_1$ and $P_2$ acting on the specimens. $P_1$ was the primary load applied by a 6600 kN MTS machine, while $P_2$ was the secondary load applied by a hydraulic jack. The test set-up, as shown in Fig.4.2, consisted of a system of curved plates and rollers at the top and bottom of the specimens. The system was used to provide a well defined center of rotation in the tapered end of the specimen.

The secondary load $P_2$ was applied using a 540 kN hydraulic jack with a system of steel plates, pins, anchor rods and bolts attached at the top and bottom arms of the specimen. The loading system was designed to have enough stiffness to prevent sudden failure when the load $P_2$ dropped off during the test.

Lateral supports were provided at the center of rotation of each system of end plates to prev ... instability and to reduce the lateral displacement at the center of rotation.

## 4.2.3 Test Method and Procedure

The load $P_1$ was applied using the stroke control system of the MTS machines, while the load $P_2$ was adjusted accordingly to obtain zero strain at a predetermined point, generally on one face of the cross-section (the left side in Fig. 4.2). A feed back control system was used to control the change in load $P_2$. The feed back control system corrected the error in the signal by moving the piston of the hydraulic jack. This movement changed the value of $P_2$ by the amount required to keep the neutral axis in the predetermined position. A slow rate of loading was chosen to reduce the fluctuation in $P_1$ and $P_2$. This involved increasing the strain on the compression face of the test region at a rate of 1000 microstrain/hour.

Unlike Specimens V7, V13 and V16 which were tested with zero strain at one face of the cross-section, Specimen V2 was tested with load $P_1$ applied at a constant eccentricity of 45 mm measured from the center line of the specimen. There was no load $P_2$ on it.

The tests were terminated when a complete destruction of the plain concrete specimens occurred or when the load $P_2$ decreased to zero for the reinforced concrete specimens.

## 4.3 Numerical Simulation of Tested Specimens

A successful numerical simulation of concrete columns requires proper representations of concrete, longitudinal and transverse reinforcement, boundary conditions, and loading procedure. In addition, convergence control of the analysis plays a significant role in obtaining a quality solution.

### 4.3.1 Modeling of Concrete

The analysis presented in the following sections was carried out using program 'ABAQUS' (Hibbitt et al., 1993). The material model is the Pramono and Willam (1989) model as modified and described in Chapter 3.

Modeling of concrete involves two aspects, the representation of concrete material and the representation of concrete structures.

*Material Parameters*

The procedure used in evaluating material parameters for the modified Willam's model has been discussed in Chapter 3. Three sets of the parameters have been evaluated in Chapter 3 based on the constitutive test in Chapter 2. However, concrete behaves differently from batch to batch. In order to simulate the tested tied column specimens, some of the parameters have to be evaluated based on the compressive stress-strain curves, fracture energy and split cylinder strength of the same batch of concrete (Ibrahim and MacGregor, 1994). The material parameters used in the numerical analysis of Specimens V2, V7, V13 and V16 are presented in Table 4.2. It was found, from the tests, that the strain on the compression face at maximum moment capacity was in the range of 0.00363 to 0.00372 for Specimens V7, V13 and V16, and 0.00458 for Specimen V2. In the numerical analysis, a lower value of Young's modulus is used for Specimen V2. The modulus of elasticity of concrete was not reported by Ibrahim and MacGregor (1994).

*The Finite Element Mesh*

Due to the symmetry of the structure, only a quarter of the column is modeled (half in the vertical direction from the mid-span; and half in the width direction from the mid-plane). The specimen actually consists of two parts: the two end blocks and the test zone which is the part between the two end blocks. Both parts are modeled with twenty-node three-dimensional quadratic solid elements.

Since the end blocks were designed to have excess flexural and shear strength, they behaved as rigid bodies in the test. In the numerical analysis, the end blocks are modeled with coarse mesh divisions. The material used in this region is linear elastic with a high value of Young's modulus (about five to ten times that of concrete).

On the other hand, one would expect the test zone to be modeled with refined mesh divisions to capture the complicated stress distribution patterns between ties. However, problems of the storage size in computation and computing time may arise because of the fact that each 20-node three-dimensional element involves 27 integration points if a standard integration rule is used. To avoid these computational difficulties and maintain proper representation of the columns, a standard is set that allows at least one element layer between adjacent ties. From observations in experiments, the behavior of the cover is significantly different from that of the core. Therefore, one element wall is used for the cover although the thickness of cover is much smaller than that of the core.

A schematic representation of the mesh of Specimen V13 is shown in Fig. 4.3A. In the analysis, the axial load $P_1$ was applied at the center of rotation of the roller assembly, leading to high stress concentrations in this vicinity. These had dissipated before the test region was reached. Fig. 4.3B shows the mid-span cross-section, with the locations of Points A, B, C and D in the rectangular tie, and the locations of the diamond-shaped 'Tie E' and 'Tie F'. The stress values at Point A, B, C and D and in 'Tie E' and 'Tie F' will be studied.

### 4.3.2 Modeling of Reinforcement

Both the longitudinal and transverse reinforcement are assumed to be elastic-perfectly plastic. The material parameters for the reinforcement are included in Table 4.2.

Reinforcing bars which are parallel to the element edges are modeled using 'embedded reinforcement formulation' based element types. In this formulation, numerical integration of the contribution of reinforcement to the element stiffness matrix is carried out along the bars only. Complete strain compatibility is assumed between the embedded bars and the concrete medium of the parent element. Reinforcements which are not parallel to the element edges (such as diamond shaped ties) are modeled with truss elements connected only at the ends.

### 4.3.3 Simulation of the Boundary Conditions

Since only a quarter of the specimen is modeled, some relevant displacements have to be suppressed along the symmetric faces. On the symmetric face in the vertical

direction, the vertical displacements are eliminated; while on the symmetric face in the width direction, the inward displacements are eliminated.

The horizontal displacement of the load point $P_1$ in the plane of specimen is suppressed as it was also the hinge point supported horizontally in the test.

## 4.3.4 Simulation of the Loading Procedure

The loading system involves two vertical loads, $P_1$ and $P_2$. For Specimens V7, V13 and V16, the magnitude of the latter is continuously adjusted accordingly to obtain a triangular axial strain distribution with zero strain on the tension face. For Specimen V2, $P_1$ was the only load which was applied at a constant eccentricity.

In the numerical simulation, $P_1$ was applied by imposing incremental vertical displacements at the load point. The size of increment varies from case to case. Usually, ten incremtnts were sufficient for the pre-peak range of $P_1$. A similar size of displacement increment was maintained over the post-peak range. However, in the peak range a refined load size is used.

For Specimens V7, V13 and V16, within each increment of $P_1$, a trial procedure is used to evaluate a correct value of the increment of $P_2$ such that zero strain on the tensile face is obtained (that is $\varepsilon_t = 0$). The procedure involves testing two initial trials for $\Delta P_2$ as $(\Delta P_2)_1$ and $(\Delta P_2)_2$. Using the 'restart job from the end of the last increment' feature of Program 'ABAQUS', two deviations for $\varepsilon_t$ can be obtained as $(\varepsilon_t)_1$ and $(\varepsilon_t)_2$. Assuming that the deviation $\varepsilon_t$ is a linear function of the trial $\Delta P_2$, the trial value can be found as:

$$(\Delta P_2)_3 = (\Delta P_2)_2 - \{(\Delta P_2)_2 - (\Delta P_2)_1\}\frac{(\varepsilon_t)_2}{(\varepsilon_t)_2 - (\varepsilon_t)_1} \qquad (4.1)$$

This procedure is repeated until the new $\varepsilon_t$ is close enough to zero. In most of the analyses presented in this chapter, convergence of strain distribution required less than four trials.

### 4.3.5  Convergence Control of the Analysis

In this study, the modified Newton-Raphson iteration method is used. The convergence is based on the increment of displacement. The criterion takes the form:

$$max\{|\delta(\Delta\ U)|\} \le \gamma_u\ max\{|\Delta\ U|\} \tag{4.2}$$

in which $max\{|\delta(\Delta\ U)|\}$ is the largest solution correction during iterations and $max\{|\Delta\ U|\}$ is the largest corresponding incremental solution value. The notation $|\ |$ represents the absolute value of the data included in the notation. $\gamma_u$ is the tolerance for the displacement control.

In this study, $\gamma_u$ is set to be 1% throughout except in the peak range where a tolerance of 5% is used.

Within each increment of $P_1$, the convergence control is also expected in evaluating a correct $\Delta\ P_2$ value. One measure of the convergence is that the strain on the tensile face $\varepsilon_t$ should be small compared with that on the compression face $\varepsilon_c$. In this study, the criterion is set as $|\varepsilon_t/\varepsilon_c| \le 0.01$.

### 4.4  Results of Numerical Analysis and Discussions

### 4.4.1  Specimen V2

Specimen V2 has rectangular transverse ties spaced at 100mm. $P_1$ is the only load applied with a constant eccentricity of 45mm towards the left side of the central line as shown in Fig.4.1.

The numerical results of load $P_1$ are plotted against the strain on the compression face in Fig.4.4, along with the test results. Fig.4.5 shows the position of the neutral axis against the strain on the compression face. The specimen had an overall depth of 300mm. The stresses in the tie at the mid-span section are presented in Fig.4.6. Stress values are given at Points A, B, C and D of the tie as shown in Fig. 4.3B. Points A and B are on the

compression side, while Points C and D are on the tension side. It can be seen, from Figs.4.4 and 4.5, that the results from numerical analysis are very close to those from the test. Stirrup strains were not measured in the test.

The load $P_1$ versus strain on compression face curve (Fig. 4.4) is linear until the longitudinal reinforcement yields. The non-linearity becomes significant when the cover of the compression face shows strain-softening. Meanwhile, the position of the neutral axis shifts into the cross section so that a small part of the concrete is in tension. With the development of the strain-softening in the compression side, ties at the compression side yield (as shown for Points A and B in Fig.4.6). Stresses in the tie at Points C and D are close to zero because there is little lateral deformation of concrete in the tension side. Immediately after the yielding of the ties, the load $P_1$ drops from the peak with increasing strain on the compression face, and the column collapses.

The axial stress (parallel to Axis 2 shown in the figure) pattern at $P_1$ peak is presented in Fig.4.7A for the outside view and in Fig.4.7B for the mid-plane view. The stress values are represented by different colors changing from dark blue to green to yellow and to red. Each color represents an equal stress increment except the dark blue and red. For all the stress patterns pictures in this chapter, the dark blue color represents the lowest stress value (the highest compression), while the red color represents the highest stress value (the highest tension). The stresses on the surface of elements are obtained using the 'ABAQUS' post-processor which extrapolates the stress values based on the information at the integration points. Neglecting the part close to the end block which may experience stress concentrations, the stress distribution has a smooth transition from the tension face to the compression face. There is a little tension developed on the tension side of the cross-section. On the other hand, part of the cover experiences the strain-softening on the compression side. This is detected as the colors change from yellow to green to blue and back to green on the compression side. The stress units in Figs. 4.7, 4.11, 4.15, 4.20, 4.21 and 4.22 are all in MPa.

### 4.4.2 Specimen V7

Specimen V7 has rectangular transvers⋯ ⋯ ⋯ ⋯aced at 200mm. There are two loads, $P_1$, which is axial, and $P_2$, which is eccentr⋯ ⋯ ⋯ ⋯pplied to the specimen.

Results from the numerical analysis are compared to the test results in Figs.4.8 and 4.9 for the moment about the neutral axis (about zero-strain face) and the total axial load against the strain on the compression face. Because load $P_2$ is applied such that the strain on the tension face is always zero, the neutral axis is always located along one edge of the cross-section. Stresses in the tie at mid-span section are presented in Fig.4.10 for Points A, B, C and D as shown in Fig. 4.3B. Points A and B are on the tension side, while Points C and D are on the compression side, opposite to Fig. 4.6 because the direction of the applied moment is opposite. It can be seen, from Figs.4.8 and 4.9, that the results from numerical analysis are close to those from the test.

The relation between the moment about the neutral axis and the strain on the compression face is linear until the longitudinal reinforcement starts to yield. It is interesting to note that there is a delay of the increase in the stress in the tie at Points C and D when the cover of the compression side shows strain-softening. Shortly after the cover experiences the strain-softening, both the moment and the total load reach the maximum. Meanwhile, stress in the ties increases dramatically at Points C and D and reaches the yield point. As a result, the column collapses completely.

The axial stress patterns for specimen V7 at the maximum load capacity are presented in Fig.4.11A for the outside view and in Fig.4.11B for the mid-plane view. Since the element height used is 100mm, the spacing of ties (200mm) is modeled over two elements. Clearly, a very localized strain-softening pattern developed in the cover between two ties on the compression side. This localized strain-softening pattern penetrates into the core with increasing axial strain gradient after the maximum load is reached. Excess deformation results in the yielding of ties. Eventually the column collapses. At the peak load point, the axial stress in a small part of the core on the mid-span section reaches over 88MPa, which is higher than the concrete strength (84.7MPa). This can be credited to the triaxial effect provided by the ties in the section.

It can be concluded that for Specimen V7 with large tie spacing (200mm), the collapse of the column is a result of the localized failure of concrete between ties. From Fig.4.11A, it can be seen there is also a little strain-softening on the side face close to the compression face. Outside the region of localized strain-softening, the stress distribution pattern is quite uniform.

### 4.4.3 Specimen V13

Specimen V13 has rectangular transverse ties spaced at 100mm. It is subjected to an axial load $P_1$ and an eccentric load $P_2$.

Results of the numerical analysis are presented in Figs.4.12 and 4.13 for the moment about the neutral axis and total axial load against the strain on the compression face respectively. Results from the test are also included in the same figures. Stresses in the ties of mid-span cross section are presented in Fig.4.14 for the Points A, B, C and D which are defined in the same way as for Specimen V7 (see Fig. 4.3B). It can be seen, from Figs.4.12 and 4.13, that the agreement between the results from numerical analysis and those from test is very good.

The moment versus axial strain gradient curve is linear until the longitudinal reinforcement yields. Both the moment and load reach the peaks shortly after the occurrence of strain-softening of the cover on the compression face. Unlike the case of the Specimen V7, there is no delay of increase in the tie stress due to the strain-softening of the cover. Instead, the increase is sharp and stresses in the tie at points C and D reach the yield point immediately. Due to the axial stress redistribution over the cross-section, stresses in the tie at points A and B also increase. It is interesting to note that there is a plateau of moment and load in the post-peak range. This can be credited to the triaxial confinement developed in the core by the ties. The triaxial effect weakens with the yielding of ties. This results in a quick drop for moment and load.

The axial stress distribution patterns for Specimen V13 at the maximum moment capacity are presented in Fig.4.15A for the outside view and in Fig.4.15B for the mid-plane view. Spacing of ties (100mm) is modeled over one element height. A number of strain-softening patterns have developed between ties over the compression face and the side face. The triaxial state provided by the ties can be observed from Fig.4.15B. A small part in the core has axial stress over 77MPa, which is higher than the compression strength (72.5MPa). The axial stress between ties is lower than those at the tie levels. Concrete between ties experiences strain-softening earlier than at the tie level because of lower confinement.

It is interesting to look at the history of the axial stress over the cross-section. In Fig.4.16, the variation of axial stress against the strain on the compression face is plotted

for five integration points. These points are at the same height closest to the mid-span. Four of these points are in a line closest to the mid-plane with one in the compression face cover, two in the core and one in the tension face cover. The fifth point is on the side cover. In Fig.4.16, $r$ is the ratio of the distance from the compression face to the total height of cross-section. It can be seen from Fig.4.16 that the cover on the compression side experiences unconfined strain-softening with maximum stress very close to uniaxial strength (72.5MPa). The core on the compression side and the side cover share almost the same pre-peak behavior since both are subjected to the same axial strain (Both have $r$=0.2806). The curves separate when the side cover, which is unconfined, shows strain-softening behavior. Meanwhile, the core on the ᵖᵣᵉˢˢion side has a maximum strength (79MPa) which is higher than the uniaxial stre.:ʳ ᴬᴸ ɜ of the triaxial effect. The axial stress in the core also has a slower descending ᵂᴬᴿᴬ ᴮ ᶜᵐpared with the covers. Fig.4.16 also indicates that the core in tension side ($r$=0./ᵢ'ᵎ-ᵢ) and the cover on the tension side ($r$=0.9694) are undamaged when the column collapses.

Although strain-softening patterns have developed over the cover, the axial stress value is still negative (in compression). This has been demonstrated in Fig.4.16. However, Figs.4.15A and 4.15B show tension stress patterns over the cover. This is simply because of the inaccuracy of the 'ABAQUS' post-processor. The 'ABAQUS' post-processor extrapolates stress values over the element surface based on the values at the integration poin*⁻ Unfortunately, the stress gradient over the cover is very dramatic so that high ter ·ess values are extrapolated but are not real.

### 4.4.4 Specimen V16

Specimen V16 has a tie spacing of 50mm and eight longitudinal bars. The arrangement of ties consists of a rectangular tie and a diamond-shaped tie. It has a much higher volumetric transverse steel ratio than the other specimens. The specimen is subjected to an axial load $P_1$ and an eccentric load $P_2$.

The moment about the neutral axis and the total axial load are plotted in Figs. 4.17 and 4.18 against the strain on the compression face from the analysis, along with results from the test. Stresses in the ties at the m.·· ⁻·an cross section are presented in Fig.4.19 for Points A, B, C and D which are define.. . .ne same way as for Specimen V7, and for

diamond-shaped 'Tie E' and 'Tie F' as shown in Fig. 4.3B. Points A and B and 'Tie E' are on the tension side, while Point C and D and 'Tie F' are on the compression side. It can be seen, from Figs.4.17 and 4.18, that the agreement betw    e numerical analysis and the test is very good.

The curves of moment and load versus axial strain on the compression face are linear until the longitudinal bars start to yield. There is a kink in the moment and load curves at the occurrence of strain-softening of cover. It is interesting to note that the development of strain-softening in the cover does not result in any loss of load carrying capacity for either moment or total axial force. Instead, a ductile behavior is observed over a long range in the post-peak regime. The strain-softening, however, results in a sharp increase of stresses in the rectangular tie for Points C and D and the diamond-shaped 'Tie F'. The rectangular tie yields over the compression side with increasing axial strain. There is no immediate loss of load carrying capacity as a result of yielding of the rectangular ties. This is because the diamond-shaped ties have not yielded and are still effective. The long moment and load plateaus end when the diamond-shaped ties have yielded.

The axial stress distribution patterns for Specimen V16 at maximum moment capacity are presented in Fig.4.20A for the outside view and in Fig.4.20B for the mid-plane view. Spacing of ties (50mm) is modeled over one element height. There are a number of strain-softening patterns developed between ties over the compression face and the side face. The triaxial state provided by ties can be observed from Fig.4.20B. The axial stress value in the core over the compression side varies from 66 to 99MPa which is much higher than the concrete strength (59.5MPa). This indicates that some parts in the core are subjected to a very high confinement. The highest triaxial states are held on in the corners of the diamond-shaped ties. Because the column is very well confined with closely spaced ties, the triaxial stress state patterns are developed even in regions between the ties.

## 4.5 A Study of the Failure Mechanism of Tied Columns

Based on the experimental observations (Ibrahim and MacGregor, 1994), the ascending part of the loading history of the reinforced specimens was the same as that for the plain concrete specimens. This indicates that the confinement has no effect on that part of the loading history.

The confinement, however, has a significant effect on the post-peak loading history as demonstrated in this chapter.

Concrete in a tied column can be divided into two parts, the cover and the core. The variation of stress distribution between these two parts is quite smooth in the early stage of loading history. In Figs. 4.21 and 4.22 the transverse stresses on the core to cover interface parallel to Axes 1 and 3, respectively, are shown at the onset of strain softening of the cover for Specimen V13. The cover, primarily subjected to a uniaxial compressive stress, $\sigma_{22}$, is the weakest part in the column. On the compression face, some parts of the cover between ties may be subjected to a small tension in the lateral direction (e.g. direction 1 in Fig.4.21). These small tensile stresses are thought to be a result of the non-uniform lateral deformation within the specimen. The ties which compress the core at the tie levels, cause tensile stresses which act to separate the core from the cover between ties at the compression side. The first occurrence of strain-softening is usually located in these areas due to the large axial strain and the nature of the stress state. At a late stage, the strain-softening of cover extends to the side faces.

Because of the reduction of the axial stress value in the cover, the first peak of the moment about the neutral axis is usually reached shortly after the strain-softening of the cover. Based on the finite element analysis, the first moment peak usually relates to the almost complete loss of axial stress $\sigma_{22}$ in the cover of compression face. This can be observed from Figs. 4.12 and 4.16 for Specimen V13. The instant of the inefficacy of the cover is also called 'spalling' in engineering terms. For a very well confined column, a kink of the load history curve is exhibited instead of the first moment peak. At spalling, the axial stress in the core of the compression side reaches the critical stress level leading to a significant increasing of lateral deformation. This increasing lateral deformation results in an increase in the stress in the ties. The ties, on the other hand, react by confining the concrete core. The core in the compression side is now subjected to a triaxial stress state at the tie level. In between ties, the confinement is less significant depending on the spacing and amount of ties. To demonstrate this point clearly, lateral stress ($\sigma_{11}$ and $\sigma_{33}$) patterns on the surface of the core at the onset of strain-softening of cover are presented in Figs. 4.21 and 4.22 for Specimen V13. As seen from Figs.4.21 and 4.22, a number of triaxial stress state patterns are developed at the corners of ties. Based on the observation of the confined cylinder test described in Chapter 2, triaxially loaded concrete will

experience an increase of maximum axial strength and a delay of failure, compared with unconfined concrete.

For well confined columns, distributed triaxial stress state patterns will be developed in the core along the compression face. Confinement is also present for the part of the core between ties. With increasing of the axial strain gradient, the axial stress capacity in the core on the compression side increases due to the triaxial effect. This may lead to higher values for moment and load to compensate for the loss caused by the spalling of the cover. For a very well confined column, the second loading peak can be higher than the first. On the other hand, the stress in the ties in the compression side increases sharply to reach the yield point because of the excess lateral deformation of concrete core. The confinement provided by the ties changes from passive to active with the yielding of ties. Eventually, the previous axial stress level can not be held for the part in the core of the compression side. This results in a decreasing of moment and load. The column collapses. For columns with both rectangular and diamond-shaped ties, the passive triaxial stress state can still be available for some parts in the core until yielding of the diamond-shaped ties. The post-peak behavior for this case can be more ductile. The failure mode for well confined columns consists of the spalling of covers along the height of the compression face and a part of the side faces, and the failure of the core along the compression face. The difference between the failure of the core and the failure of the cover is that the cover experiences nearly unconfined strain-softening while the core experiences confined strain-softening. At failure, the separation between the core and the cover on the compression face is complete.

For poorly confined columns, such as Specimen V7, triaxial stress state patterns are developed only at the tie level. For the parts between ties, the stress state is still close to unconfined. Strain-softening of the cover between ties extends into the core, and there is no increase of moment and load after the first peak. Instead, the load capacity drops very fast with the failure of the core. The axial stress regained by the triaxial effect at the tie level can not compensate the stress loss caused by the localized failure of core concrete. The failure mode consists of a localized spalling of cover and a localized collapse of core. The post-peak behavior is very brittle.

## 4.6 Summary

In this chapter, four specimens tested by Ibrahim and MacGregor (1994) with different layouts of ties and loading conditions are modeled and analyzed using the modified Pramono and Willam's finite element model. The finite element model successfully captured the load-deformation behavior for these four specimens as compared with the test results. This verifies the modified constitutive model and the method of analysis.

Examination of the stress patterns and stress history of the different points in the finite element simulation provides insight into the behavior of the tied columns. It is concluded that although the confinement has no effect on the pre-peak loading history, it has a significant effect on the post-peak behavior. The failure mode for well confined columns is distributed and the behavior is ductile. For poorly confined columns, a localized failure mode and brittle post-peak behavior can be expected.

Table 4.1   Details of rectangular specimens

| Specimen | V2 | V7 | V13 | V16 |
|---|---|---|---|---|
| Width x depth  (mm) | 200x300 | 200x300 | 200x300 | 200x300 |
| Compressive Strength (MPa) | 82.8 | 84.7 | 72.5 | 59.3 |
| Cover (mm) | 14 | 14 | 14 | 14 |
| Longitudinal Reinforcement | 4#15 | 4#15 | 4#15 | 8#10 |
| Tie Diameter (mm) | 8 | 8 | 8 | 8 |
| Tie Spacing (mm) | 100 | 200 | 100 | 50 |
| Ties Outer Dimension (mm) | 172x272 | 172x272 | 172x272 | 172x272 |
| Volumetric Ratio | 0.01122 | 0.00561 | 0.01122 | 0.0387 |
| Tie Arrangement | Rectangular | Rectangular | Rectangular | Rectangular + Diamond |
| Test Method (Strain distribution) | Constant eccentricity | Triangular | Triangular | Triangular |

Table 4.2 Material parameters used for modeling test specimens

| Specimen | | V2 | V7 | V13 | V16 |
|---|---|---|---|---|---|
| Concrete | E (MPa) | 28000 | 37500 | 34855 | 33000 |
| | $f_c'$ (MPa)* | 82.8 | 84.7 | 72.5 | 59.3 |
| | $f_t'$ (MPa)* | 4.0 | 4.78 | 3.43 | 3.55 |
| | $G_{cr}^I$ (N/mm)* | 0.188 | 0.197 | 0.161 | 0.166 |
| | $A_h$ | 0.02142 | 0.002142 | 0.002142 | 0.002142 |
| | $B_h$ | -0.032 | -0.032 | -0.032 | -0.032 |
| | $C_h$ | 0.0025 | 0.0025 | 0.0025 | 0.0025 |
| | $A_s$ | 24.0 | 16.0 | 16.0 | 16.0 |
| | $B_s$ | -4.0 | -4.0 | -4.0 | -4.0 |
| Longitudinal Reinforcement | E(MPa) | 188200 | 188200 | 188200 | 188500 |
| | $f_y$*(MPa) | 433.2 | 433.2 | 433.2 | 423.0 |
| Transverse Reinforcement | E(MPa) | 216400 | 216400 | 216400 | 216400 |
| | $f_{yh}$*(MPa) | 401.0 | 401.0 | 401.0 | 401.0 |

* Measured values from control tests.
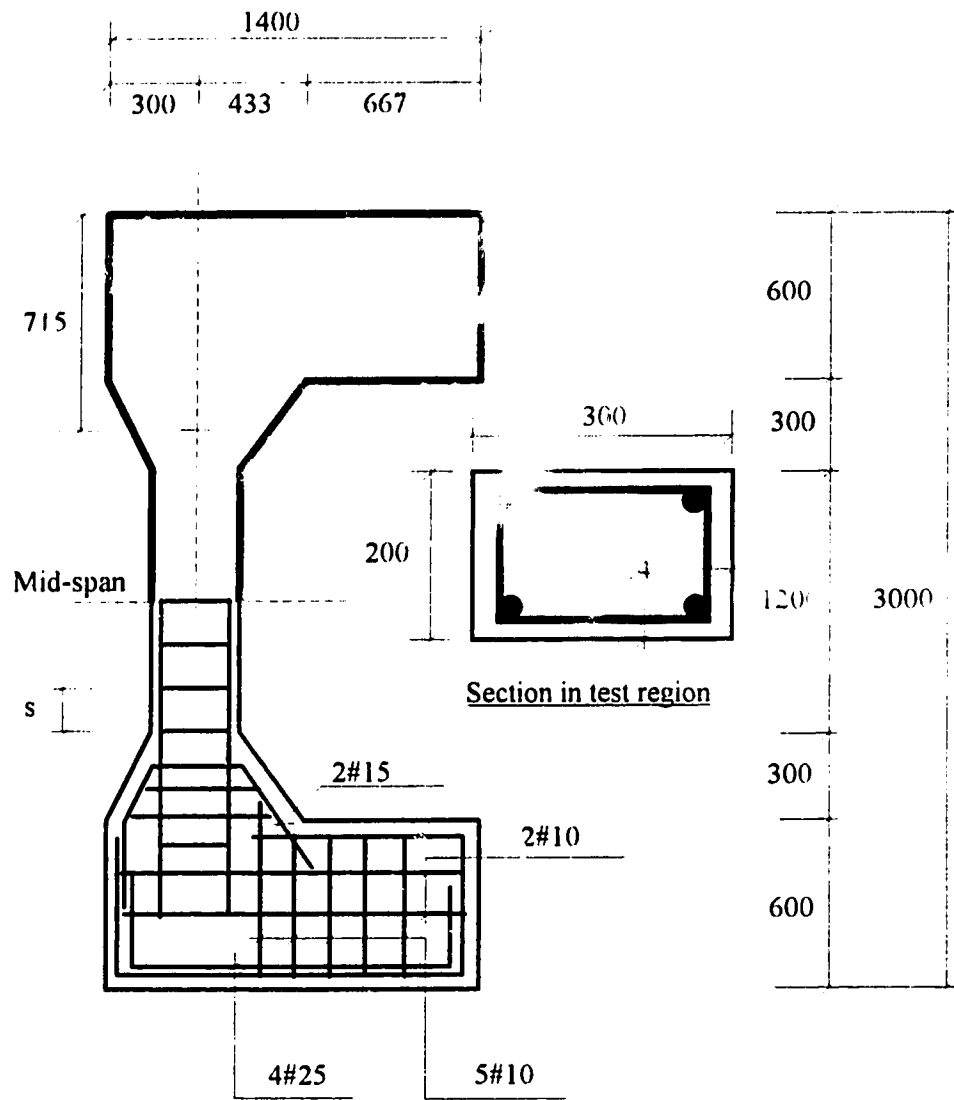
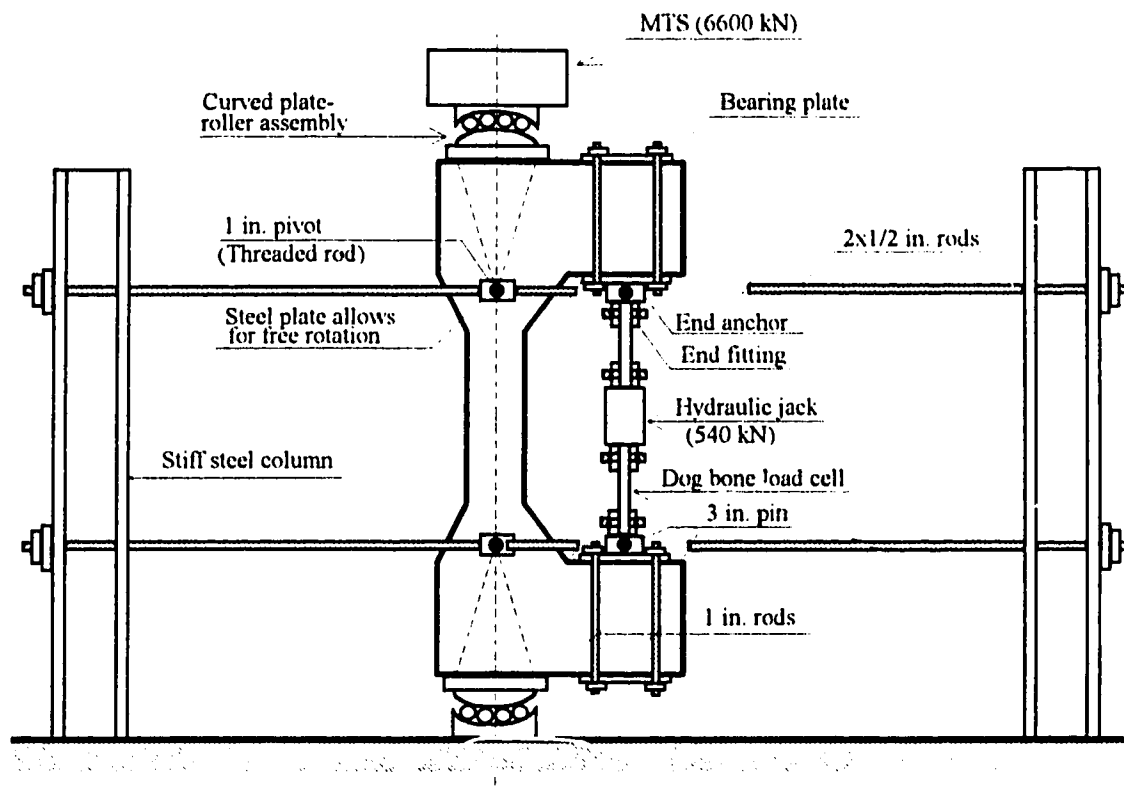Fig.4.1 Elevation and cross-sectional view of rectangular column specimens
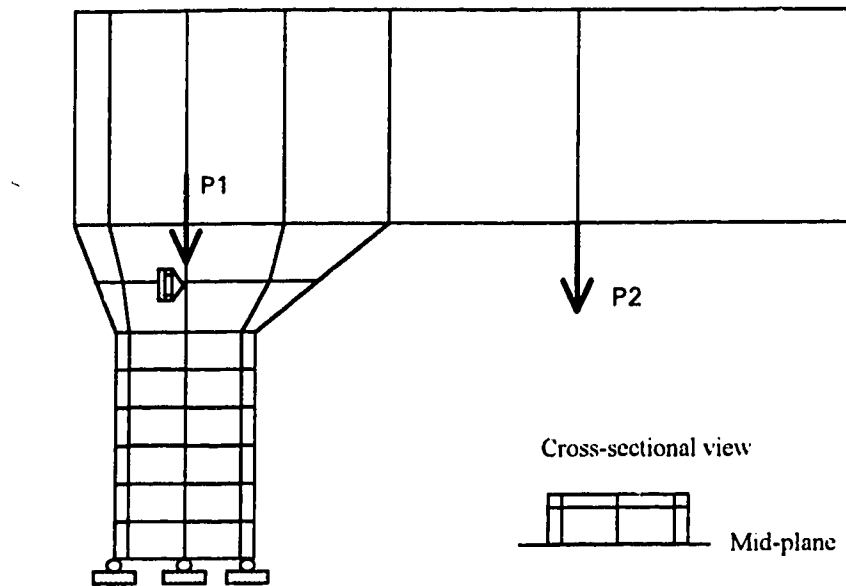
77

Fig. 4.2  Details of test set-up

MTS (6600 kN)

Curved plate-
roller assembly

Bearing plate

1 in. pivot
(Threaded rod)

2x1/2 in. rods

Steel plate allows
for free rotation

End anchor

End fitting

Hydraulic jack
(540 kN)

Stiff steel column

Dog bone load cell

3 in. pin

1 in. rods

Fig.4.3A A schematic representation for mesh divisions of Specimen V13
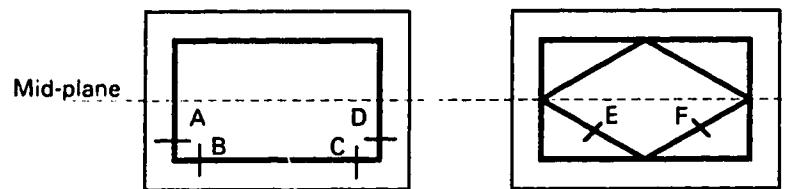


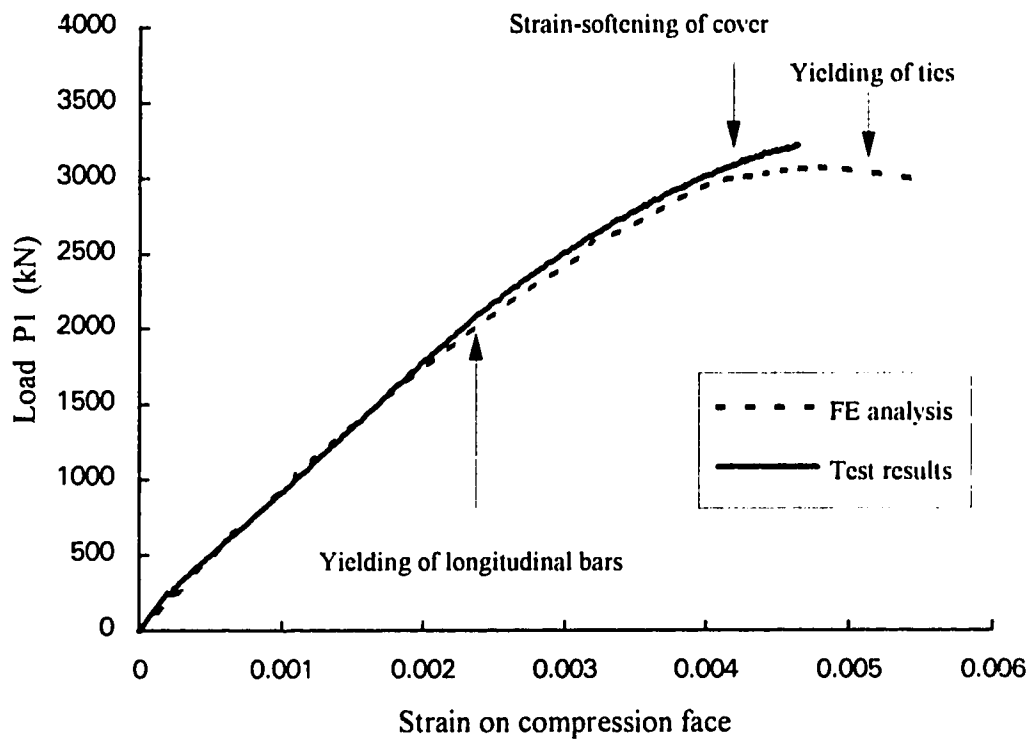Fig.4.3B Locations of points in ties of the mid-span cross-section

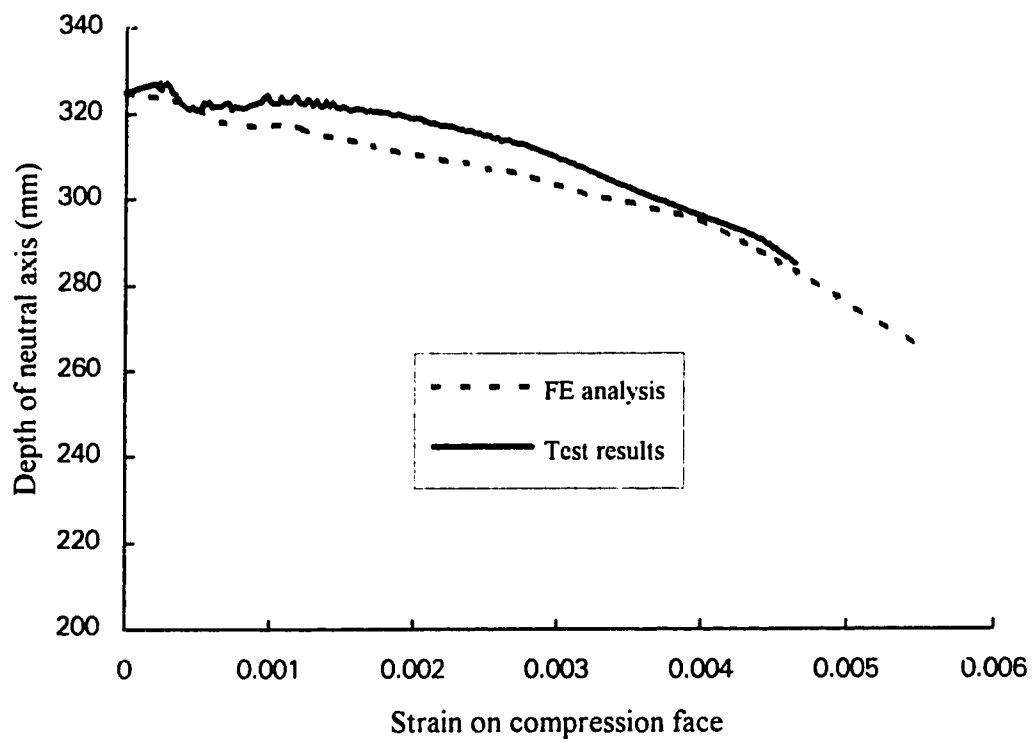Fig.4.4   Load vs strain on compression face for Specimen V2
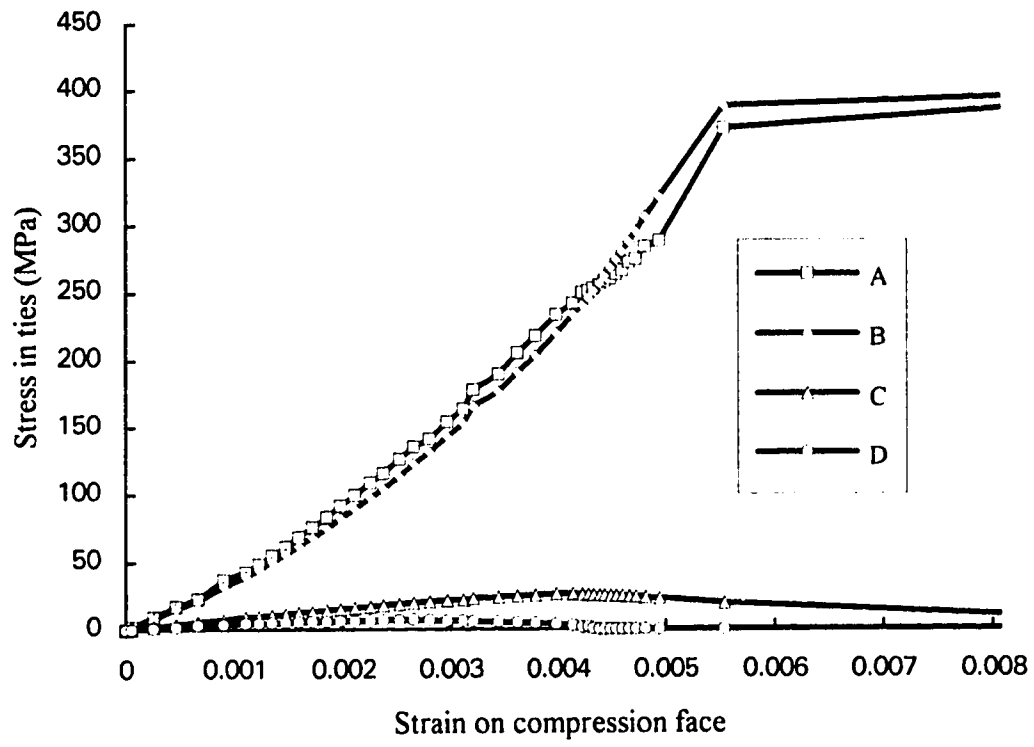
Fig.4.5  Neutral axis of Specimen V2

Fig.4.6  Stress in ties for Specimen V2

Specimen V2
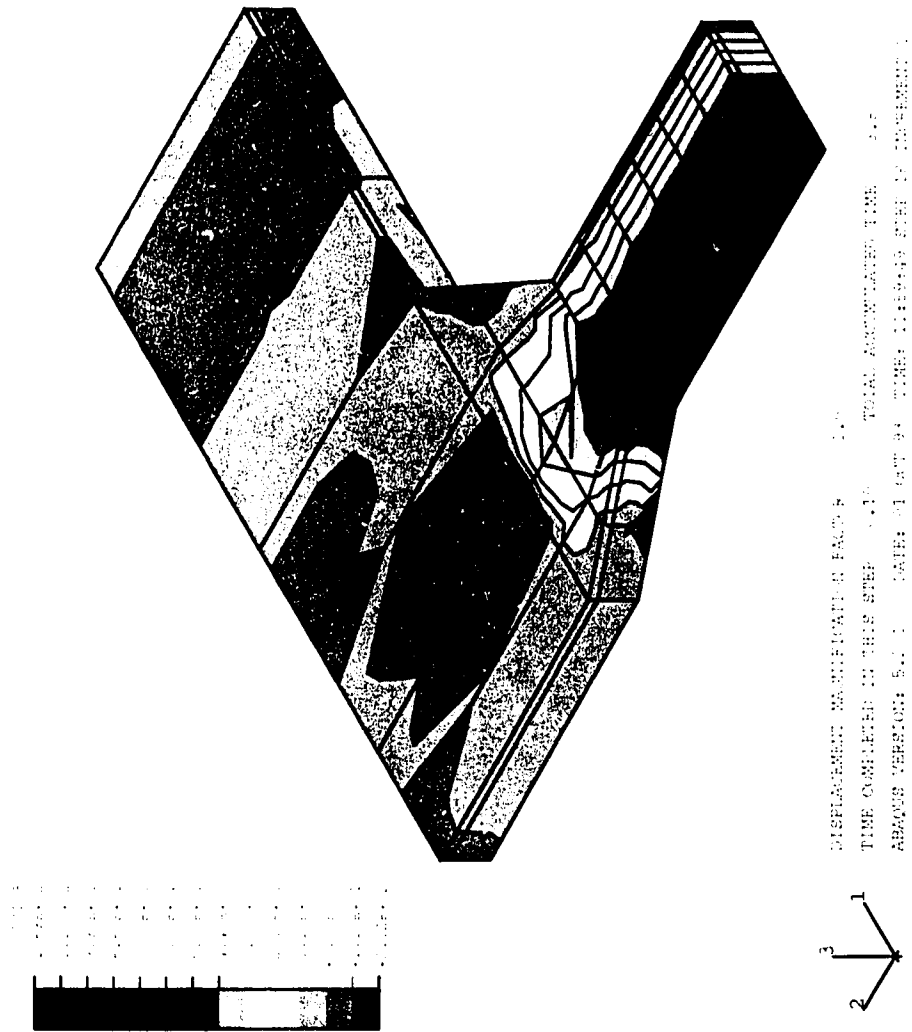


Fig.4.7A  Axial stress (Direction 2) pattern for Specimen V2  (Outside view)
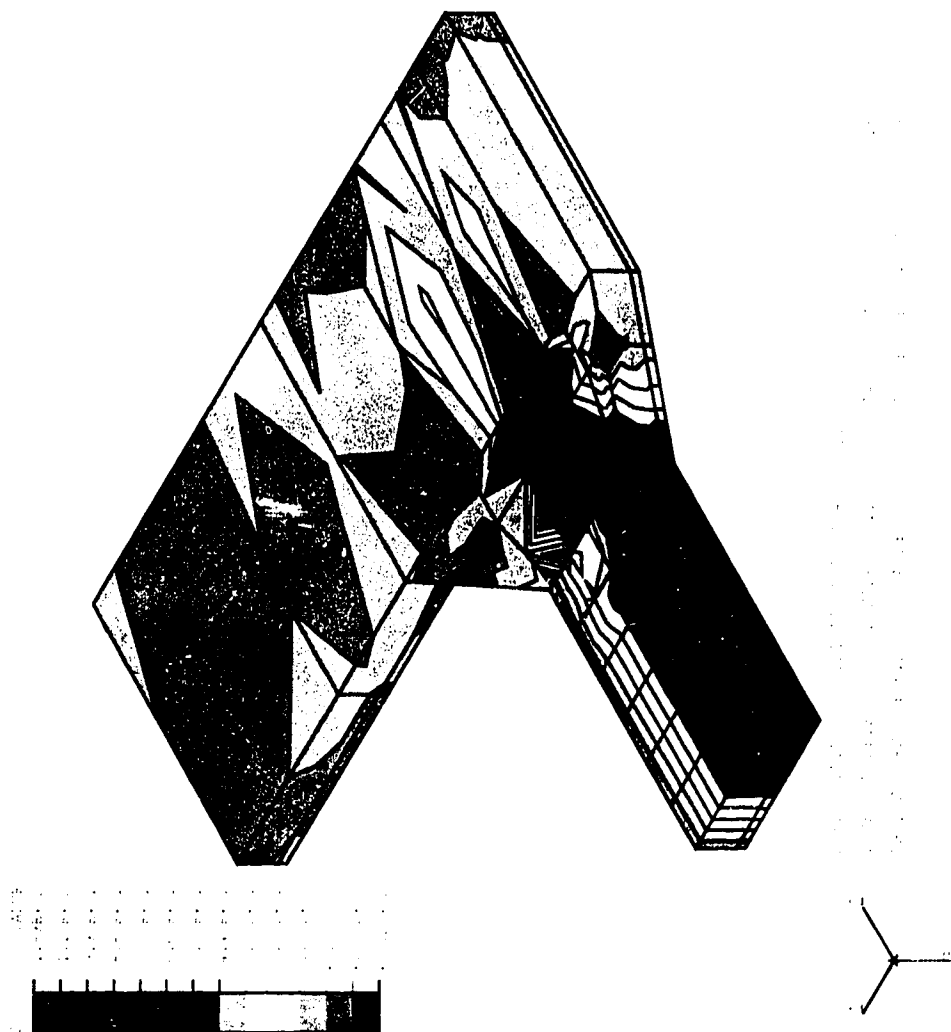
83

Specimen V2



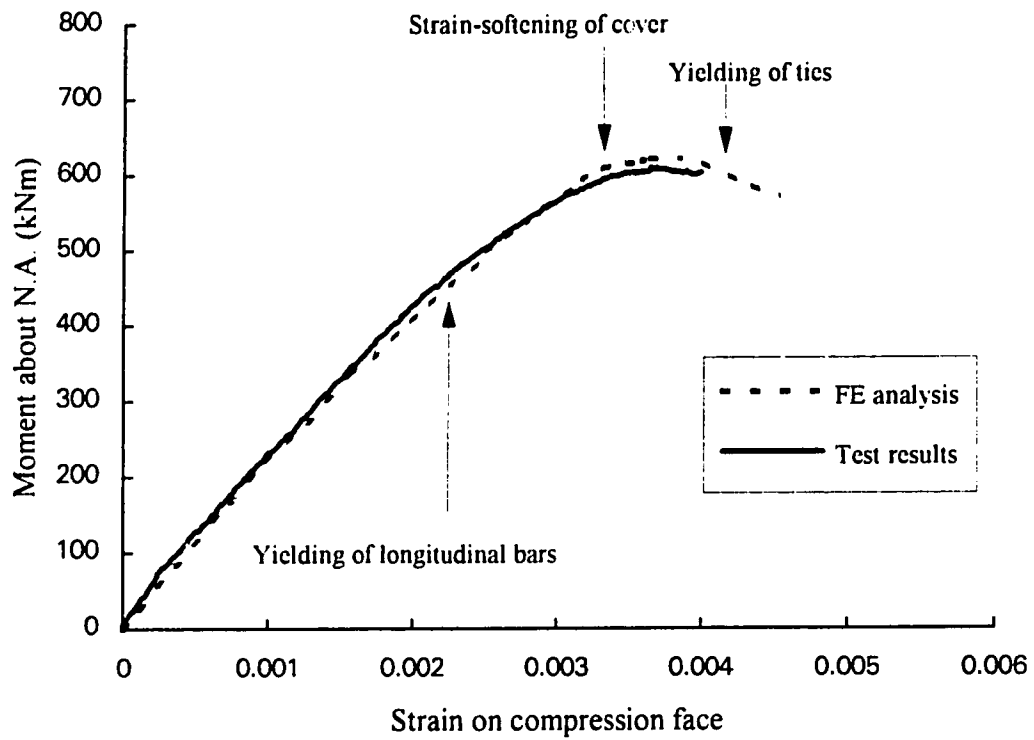Fig. 4.7B  Axial stress (Direction 2) pattern for Specimen V2 (Mid-plane view)

84

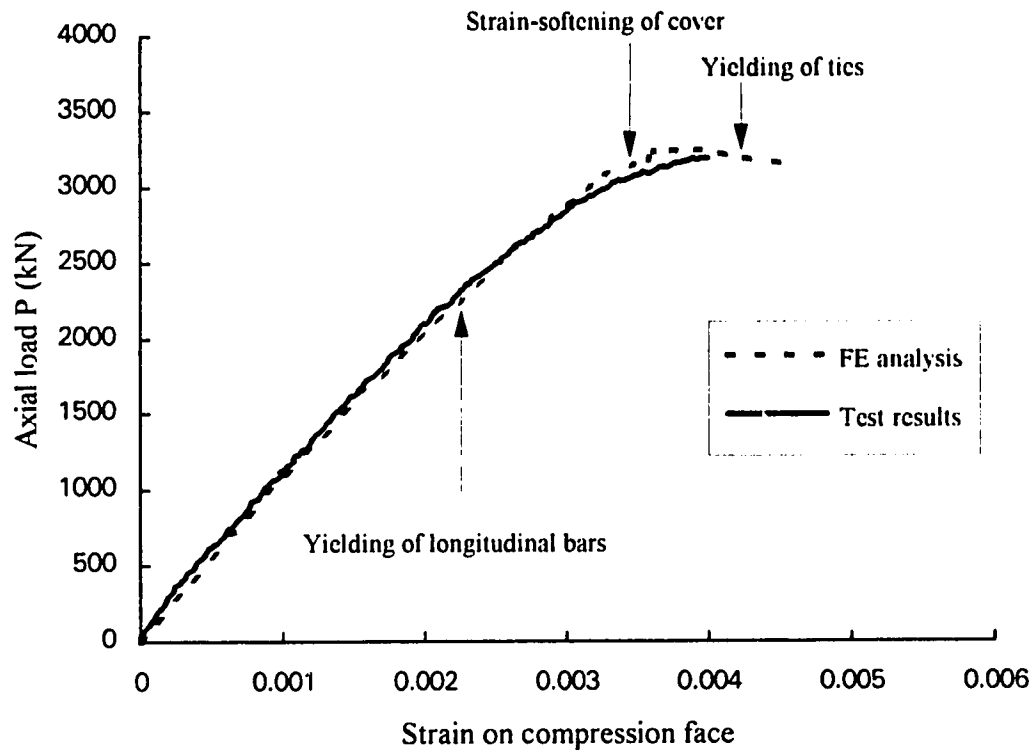Fig.4.8   Moment vs strain on compression face for Specimen V7

Fig.4.9 Axial load vs strain on compression face for Specimen V7

Fig.4.10 Stress in ties for Specimen V7

Specimen V7



Fig.4.11A Axial stress (Direction 2) pattern for Specimen V7 (Outside view)

Specimen V7



DISPLACEMENT MAGNIFICATION FACTOR    1.
TIME COMPLETED IN THIS STEP    0.5    TOTAL ACCUMULATED TIME
ABAQUS VERSION: 5.3-1    DATE: 29 SEP 93    TIME: 16:06:24 STEP    INCREMENT

Fig.4.11B  Axial stress (Direction 2) pattern for Specimen V7 (Mid-plane view)

Fig.4.12 Moment vs strain on compression face for Specimen V13

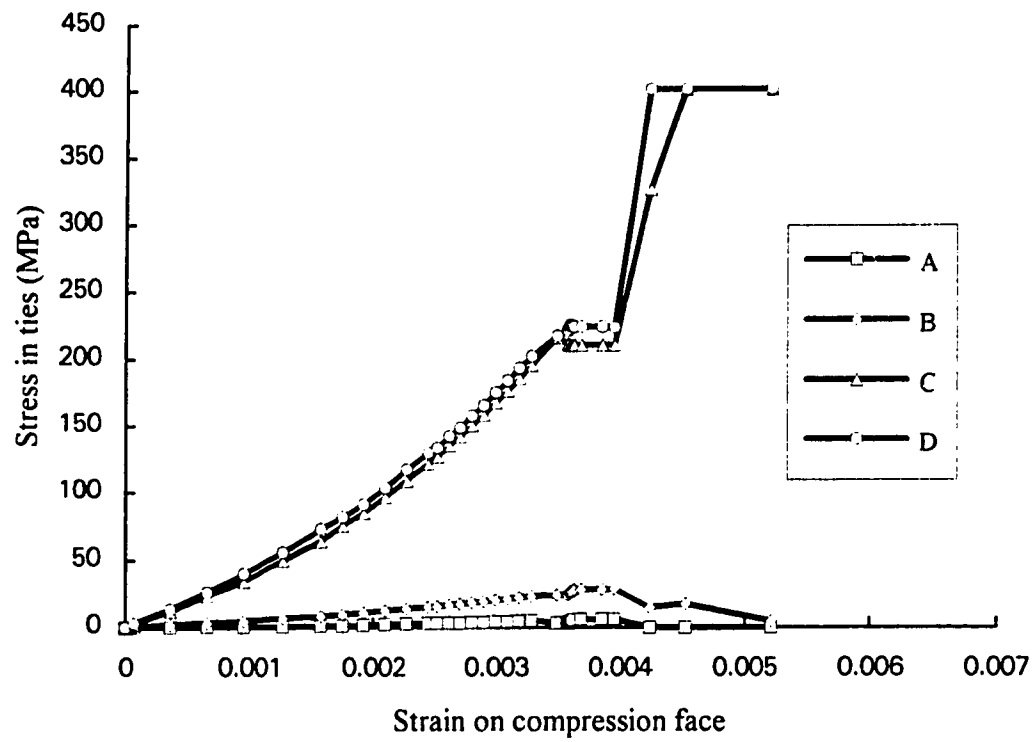Fig.4.13  Axial load vs strain on compression face for Specimen V13

Fig.4.14  Stress in ties for Specimen V13

# Specimen V13



VALUE
S22
-1.73E+02
-1.10E+02
-9.90E+01
-8.80E+01
-7.70E+01
-6.60E+01
-5.50E+01
-4.40E+01
-3.30E+01
-2.20E+01
-1.10E+01
+0.00E-00
+1.10E+01
+1.96E+02

DISPLACEMENT MAGNIFICATION FACTOR =    1.00
TIME COMPLETED IN THIS STEP   0.500    TOTAL ACCUMULATED TIME    3.60
ABAQUS VERSION: 5.2-1    DATE: 11-SEP-93  TIME: 23:05:15 STEP 7 INCREMENT 5
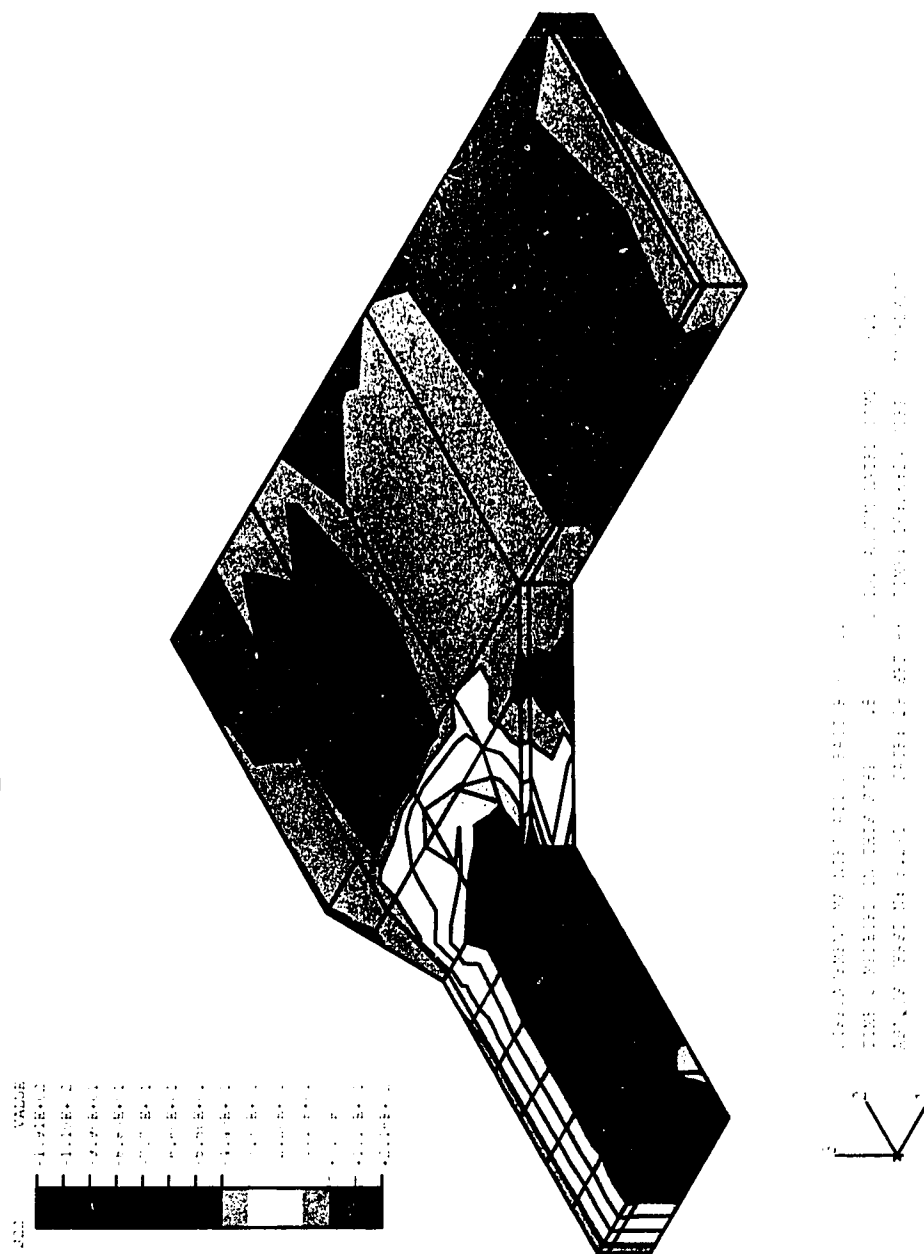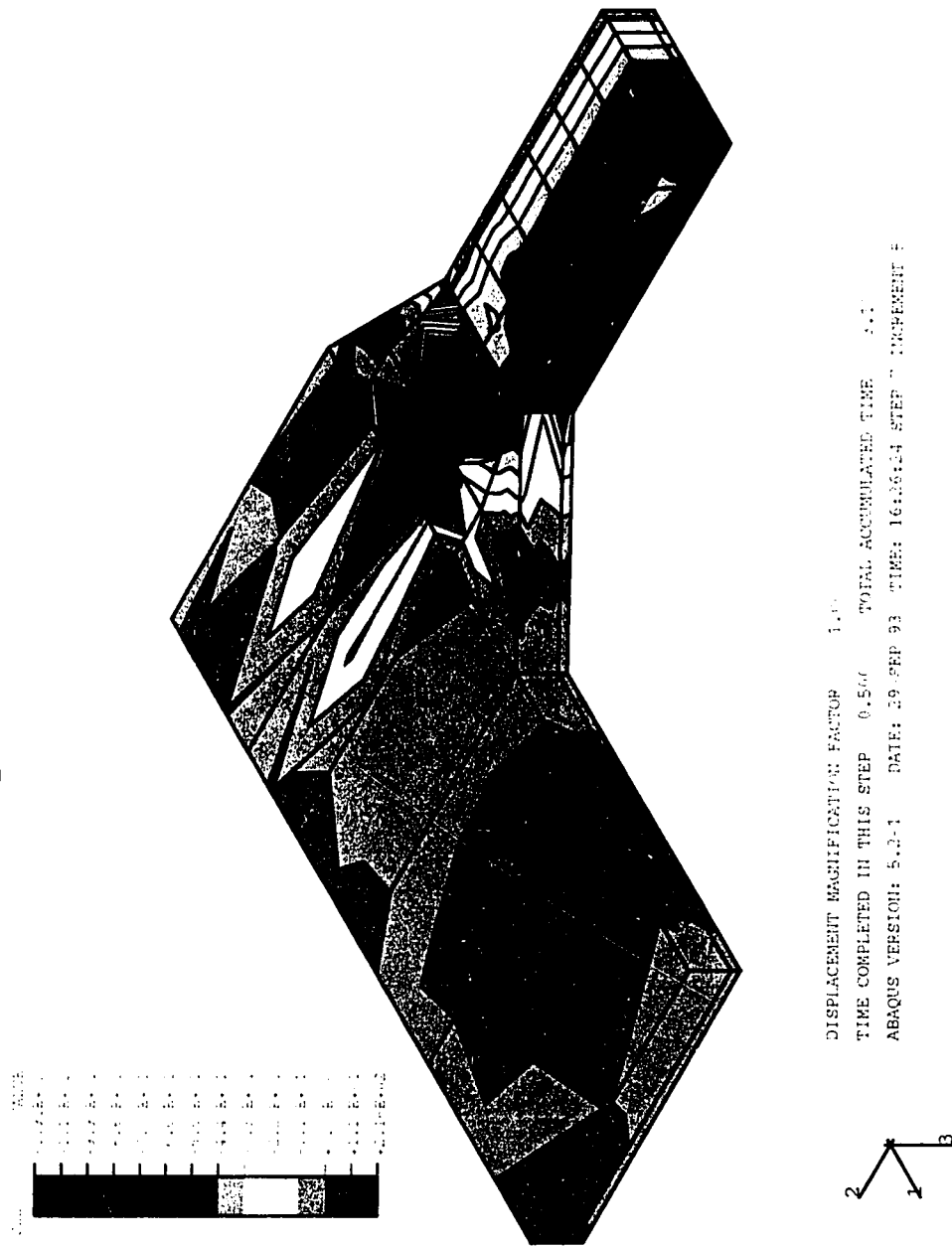
Fig.4.15A   Axial stress (Direction 2) pattern for Specimen V13 (Outside view)

93

Specimen V13



Fig.4.15B  Axial stress (Direction 2) pattern for Specimen V13 (Mid-plane view)

94

Mid-plane

Mid-plane

Zero strain
face

Compression
face

I1  I2  I3  I4

I5

Axial stress (MPa)

80

70

60

50

40

30

20

10

0

0   1   2   3   4   5   6   7

Strain on compression face (x0.001)

I4

I3

I5

I2

I1

Cover (r=0.0306)

Core (r=0.2806)

Core (r=0.7194)

Cover (r=0.9694)

Side Cover (r=0.2806)

$$r = \frac{Distance\ from\ the\ compression\ face}{Height\ of\ cross-section}$$

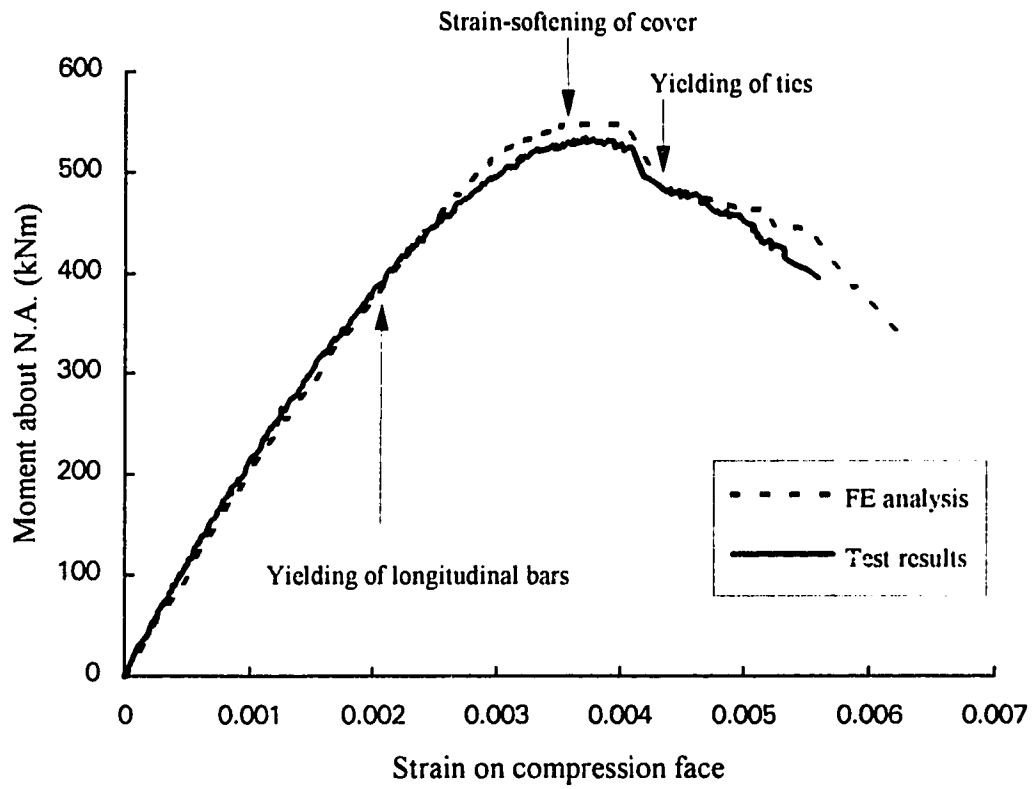Fig.4.16   Axial stress history for Specimen V13
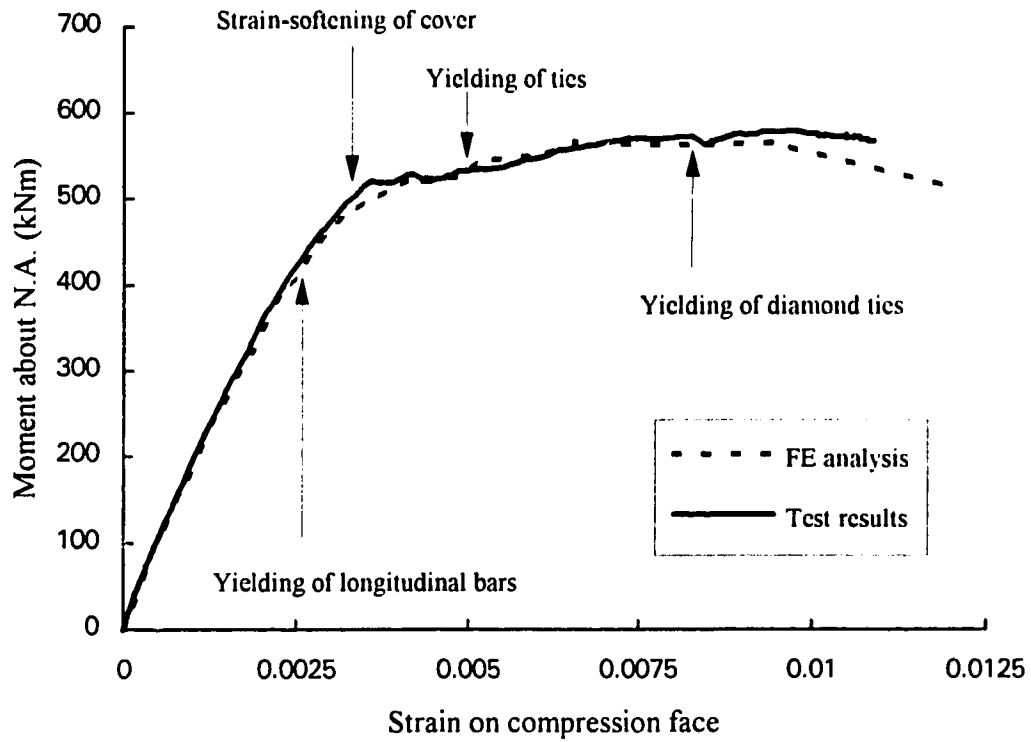
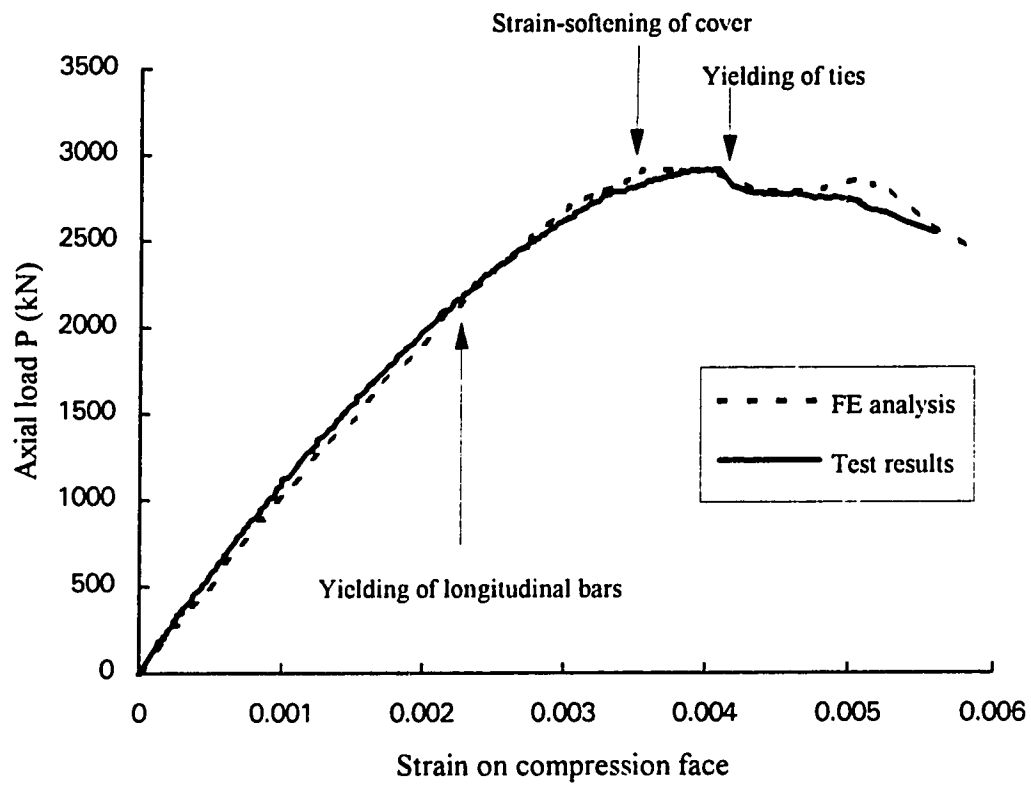Fig.4.17   Moment vs strain on compression face for Specimen V16
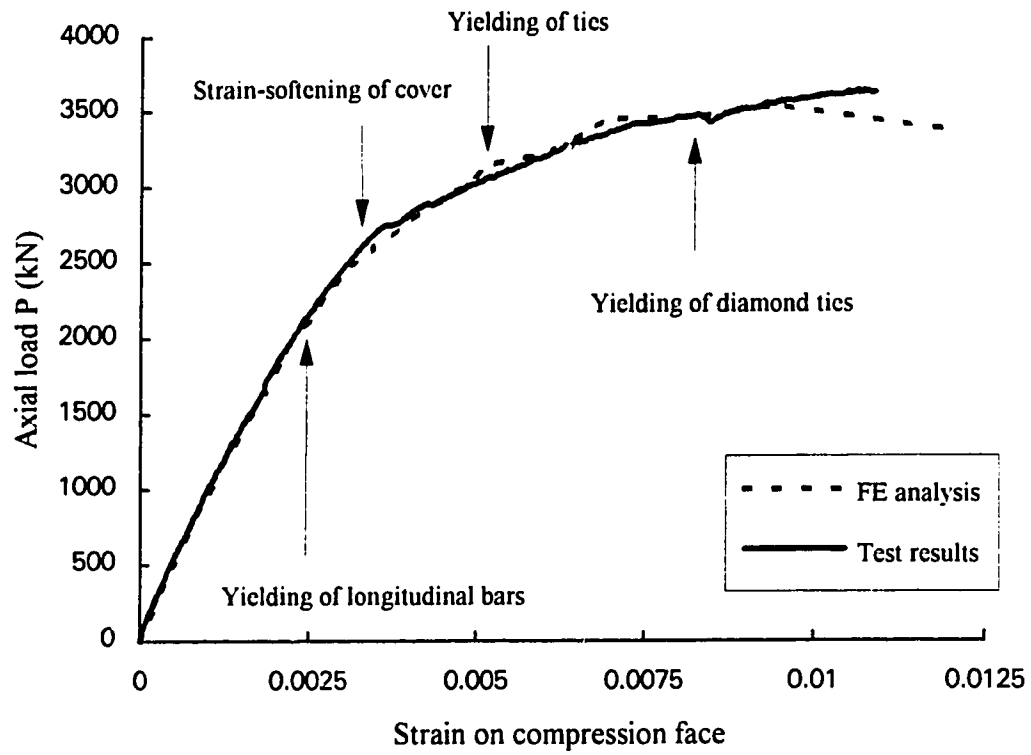
Fig.4.18   Axial load vs strain on compression face for Specimen V16
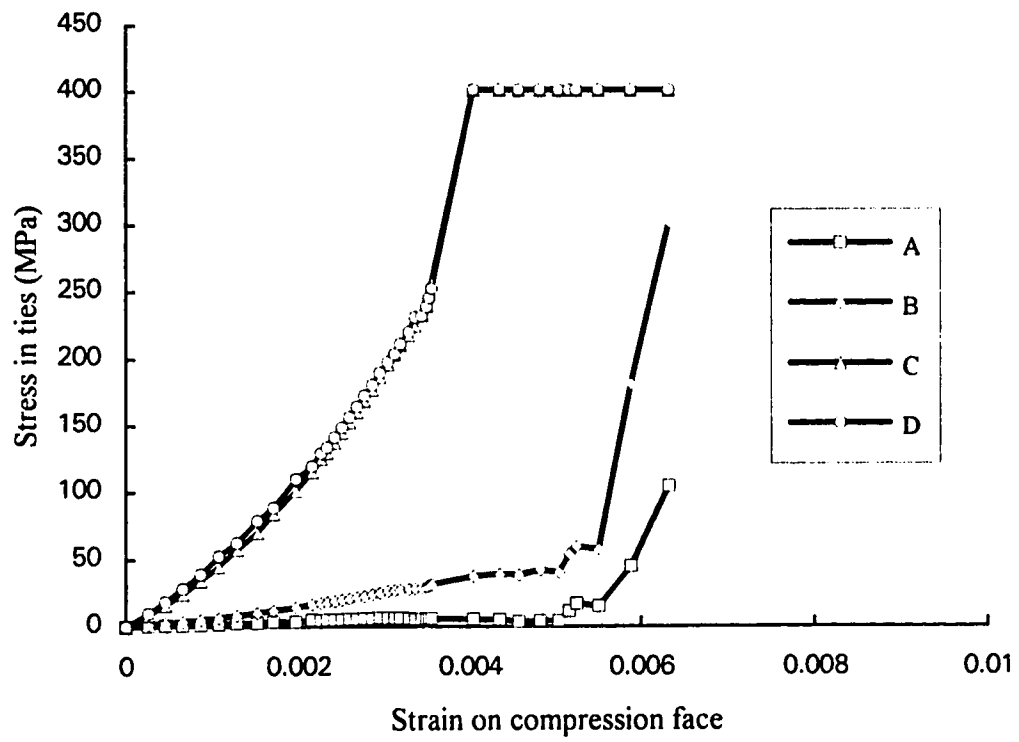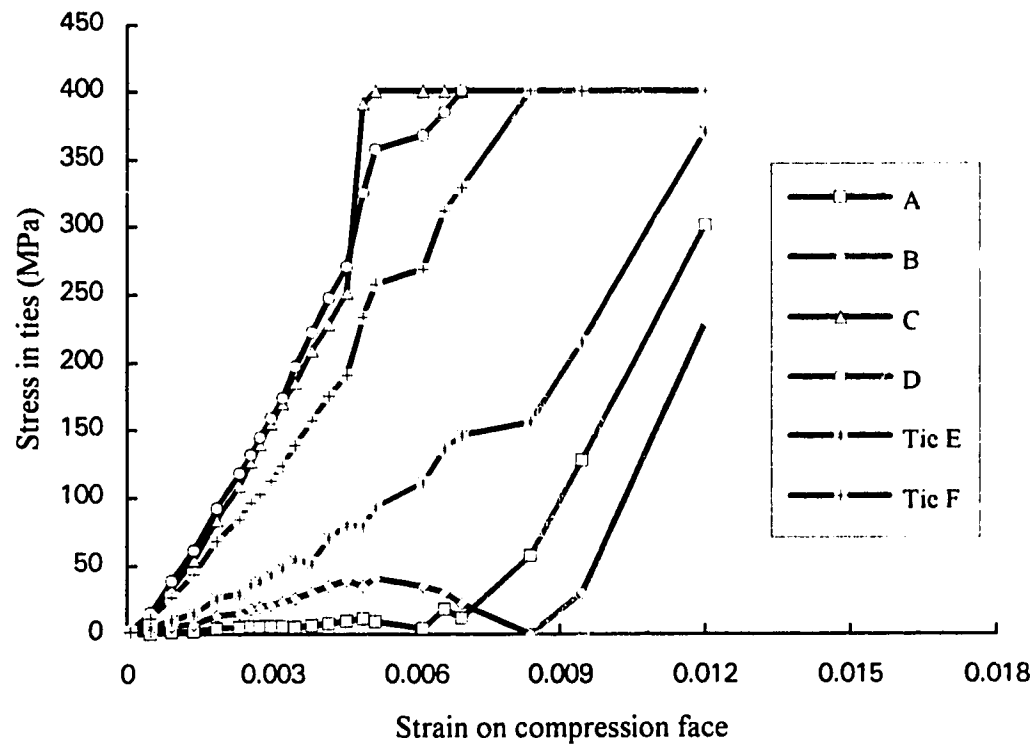
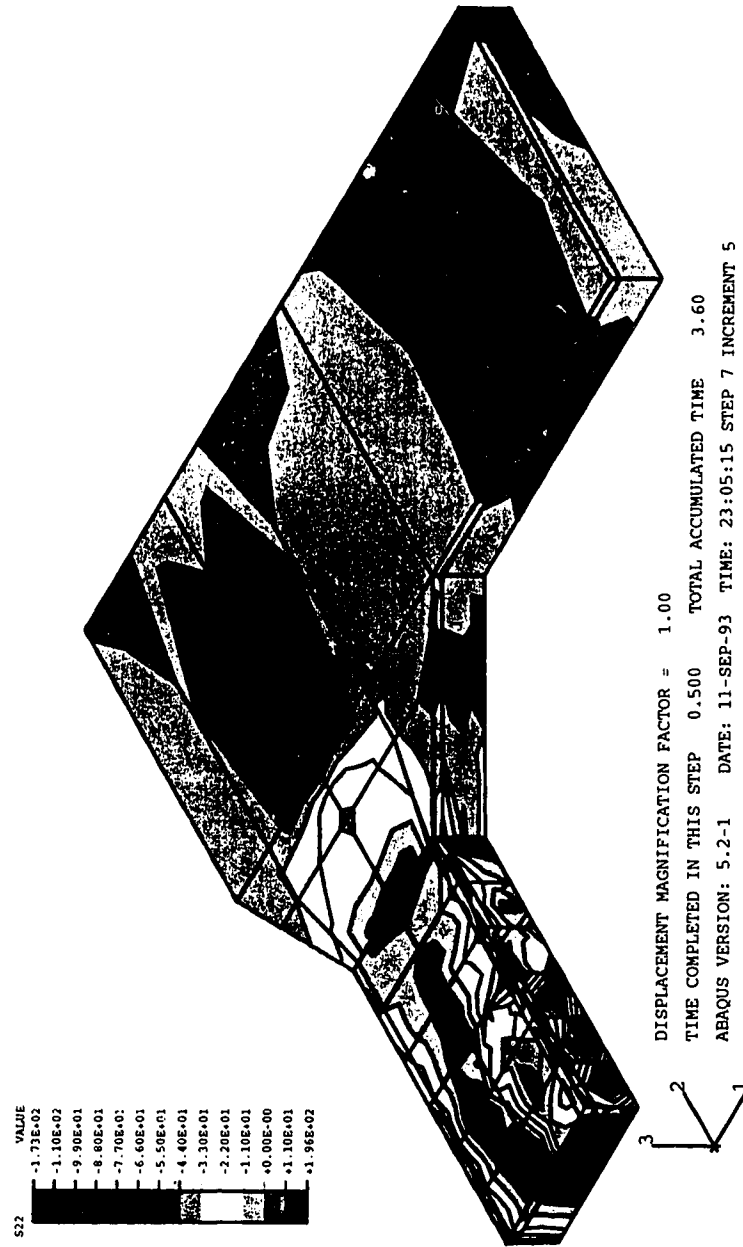Fig. 4.19   Stress in ties for Specimen V16

Specimen V16
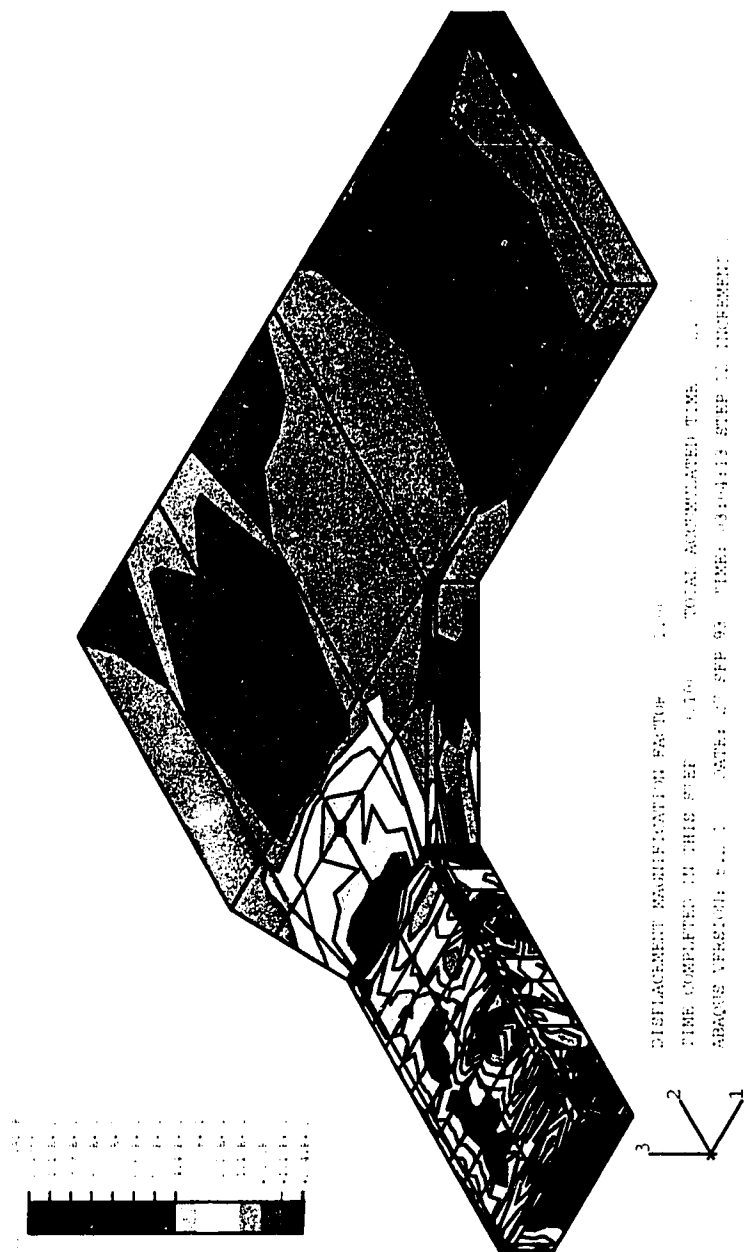


Fig.4.20A  Axial stress (Direction 2) pattern for Specimen V16 (Outside view)
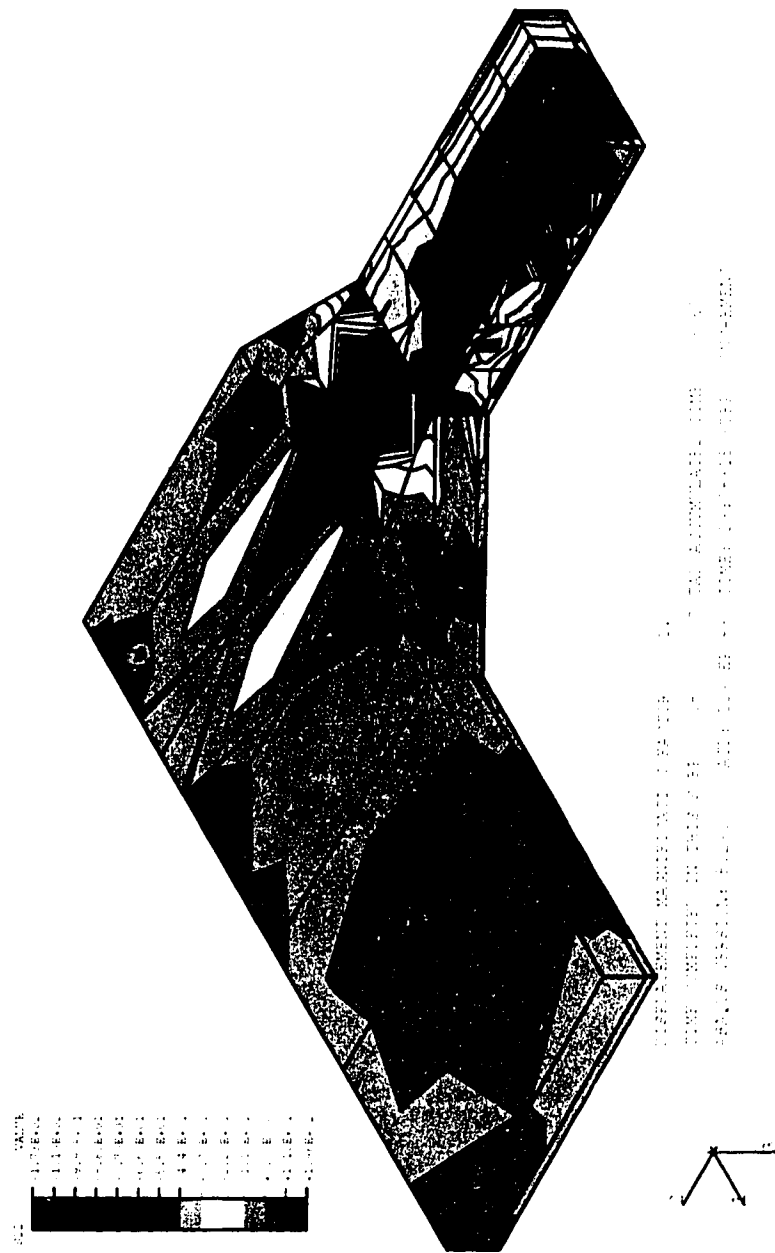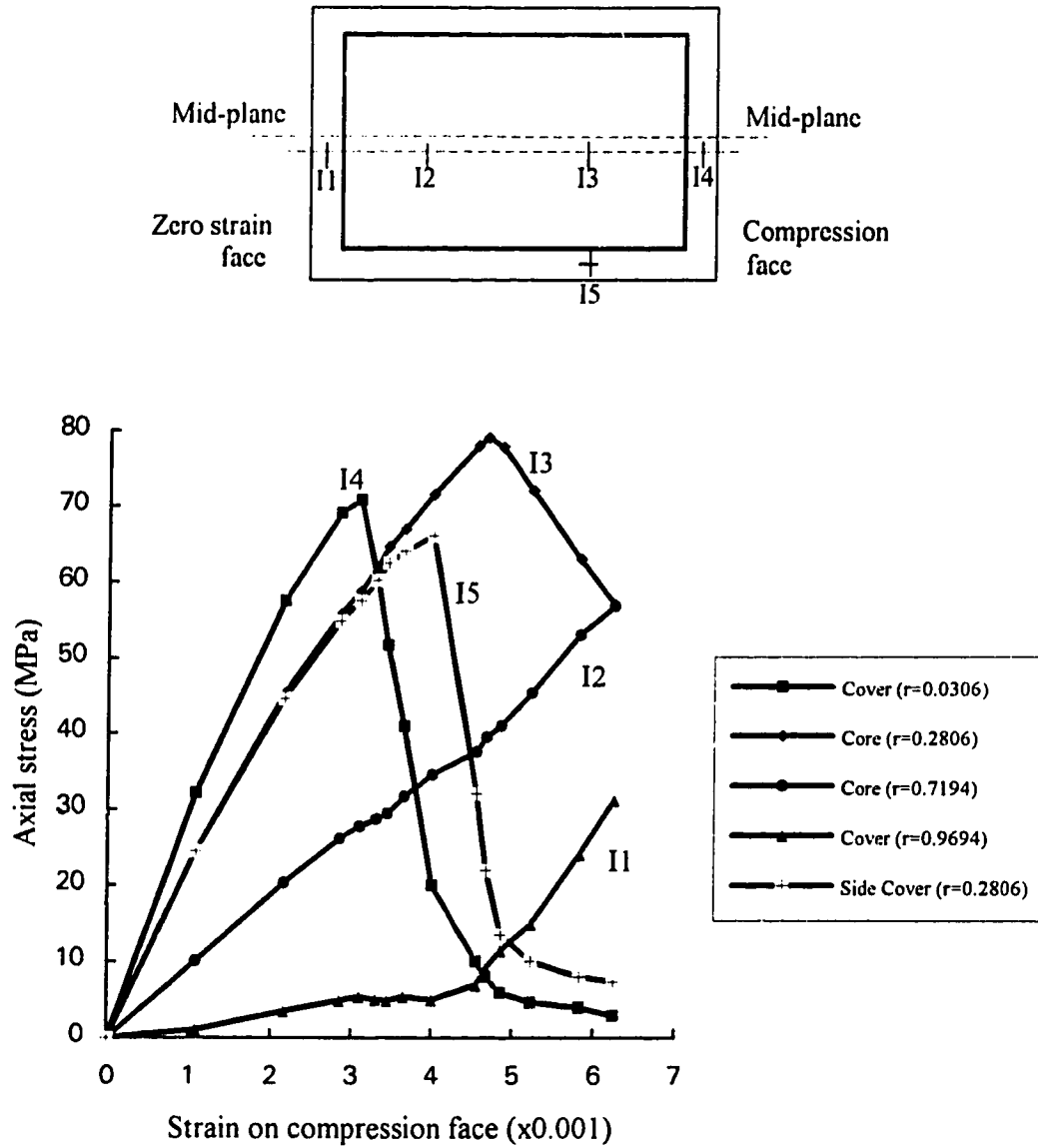
99
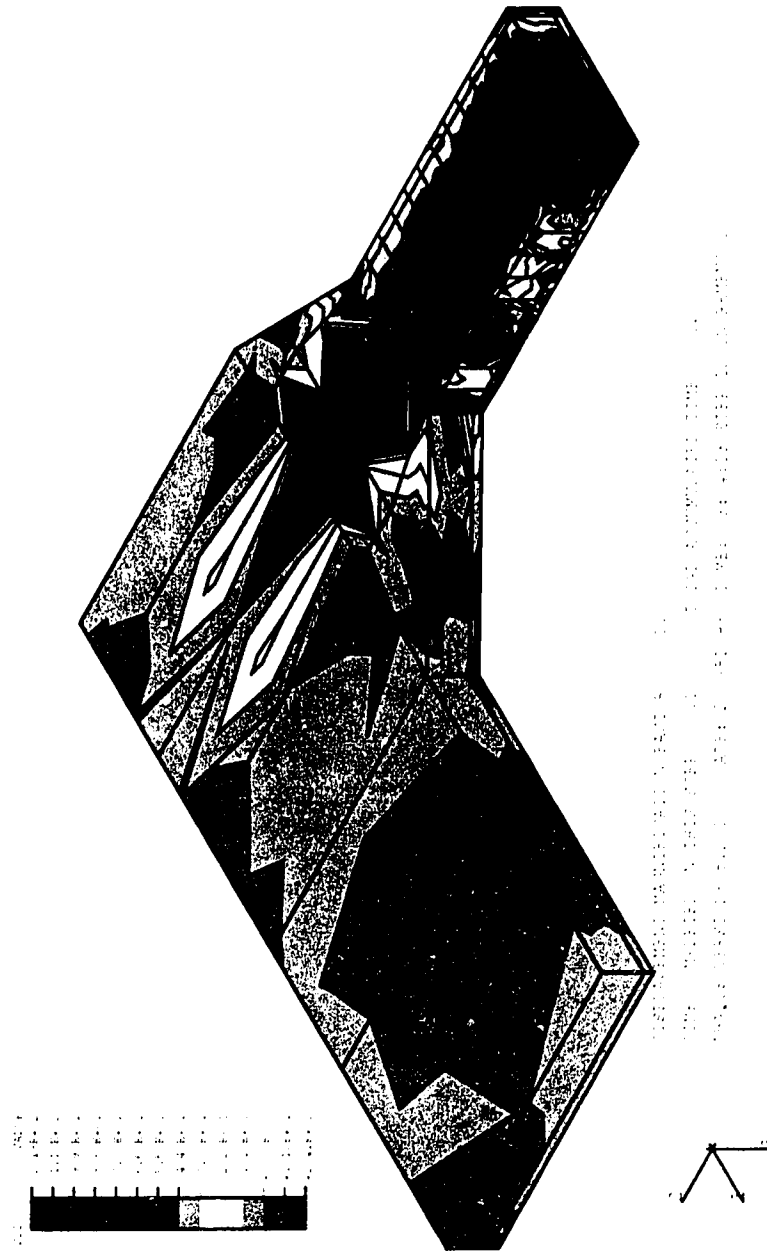
Specimen V16



Fig.4.20B  Axial stress (Direction 2) pattern for Specimen V16 (Mid-plane view)

Specimen V13

DISPLACEMENT MAGNIFICATION FACTOR : 1.00    TOTAL ACCUMULATED TIME : -.1
TIME COMPLETED IN THIS STEP    0.500    TIME: 16:55:19 STEP 4 INCREMENT 1
ABAQUS VERSION: 5.3-1    DATE: 29-SEP-93    TIME: 16:55:19 STEP 4 INCREMENT 1

Fig.4.21   Transverse stress (Direction 1) pattern on the core face of Specimen V13
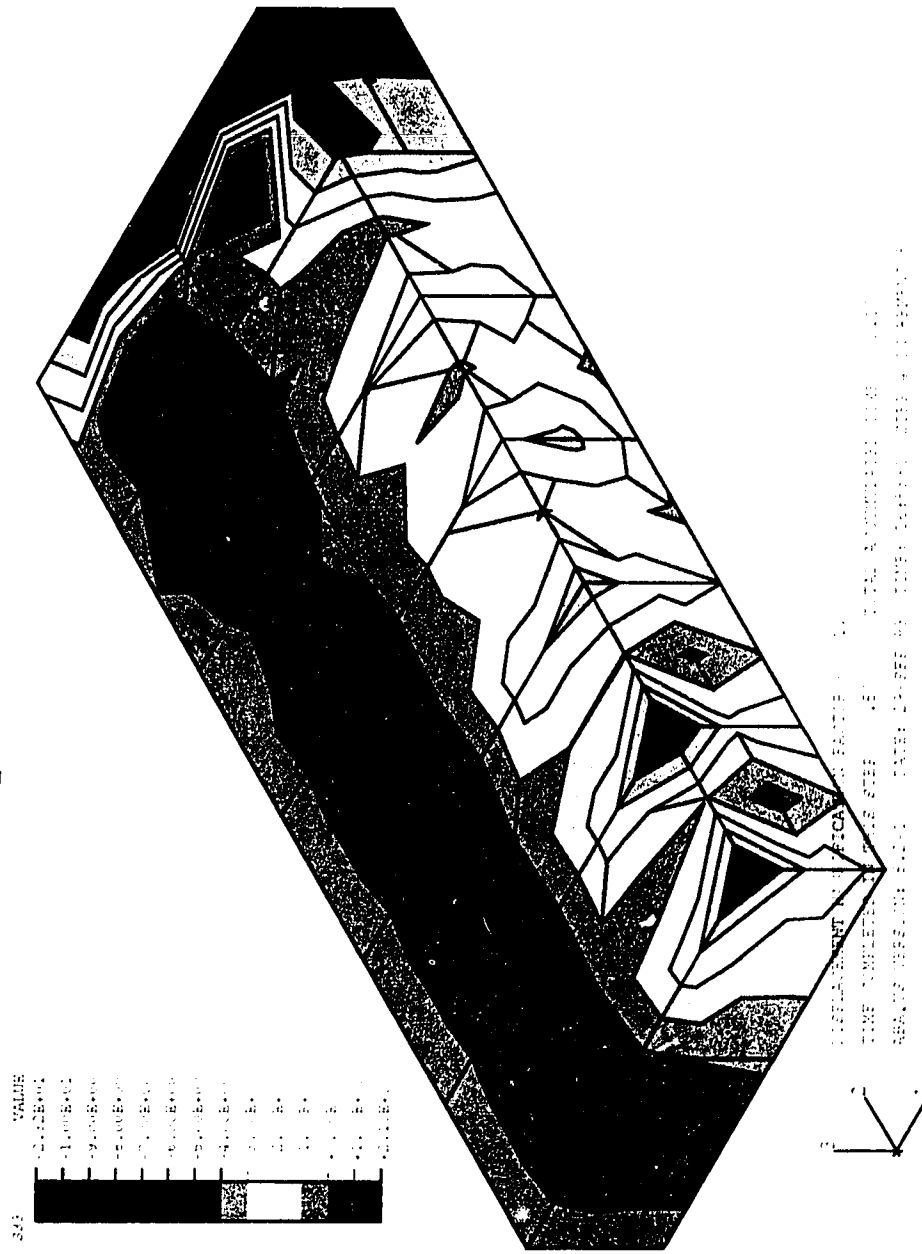
Fig. 4.22  Transverse stress (Direction 3) pattern on the core face of Specimen V13

# CHAPTER FIVE

# PARAMETRIC STUDY OF TIED HIGH STRENGTH CONCRETE COLUMNS

## 5.1 Introduction

In order to examine the performance of current design codes related to tied concrete columns, it is important to understand the behavior of concrete columns with a range of variables. Tied concrete columns involve a variety of parameters such as cross-sectional dimension, concrete strength, strength and amount of longitudinal reinforcement, and strength, amount and distribution of transverse reinforcement, etc. It is not realistic to conduct a full-fledged experimental investigation with these different parameters because of the expense. Instead, a parametric study using a verified finite element model becomes a practical and alternative approach.

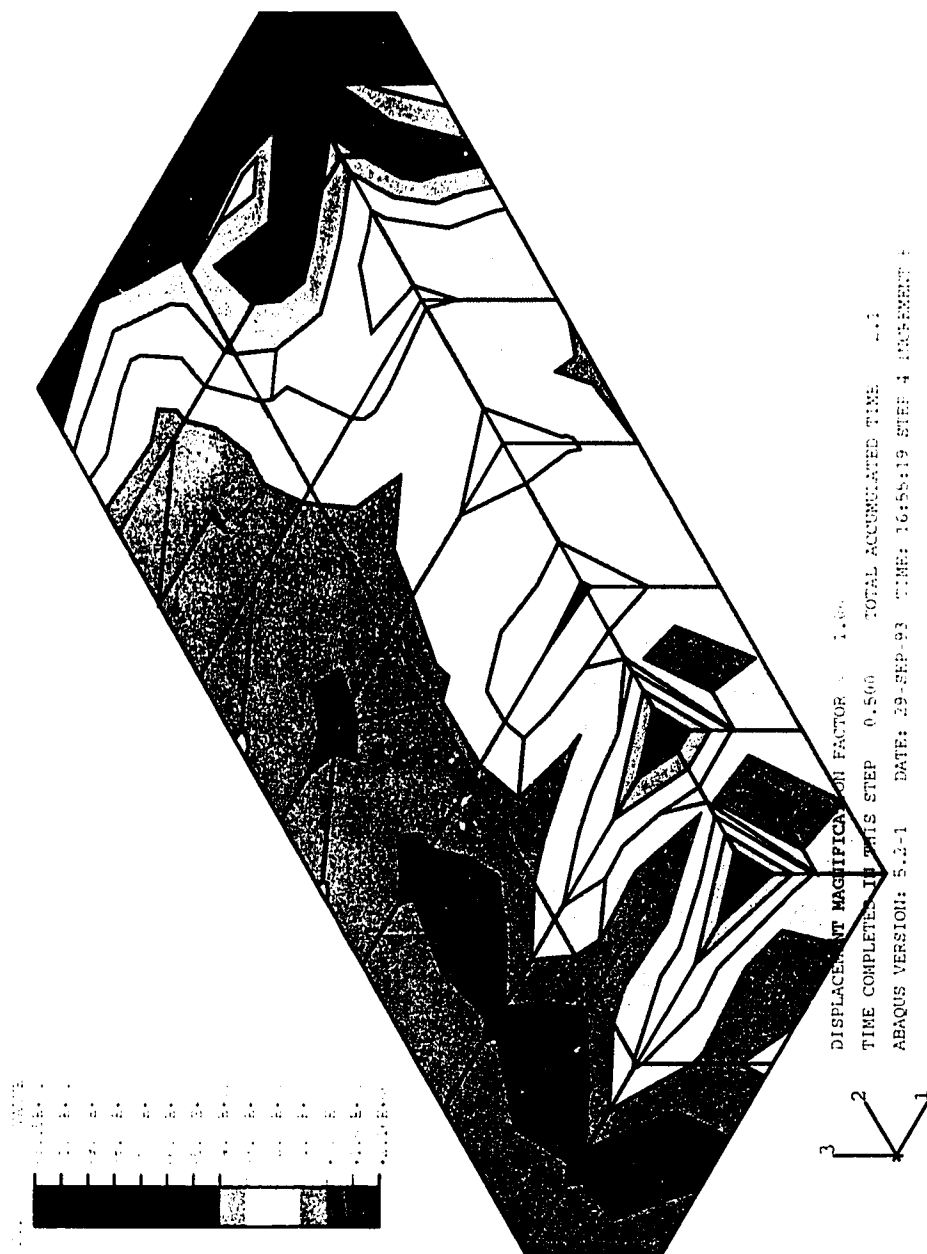In this Chapter, a parametric study of a large number of tied high strength concrete columns loaded eccentrically is presented. The study was conducted using the finite element model described in Chapter 3. The model has been verified, in Chapter 4, against the observed behavior of tied high strength concrete columns tested by Ibrahim and MacGregor (1994).

This chapter starts with a brief review of the outline of ACI Code sections related to tied concrete columns. The code provides guidelines in selecting parameters of tied columns for the study presented here. Numerical results of the parametric study are then presented and discussed.

## 5.2 Outline of ACI Code Related to Tied Concrete Columns

The brittle behavior of high strength concrete in compression has been shown to become much more ductile when it is effectively confined. Reinforced concrete columns used in seismic active zones are usually provided with closely spaced ties. This provides effective confinement and may allow the use of extremely high strength concrete.

The guidelines for seismic design of frame members subjected to bending and axial load are addressed in Section 21.4 of ACI Building Code. In the following this code section is outlined.

*Cross-section*

Clause 21.4.1.1 requires that the shortest cross-sectional dimension, measured on a straight line passing through the geometric center, shall not be less than 12in. (304.8mm). In addition, Clause 21.4.1.2 requires that the ratio of the shortest cross-sectional dimension to the perpendicular dimension shall not be less than 0.4.

*Longitudinal reinforcement*

Clause 21.4.3.1 requires that the reinforcement ratio, $\rho_g$, shall not be less than 0.01 and shall not exceed 0.06.

*Minimum flexural strength of columns*

Clause 21.4.2.1 requires that the flexural strength of any column proportioned to resist a factored axial compressive force exceeding $A_g f_c' / 10$ (in which $A_g$ is the gross area of section, and $f_c'$ is the concrete strength) shall satisfy:

$$\sum M_e \geq (6/5) \sum M_g \qquad (5.1)$$

in which $\sum M_e$ is the sum of moments, at the center of the joint, corresponding to the design flexural strength of the columns framing into that joint, while $\sum M_g$ is the sum of moments, at the center of the joint, corresponding to the design flexural strength of the

girders framing into that joint. If the above equation can not be satisfied at a joint, columns supporting reactions from that joint shall be provided with closely spaced transverse reinforcement (specified in the next paragraph) over their height. If it is satisfied, the closely spaced transverse reinforcement is only required adjacent to hinging regions.

*Transverse reinforcement*

Clause 21.4.4.1 requires that the total cross-sectional area of rectangular hoop reinforcement (single or overlapping hoops, or crossties) shall not be less than either of the following two values:

$$A_{sh} = 0.3(sh_c f_c' / f_{yh})[(A_g / A_{ch}) - 1] \qquad \text{(ACI 318-89 Eq.21-2)} \qquad (5.2)$$

$$A_{sh} = 0.09 sh_c f_c' / f_{yh} \qquad \text{(ACI 318-89 Eq.21-3)} \qquad (5.3)$$

in which $A_{ch}$ is the cross-sectional area of a structural member measured out-to-out of the transverse reinforcement, $s$ is the spacing of transverse reinforcement measured along the longitudinal axis of the structural member, $h_c$ is the cross-sectional dimension of the column core measured center-to-center of the confining reinforcement, and $f_{yh}$ is the specified yield strength of the transverse reinforcement.

To simplify the presentation, an equivalent transverse reinforcement ratio $\rho_t$ is introduced as:

$$\rho_t = \frac{A_{sh}}{sh_c(f_c' \cdot f_{yh})} \qquad (5.4)$$

Equations 5.2 and 5.3 can be rearranged so that the equivalent transverse reinforcement ratio $\rho_t$ should satisfy the following two conditions:

$$\rho_t \geq 0.3[(A_g / A_{ch}) - 1] \qquad (5.5)$$

$$\rho_t \geq 0.09 \qquad (5.6)$$

In addition, Clause 21.4.4.2 requires that the transverse reinforcement shall be spaced at distances not exceeding (a) one-quarter of the minimum member dimension and (b) 4in. (102mm).

## 5.3 Parameters Involved and Design of the Parametric Study

Nine series of tied high strength concrete columns, denoted as Series PA, PB, PC, PD, PE, PF, PG, PH and PV13, are studied here. These nine series include 21 different analytical specimens with a variety of parameters involving tie configuration, tie size, yield strength of ties, uniaxial compressive strength of concrete, cover depth, amount of longitudinal reinforcement, and cross-sectional dimension.

Except for Series PH and PV13, all specimens have the cross-sectional dimension of 350mm x 350mm, which satisfies the ACI Code Clause 21.4.1, and have a length of 960mm. The same specimen size was used by Ozcebe and Saatcioglu (1987) in an experimental program. For Series PH, the cross-sectional dimension of the specimens is 700mm x 700mm and the length is 1920mm. Series PV13 is an extension of Specimen V13 (discussed in Chapter 4) with various values of yield strength of ties. The cross-sectional dimension for Series PV13 is 200mm x 300mm.

Except for Series PG, PH and PV13, all specimens have a longitudinal reinforcement arrangement consisting of 8 No.25M bars. The longitudinal reinforcement ratio $\rho_g$ is 0.0326 which satisfies the ACI Code Clause 21.4.4. For Series PG, the longitudinal reinforcement arrangement is 8 No.15M bars for Specimen PG1, and 8 No.20M bars for Specimen PG2. For Series PH, the longitudinal reinforcement arrangement is 16 No.25M bars with 5 bars on each side. For Series PV13, the arrangement is 4 No.15M bars, which is similar to that in Specimen V13.

Except for Series PD and PV13, all specimens have concrete uniaxial compressive strength of 75MPa. For Series PD, the concrete strength is 37.5MPa for Specimen PD1, and 50MPa for Specimen PD2. For Series PV13, all specimens have concrete uniaxial compressive strength of 72.5MPa.

Except for Series PF, PH and PV13, all specimens have concrete cover depth of 20mm. For Series PF, the cover depth is 20mm for Specimen PF1, 30mm for Specimen PF2, and 40mm for Specimen PF3. The cover depth is 40mm for all specimens in Series PH. For Series PV13, all specimens have the cover depth of 14mm.

Except for Specimens PE1 and PE2 in Series PE and all three specimens in Series PV13, all specimens are designed to satisfy the ACI Code seismic design requirement of transverse reinforcement (Eqs.5.2 and 5.3).

The parameters for all series are summarized in Table 5.1. Special considerations in the design of individual series are addressed in the following sections.

## 5.4 The Analytical Model

The finite element model and loading system are similar to those used in Chapter 4. There are two vertical loads on the specimen, an axial load and an eccentric load. The amount of the eccentric load is adjusted such that the strain on the tension face is zero. Therefore, the neutral axis is located on the tension face of all the specimens in this chapter. The loading strategy in the finite element analysis here is also the same as used in Chapter 4. The analysis was carried out on a SUN SPARC IPX station using program 'ABAQUS' (Hibbitt et al. 1993) Version 5.2. The material model is user-defined as described in Chapter 3.

Material parameters used for the finite element analysis here are included in Table 5.2. Determination of the material parameters is based on the constitutive tests discussed in Chapter 2. For concrete with compressive strength of 75MPa, the strain corresponding to unconfined compressive strength is 0.0038 for the finite element analysis with the chosen material parameters.

## 5.5 Results and Discussions

In the following the results of the different series are presented and discussed.

In this chapter, the moment mentioned is about the center line instead of about the neutral axis as used in Chapter 4. This is primarily for the convenience of comparing the numerical results with the ACI predictions.

### 5.5.1 Series PA: Effect of Tie Configuration

Series PA is designed to study the effect of the tie configuration. There are four specimens, PA1, PA2, PA3 and PA4, in this group. The depth of cover to the surface of the ties is 20mm which results in $0.3[(A_g / A_{ch}) - 1] = 0.0824$. As indicated in Eqs.5.5 and 5.6, the ACI Code requires that the equivalent transverse reinforcement ratio be $\rho_t \geq 0.09$.

Specimen PA1 is designed with No.10M ties in a rectangular layout. The tie spacing is chosen as 40mm such that $\rho_t = 0.09$. Based on the tie configuration of Specimen PA1, Specimen PA2 is designed with additional single crossties, Specimen PA3 with additional double crossties, and Specimen PA4 with additional diamond-shaped ties. In order to keep the equivalent transverse reinforcement ratio $\rho_t$ the same in the group, Specimen PA2 is designed with tie spacing of 60mm, Specimens PA3 and PA4 are designed with tie spacing of 80mm. Therefore, all specimens satisfy the minimum ACI Code requirement of transverse reinforcement (Eq.5.6) exactly.

Results of the finite element analysis are presented in Figs.5.1 and 5.2 for the moment and axial load versus the strain on the compression face.

As shown in Fig.5.1, all four specimens have a very similar pre-peak moment behavior. The moment reaches its first peak immediately after the occurrence of strain-softening of the cover on the compression face. However, the tie configuration has a significant effect on the post-peak moment behavior. Although all four specimens have the same equivalent transverse reinforcement ratio, specimens with small tie spacing have a better post-peak moment performance than those with large tie spacing. For Specimens PA3 and PA4 the yielding of ties takes place earlier than Specimens PA1 and PA2,

partially because of excessive localized strain-softening developed between the ties. Specimens PA3 and PA4 have almost the same post-peak moment behavior until the yielding of the rectangular ties. For Specimen PA3, the moment capacity is reduced significantly after the yielding of the rectangular ties. On the other hand, for Specimen PA4, the decrease of moment capacity is delayed until the yield of the diamond-shaped ties at a compression face strain of 0.0056. This indicates that the additional diamond-shaped ties provide more confinement than double crossties.

## 5.5.2 Series PB and PE: Effect of Tie Size

Series PB and Series PE are designed to study the effect of tie size. All specimens of both series have the rectangular layout of ties similar to Specimen PA1. For Series PB, Specimen PB2 is identical to Specimen PA1 with No.10M ties spaced at 40mm, Specimen PB1 has No.8M ties spaced at 20mm, and Specimen PB3 has No.15M ties spaced at 80mm. Therefore, all specimens in Series PB have the equivalent transverse reinforcement ratio $p_t$=0.09, which is again the minimum ACI Code seismic design requirement. Specimen PB1 is designed for parametric study only as the spacing of 20mm is not realistic in engineering practice.

All specimens of Series PE are designed with practical tie spacing of 80mm. Specimen PE1 has No.8M ties, Specimen PE2 has No.10M ties, and Specimen PE3 has No. 15M ties. The equivalent transverse reinforcement ratios $p_t$ for Specimens PE1, PE2 and PE3 are 0.0225, 0.045 and 0.09 respectively. Therefore, Specimens PE1 and PE2 meet the ACI Code requirement of transverse reinforcement for non-seismic design but not the seismic design requirement. Specimen PE3 and Specimen PB3 are identical.

Results of the finite element analysis of Series PB are presented in Figs.5.3 and 5.4 for moment and axial load versus strain on the compression face. Results of the finite element analysis of Series PE are presented in Figs.5.5 and 5.6 for the moment and axial load versus strain on the compression face respectively.

As shown in Fig.5.3, all specimens in Series PB have almost the same pre-peak moment behavior. In the post-peak regime, specimens with smaller tie size (i.e. with small

tie spacing) have higher moment and load carrying capacity than ones with larger ties sizes (i.e. with larger tie spacing). There is no direct relationship between ...e onset of yielding of ties and the tie size as the tie spacing changes with the tie size to keep $\rho_t$ the same in this group.

For Series PE, as shown in Figs.5.5 and 5.6, all specimens have the same pre-peak moment and axial load behavior until the occurrence of strain softening of cover. As expected, specimens with smaller tie sizes have lower moment and load carrying capacity than ones with larger tie sizes. The yielding of ties also takes place earlier for specimens with smaller tie sizes. For Specimens PE1 and PE2, which do not meet the seismic design requirement of transverse reinforcement, the post-peak moment behavior is very brittle, while the axial load is not maintained at maximum value. On the other hand, all of specimens of Series PA, PB and Specimen PE3 maintained the maximum axial load while the moment peaked and then reduced to zero. The amount of transverse reinforcement is not sufficient for Specimens PE1 and PE2 to maintain a triaxial stress state in the cores. This indicates that the ACI Code requirement is necessary in order to avoid a poor post-peak performance.

### 5.5.3  Series PC and PV13: Effect of Yield Strength of Ties

Series PC and Series PV13 are designed to study the effect of yield strength of the ties. All specimens in Series PC have No.10M size ties in a rectangular layout similar to Specimen PA1. Specimen PC1 is identical to Specimen PA1 with yield strength of ties of 400MPa and tie spacing of 40mm. Specimen PC2 has tie yield strength of 600MPa and tie spacing of 60mm. Specimen PC3 has tie yield strength of 800MPa and tie spacing of 80mm. The tie spacing is adjusted with the variation of tie yield strength so that all specimens in Series PC have an equivalent transverse reinforcement ratio $\rho_t$=0.09. All specimens in this group meet the ACI Code seismic design requirement of transverse reinforcement.

Series PV13 is an extension of Specimen V13, which has been tested by Ibrahim and MacGregor (1994) and simulated in Chapter 4. Specimen V13 had tie yield strength of 401MPa, Specimen V13A has ties strength of 600MPa, and Specimen V13B has a tie

yield strength of 800MPa. All specimens in Series PV13 have No.8M ties spaced at 100mm in a rectangular layout. The equivalent transverse reinforcement ratios $\rho_t$ for Specimens V13, V13A and V13B are 0.02, 0.04 and 0.06 respectively. Therefore, none of the specimens in Series PV13 met the ACI Code seismic design requirement of transverse reinforcement.

Results of the finite element analysis of Series PC are presented in Figs.5.7 and 5.8 for the moment and axial load versus strain on the compression face. Results of the finite element analysis of Series PV13 are presented in Figs.5.9 and 5.10 for moment and axial load versus strain on the compression face.

As shown in Fig.5.7, the pre-peak moment behavior is almost the same for all specimens of Series PC. In the post-peak regime, specimens with lower tie yield strength (i.e. with small tie spacing) have higher moment and axial load carrying capacity than ones with higher tie yield strength (i.e. with large tie spacing). The yielding of ties takes place at almost the same strain for all specimens of Series PC.

Since all specimens in Series PV13 are identical except for the tie yield strength, they experience the same pre-peak and initial post peak moment and axial load behavior. As shown in Figs.5.9 and 5.10, the differences become significant when ties of Specimen V13 yield. As expected, the yielding of ties is delayed for specimens with higher tie yield strengths. This allows a higher moment and axial load carrying capacity for these specimens in the post-peak regime. However, all specimens in this group have a brittle post-peak moment behavior as compared with the specimens of Series PC. Because the amount of transverse reinforcement is not sufficient, collapse of columns takes place before the triaxial stress state in the core is sufficiently developed.

### 5.5.4 Series PD: Effect of Concrete Strength

Series PD is designed to study the effect of concrete strength. Specimen PD3 is identical to Specimen PA1 with concrete strength of 75MPa. Specimen PD1 is designed with concrete strength of 37.5MPa, and Specimen PD2 with concrete strength of 50MPa. Specimen PD1 has No.10M ties spaced at 80mm, Specimen PD2 has No.10M ties spaced

at 60mm, and Specimen PD3 has No.10M ties spaced at 40mm. The rectangular layout of transverse reinforcement is used for all specimens in this series. All the specimens are designed with an equivalent transverse reinforcement ratio $\rho_t$=0.09 so that the ACI Code seismic design requirement of transverse reinforcement is met.

Results of the finite element analysis of Series PD are presented in Figs.5.11 and 5.12 for the moment and axial load versus strain on the compression face. Three different sets of material parameters, as shown in Table 5.2, are used in the finite element analysis of Series PD. The material parameters are chosen based on the material test results as presented in Chapter 2.

As shown in Fig.5.11, each specimen has a different behavior in both the pre-peak and the post-peak regimes. The difference in the pre-peak regime is primarily because of different values of Young's modulus used in the analysis. The common feature is that the moment reaches its first peak immediately after the strain-softening of the cover. Specimens PD1 and PD2 have a very steady axial load capacity in the post-peak regime.

Although Specimen PD3 has concrete strength and amount of transverse reinforcement twice as much as those of Specimen PD1, the increase of the moment capacity is about 78%. This suggests that the increase of moment capacity is not proportional to the concrete strength. The post-peak moment branch becomes slightly steeper with increasing concrete strength. Generally speaking, however, the post-peak performance for high strength concrete is acceptable if the ACI Code seismic design requirement of ties is met.

### 5.5.5 Series PF: Effect of Cover Depth

Series PF is designed to study the effect of cover depth. Specimen PF1 is identical to Specimen PB3 with a cover depth of 20mm. Specimen PF2 is designed with the cover depth of 30mm, while Specimen PF3 has a cover depth of 40mm. Since the value of $A_{ch}$ is dependent on the cover depth, different amounts of the equivalent transverse reinforcement ratios $\rho_t$ from Eq.5.5 are required in this group. In particular, Specimen PF2 needs $\rho_t \geq 0.137$, and Specimen PF3 needs $\rho_t \geq 0.204$. To meet the ACI Code seismic

design requirement of transverse reinforcement, Specimen PF2 is designed with 3 No.10M ties spaced at 80mm ($\rho_t$=0.145), and Specimen PF3 with 2 No.15M ties spaced at 80mm ($\rho_t$=0.209).

Results of the finite element analysis of Series PF are presented in Figs.5.13 and 5.14 for the moment and axial load versus the strain on the compression face.

As shown in Fig.5.13, the three specimens have almost the same pre-peak behavior. This confirms the observation by Ibrahim and MacGregor (1994) who indicated that the transverse reinforcement has no effect on the pre-peak moment behavior. In the post-peak regime, both moment and axial load carrying capacities are reduced with increasing cover depth as shown in Figs.5.13 and 5.14. Specimen PF3, which has the largest cover depth of 40mm, fails before yielding of the ties. In fact, the effect of strain-softening of the cover becomes more and more significant with increasing cover depth. Generally speaking, the larger the depth of cover, the less the confined volume in the columns, and the less the confined strength generated in the core to compensate the loss of axial stress in the cover due to strain-softening. For columns with very large cover depth, the losing of cover may result in column collapse before yielding of the ties. The use of large amounts of transverse reinforcement in columns with small cores is not economical.

### 5.5.6 Series PG: Effect of Longitudinal Reinforcement

Series PG is designed to study the effect of longitudinal reinforcement. All three specimens are same except the amount of longitudinal reinforcement. Specimen PG3 is identical to Specimen PB3 with longitudinal reinforcement of 8 No.25M ($\rho_g$=0.0326). Specimen PG1 has longitudinal reinforcement of 8 No.15M ($\rho_g$=0.013), and Specimen PG2 has longitudinal reinforcement of 8 No.20M ($\rho_g$=0.0196). All specimens fall within the range of longitudinal reinforcement allowed by the ACI Code. All specimens are designed with No.15M ties spaced at 80mm ($\rho_t$=0.09).

Results of the finite element analysis of Series PG are presented in Figs.5.15 and 5.16 for the moment and axial load versus the strain on the compression face.

113

As shown in Figs.5.15 and 5.16, the amount of the longitudinal reinforcement has affected both the pre-peak and post-peak behavior of the column. As expected, the moment and axial load carrying capacities increase with increasing amount of longitudinal reinforcement. On the other hand, the decreasing slope of moment capacity in the post-peak regime seems not affected by the longitudinal reinforcement.

### 5.5.7 Series PH: Columns with Practical Sizes

For Series PA to PG, the cross-sectional dimension is 350mm x 350mm. This cross-sectional dimension is not very realistic in engineering practice. In order to study the behavior of columns with practical sizes, Series PH is designed which has the cross-sectional dimension of 700mm x 700mm and length of 1920mm. The cover depth is 40mm, and the longitudinal reinforcement arrangement is 16 No.25M with 5 rebars on each side ($\rho_g$=0.0163). Since the ACI Code requires the distance between tie legs in the direction perpendicular to the longitudinal reinforcement to be less than 14in. (350mm), both Specimens PH1 and PH2 are designed with rectangular tie layouts and additional crossties to reduce this distance to 305mm. Specimen PH1 is designed with 3 No.10M ties spaced at 80mm vertically, while Specimen PH2 with 3 No.15M ties spaced at 160mm vertically.

Results of the finite element analysis of Series PH are presented in Figs.5.17 and 5.18 for the moment and axial load versus the strain on the compression face.

As shown in Fig. 5.17, both specimens have almost the same pre-peak moment behavior. The moment reaches its peak when the cover starts strain-softening. In the post-peak regime, Specimen PH1 with smaller tie size and tie spacing shows a much better moment performance as compared with Specimen PH2. However, the difference of tie size and tie spacing has little effect on the axial load carrying capacity as shown in Fig.5.18.

## 5.6 Summary

A parametric study consisting of nine series involving twenty-one specimens is carried out in this chapter.

It is concluded that, although the pre-peak moment and axial load behavior may be affected by concrete strength and amount of longitudinal reinforcement, they are not sensitive to the cover depth and the amount of transverse reinforcement. On the other hand, the cover depth and the amount of transverse reinforcement have a significant effect on the post-peak behavior of columns. Generally speaking, the moment and axial load carrying capacities are increased with increasing amount of transverse reinforcement if the tie spacing is kept as a constant. However, if the same equivalent transverse reinforcement ratio $p_t$ is used, columns with larger tie spacing usually show poorer moment and, sometimes, poorer axial load performance in the post-peak regime.

Table 5.1   Details of tied concrete columns for parametric study

| Series | Speci-men | $f_c'$ (MPa) | Cover (mm) | Longi-tudinal Reinf. | Transverse Reinforcement | | | | ACI Code |
|---|---|---|---|---|---|---|---|---|---|
| | | | | | Size | $f_{yh}$ (MPa) | Spacing (mm) | Configuration | |
| PA | PA1 | 75 | 20 | 8#25M | #10M | 400 | 40 | Square | Yes |
| | PA2 | 75 | 20 | 8#25M | #10M | 400 | 60 | Square + S.C. | Yes |
| | PA3 | 75 | 20 | 8#25M | #10M | 400 | 80 | Square + D.C. | Yes |
| | PA4 | 75 | 20 | 8#25M | #10M | 400 | 80 | Square + Dmd | Yes |
| PB | PB1 | 75 | 20 | 8#25M | #8M | 400 | 20 | Square | Yes |
| | PB2 | 75 | 20 | 8#25M | #10M | 400 | 40 | Square | Yes |
| | PB3 | 75 | 20 | 8#25M | #15M | 400 | 80 | Square | Yes |
| PC | PC1 | 75 | 20 | 8#25M | #10M | 400 | 40 | Square | Yes |
| | PC2 | 75 | 20 | 8#25M | #10M | 600 | 60 | Square | Yes |
| | PC3 | 75 | 20 | 8#25M | #10M | 800 | 80 | Square | Yes |
| PD | PD1 | 37.5 | 20 | 8#25M | #10M | 400 | 80 | Square | Yes |
| | PD2 | 50 | 20 | 8#25M | #10M | 400 | 60 | Square | Yes |
| | PD3 | 75 | 20 | 8#25M | #10M | 400 | 40 | Square | Yes |
| PE | PE1 | 75 | 20 | 8#25M | #8M | 400 | 80 | Square | No |
| | PE2 | 75 | 20 | 8#25M | #10M | 400 | 80 | Square | No |
| | PE3 | 75 | 20 | 8#25M | #15M | 400 | 80 | Square | Yes |
| PF | PF1 | 75 | 20 | 8#25M | #15M | 400 | 80 | Square | Yes |
| | PF2 | 75 | 30 | 8#25M | 3#10M | 400 | 80 | Square | Yes |
| | PF3 | 75 | 40 | 8#25M | 2#15M | 400 | 80 | Square | Yes |
| PG | PG1 | 75 | 20 | 8#15M | #15M | 400 | 80 | Square | Yes |
| | PG2 | 75 | 20 | 8#20M | #15M | 400 | 80 | Square | Yes |
| | PG3 | 75 | 20 | 8#25M | #15M | 400 | 80 | Square | Yes |
| PH | PH1 | 75 | 40 | 16#25M | 3#10M | 400 | 80 | Square + M.C. | Yes |
| | PH2 | 75 | 40 | 16#25M | 3#15M | 400 | 160 | Square + M.C. | Yes |
| PV13 | V13 | 72.5 | 14 | 4#15M | #8M | 401 | 100 | Rectangular | No |
| | V13A | 72.5 | 14 | 4#15M | #8M | 600 | 100 | Rectangular | No |
| | V13B | 72.5 | 14 | 4#15M | #8M | 800 | 100 | Rectangular | No |

Note:

S.C.: single crossties: D.C.: double crossties; M.C.: multiple crossties; Dmd: diamond-shaped ties

For Series PA to PG:
(1) The cross-sections are 350mm x 350mm;
(2) Specimens PA1, PB2, PC1 and PD3 are identical;
(3) Specimens PB3, PE3, PF1 and PG3 are identical.

For Series PH:
(1) The cross-sections are 700mm x 700mm.

For Series PV13:
(1) The cross-sections are 200mm x 300mm.

Table 5.2   Material parameters used for parametric study

| Specimen | | All series but PD and PV13 | Specimen PD1 | Specimen PD2 | Series PV13 |
|---|---|---|---|---|---|
| Concrete | E (MPa) | 28480 | 20871 | 23713 | 34855 |
| | $f_c'$ (MPa) | 75 | 37.5 | 50 | 72.5 |
| | $f_t'$ (MPa) | 5.6 | 3.3 | 4.25 | 3.43 |
| | $G_{cr}^f$ (N/mm) | 0.261 | 0.153 | 0.198 | 0.161 |
| | $A_h$ | 0.02142 | 0.002142 | 0.002142 | 0.002142 |
| | $B_h$ | -0.032 | -0.032 | -0.032 | -0.032 |
| | $C_h$ | 0.0025 | 0.0025 | 0.0025 | 0.0025 |
| | $A_s$ | 24.0 | 24.0 | 24.0 | 16.0 |
| | $B_s$ | -4.0 | -4.0 | -4.0 | -4.0 |
| Longitudinal Reinforcement | E (MPa) | 200000 | 200000 | 200000 | 188200 |
| | $f_y$ (MPa) | 400.0 | 400.0 | 400.0 | 433.2 |
| Transverse Reinforcement | E (MPa) | 200000 | 200000 | 200000 | 216400 |
| | $f_{yh}$ (MPa) | 400 600 (PC2) 800 (PC3) | 400 | 400 | 401 (V13) 600 (V13A) 800 (V13B) |
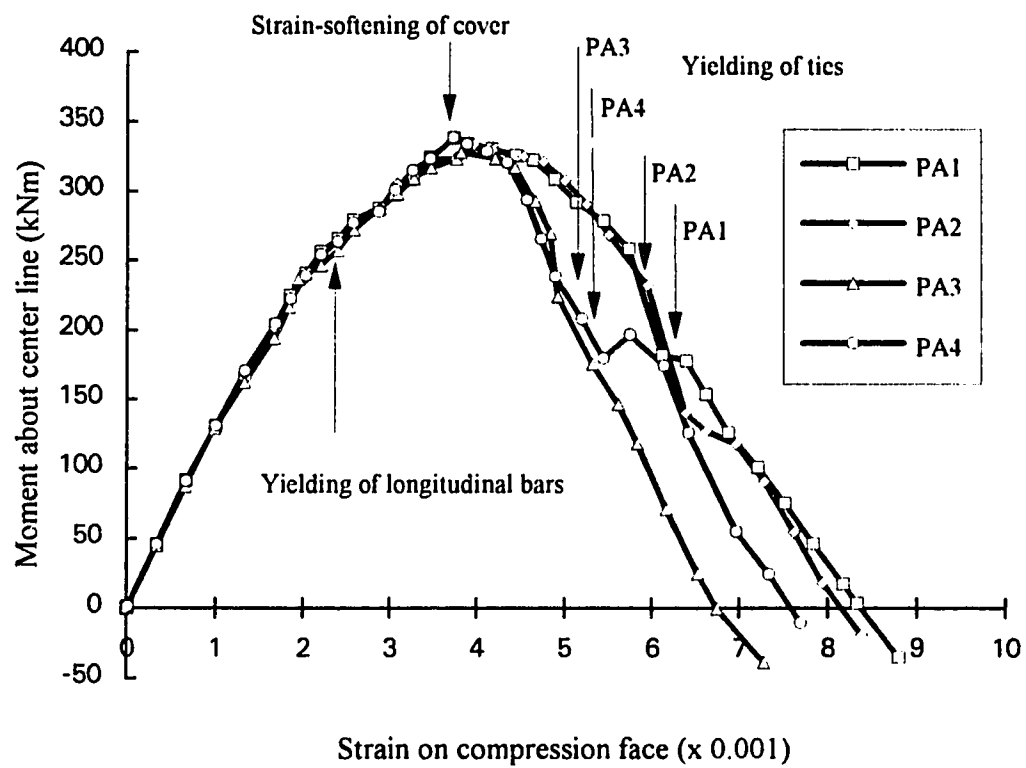
Fig.5.1 Moment vs strain on compression face for Series PA
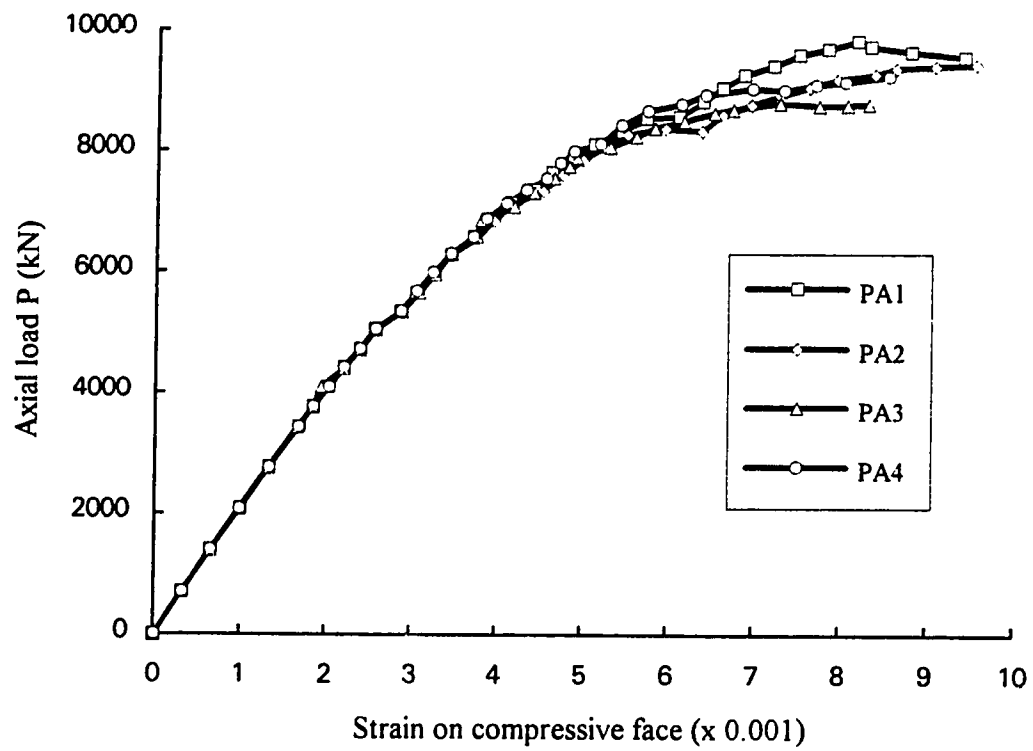
Fig.5.2 Axial load vs strain on compression face for Series PA
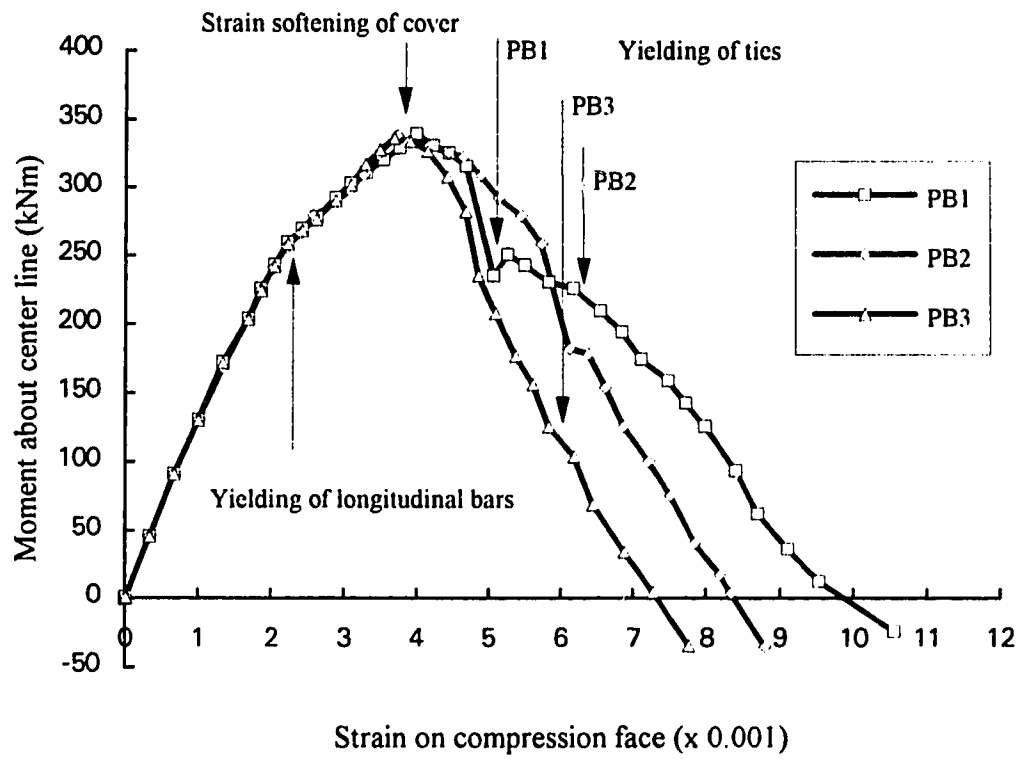
Fig.5.3 Moment vs strain on compression face for Series PB

120
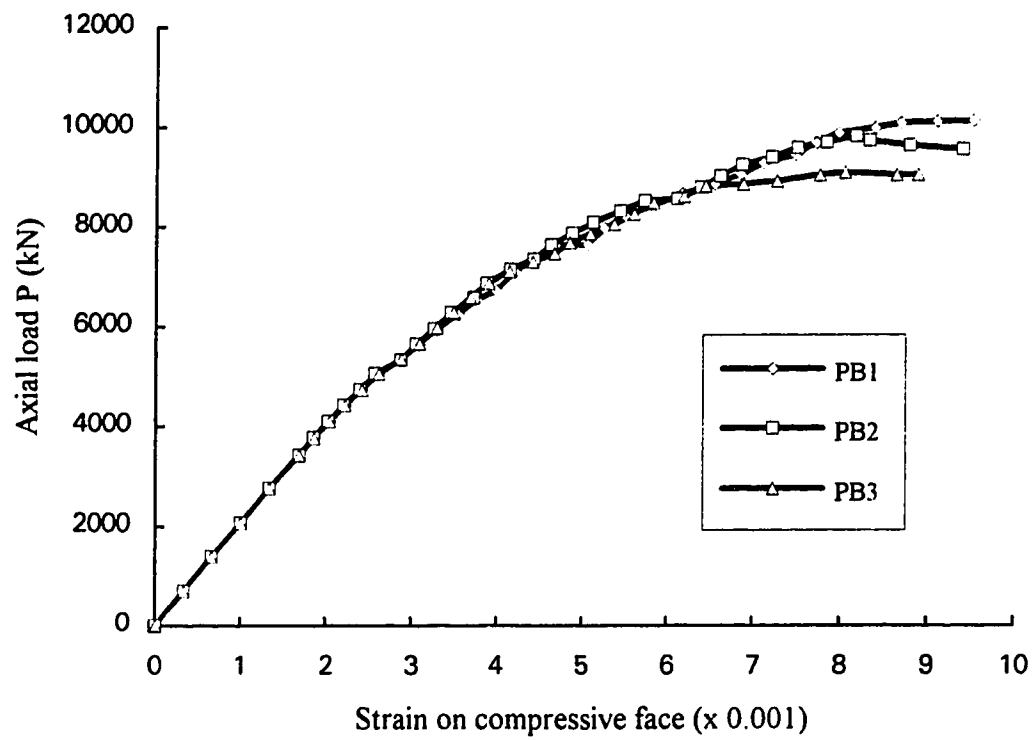
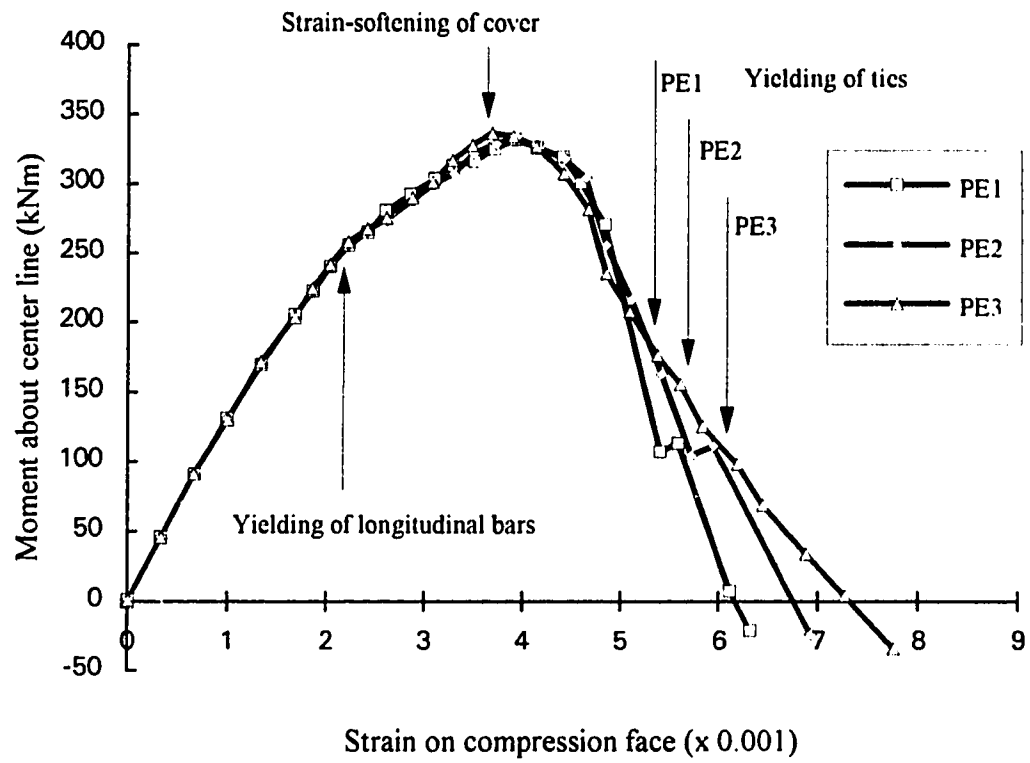Fig.5.4   Axial load vs strain on compression face for Series PB

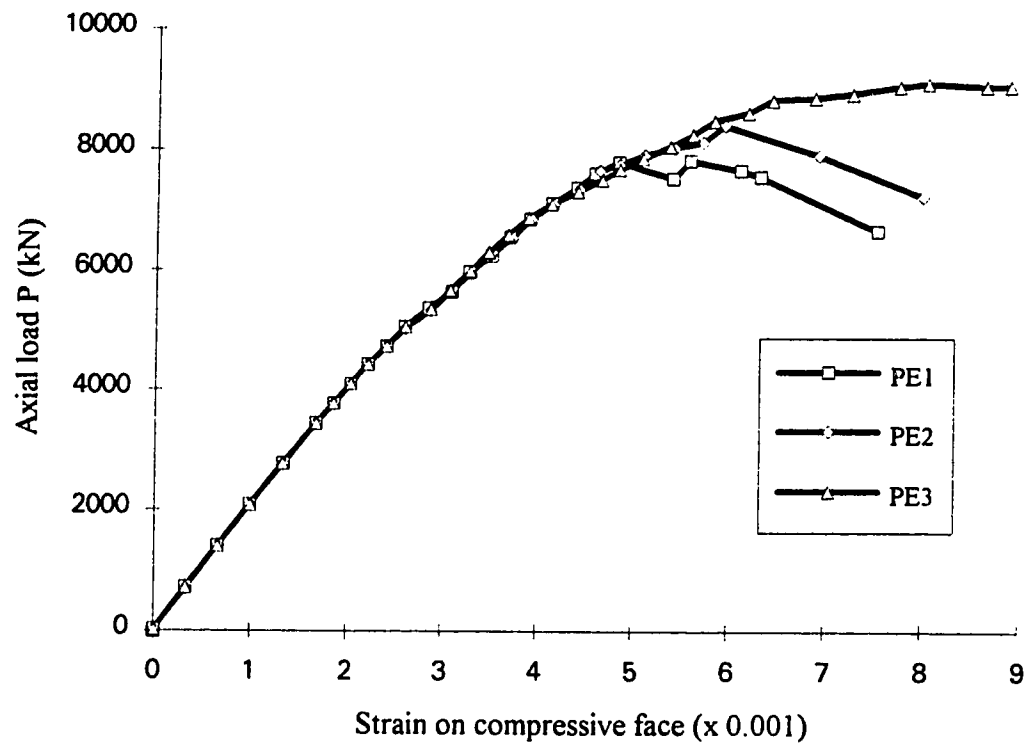Fig.5.5  Moment vs strain on compression face for Series PE

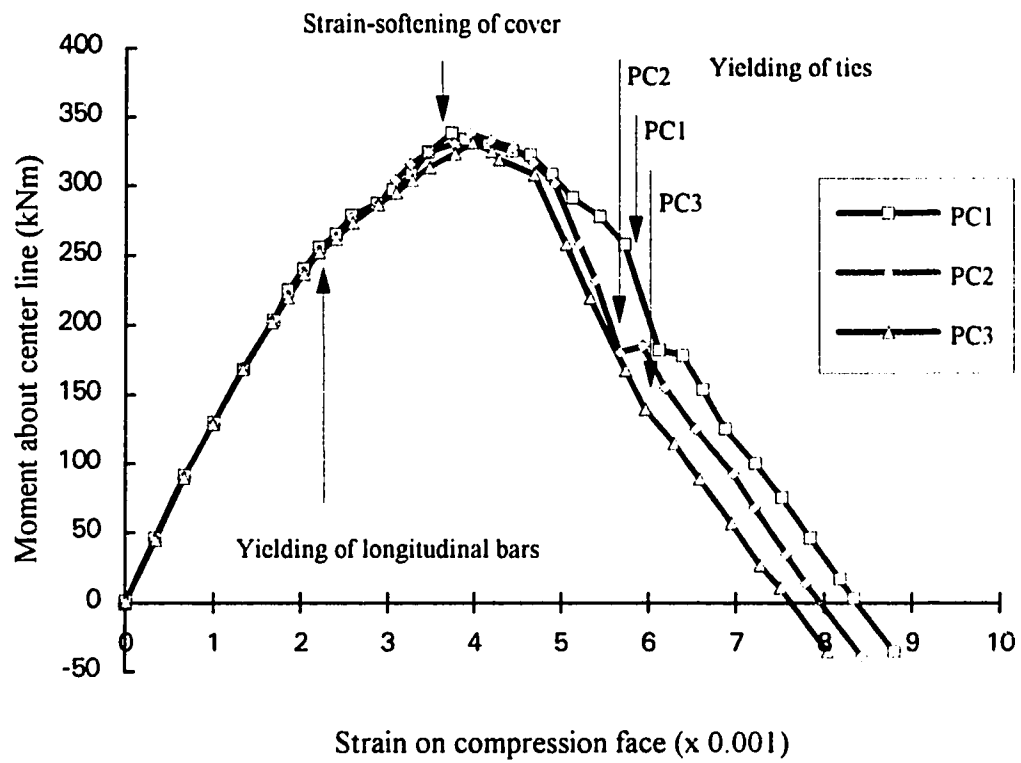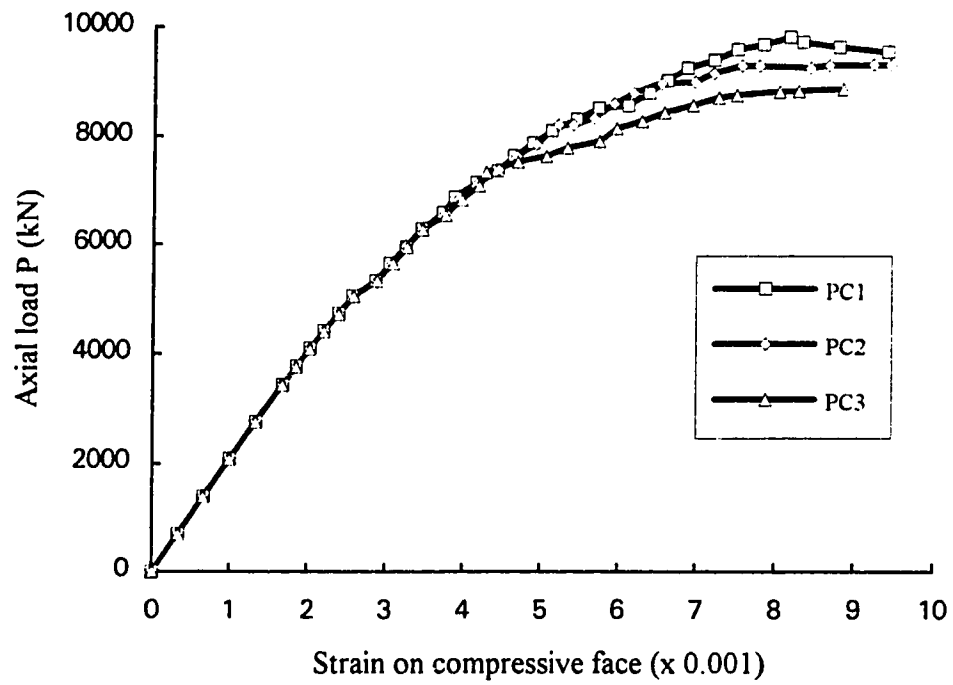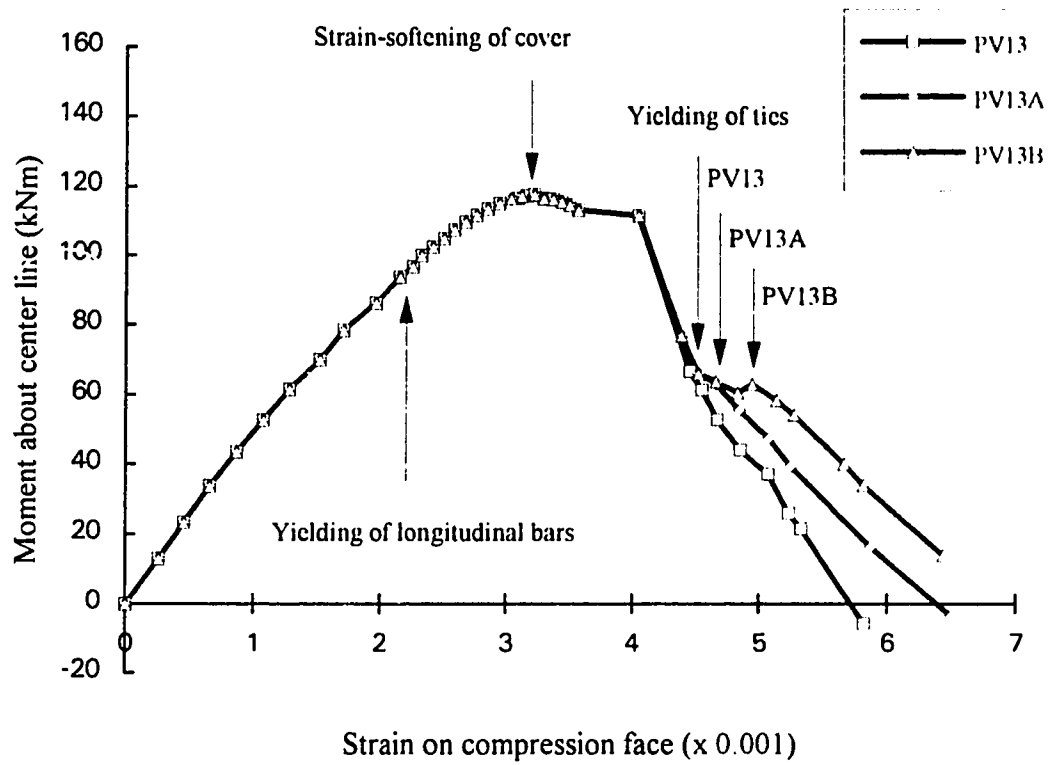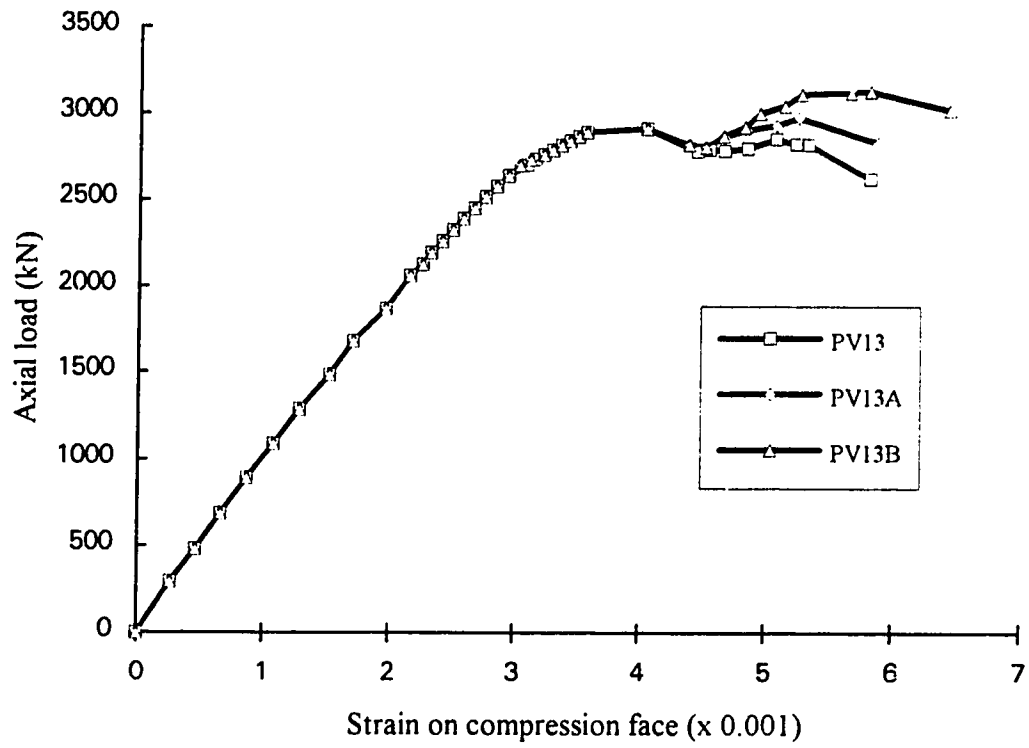Fig.5.6   Axial load vs strain on compression face for Series PE

Fig.5.7  Moment vs strain on compression face for Series PC

124

Fig.5.8   Axial load vs strain on compression face for Series PC

Fig.5.9   Moment vs strain on compression face for Series PV13

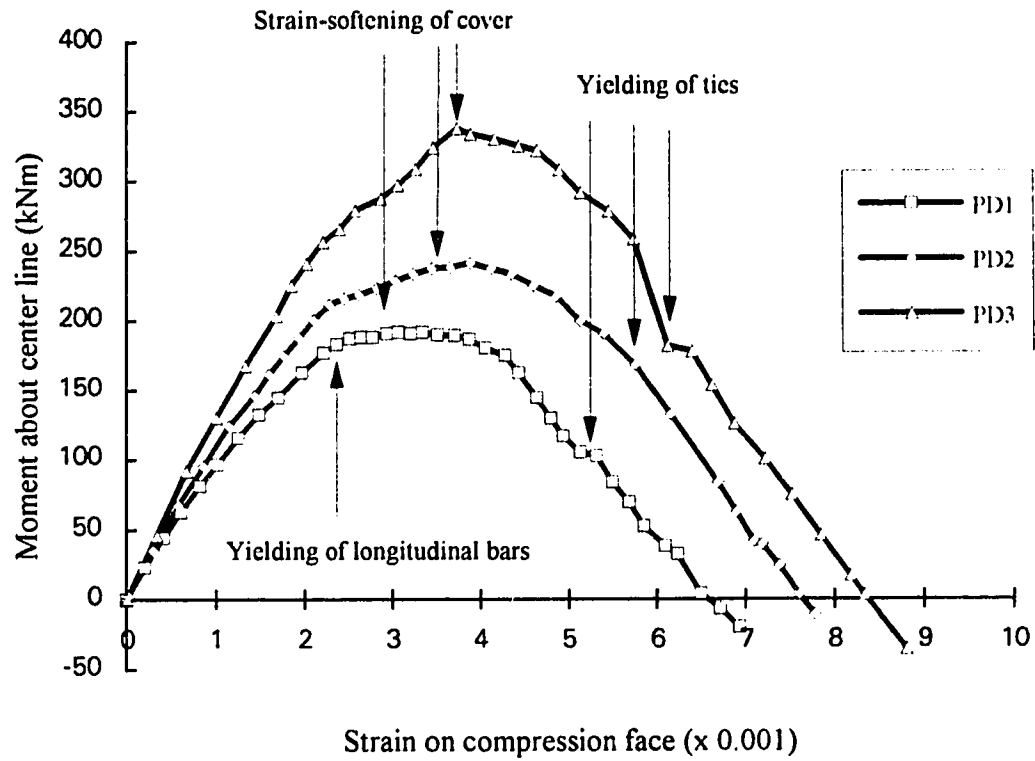Fig.5.10 Axial load vs strain on compression face for Series PV13

127

Fig.5.11  Moment vs strain on compression face for Series PD
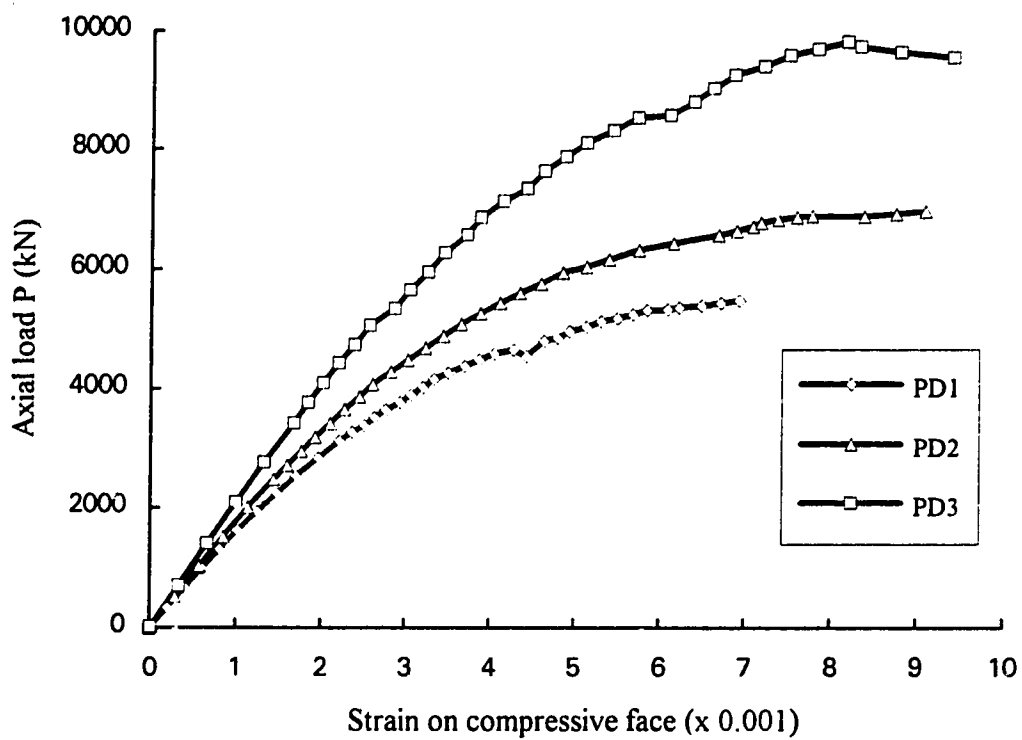
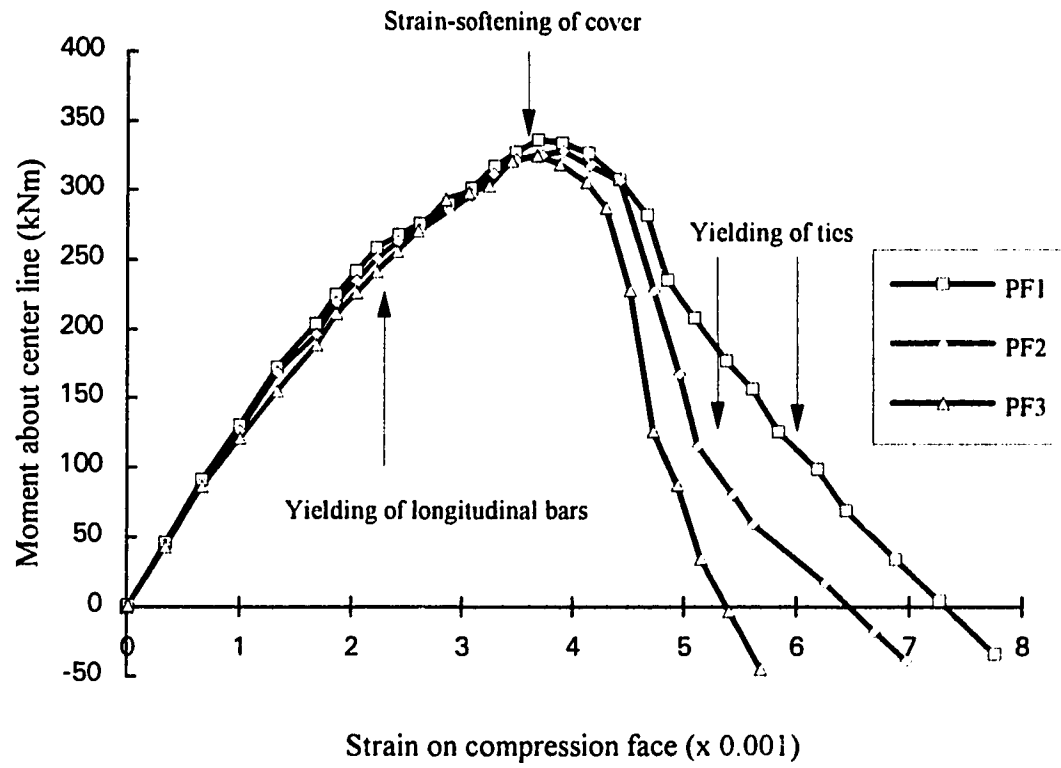Fig.5.12   Axial load vs strain on compression face for Series PD

Fig.5.13 Moment vs strain on compression face for Series PF
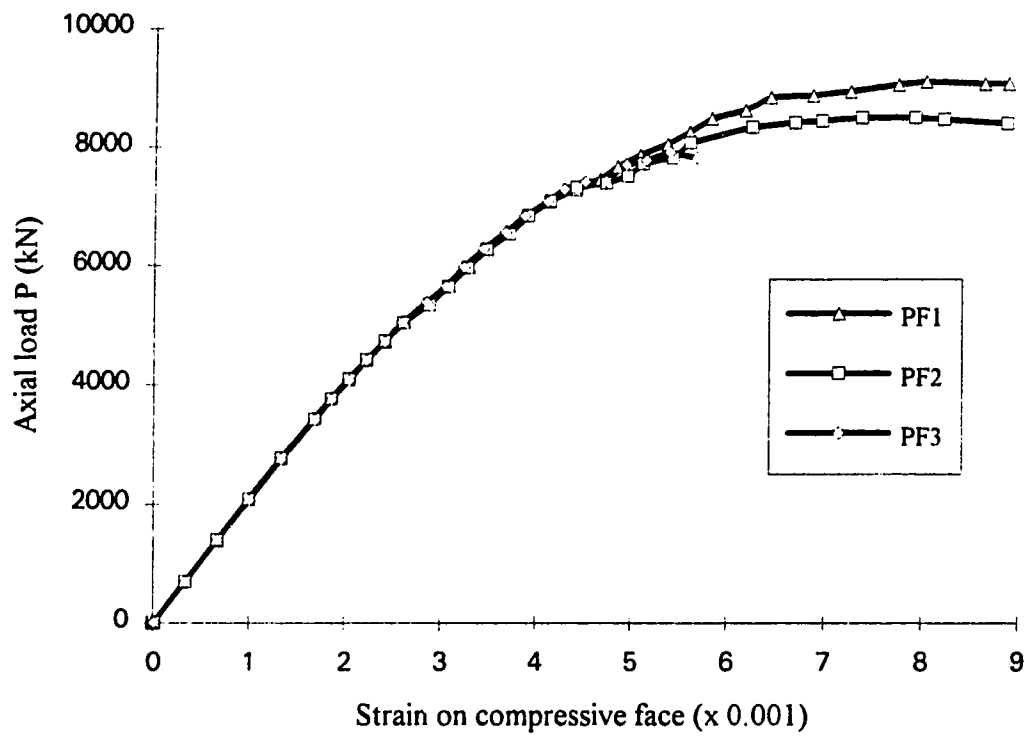
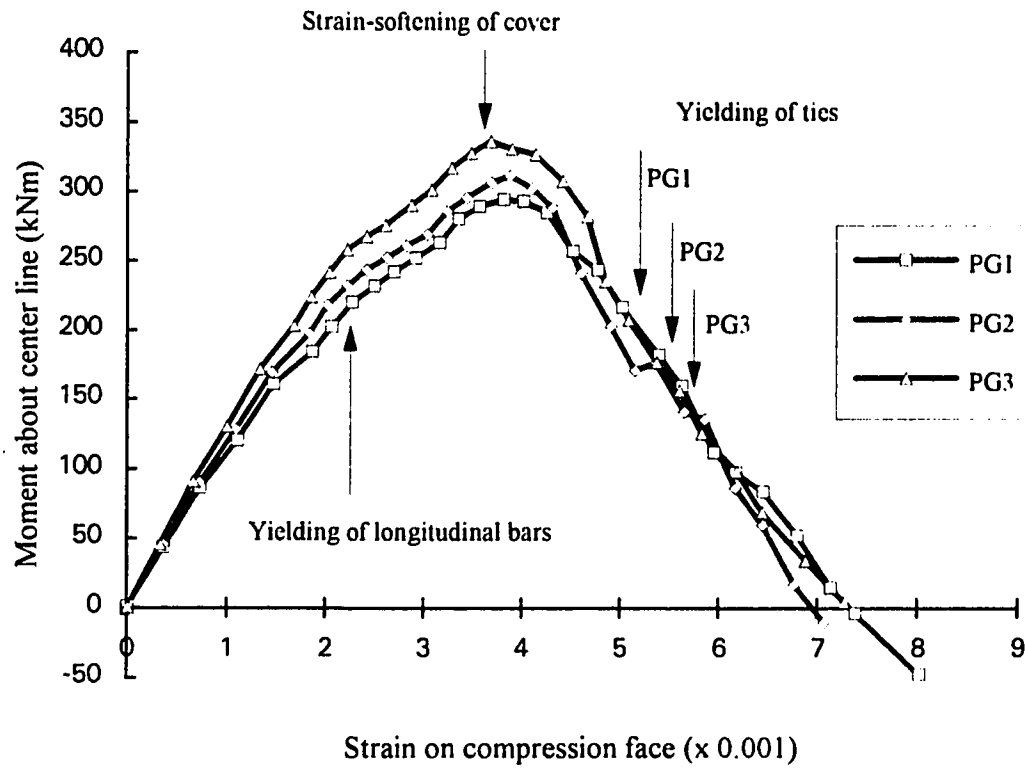Fig.5.14 Axial load vs strain on compression face for Series PF

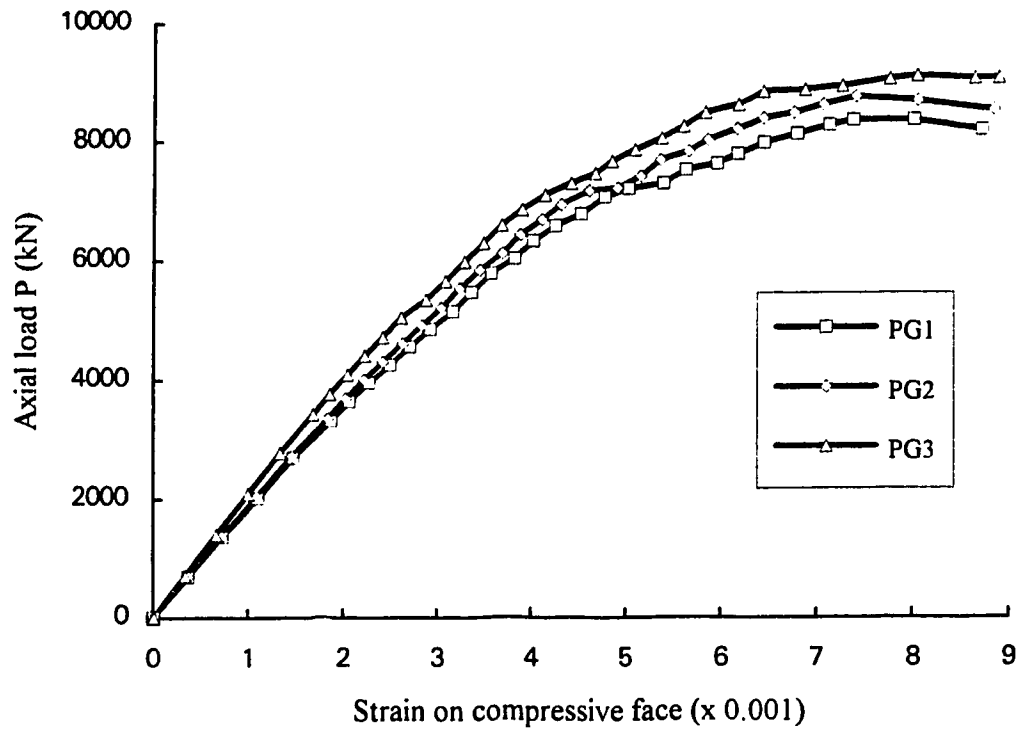Fig.5.15   Moment vs strain on compression face for Series PG

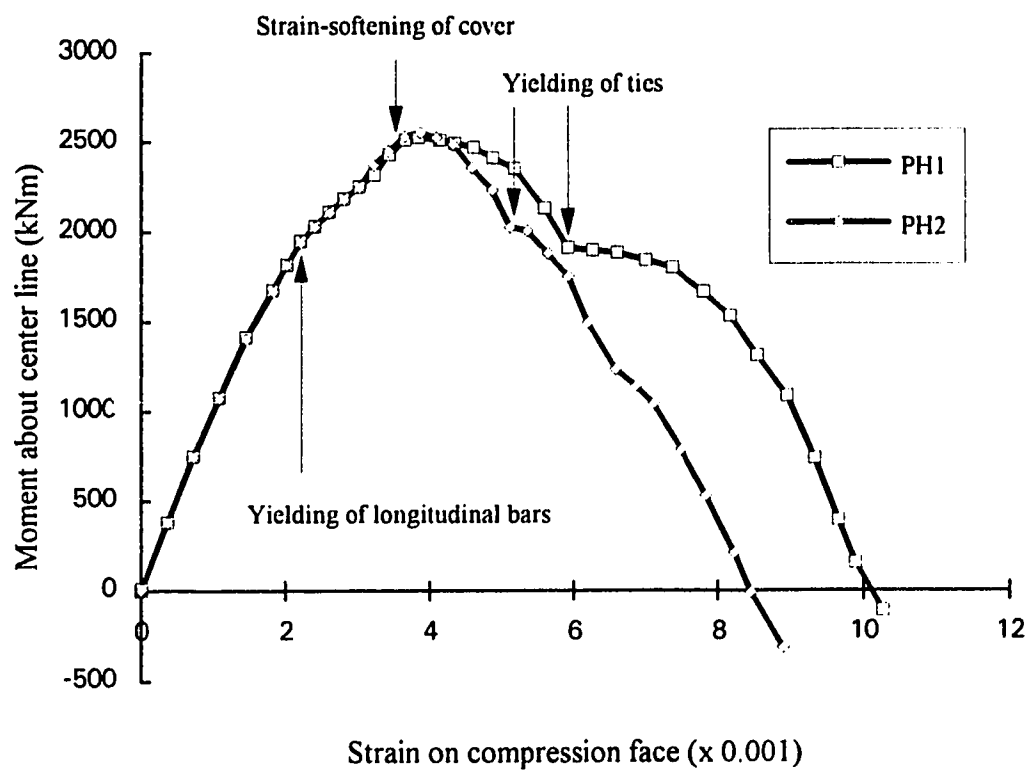Fig.5.16 Axial load vs strain on compression face for Series PG

133

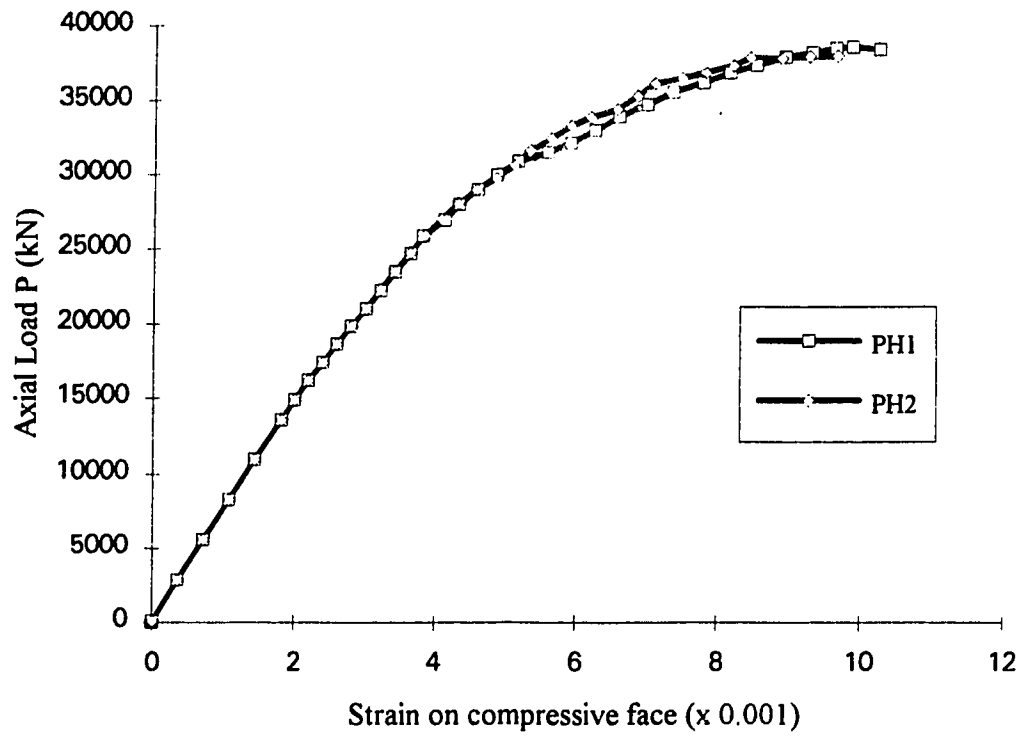Fig.5.17  Moment vs strain on compression face for Series PH

134

Fig.5.18   Axial load vs strain on compression face for Series PH

# CHAPTER SIX

# EXAMINATION OF ACI DESIGN CODE FOR CONCRETE COLUMNS

## 6.1 Introduction

The outline of the ACI Code sections related to seismic design of tied concrete columns has been reviewed in Chapter 5. The existing codes were based on experiments and engineering practice for low and medium strength concrete. Therefore, more research is needed to study the applicability of the codes to high strength concrete members. For instance, a rectangular stress block is recommended for the flexural strength design of concrete members by most current design codes (e.g. US Code ACI 318-89 and Canadian Code CAN3-A23.3-M84). The validity of the assumed rectangular stress block is questioned as it was based on the stress-strain response of low and medium strength concrete.

A parametric study of tied high strength concrete columns has been conducted in Chapter 5. The behavior of concrete columns with variable parameters has been qualitatively discussed in the same chapter. The results of the parametric study provide a background for examining the performance of existing design code guidelines related to tied high strength concrete columns.

This chapter starts with a review of the ACI assumed stress block and interaction diagrams for the strength design of concrete columns. The moment versus axial load response curves from the parametric study are presented, along with moment versus axial load interaction curves predicted by the code. A comprehensive discussion of the numerical results is carried out to examine the performance of the design codes.

## 6.2 ACI Stress Block and Interaction Diagrams

The ACI Code sections related to seismic design for tied concrete columns has been reviewed in Chapter 5, including the distribution of longitudinal reinforcement and the distribution of transverse reinforcement. Most design codes use an assumed rectangular stress block involving a number of stress block parameters (e.g. $K_1$, $K_2$ and $K_3$) in the assessment of the flexural strength. A schematic representation of the stress block is shown in Fig.6.1(c). As shown in the figure, the parameter $K_1$ is defined as the ratio of the average compressive stress to the maximum compressive stress. The parameter $K_2$ is the ratio of distance between the extreme fiber and the resultant of compressive stress to distance between the extreme fiber and the neutral axis. The parameter $K_3$ is the ratio of the maximum compressive stress to the cylinder strength.

The ACI 318-89 and the CAN3-A23.3-M84 Codes use a simplified set of stress block parameters based on the rectangular stress block. By keeping the resultant of the forces in the middle of the assumed rectangular stress block, the rectangular stress block is defined by two parameters only $K_1$ and $K_3$. Here $K_2$ is equal to $K_1/2$.

In the codes, the parameter $K_3$ is assumed to have a constant value of 0.85. The parameter $K_1$ is equal to 0.85 for concrete uniaxial compressive strengths, $f_c'$, up to 30 MPa and is reduced continuously at a rate of 0.08 for each 10 MPa of strength in excess of 30 MPa. The parameter $K_1$ is not taken less than 0.65. The codes also assume a constant value of 0.003 for the limiting compressive strain $\varepsilon_u$.

From the equilibrium of the external and internal loads, the axial load and the moment about the central line of an unreinforced column with zero strain on one face can be determined as:

$$P = C = K_1 K_3 f_c' b h \tag{6.1}$$

$$M = P(0.5 - K_2)h \tag{6.2}$$

in which $b$ is the width of cross-section, and $h$ is the height of the compression zone.

For a concrete column subjected to an axial load and a bending moment, an interaction diagram for the cross-section can be generated based on the strain compatibility assumption. The procedure involves assuming a series of strain distributions, each corresponding to a particular point on the interaction diagram, and computing the corresponding values of the axial load $P$ and moment $M$. Once enough such points have been computed, the results are summarized in an interaction diagram. Details of the computing procedure are given by MacGregor (1992).

The interaction diagrams used in the following discussions are generated based on the strain compatibility assumption and are noted as the ACI predictions.

## 6.3  Interaction Diagrams: Numerical Results and ACI Predictions

The moment versus axial load response curves from the parametric study are presented in Figs.6.2 to 6.10 for Series PA, PB, PE, PC, PV13, PD, PF, PG and PH respectively. The interaction curves of the ACI predictions are also included in all figures.

The response curves have a similar shape for most specimens in the parametric study. The moment versus axial load response curve starts with a linear part, indicating that the column is primarily subjected to a nearly constant eccentric load at the beginning. Because of the special loading strategy used, which imposes a triangular axial strain distribution with zero strain on the tension face, the height of the compression zone is held equal to the height of the cross-section. With increases in the axial strain, the stress distribution over the cross-section changes from a linear triangle to a non-linear variation. As the cover experiences strain-softening, the maximum compressive stress in the nonlinear stress distribution shifts from the extreme fiber to a point inside the core. Therefore, the numerical moment versus load response curve bends upwards instead of downwards as usually displayed for slender columns under an eccentric load where deflections cause an increase in moments. The moment peak occurs ahead of the axial load peak. In the post-peak regime of moment, the axial load is generally quite steady with decreasing moment.

Although the ACI prediction is based on the failure of the cross-section, it does not enclose the response curves generated numerically except for Series PV13. The ACI

approach represents the point at the moment peak with the limit strain $\varepsilon_u$ assumed to be 0.003. The moment versus axial load response curve from the finite element analysis represents a complete moment versus axial load response with the strain on the compression face varying from 0.0038 at the moment peak to 0.007 in the post-peak regime. This allows a triaxial stress state redistribution over the cross-section if the column is well confined. The stress redistribution usually results in a lower moment capacity and at the same time a higher axial load capacity. This did not occur for Series PV13 due to the poor confinement. The response curves, in this case, fall inside the ACI predicted interaction curve.

## 6.4 Numerical Results Compared with Code Predictions

A schematic representation of the moment versus axial load response curves and interaction curves are schematically represented in Fig.6.11, in which the solid curve is the finite element analysis result, the dashed curve is the ACI prediction. As mentioned in Section 6.2, the ACI interaction curve was obtained by assuming different linear axial strain distributions with the strain on the compression face always equal to 0.003. Hence, there is only one point (denoted as Point C) in the ACI interaction curve that has the strain on the compression face equal to 0.003, while the strain on the tension face is equal to zero. Since all specimens of the parametric study are subjected to a linear triangular strain distribution, the Point C (with moment of $M_c$ and axial load of $P_c$) can be used as the ACI predicted failure point.

Discussion of the behavior of a concrete column is usually made on two aspects, the strength and the ductility.

For the discussion of column strength, two points (Point 1 and Point 3) are of interest. Point 1 (with moment $M_1$ and axial load $P_1$) has the maximum moment capacity, while Point 3 (with moment $M_3$ and axial load $P_3$) has the maximum axial load capacity. Therefore, $M_1$ is the maximum moment capacity and $P_3$ is the maximum axial load capacity for a column.

In order to discuss the ductility of a column, Point 2 is introduced which has a moment $M_2$ equal to 50% of the maximum moment capacity $M_1$. The ratio of the axial load at Point 2 to the axial load at Point 1, $P_2/P_1$, can be used as an indicator of the ductility behavior.

Another ductility measure is the energy absorbed over the failed cross-section before a complete collapse of a column. The instant of a complete collapse can be thought of as the point at which the moment capacity drops to zero. The strain at the compression face related to that point is noted as $\varepsilon_{cf}$ in Fig. 6.12A.

Figs.6.12A and 6.12B are schematic representations of moment and axial load response versus the strain on the compression face. The energy absorbed can be divided into two parts, the moment energy absorbed, $W_m$, and the axial load energy absorbed, $W_p$. These two parts can be computed using numerical integration:

$$W_m = \frac{1}{d} \int_0^{\varepsilon_{cf}} M d\varepsilon_c \qquad \text{(per unit length)} \qquad (6.3)$$

$$W_p = \frac{1}{2} \int_0^{\varepsilon_{cf}} P d\varepsilon_c \qquad \text{(per unit length)} \qquad (6.4)$$

in which $d$ is the depth of the cross-section and $\varepsilon_c$ is the strain on the compression face.

The total energy absorbed can be computed by:

$$W_{total} = W_m + W_p \qquad (6.5)$$

The moment and axial load values at Points 1, 2 and 3 of the parametric study are presented in Table 6.1 with the ACI predictions $M_c$ and $P_c$ as references. The energies absorbed, $W_m$ and $W_p$ are also included in the same table.

The results will also be presented graphically in order to reach a better understanding of the problem.

For Series PA, PB, PC and PD, the parameters involved are tie configuration, tie size, tie yield strength and concrete strength. The tie spacing is adjusted from 20mm to 80mm such that the equivalent transverse reinforcement ratio $\rho_t$ is a constant. Therefore, the results of these four series can be presented in the same figure with the tie spacing as the variable. The values of $M_1/M_c$, $P_1/P_c$, $P_3/P_c$, $P_2/P_1$ and $W_{total}$ are presented in Figs.6.13, 6.14, 6.15, 6.16 and 6.17 respectively. The data point for Specimen PA3 is plotted at tie spacing 80mm, and for Specimen PA4 at 81mm (80mm in real) to distinguish between them.

As shown in Figs.6.13 and 6.14, all but Specimen PD1 (with concrete strength of 37.5 MPa) have the peak moment lower than the ACI predicted value. The ratio $M_1/M_c$ varies from 0.897 to 0.922 with exception of 1.061 for Specimen PD1 and 0.939 for Specimen PD2. Not withstanding the constraints on load path, this suggests that although the current ACI Code interaction diagrams work well for low strength concrete columns, they may be unconservative for high strength concrete columns. A different series with constant eccentricity may be necessary to test this statement.

For Series PA, PB and PC, the peak moment decreases only slightly with increasing spacing of ties with exception of Specimen PA4. The values of $M_1/M_c$ are between 0.897 and 0.922. The lowest value belongs to Specimen PA3 which has the poorest tie configuration among this group. As discussed in Chapter 4, columns with larger tie spacing may experience the strain-softening of the cover a little earlier due to the fact that the strain-softening pattern is usually developed between ties at the beginning. But generally speaking, the effect of transverse reinforcement on the pre-peak moment behavior and moment peak is very minor.

As shown in Fig.6.15, the peak axial load value decreases with increasing spacing of ties with exception of Specimen PA4. For columns with larger tie spacing, the strain-softening pattern between ties may penetrate a little further into the core than ones with smaller tie spacing. This results in a reduction of axial load capacity for columns with large tie spacing. For most specimens, the axial load peak is related to the near zero moment.

From Figs.6.16 and 6.17, both $P_2/P_1$ and $W_{total}$ values decrease with increasing spacing of ties except for Specimen PA4. This suggests that columns with large tie spacing may experience poorer ductility behavior in the post-peak regime.

Specimen PA4, with rectangular and diamond-shaped ties, has higher $M_1/M_c$ and $P_2/P_1$ values than Specimens PA2 and PA3 and higher $W_{total}$ value than Specimen PA3. This suggests that the tie configuration for Specimen PA4 is approaching an optimum. The 20mm tie spacing of Specimen PB1 is considered impractical.


*Series PE*

For Series PE, the tie spacing is kept constant at 80mm, while the tie size is the only variable which changes from 50 to 200mm$^2$. As discussed in Chapter 5, Specimens PE1 and PE2 do not meet the ACI Code seismic design requirement of transverse reinforcement. The values of $M_1/M_c$, $P_1/P_c$, $P_3/P_c$ and $P_2/P_1$ are presented in Fig.6.18. The energies absorbed, $W_m$, $W_p$ and $W_{total}$ are presented in Fig.6.19.

As shown in Fig.6.18, the $M_1/M_c$, $P_1/P_c$ values are almost the same for all three specimens in this series. This suggests that the tie size has little effect on the first moment peak if the tie spacing is maintained as a constant. The ACI code prediction is unconservative as the $M_1/M_c$ value is under 1.0.

On the other hand, as expected, the values of $P_3/P_c$, $P_2/P_1$ and $W_{total}$ decrease with decreasing tie size. If the ACI Code seismic requirement of transverse reinforcement is not met, the ductility of concrete columns in the post-peak regime is the main concern in the structural design.

It is interesting to note that the peak of axial load for Specimens PE1 and PE2 (Fig. 6.4) is not related to the near zero moment. These two specimens collapse before a complete stress redistribution is achieved due to the low degree of confinement.

For Series PF, the tie spacing is a constant of 80mm, while the cover depth is the only variable which changes from 20 to 40mm with the equivalent transverse reinforcement ratio maintained as a constant. The values of $M_1/M_c$, $P_1/P_c$, $P_3/P_c$ and $P_2/P_1$ are presented in Fig.6.20. The energies absorbed, $W_m$, $W_p$ and $W_{total}$ are presented in Fig.6.21.

As shown in Fig.6.20, the $M_1/M_c$, $P_1/P_c$ values are almost the same for all three specimens in this series. This suggests that the cover depth has little effect on the first moment peak. The ACI code prediction is unconservative as the $M_1/M_c$ value is under 1.0. However, the values of $P_3/P_c$, $P_2/P_1$ and $W_{total}$ decrease with increasing cover depth. Columns with larger depth of cover usually have a smaller confined volume of the core. The behavior of the columns becomes brittle when the cover is lost in the post-peak regime.

According to Yong's (1988) observation, the axial load capacity and the ductility were not affected by cover depth as all specimens failed with a single shear failure plane. Yong's tests were on the concentrically loaded concrete columns with unconfined or poorly confined conditions (lateral steel volume ratio was from zero to 0.0164). The parametric study here involved eccentrically loaded columns with well confined conditions (the lateral steel volume ratio was around 0.0333). The failure of columns here seems to be related to the spalling of cover and yielding of ties. More research is needed on the changing of failure mode with increasing cover depths.

*Series PG*

For Series PG, the tie spacing is a constant of 80mm, while the amount of longitudinal reinforcement is the only variable which changes from 1500 to 4000mm$^2$. The values of $M_1/M_c$, $P_1/P_c$, $P_3/P_c$ and $P_2/P_1$ are presented in Fig.6.22. The energies absorbed, $W_m$, $W_p$ and $W_{total}$ are presented in Fig.6.23.

As shown in Figs.6.22 and 6.23, there is only a small variation of $M_1/M_c$, $P_1/P_c$ and $P_2/P_1$ values with increasing amounts of longitudinal reinforcement. The changing of $W_{total}$ is also not significant. Since the $M_c$, $P_c$ values are different for all three specimens, the ACI code prediction is very consistent for this series with different layouts of longitudinal reinforcement.

The distribution of longitudinal bars was constant in this series. Also, the flexural stiffness of longitudinal bars was not included in the analytical model. Therefore, the study here could not confirm Yong's (1988) observation on axially loaded columns that increasing the number of longitudinal bars and distributing them around the core perimeter increased the effectiveness of the confinement of the concrete core.

*Series PV13*

For Series PV13, the tie spacing is a constant of 100mm, while the yield strength of the ties is the only variable which changes from 401 to 800MPa. All specimens in this series do not meet the ACI Code seismic design requirement of transverse reinforcement. The values of $M_1/M_c$, $P_1/P_c$, $P_3/P_c$ and $P_2/P_1$ are presented in Fig.6.24. The energies absorbed, $W_m$, $W_p$ and $W_{total}$ are presented in Fig.6.25.

As shown in Figs.6.24 and 6.25, the strength of ties has no effect on the moment peak values $M_1/M_c$ and $P_1/P_c$ as the tie has not yielded then. Because it had the lowest equivalent transverse reinforcement ratios, this series had the lowest $M_1/M_c$ value among all analyzed specimens. The strength of ties has an effect only on the post-peak behavior of columns. The values of $P_3/P_c$, $P_2/P_1$ and $W_{total}$ increase with increasing strength of ties. Therefore, an increase in the yield strength of ties with everything else held constant improves the ductility behavior of columns.

It is interesting to note that some of Cusson et al. (1994) tests on axially loaded columns had the yielding of ties before or near the occurrence of strain-softening of covers. Under this kind of circumstances, the yield strength of ties could affect both the strength and ductility if the column is well confined.

There are only two specimens in Series PH. The results can be readily observed in Table 6.1 and are not presented graphically. The behavior of the two specimens is almost the same except for the post-peak regime. Specimen PH2 has lower values of $P_3/P_c$, $P_2/P_1$ and $W_{total}$ than Specimen PH1. The increase in the tie spacing led to poorer post-peak ductility performance. The ACI prediction of moment capacity is unconservative for Series PH. The $M_1/M_c$ value is 0.896, the lowest among all specimens except for Series PV13.

## 6.5 Examination of ACI Stress Blocks

The ACI assumed stress block was suggested based on experiments and engineering practice for low and medium strength concrete members. Questions may arise for the applicability of the stress block to high strength concrete members since the ACI code prediction tends to be unconservative as demonstrated in Section 6.4.

The behavior of low and high strength concretes differs in both the pre-peak and the post-peak uniaxial compression response. Usually, high strength concrete has less plastic strain in the pre-peak regime. Therefore, the pre-peak uniaxial compression stress versus strain curve is more linear for high strength concrete. Also, high strength concrete has a steeper descending behavior in the post-peak regime.

As observed in the finite element analysis, the moment peak is usually reached when the cover starts to experience strain-softening. The distribution of axial stress at the moment peak (Point 1) is crucial in examining the authenticity of the assumed stress block. On the other hand, the development of strain-softening of the cover is very fast for high strength concrete members. It is also very important to understand the stress distribution in the post-peak regime. Point 2, which has a moment equal to $M_1/2$, can be used to examine the post-peak behavior.

The stress patterns for three specimens of Series PD are discussed here. These three specimens, PD1, PD2 and PD3, represent low, medium and high strength concrete

columns respectively. The ties were selected to satisfy the ACI Code requirement for seismic columns.

Fig.6.26 shows the axial stress patterns at Point 1 for Specimens PD1, PD2 and PD3, while Fig.6.27 shows the axial stress patterns at Point 2 for these specimens respectively. The stress values are given from four lines of integration points located at varying distances from the vertical mid-plane, at the height nearest to the mid-span section. The line at 162.5 mm from the mid-plane was in the side cover.

As shown in Fig. 6.26, the stress distribution pattern at the moment peak (Point 1) varies with increasing concrete strength. The common feature is that at the moment peak, the cover on the compression face starts to experience strain-softening. For Specimen PD3 with $f_c'$=75MPa, the development of strain-softening of cover is relatively fast. In contrast, for Specimen PD1 with $f_c'$=37.5MPa, the reduction of axial stress in the cover due to strain-softening is less significant at the moment peak.

Another important observation is that for high strength concrete specimens (e.g. PD3), the stress redistribution is relatively more linear from the tension face to the peak point along the compression side of the core. Since the strain distribution imposed is triangular and the triaxial stress state is yet not developed in the pre-peak regime, the stress distribution pattern at the maximum moment reflects the pre-peak uniaxial stress versus strain curve. The lower plastic strain of the material in the pre-peak regime is the main reason for the more linear stress distribution pattern for the high strength concrete member.

In the post-peak regime, however, the stress distribution patterns are more complicated as shown in Fig. 6.27. The cover on the compression side has almost completely fallen off at the stage of Point 2. The side cover has also experienced a severe loss of axial stress due to strain-softening. Meanwhile, a triaxial stress state has developed inside the core. As a result, the axial stress value in some parts of the core is higher than the uniaxial strength. The stress redistribution pattern for Specimen PD1 is relatively uniform within the core zone, as compared with Specimen PD3.

The stress distribution at the moment peak confirms that the height of the assumed rectangular stress block should be reduced with increasing concrete strength. This factor

has been accounted for in the current ACI Code by reducing the $K_1$ value with increasing concrete strength. Fig.6.28 shows the $K_1 K_3$ values from some selected tests (represented by solid symbols) and from this finite element analysis (represented by small circle symbols), along with the ACI Code 318-89 prediction. The finite element predictions were obtained from Eqs. 6.1 and 6.2 with $M$ and $P$ values substituted by $M_1$ and $P_1$. It can be seen that the ACI Code prediction of $K_1 K_3$ is generally lower than the results of tests and analysis, and therefore is on the safe side for the axial load at moment peak.

On the other hand, the ACI Code prediction of the moment capacity is not on the safe side. This is demonstrated by the $K_2$ values in Fig.6.29 with the solid symbols representing test results, small circle symbols representing the finite element analysis, and a dashed line representing the ACI Code prediction. By falling below the test data, the ACI Code predicts values of $K_2$ which are too small. These lead to over-estimates of the lever arm and hence the moment capacity for high strength concretes. The $K_2$ value should be about 0.333 if the axial stress distribution is very close to a triangle. For high strength concrete members, the axial stress in the cover is reduced due to strain-softening at the moment peak. This suggests that the $K_2$ value should be no less than 0.333 for high strength concrete members. However, in the current ACI Code, the equation $K_2=K_1/2$ is used, based on the assumption that the rectangular stress block starts from the compression face. This leads to $K_2=0.325$ if the concrete strength is 75 MPa as used in the parametric study. Therefore, the current ACI Code over-estimates the lever arm of the resultant for high strength concrete sections.

In fact, the equation $K_2=K_1/2$ is not necessary as the assumption of the rectangular stress block starting from the compression face is not necessary. In this study, it is suggested that the $K_2$ value be determined independently from $K_1$ value. The proposed equation for $K_2$ takes the form:

$$K_2 = 0.425 \qquad \text{for } f_c' \leq 30MPa \qquad (6.6A)$$

$$K_2 = 0.457 - 0.00107 f_c' \qquad \text{for } 30MPa \leq f_c' \leq 100MPa \qquad (6.6B)$$

$$K_2 = 0.35 \qquad \text{for } f_c' \geq 100MPa \qquad (6.6C)$$

This proposed equation is represented by a solid line in Fig.6.29.

The predicted moment and axial load values at moment peak using Eq.6.6 are denoted by $M_c^*$ and $P_c^*$. Values of $M_I / M_c^*$ and $P_I / P_c^*$ are computed for some selected tests of Ibrahim and MacGregor (1994) and the finite element analysis here, and are presented in Figs.6.30 and 6.31 respectively. It can be seen that the predicted moment value based on Eq.6.6 is now on the safe side.

## 6.6 Comments on the Performance of ACI Code

Some comments on the performance of ACI Code sections related to tied columns are made based on the observation in the preceding sections.

(1) Generally speaking, the effect of transverse reinforcement on the pre-peak moment behavior and the moment peak is not significant.

(2) Transverse reinforcement has a significant effect on the post-peak moment behavior. The amount of transverse reinforcement required for seismic design in the ACI Code is necessary and also sufficient to ensure a ductile post-peak performance.

(3) The ACI code stress block for the flexural strength design of tied columns is unconservative for high strength concrete members. The assumed rectangular stress block is not realistic for high strength concrete sections. The lever arm of the resultant should be reduced for high strength concrete members if the rectangular stress block is used.

(4) There should be a minimum size limit for a given cover depth in the design of tied columns. Columns with small ratios of core area to gross area should not be proportioned as their post-peak behavior is very poor. There is no need to increase the amount of transverse reinforcement for columns with small core zones. Failure of such columns is usually related to the loss of the cover due to strain-softening before the yielding of ties.

148

Table 6.1   Results of parametric study

| Series | Speci-men | ACI approach $M_c$ (kNm) | ACI approach $P_c$ (kN) | Point 1 $\dfrac{M_1}{M_c}$ | Point 1 $\dfrac{P_1}{P_c}$ | Point 2 $\dfrac{M_2}{M_c}$ | Point 2 $\dfrac{P_2}{P_c}$ | Point 3 $\dfrac{M_3}{M_c}$ | Point 3 $\dfrac{P_3}{P_c}$ | Energy absorbed $W_m$ (kN) | Energy absorbed $W_p$ (kN) |
|---|---|---|---|---|---|---|---|---|---|---|---|
| PA | PA1 | 368 | 5940 | 0.918 | 1.126 | 0.459 | 1.489 | 0.048 | 1.652 | 4.793 | 26.39 |
|  | PA2 | 368 | 5940 | 0.907 | 1.149 | 0.454 | 1.400 | 0.049 | 1.543 | 4.701 | 23.89 |
|  | PA3 | 368 | 5940 | 0.897 | 1.153 | 0.447 | 1.356 | 0.000 | 1.460 | 3.756 | 18.61 |
|  | PA4 | 368 | 5940 | 0.916 | 1.126 | 0.458 | 1.473 | 0.150 | 1.518 | 4.188 | 21.58 |
| PB | PB1 | 368 | 5940 | 0.922 | 1.126 | 0.461 | 1.573 | 0.033 | 1.703 | 5.317 | 32.18 |
|  | PB2 | 368 | 5940 | 0.918 | 1.126 | 0.459 | 1.489 | 0.048 | 1.652 | 4.793 | 26.39 |
|  | PB3 | 368 | 5940 | 0.914 | 1.127 | 0.457 | 1.370 | 0.012 | 1.503 | 3.929 | 20.98 |
| PC | PC1 | 368 | 5940 | 0.918 | 1.126 | 0.459 | 1.489 | 0.048 | 1.652 | 4.793 | 26.39 |
|  | PC2 | 368 | 5940 | 0.918 | 1.152 | 0.459 | 1.464 | 0.095 | 1.565 | 4.447 | 23.57 |
|  | PC3 | 368 | 5940 | 0.902 | 1.146 | 0.451 | 1.329 | 0.029 | 1.493 | 4.139 | 21.56 |
| PD | PD1 | 181 | 3980 | 1.061 | 1.044 | 0.531 | 1.314 | 0.022 | 1.351 | 2.300 | 11.60 |
|  | PD2 | 257 | 4490 | 0.939 | 1.107 | 0.470 | 1.442 | 0.014 | 1.527 | 3.395 | 17.37 |
|  | PD3 | 368 | 5940 | 0.918 | 1.126 | 0.459 | 1.489 | 0.048 | 1.652 | 4.793 | 26.39 |
| PE | PE1 | 368 | 5940 | 0.902 | 1.151 | 0.451 | 1.284 | 0.308 | 1.316 | 3.603 | 15.59 |
|  | PE2 | 368 | 5940 | 0.907 | 1.150 | 0.454 | 1.337 | 0.285 | 1.414 | 3.744 | 17.10 |
|  | PE3 | 368 | 5940 | 0.914 | 1.127 | 0.457 | 1.370 | 0.012 | 1.503 | 3.929 | 20.98 |
| PF | PF1 | 368 | 5940 | 0.914 | 1.127 | 0.457 | 1.370 | 0.012 | 1.503 | 3.929 | 20.98 |
|  | PF2 | 361 | 5960 | 0.912 | 1.143 | 0.456 | 1.274 | 0.048 | 1.397 | 3.371 | 17.20 |
|  | PF3 | 353 | 5990 | 0.911 | 1.149 | 0.456 | 1.237 | 0.098 | 1.297 | 2.946 | 12.40 |
| PG | PG1 | 334 | 5420 | 0.881 | 1.141 | 0.441 | 1.397 | 0.044 | 1.525 | 3.520 | 18.40 |
|  | PG2 | 345 | 5590 | 0.903 | 1.130 | 0.452 | 1.391 | 0.048 | 1.516 | 3.528 | 18.88 |
|  | PG3 | 368 | 5940 | 0.914 | 1.127 | 0.457 | 1.370 | 0.012 | 1.503 | 3.929 | 20.98 |
| PH | PH1 | 2850 | 22900 | 0.896 | 1.128 | 0.448 | 1.656 | 0.055 | 1.682 | 23.69 | 128.7 |
|  | PH2 | 2850 | 22900 | 0.896 | 1.128 | 0.448 | 1.518 | 0.000 | 1.649 | 18.48 | 102.6 |
| PV13 | V13 | 140 | 2590 | 0.841 | 1.053 | 0.421 | 1.058 | 0.266 | 1.087 | 1.327 | 6.00 |
|  | V13A | 140 | 2590 | 0.841 | 1.053 | 0.421 | 1.098 | 0.383 | 1.134 | 1.407 | 7.03 |
|  | V13B | 140 | 2590 | 0.841 | 1.053 | 0.421 | 1.147 | 0.244 | 1.155 | 1.533 | 7.40 |

149
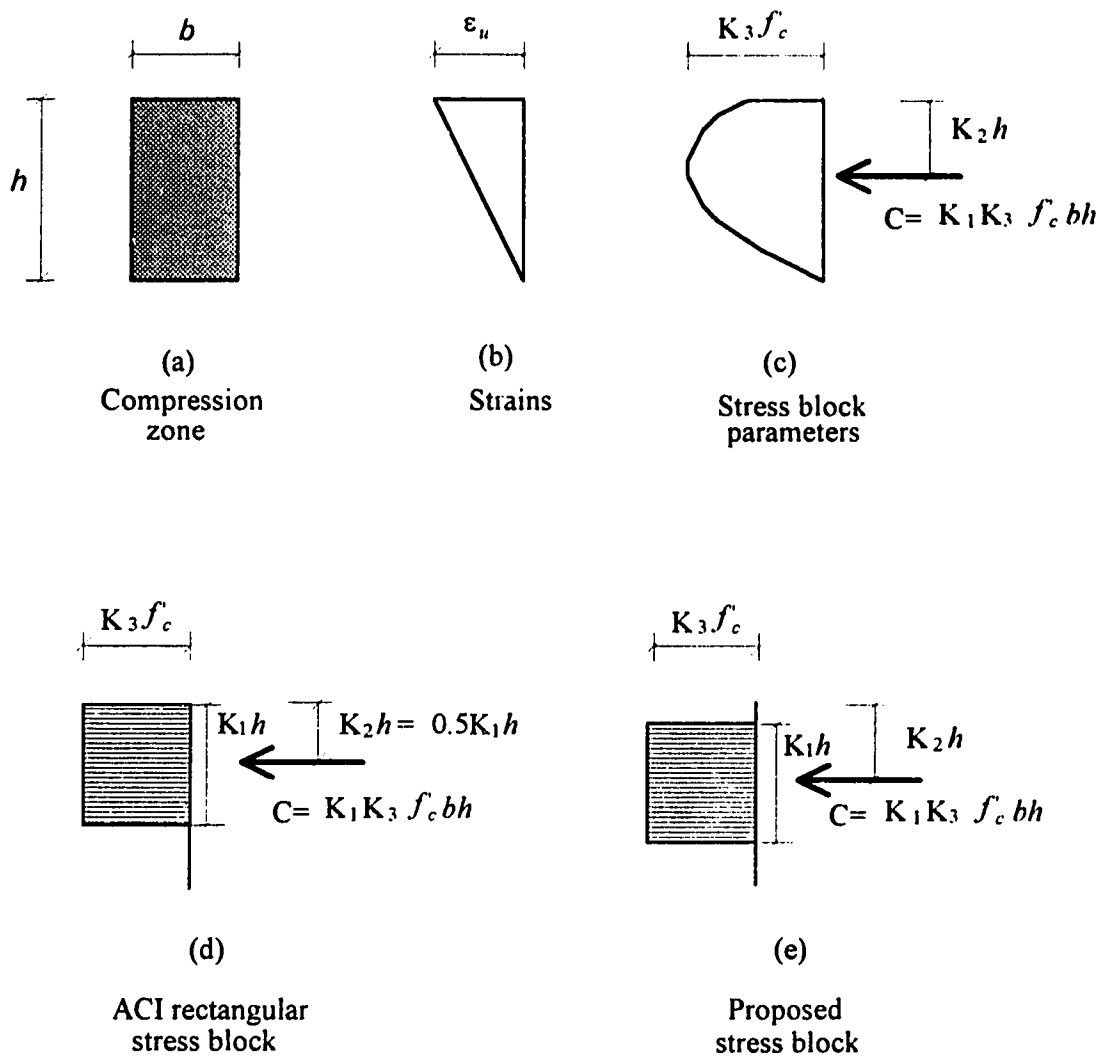
Fig. 6.1   Stress block parameters for the rectangular sections
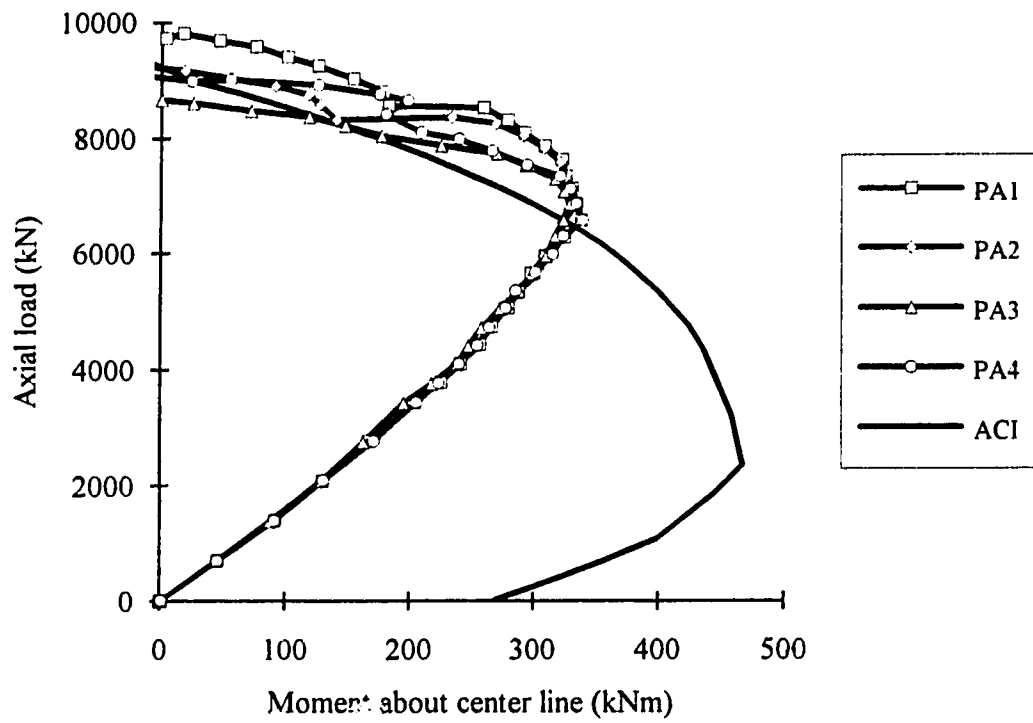
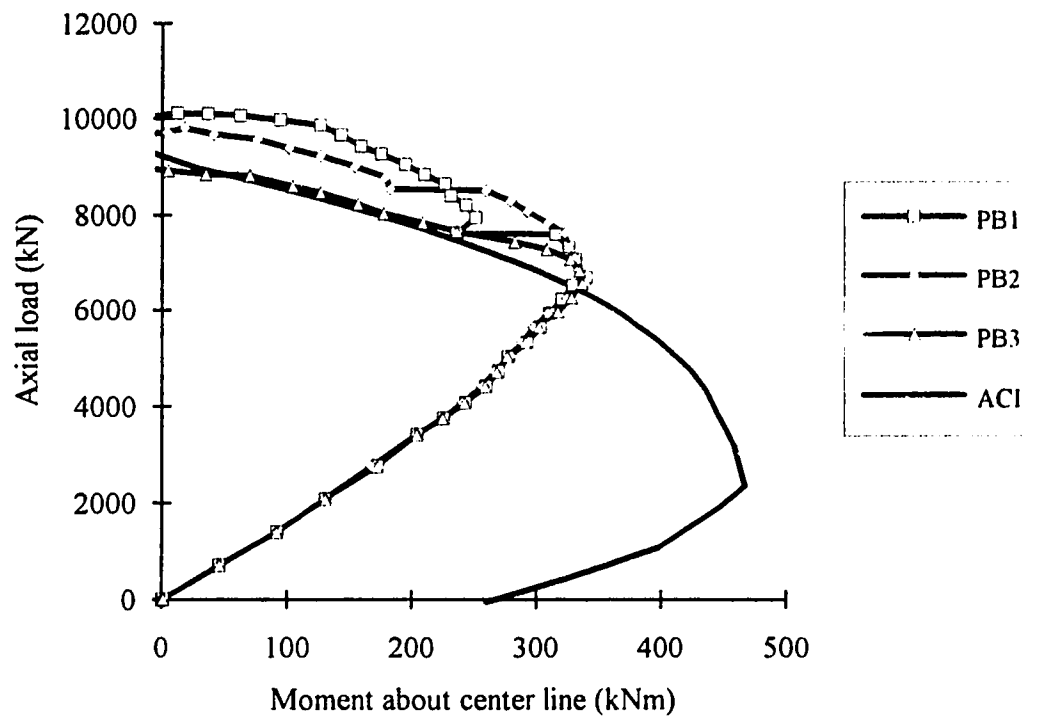Fig. 6.2 Moment vs axial load curves for Series PA

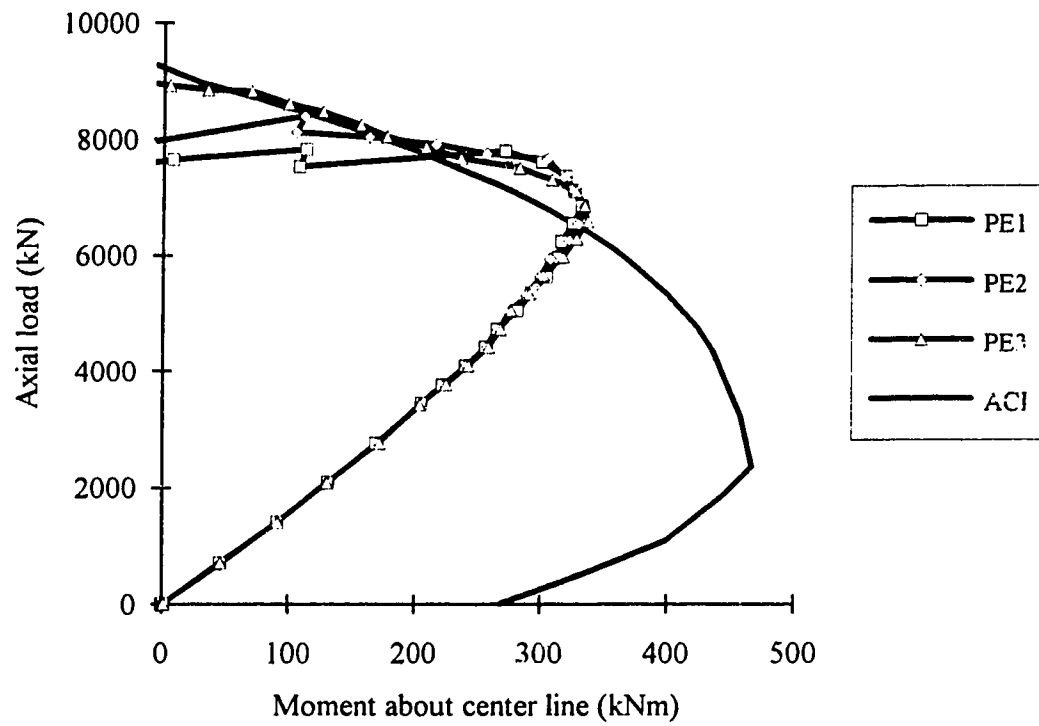Fig. 6.3  Moment vs axial load curves for Series PB

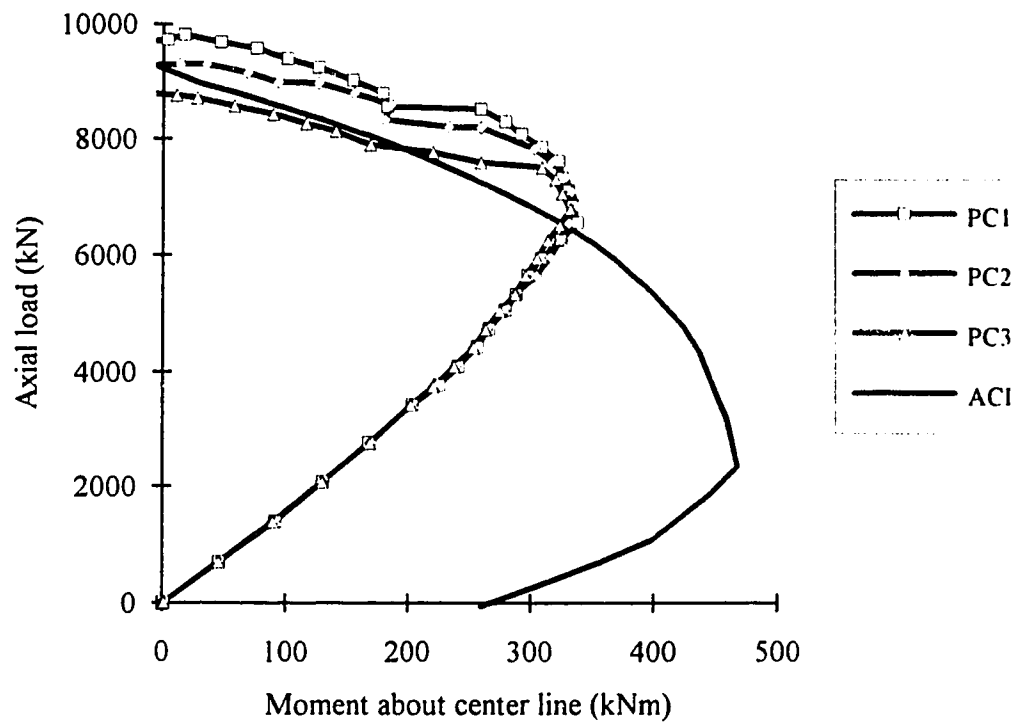Fig. 6.4   Moment vs axial load curves for Series PE
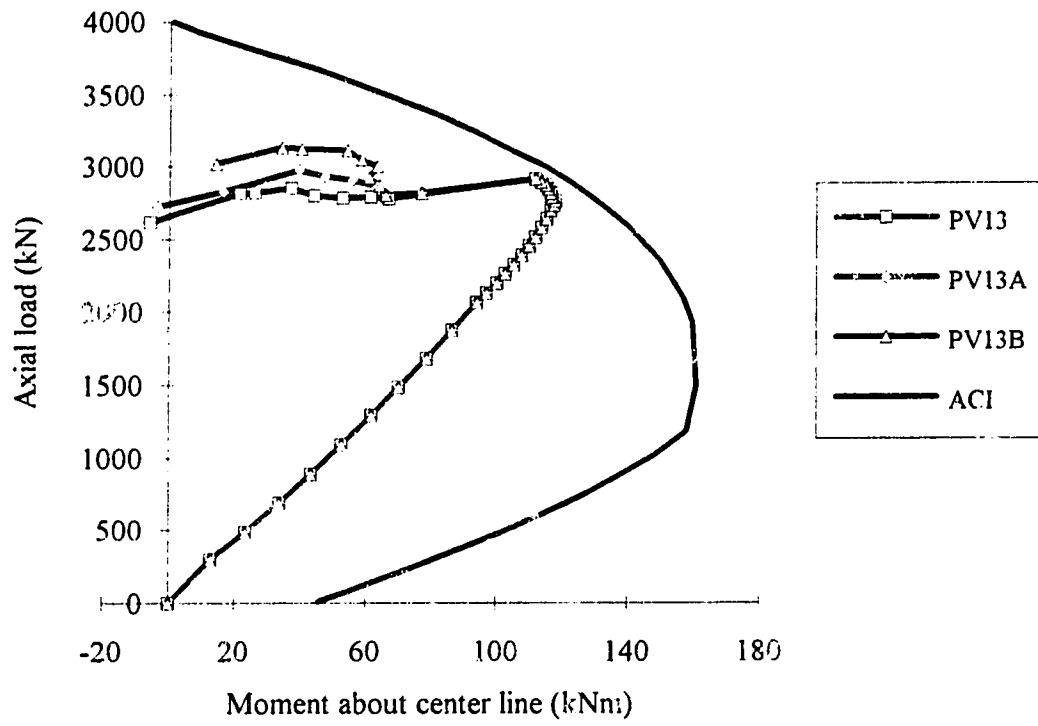
Fig. 6.5 Moment vs axial load curves for Series PC

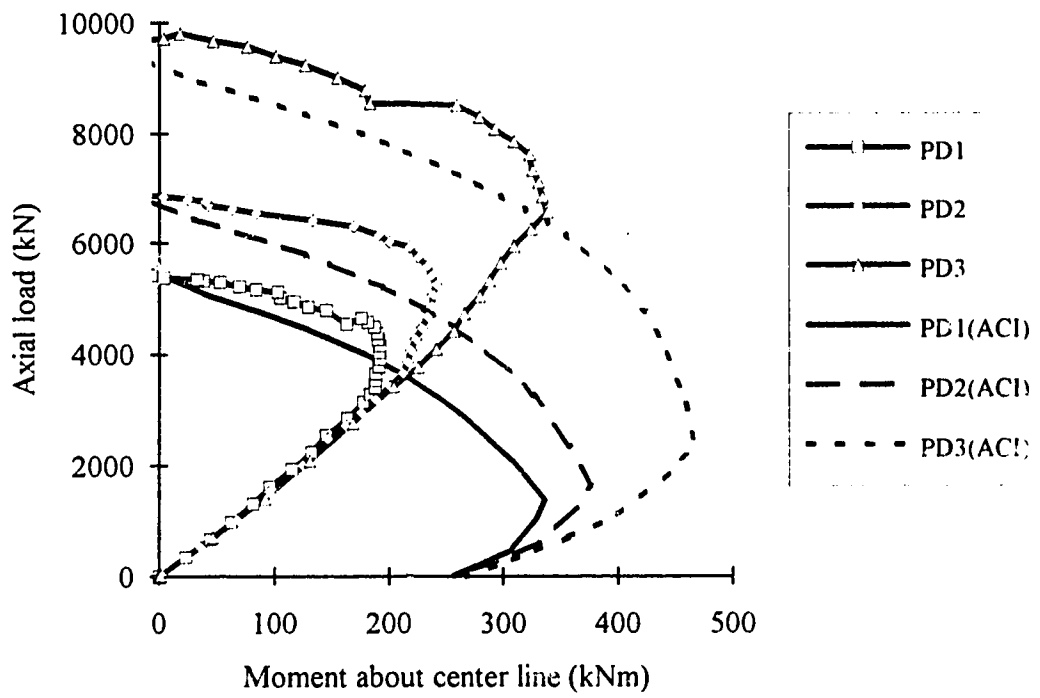154

Fig. 6.6   Moment vs axial load curves for Series PV13

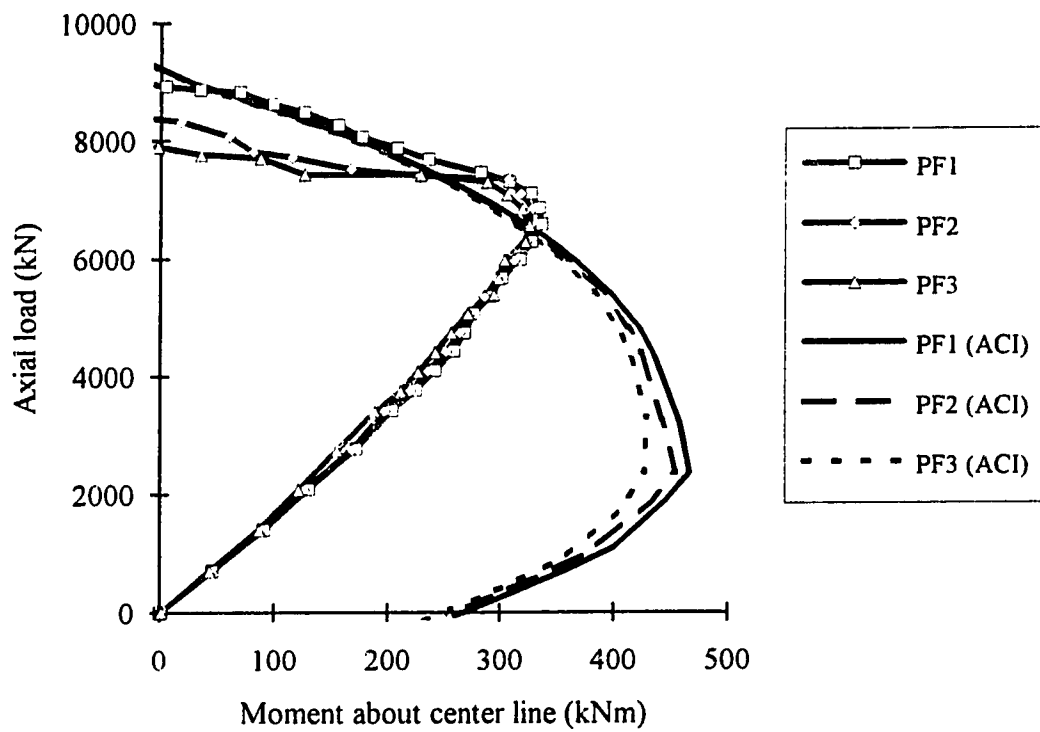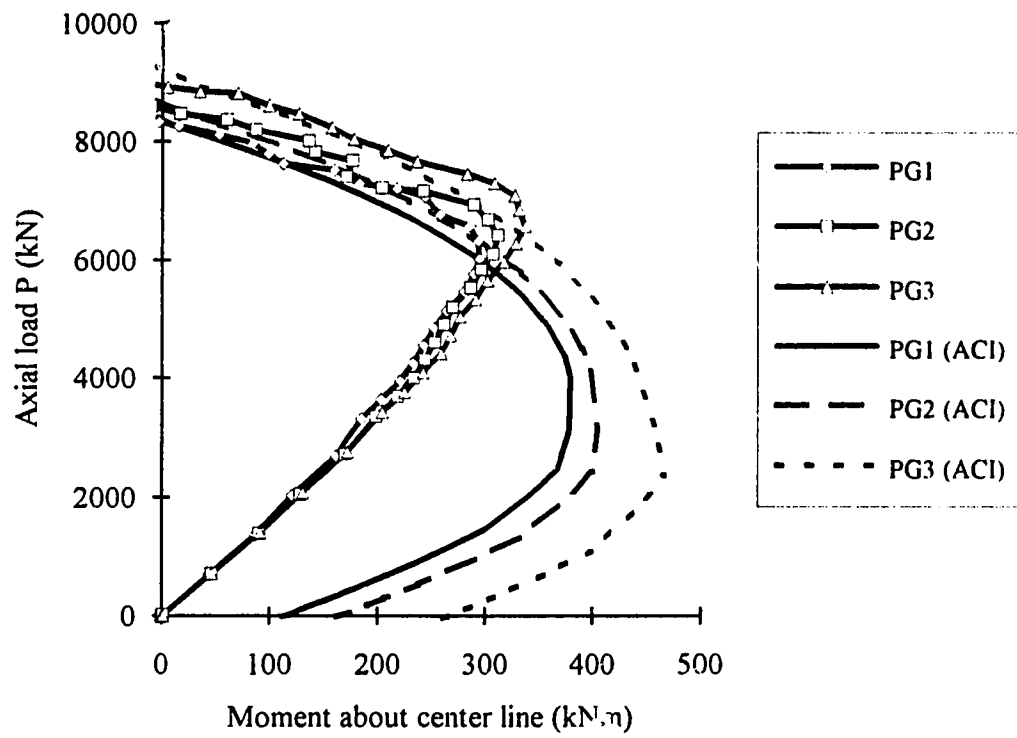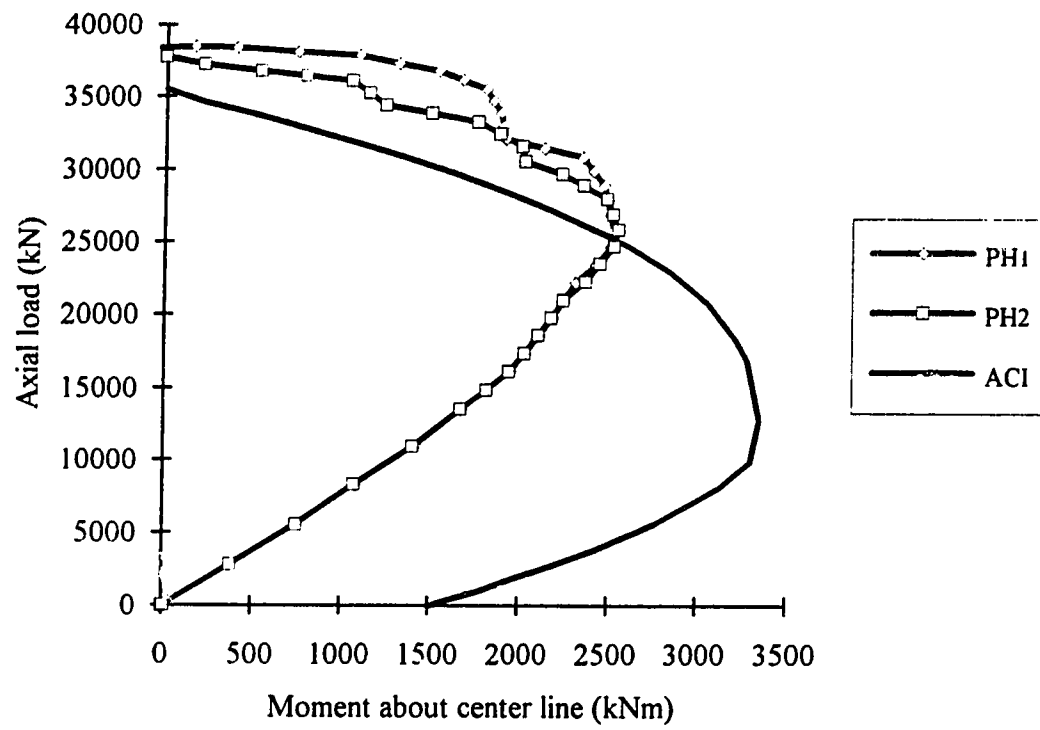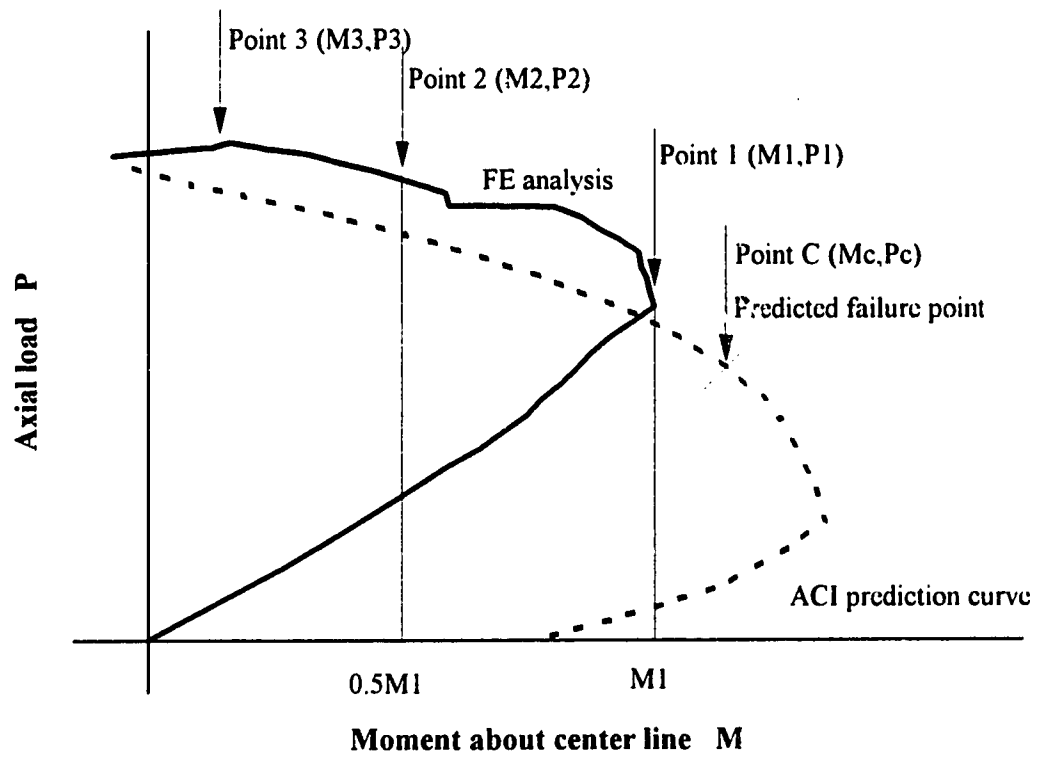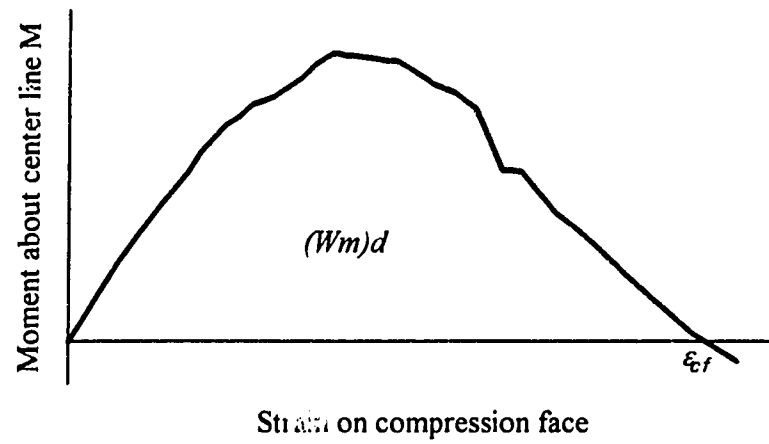Fig. 6.7   Moment vs axial load curves for Series PD

156

Fig. 6.8 Moment vs axial load curves for Series PF

Fig. 6.9 Moment vs axial load curves for Series PG

158

Fig. 6.10 Moment vs axial load curves for Series PH

159

Fig. 6.11  A schematic representation of moment vs axial load curve

160

Fig. 6.12A  A schematic representation of moment vs strain on compression face curve
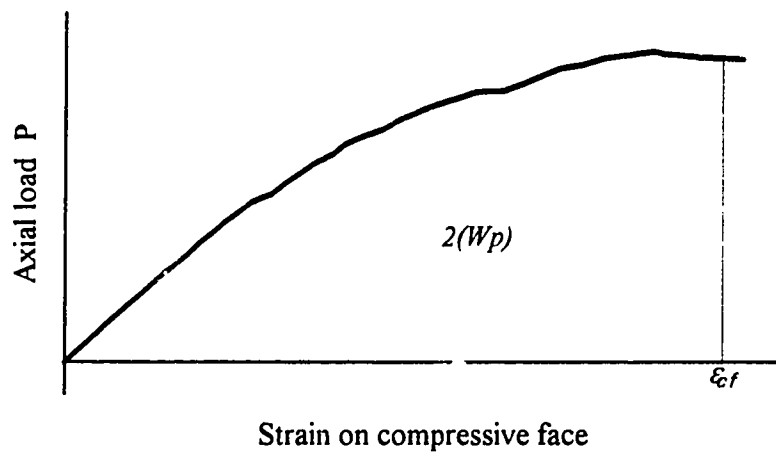


Fig. 6.12B  A schematic representation of axial load vs strain on compression face curve

161
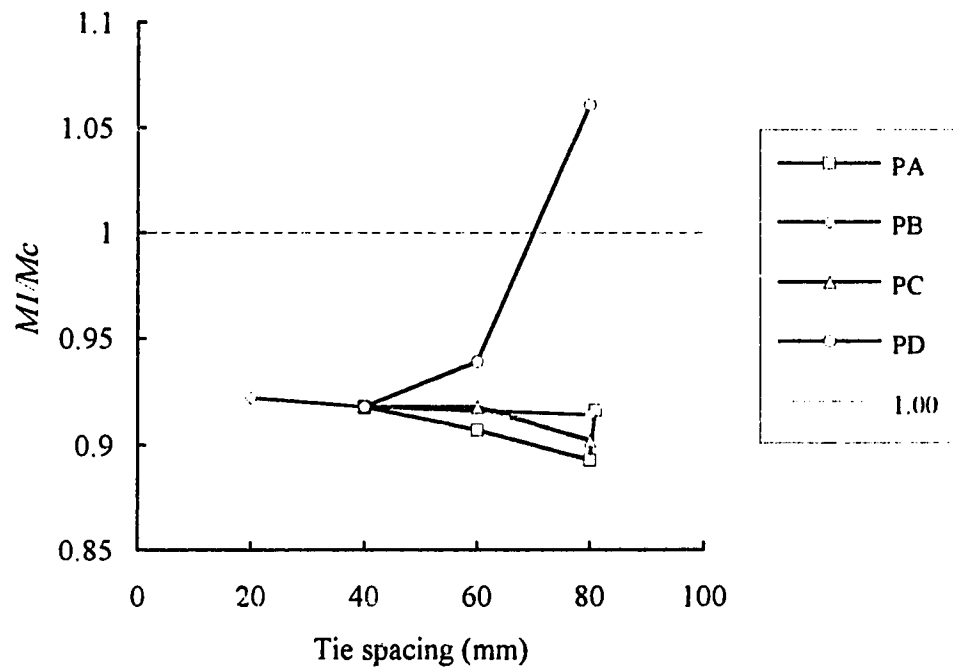
Fig. 6.13 $M_1/M_c$ values for Series PA, PB, PC and PD

162
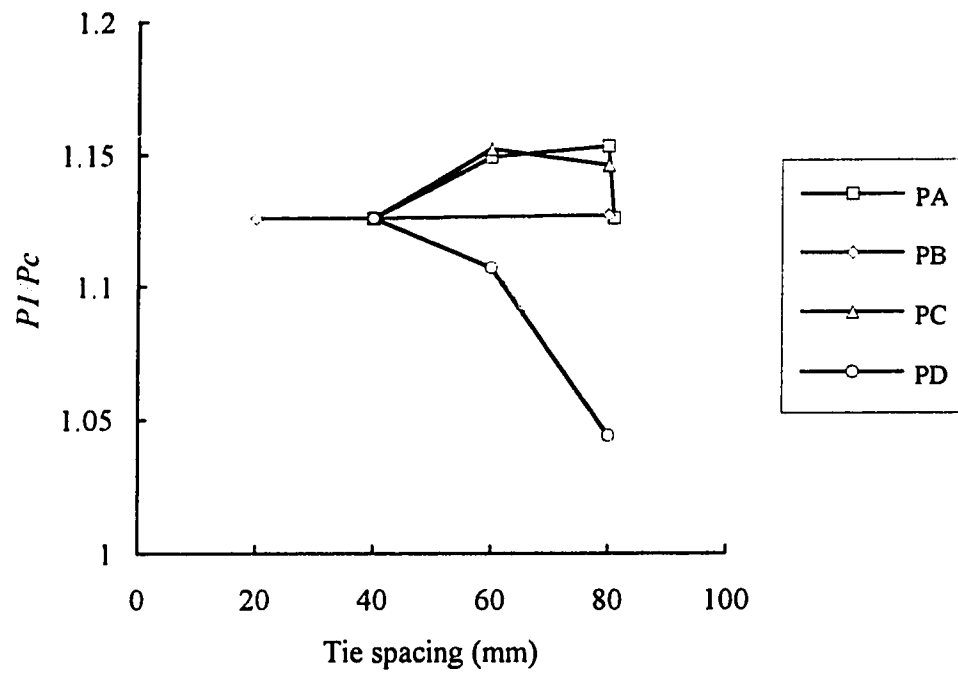
Fig. 6.14 $P_1/P_c$ values for Series PA, PB, PC and PD
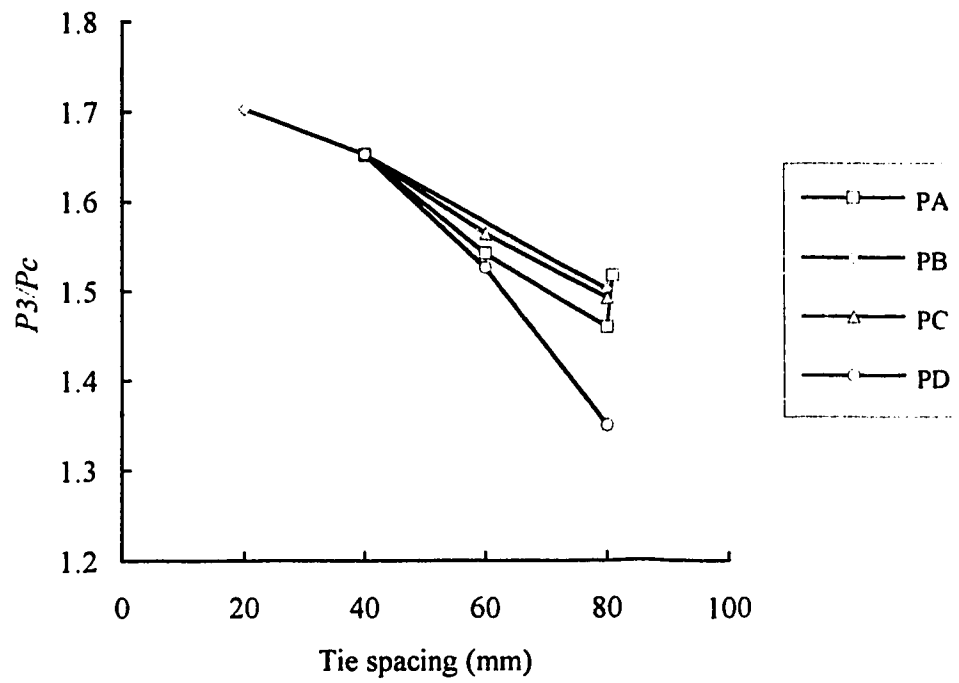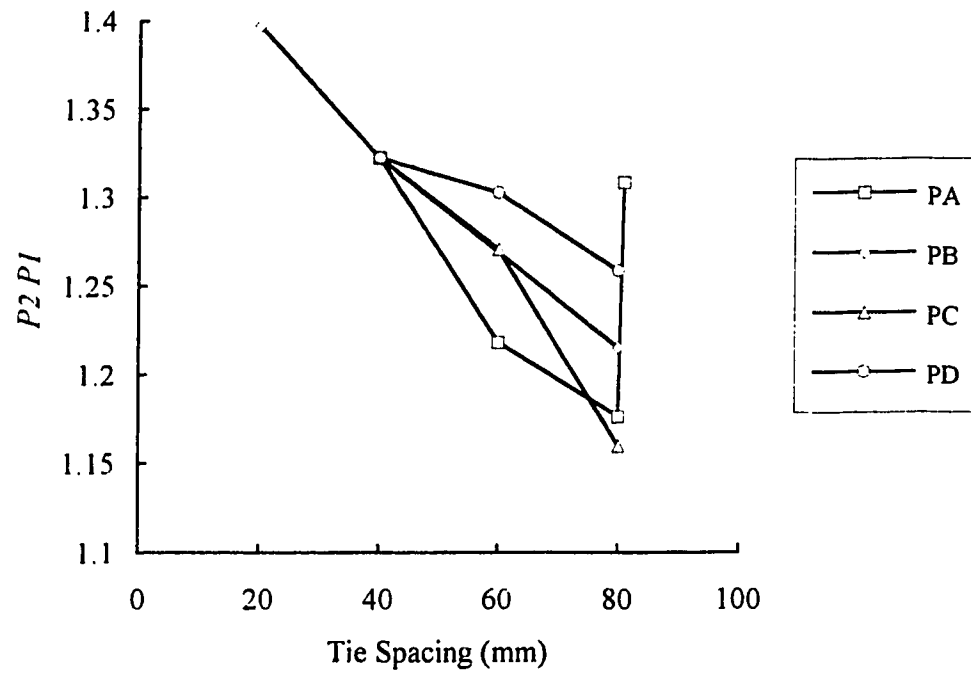
Fig. 6.15 $P_3/P_c$ values for Series PA, PB, PC and PD
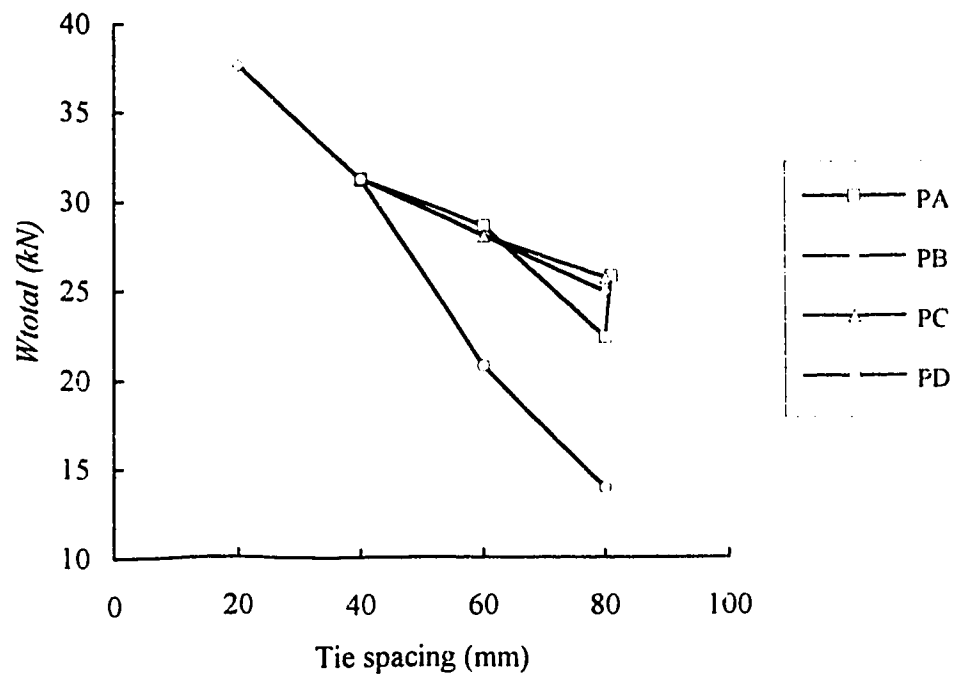
Fig. 6.16 $P_2/P_1$ values for Series PA, PB, PC and PD

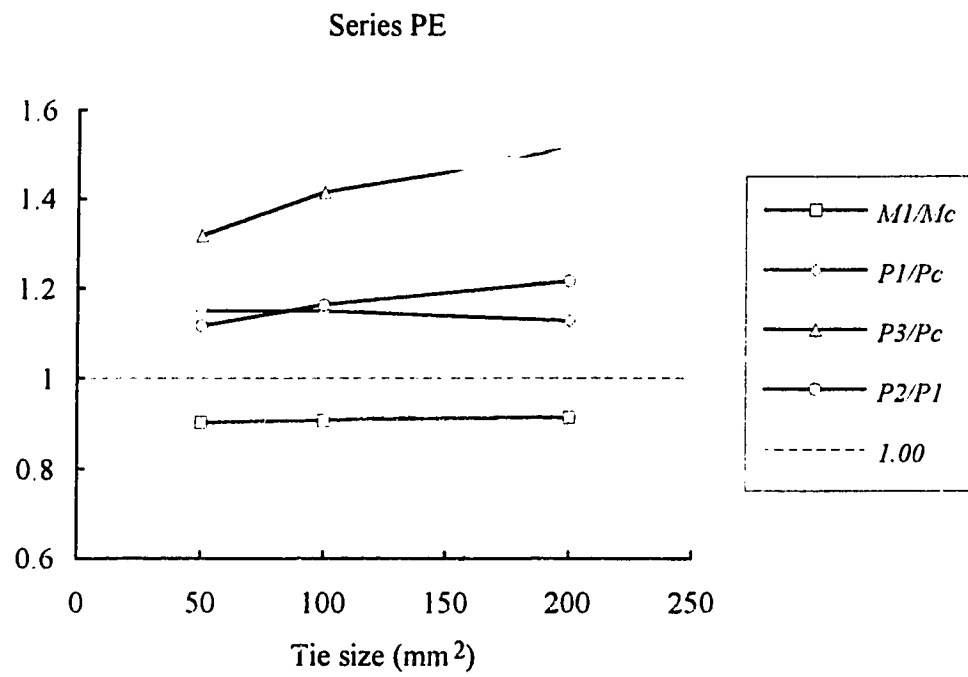Fig. 6.17 $W_{total}$ values for Series PA, PB, PC and PD

Series PE

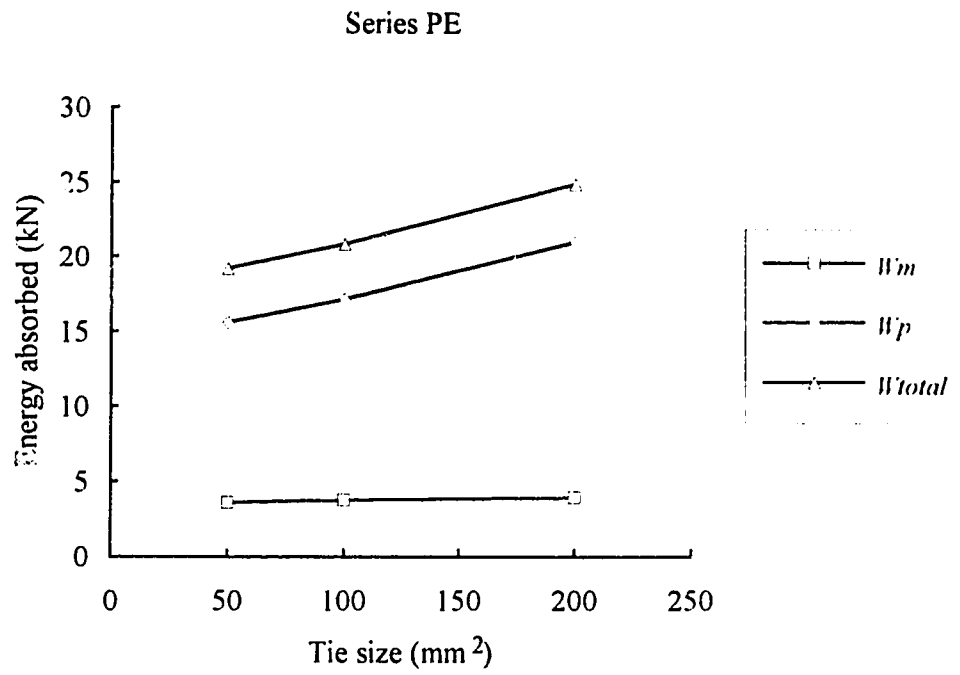Fig. 6.18 $M_1/M_c$, $P_1/P_c$, $P_3/P_c$ and $P_2/P_1$ values for Series PE

Series PE



Fig. 6.19 $W_m$, $W_p$ and $W_{total}$ values for Series PE
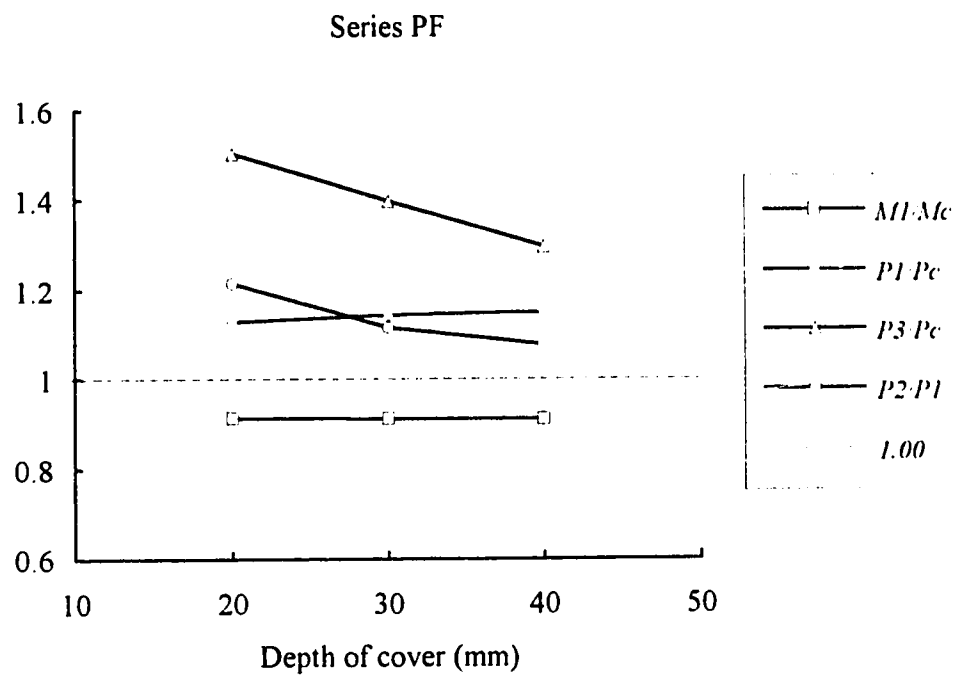
Series PF

Fig. 6.20 $M_1/M_c$, $P_1/P_c$, $P_3/P_c$ and $P_2/P_1$ values for Series PF
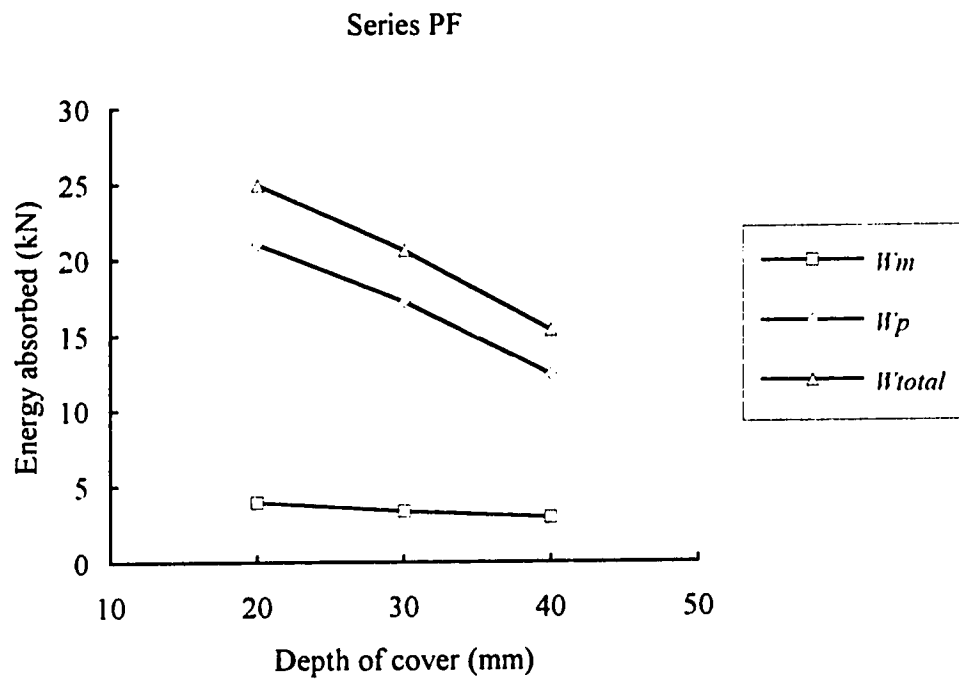
Series PF



Fig. 6.21  $W_m$, $W_p$ and $W_{total}$ values for Series PF
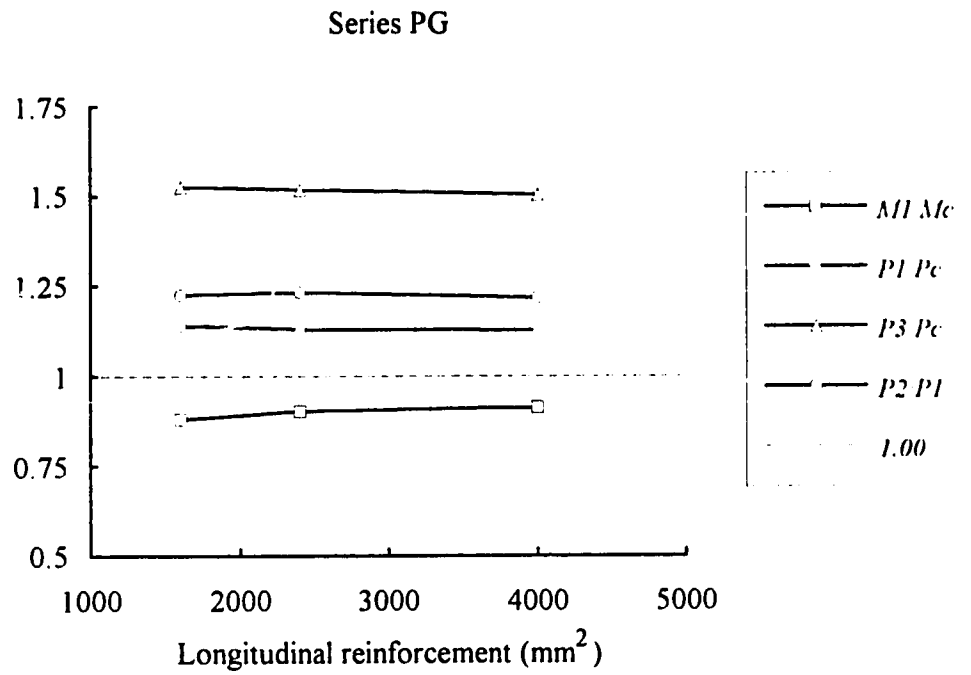
Series PG



Fig. 6.22  $M_1/M_c$, $P_1/P_c$, $P_3/P_c$ and $P_2/P_1$ values for Series PG
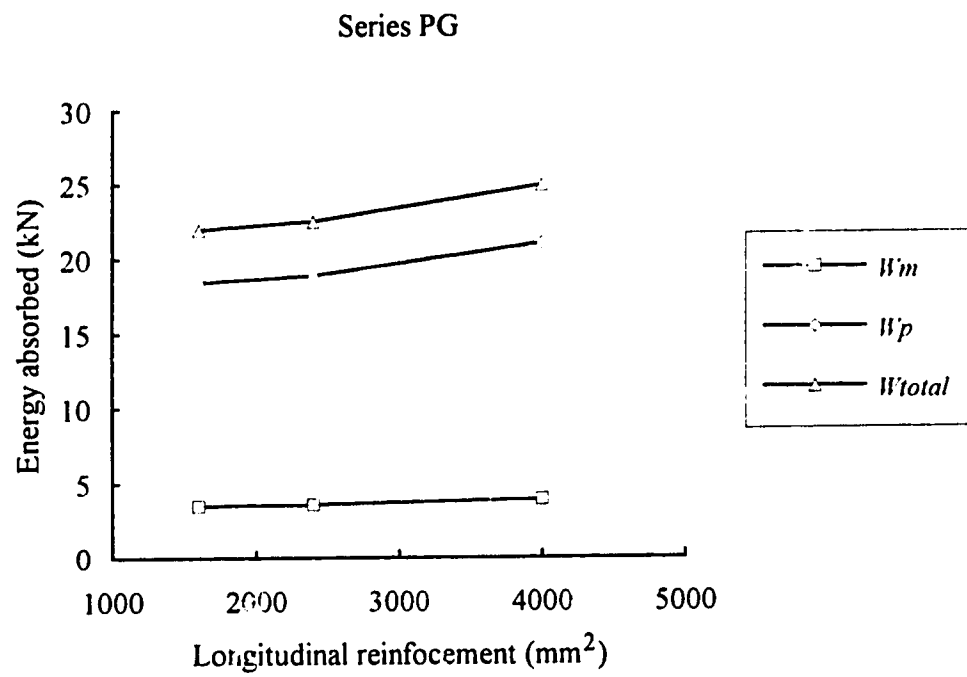
Series PG

Fig. 6.23   $W_m$, $W_p$ and $W_{total}$ values for Series PG

Series PV13

Fig. 6.24 $M_l/M_c$, $P_l/P_c$, $P_3/P_c$ and $P_2/P_l$ values for Series PV13

173
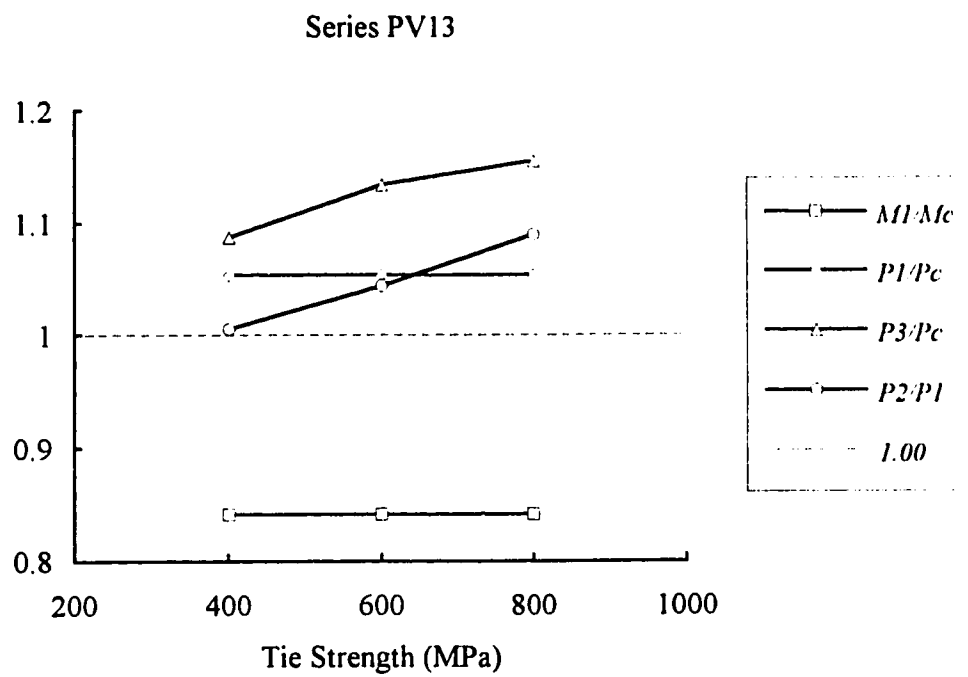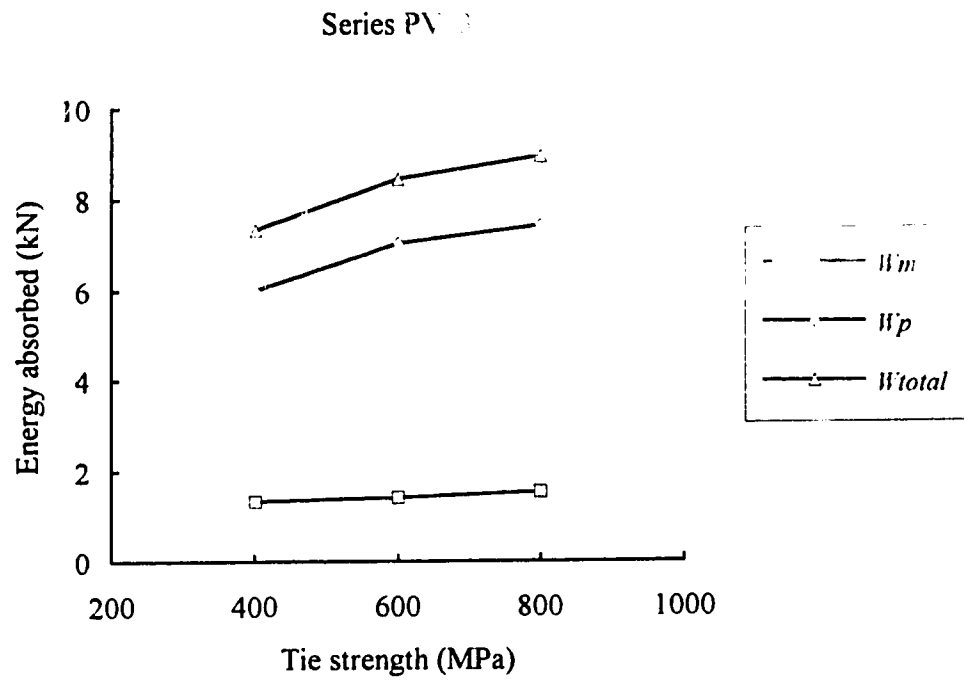
Series PV13

Fig. 6.25  $W_m$, $W_p$ and $W_{total}$ values for Series PV13

174

Distance from mid-plane:

Specimen PD1

Axial stress (MPa)

Distance from center line (mm)

Fig. 6.26   Axial stress distribution pattern at moment peak (Point 1) for Series PD

Fig. 6.27 Axial stress distribution pattern at Point 2 for Series PD

Fig. 6.28  $K_1K_3$ values vs concrete strength

Fig. 6.29  $K_2$ values vs concrete strength

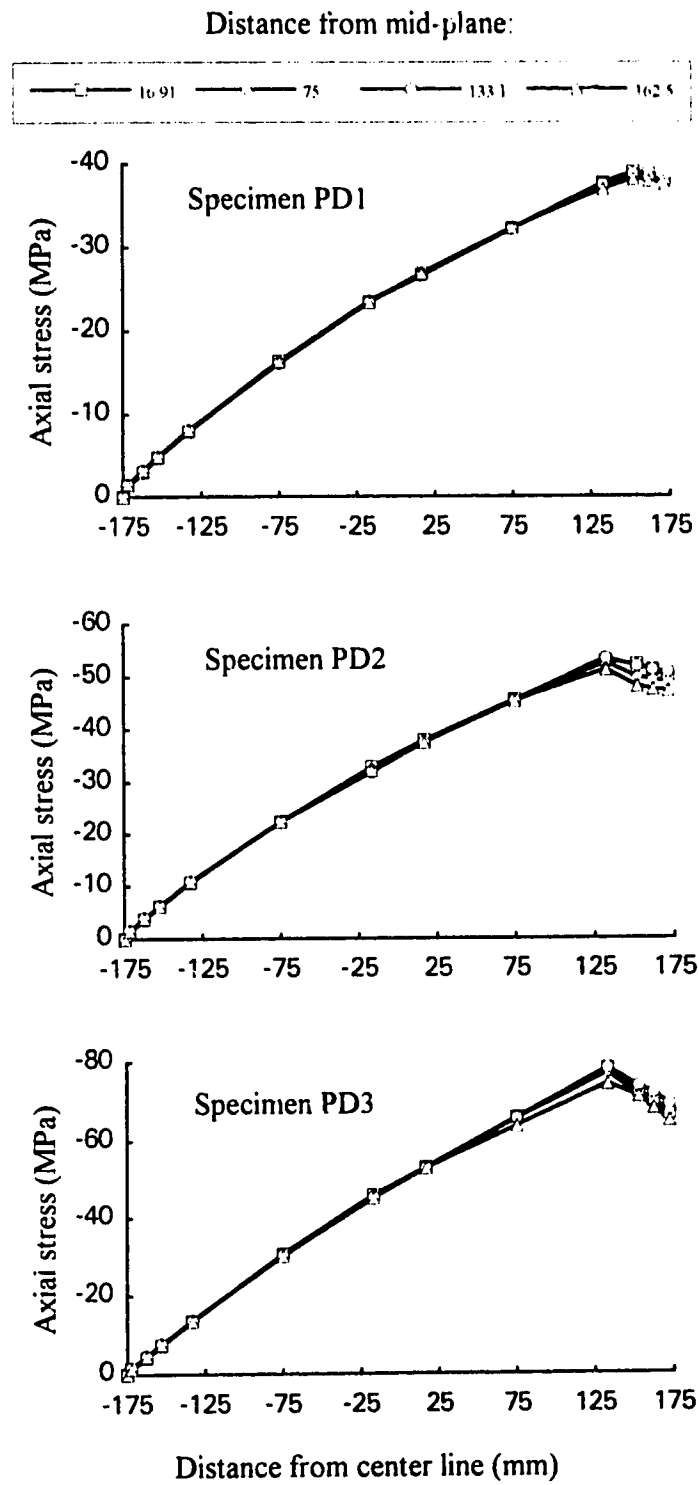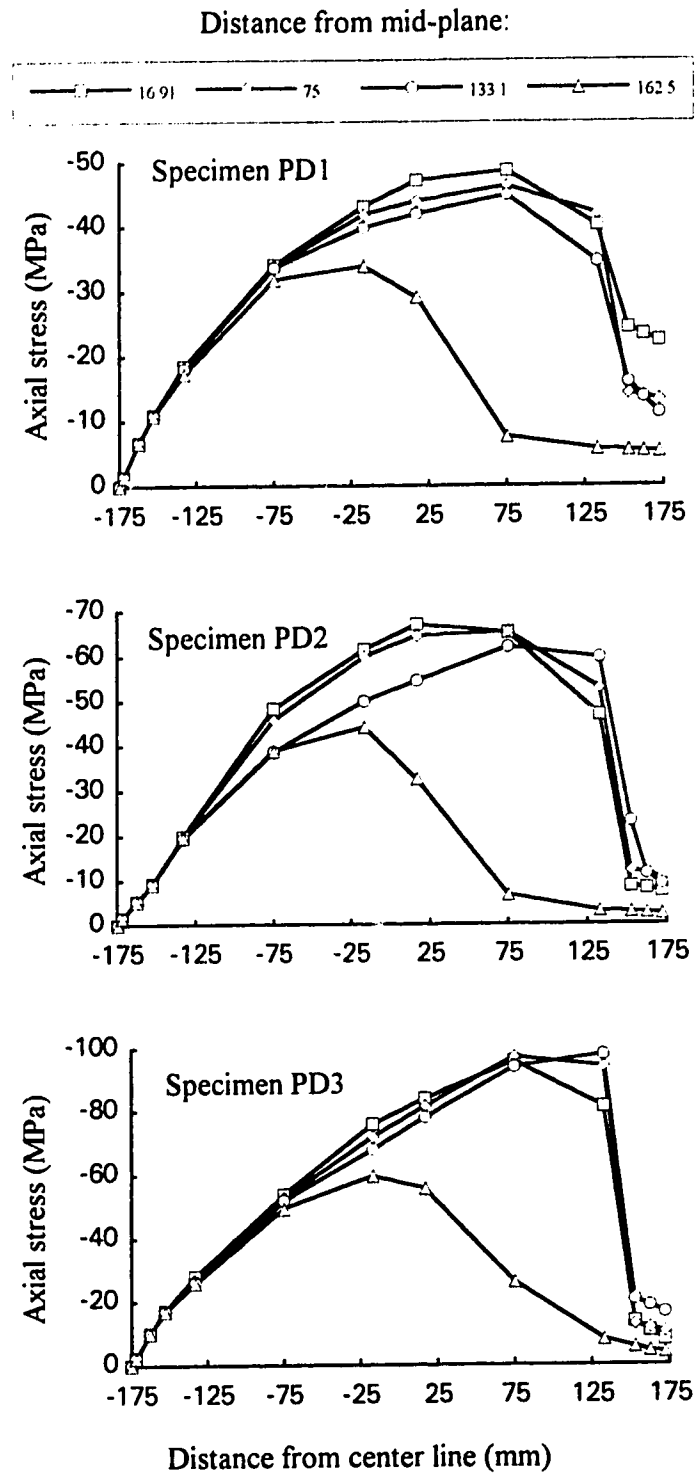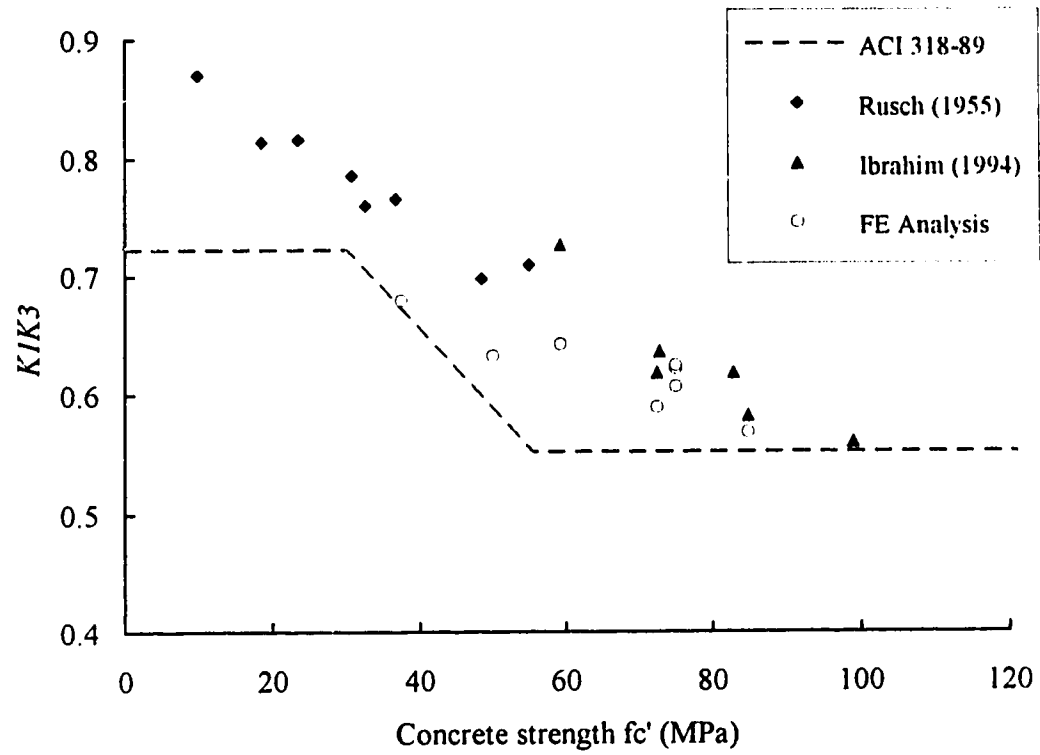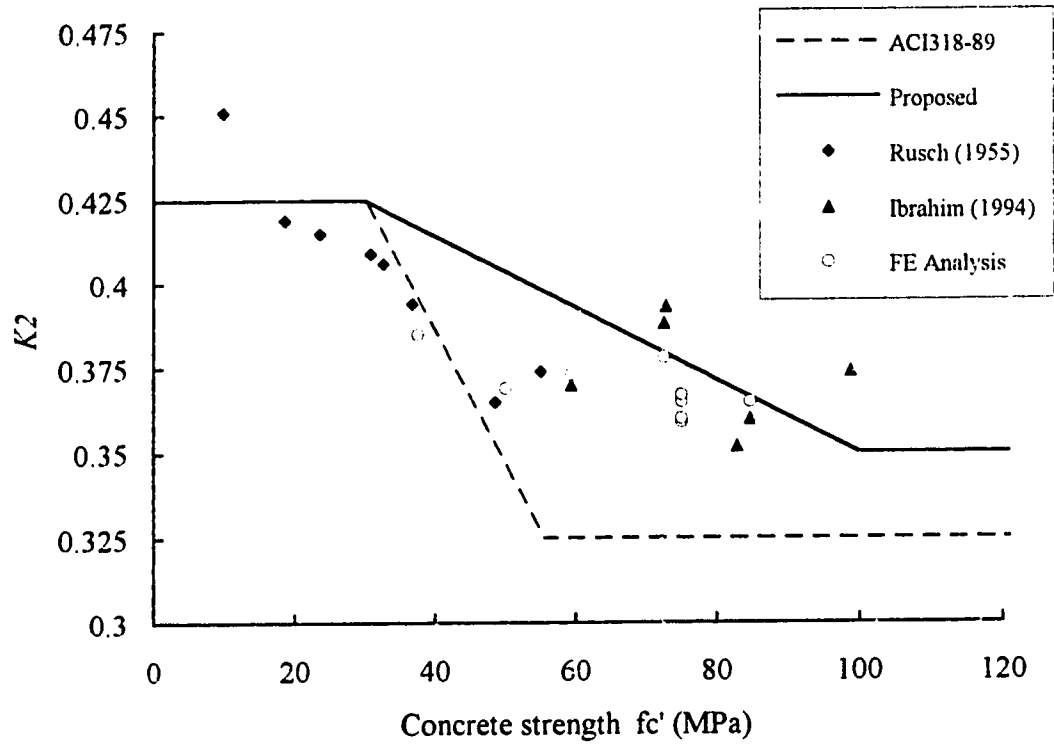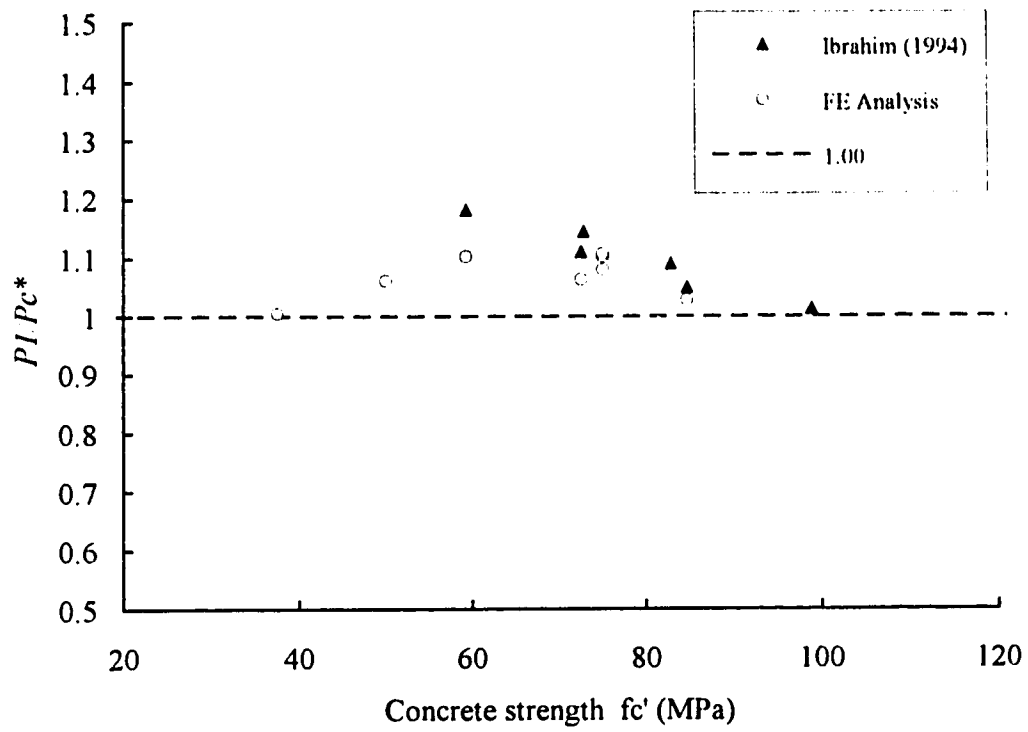Fig. 6.30 $P_l / P_c^*$ values vs concrete strength
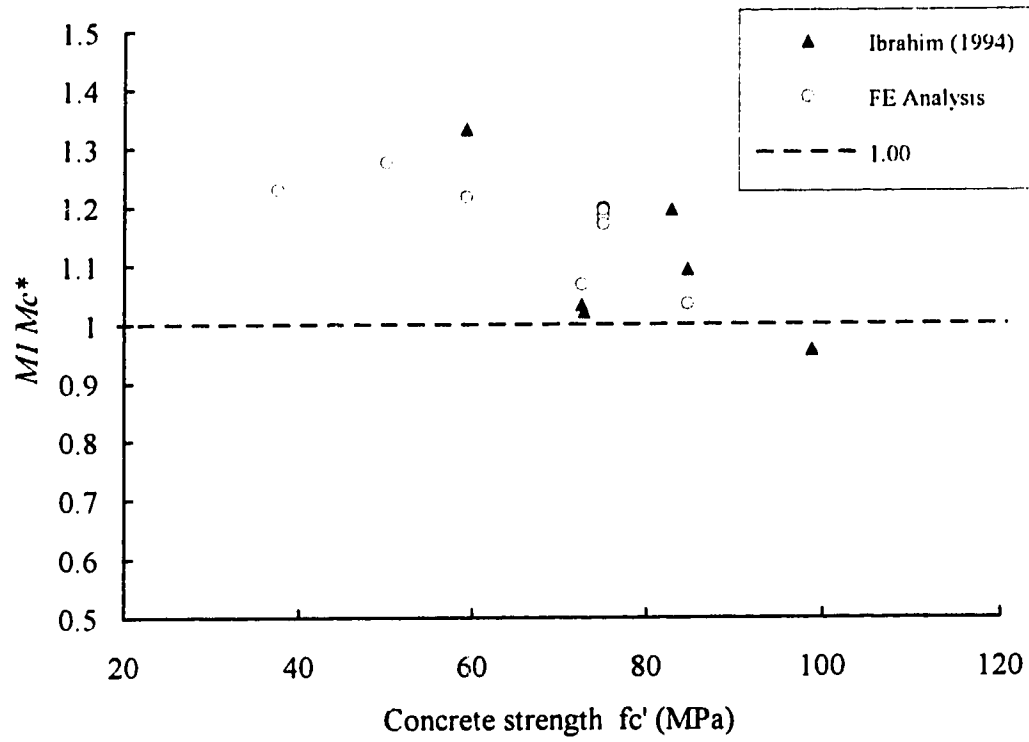
Fig. 6.31 $M_I$ $M_c^*$ values vs concrete strength

# CHAPTER SEVEN

# SUMMARY, CONCLUSIONS AND RECOMMENDATIONS

## 7.1 Summary

This study started with a material test program to define the mechanical properties of three high strength concretes containing silica fume. The test program consisted of nine uniaxial compression tests, nine split cylinder tests, nine notched beam tests, and 33 triaxial compression tests. The concrete was designed to have compressive strength of 60, 90 and 120 MPa.

Based on the results of the material tests, a fracture energy-based non-associated plastic model originally proposed by Pramono and Willam (1989) was modified and calibrated for high strength concrete. The model was extended to have the capacity for three-dimensional stress analysis of concrete structures.

Verification of the model was made by analyzing four tied high strength concrete columns tested by Ibrahim and MacGregor (1994). The finite element analysis has successfully captured the load-deformation response, along with important features such as the strain softening and spalling of the cover, the development of triaxial stress state of concrete in the column core, and the yielding of ties. The failure mechanism of tied high strength concrete columns was discussed.

A parametric study on tied high strength concrete columns subjected to eccentric loading was conducted. A total of 21 specimens forming nine series were analyzed. The parameters involved were the configuration, size and yielding strength of the ties, concrete strength, depth of cover, and amount of longitudinal reinforcement. The behavior of these specimens in both pre-peak and post-peak regimes was discussed.

Results of the parametric study were used to examine the performance of the related current ACI Code sections. Suggestions were made on the amendment of the parameters defining the ACI rectangular stress block.

## 7.2 Conclusions

(1) Based on the results of the material test, it was concluded that although the tensile strength and fracture energy increase with increasing compressive strength, high strength concrete is less ductile than normal concrete in both tension and compression. This conclusion has been reached by a number of investigators. It was also concluded that confinement of the concrete will increase the maximum and residual compressive strength significantly and also improve the ductility of the concrete. A relationship between compressive strength and confining pressure was proposed in Eq. 2.5. The confinement was found to be more effective than reported in the literature.

(2) Analysis of four of the tied high strength concrete columns tested by Ibrahim and MacGregor (1994) provided a theoretical insight into the failure mechanism. It was found that the failure mode of tied high strength concrete columns varies with the amount of confinement provided by the ties. For poorly confined columns, the post-peak behavior is brittle with the formation of a localized damage zone. For well confined columns, the damage zones are distributed and the post-peak behavior is ductile.

(3) Based on the results of the parametric study, it was found that the ties have no effect on the peak moment and pre-peak behavior. However, the post-peak performance of tied columns is affected by the amount of transverse reinforcement. Increasing the cover depth, reducing the amount of transverse reinforcement, and the use of improper tie configurations are responsible for poor ductility behavior and poor post-peak performance.

(4) It was found that minimum requirement for transverse reinforcement in columns in seismic zones in the ACI Code is sufficient and necessary in order to ensure a non-brittle performance of tied high strength concrete columns. However, the ACI

rectangular stress block over-estimates the moment capacity of tied high strength concrete columns. It was suggested that the lever arm of the resultant of the ACI assumed rectangular stress block be reduced for high strength concrete members.


## 7.3 Recommendations for Future Study

### 7.3.1 Material Test

Mechanical properties of high strength concrete vary with material mixes and test conditions. More tests are needed to reach a conclusive understanding of the new material, in particular in the presence of small lateral tensile stresses. Future work on triaxial compressive behavior of high strength concrete is also advised to monitor the volumetric strain. This information would allow a better definition of the stresses in the transverse reinforcement.


### 7.3.2 Performance of Tied High Strength Concrete Columns under Cyclic Loading

Tests of tied low and medium strength concrete columns under cyclic loading have been done by a number of investigators (e.g. Ozcebe et al. (1987)). Experimental and analytical investigations are needed to reach a better understanding of the behavior of tied high strength concrete columns subjected to seismic loading and factors affecting such response. The study will provide a background for examining the seismic design codes related to tied high strength concrete columns.


### 7.3.3 A More Realistic Representation of Longitudinal Reinforcement

Based on experiments of tied concrete columns, Yong et al. (1988) concluded that increasing the number of longitudinal bars and distributing them around the core perimeter increased the effectiveness of the confinement of the concrete core. Ibrahim and MacGregor (1994) concluded that rectangular specimens with very light confinement

reinforcement failed when the concrete cover spalled off with buckling of longitudinal bars near the compression face. These findings suggest that the flexural stiffness of longitudinal reinforcement could be a factor affecting the concrete performance. To include this consideration into the analysis, the longitudinal reinforcement has to be modeled with three dimensional beam-column elements. The material model for reinforcement must include an elastic-plastic-strain hardening behavior with strain reversal provisions. There has been only limited published research in this field. Mau et al. (1989) developed a special beam-column element for modeling the reinforcement. The work was done on a theoretical basis and was not extended to practical problems.

Perhaps the most difficult part is the modeling of the interface between the reinforcement and concrete. Initially well embedded in concrete, longitudinal bars provide some confinement to the core like ties do. Upon spalling of the cover, the adjacent longitudinal bars are partially exposed to air and can separate from the core. It will be helpful to verify the required theoretical background before a finite element analysis of the complete problem is conducted.

# REFERENCES

Abdel-Halim, M.A.H., and Abu-Lebdeh, T.M. (1989), "Analytical Study for Concrete Confinement in Tied Columns", *Journal of Structural Engineering, Vol.115, No.11, November, 1989., ASCE*, pp.2810-2828.

ACI 318-89 (1989),"Building Code Requirements for Reinforced Concrete", *ACI Committee 318, American Concrete Institute*, Detroit, 1989, 353pp.

Ahmad, S.H., and Shah, S.P. (1982), "Stress-Strain Curves of Concrete Confined by Spiral Reinforcement", *ACI Journal, Vol.79, Nov.-Dec.*, pp.484-490.

Bartlett, F. M. and MacGregor, J. G. (1994), *Assessment of Concrete Strength in Existing Structures*, Structural Engineering Report No. 198, Department of Civil Engineering, University of Alberta, 293pp.

Bazant, Z. P. (1976), "Instability, Ductility, and Size Effect in Strain-Softening Concrete", *Journal of Engineering Mechanics, ASCE, Vol.102, No.EM2*, April 1976, pp.331-344.

Bazant, Z. P., and Kim, S. S. (1979), "Plastic-Fracturing Theory for Concrete", *Journal of Engineering Mechanics, ASCE, Vol.105, No.EM3*, 1979, pp.407-428.

Bazant, Z. P., and Ozbolt, J. (1992), "Compressive Failure of Quasibrittle Material: Nonlocal Microplane Model", *Journal of Engineering Mechanics, ASCE, Vol.118, No.3*, March 1992, pp.540-556.

Bjerkeli, L., Tomaszewicz, A., and Jensen, J.J. (1990), "Deformation Properties and Ductility of High Strength Concrete", *Utilization of High Strength Concrete, Proceedings, Second International Symposium in Berkeley, California*, pp.215-238.

CAN3-A23.3 M84 (1984), "Design of Concrete Structures for Building", *Canadian Standard Association*, Rexdale, Ontario, Canada, December, 1984, 280pp.

Carrasquillo, R. L., Nilson, A. H. and Slate, F. D. (1981), "Properties of igh Strength Concrete Subjected to Short-Term Loading," *ACI Journal*, May-June, 1981, pp.171-178.

CEB/FIP Report (1991), *High Strength Concrete - State of the Art Report, 1991.*

Cedolin, L., Crutzen, Y.R.J., and Deipoli, S. (1977), "Triaxial Stress-Strain Relationship for Concrete", *Journal of Engineering Mechanics, ASCE,* 103(3), pp.423-439.

Chen, B., and Mau, S.T. (1989), "Recalibration of a Plastic-Fracturing Model for Concrete Confinement", *Cement and Concrete Research, Vol.19,* 1989, pp.143-154.

Chen, W. F., and Han, D. J. (1988), *Plasticity for Structural Engineers,* Springer-Verlag, NY Inc., 1989.

Cusson, D., and Paultre P. (1994), "High Strength Concrete Columns Confined by Rectangular Ties", *Journal of Structural Engineering, Vol.120, No.3, March, 1994. ASCE,* pp.783-804.

Dal Busco, A. (1988), "Deformabilite et Capacite Portante des Colonnes en Beton Arme", *These No. 734, Ecole Polytechnique Federale de Lausanne,* 1988.

Darwin, D and Pecknold, D.A. (1977), "Non-linear Biaxial Stress-Strain Law for Concrete", *Journal of Engineering Mechanics Division, ASCE, Vol.103, No. EM2,* pp.229-241.

Gopalaratnam, V. S. and Shah, S. P. (1984), "Softening Response of Concrete in Direct tension", *Technological Institute Report, Northwestern University, Evanston,* 1984.

Han, D. J., and Chen, W. F. (1985), "A Nonuniform Hardening Plasticity Model for Concrete Materials", *Mech. of Materials, 4(4),* pp.283-302.

Hibbitt, Karlsson and Sorensen Inc. (1993), *ABAQUS User's Manuals.*

Hillerborg, A., Modeer, and Peterson, P. E. (1976), "Analysis of Crack Formation and Crack Growth in Concrete by means of Fracture Mechanics and Finite Elements", *Cement and Concrete Research,* 6, pp.776-781.

Hillerborg, A. (1985A), "The Theoretical Basis of a Method to Determine the Fracture Energy $G_F$ of Concrete", *Rilem Technical Committee 50,* 1985.

Hillerborg, A. (1985B), "Numerical Methods to Simulate Softening and Fracture of Concrete." *Fracture Mechanics of Concrete: Structural Application and Numerical Calculation*, Ed. by Sih, C.C., Tomaso, D. and Kluwer, A., Academic Publishers, U.S.A., pp.141-170.

Hillerborg, A. (1985C), "Results of Three Comparative Test Series to Determine the Fracture Energy $G_F$ of Concrete", *Materials and Structures*, No.107, 1985.

Hurlbut, B. J. (1985), *Experimental and Computational Investigation of Strain-Softening in Concrete, Thesis Presented to the University of Colorado*, Boulder, Colorado, in partial fulfillment of the requirements for the degree of Master of Science.

Ibrahim, H. H. H., and MacGregor, J. G. (1994), Flexural Behavior of High Strength Concrete Columns, Structural Engineering Report No. 196, Department of Civil Engineering, University of Alberta, 197pp.

Jensen, J.J. and Bjerkeli, L. (1990), "Effect of Water Pressure on Concrete Structures." *Water Absorption, Static Strength and Strain Development Tests, SINTEF report*, STF65, F87037.

Launay, P. and Gachon, H. (1970), "Strain and Ultimate Strength of Concrete under Triaxial Stress", *SP-34, ACI, Vol.1*, 1970, pp.269-282.

MacGregor, J. G. (1992), *Reinforced Concrete Mechanics and Design*, Second Edition, Prentice Hall, Englewood Cliffs, New Jersy.

Madsen, H. O., Krenk, S. and Lind, N.C. (1986), *Method of Structural Safety*, Prentice-Hall Inc, Engle wood Cliffs New Jersy.

Maekawa, K., and Okamura, H. (1983), "The Deformational Behavior and Constitutive Equation of Concrete Using the Elasto-Plastic and Fracture Model", *J. Fracture Engrg., University of Tokyo (B), XXXVII(2)*, pp.253-328.

Mander, J.B., Priestley, M.J.N, and Park, R. (1988) "Observed Stress-Strain Behavior of Confined Concrete", *Journal of Structural Engineering, Vol.114, No.8, August, 1988, ASCE*, pp.1827-1849.

Martinez, S., Nilson, A.H., Slate, F.O. (1984), "Spirally Reinforced High-Strength Concrete Columns", *ACI Journal Sept.-Oct.* 1984.

Mau, S.T., and El-Mabsout, M. (1989), "Inelastic Buckling of Reinforcing Bars", *Journal of Engineering Mechanics, Vol.115, No.1, January, 1989, ASCE*, pp.1-17.

Mills, L. L., and Zimmerman, R. M. (1970), "Compressive strength of plain concrete under multiaxial loading conditions", *ACI Journal*, October, 1970.

Morales, S. M., Nilson, A. H. and Slate, F. O. (1982), *Spirally-Reinforced High Strength Concrete Columns*, Department of Structural Engineering, Cornell University, August 1982, Report, No. 82-10.

Muguruma, H., Watanabe, F., Iwashimizu, T., and Mitsueda, R. (1983), "Ductility Improvement of High Strength Concrete by Lateral Confinement", *Trans. Japan Concrete Institute, Vol.5*, pp.403-410.

Ngo, D., and Scordelis, A. C. (1967), "Finite Element Analysis of Reinforced Concrete Beams", *ACI Journal*, 64(3), pp.152-163.

Ozcebe, G. and Saatcioglu, M. (1987), "Confinement of Concrete Columns for Seismic Loading", *ACI Structural Journal*, July-Aug., 1987, pp.308.

Palaniswamy, R. and Shah, S. P. (1974), "Fracture and Stress-Strain Relationship of Concrete under Triaxial Compression." *Journal of the Structural Division, Vol. 100, No. ST5, ASCE*, May, 1974, pp.901-916.

Peterson, P. E. (1980), "Fracture Energy of Concrete: Practical Performance and Experimental Results." *Cement and Concrete Research*, Vol.10, pp.91-101.

Pramono, E., and Willam, K. (1989), "Fracture Energy-Based Plasticity Formulation of Plain Concrete", *Journal of Engineering Mechanics, ASCE, Vol.115, No.6*, 1989, pp.1183-1204.

Reinhart, H. W. (1984), "Fracture Mechanics of an Elastic Softening Material Like Concrete", *Heron Publication, Vol.29, No.2*, 1984, pp.42.

Richart, F. E., Brandtzaeg, A., and Brown, R. L. (1928), *A Study of the Failure of Concrete under Combined Compressive Stresses, Bulletin 185, University of Illinois Engineering Station, Urbana, Ill.*, Nov. 1928, pp.104.

RILEM Technical Committee 50 (1985), "Determination of the Fracture Energy of Mortar and Concrete by Means of Three-Point Load Tests on Notched Beams", *RILEM Draft Recommendation, Materiaux et Constructions, Vol.18, No.106,* 1985, pp.285-290.

Romano, M. (1969), "On Leon's Criterion", *Meccanica,* pp.48-66.

Rusch, H. (1955), "Tests on the Strength of Flexural Compression Zone", *Bulletin No.120, Deutscher Ausschuss Fur Stahlbeton, Berlin,* 94pp.

Sargin, M., Ghosh, S.K., and Handa, V.K. (1971), "Effects of Lateral Reinforcement upon the Strength and Deformation Properties of Concrete", *Magazine of Concrete Research, Vol.23, No.75-76, June-Sept,* pp.99-110.

Scott, B.D., Park, R. and Priestley, M.J.N. (1982), "Ductility of Square-Confined by overlapping hoops at low and high strain rates", *ACI Journal, 97, Jan.-Feb., 1982,* pp.13-17.

Sheikh, S.A, and Yeh, C.C. (1990), "Tied Concrete Columns under Axial Load and Flexure", *Journal of Structural Engineering, Vol.116, No.10, October, 1990, ASCE,* pp.2780-2800.

Slate, F. O., Nilson, A. H. and Martinez, S. (1987), "Mechanical Properties of High-Strength Lightweight Concrete", *May-June 1987 ACI Journal,* pp.606-613.

Stankowski, T., and Gerstle, K. H. (1985), "Simple Formulation of Concrete Behavior under Multiaxial Load Histories", *ACI J. 82(3),* pp.213-221.

Swamy, R. N., (1986), "Properties of High Strength Concrete", *Cement, Concrete and Aggregates, CCAGDP, Vol.8, No.1,* Summer 1986, pp.33-41.

von Mier, J. G. M. (1984), *Strain-Softening of Concrete under Multiaxial Loading Conditions,* Thesis Presented to De Technische Hogeschool Eindhoven, the Netherlands, in Partial Fulfillment of the Requirements for the Degree of Doctor of Philosophy.

Willam, K., Hurlbut, B., and Sture, S. (1985),. "Experimental and Constitutive Aspects of Concrete Failure." *Proc. US-Japan Seminar on Finite Element Analysis of Reinforced Concrete Structure, Tokyo, 1985, ASCE, Special Publication*, New York, N.Y., pp.226-254.

Xie, J., Elwi, A. E., and MacGregor, J. G. (1994),"Mechanical Properties of Three High Strength Concretes Containing Silica Fume", forthcoming, *ACI Material Journal*.

Yamaguchi, E., and Chen, W. F. (1991), "Microcracking Propagation Study of Concrete under Compression", *Journal of Engineering Mechanics, ASCE, Vol.117, No.3*, 1991, pp.653-672.

Yong, Y.K., Nour, M.G., and Nawy, E.G. (1988), "Behavior of Laterally Confined High Strength Concrete under Axial Loads", *Journal of Structural Engineering, Vol.114, No.2, February, 1988, ASCE*, pp.332-351.